Developing an Enhanced Photogrammetric Methodology for Mapping Water Bodies Using Low-cost Drones

by

Bernard Essel BSc., MSc.

This thesis is presented in fulfillment of the requirements for the degree of Doctor of Philosophy

Department of Geography

Faculty of Social Sciences

Maynooth University

May, 2024

Head of the Department: Dr. Stephen McCarron

Supervisors: Dr. Conor Cahalane & Prof. John McDonald

Acknowledgments

This thesis would not have been possible without the assistance and support of many people. First and foremost, I would like to express my deepest gratitude to my supervisors, Dr. Conor Cahalane and Prof. John McDonald. Your advice throughout the four-year period challenged me to improve every aspect of this thesis. A special thanks to Conor for the exceptional mentorship I have received – it is truly irreplaceable. I am incredibly grateful for the countless opportunities and unwavering support you offered me. As the saying goes, one can repay a loan of gold, but one can never repay a debt of kindness.

I would also like to extend my thanks to my family, friends, and MSCI members for their unwavering support. This has been a long journey, but your patience and encouragement provided me with the strength to complete it. I would like to thank Mick and everyone in the Department of Geography who, in one way or another, offered a helping hand – thank you!

I owe a special debt of gratitude to my wife, Araba. Your endless patience, support, and care over the past few years have been invaluable. You have been there for me from the beginning to the end, and you understood the journey better than anyone. Thank you so much for all the unseen work you have done.
Finally, though words may fail me, I express my deepest gratitude to God for everything. I owe my achievements to Him.

The research presented in this thesis was funded by the Maynooth University John and Pat Hume Scholarship and with additional financial support from the MU HEA Covid-19 Costed Extension Fund (2023).

Abstract

Water bodies face continuous pressure from human activities, particularly from nitrogen and phosphorus from agricultural activities and urban wastewater discharges, leading to water pollution. Studies have shown that monitoring water quality using the traditional method of water sampling is time-consuming, labour-intensive, costly and cannot be done frequently. In environmentally sensitive areas, these techniques can encounter additional restrictions in relation to access, team size, etc. Studies have indicated that although satellite-based imagery has clear potential as a non-contact methodology, it has limitations due to the coarse spatial resolution and potential for the site to be obscured due to cloud cover. Additionally, while commercial or airborne imagery can provide high spatial resolution, they are often expensive to use. Drones have shown the potential to provide very high spatial resolution at regular intervals and at a lower cost, acting as a middle ground between satellite, manned aircraft, and terrestrial in-situ methods. However, issues concerned when mapping water bodies using low-cost drones are largely unknown. To date, no methods involving low-cost drones have been investigated to (i) understand their suitability, (ii) the associated errors have never been quantified, and (iii) there have been no attempts to improve accuracy. To undertake this investigation, a theoretical analysis was first carried out to benchmark the accuracy of the Direct Georeferencing (DG) method for mapping water bodies and validate with real-world data. Following this, the errors associated with the DG method were identified and quantified, resulting in the development of photogrammetric methods to improve accuracy by correcting for these errors. The first method developed an analytical photogrammetric approach to improve the accuracy of drone imagery over water. The second method was an advanced approach that exploited the shore to enhance the accuracy of drone imagery when mapping water bodies. The final approach developed a scalable method that could improve the accuracy and map water bodies at different geographic scales. The developed methods presented a novel approach to improve the accuracy of drone imagery for mapping water bodies. Institutions,

organisations and researchers can utilise the methods developed in this thesis to generate accurate drone imagery of water bodies which can be used to measure various water quality parameters.

Acronyms

AKANZE	Accelerated-KAZE
AT	Aerial triangulation
ARMFET	Analytical Rectification Method for Featureless Terrain
ANN	Artificial Neural Network
CHL-A	Chlorophyll-a
DL	Deep Learning
DOF	Degrees of Freedom
DGPS	Differential GPS
DEM	Digital Elevation Models
DSM	Digital Surface Model
DG	Direct Georeferencing
DLT	Direct Linear Transform
ECEF	Earth-Centered Earth-Fixed Coordinates
EPA	Environmental Protection Agency
OEEPE	European Organization for Experimental Photogrammetric Research
EuroSDR	European Spatial Data Research Group
EXIF	Exchangeable Image File Format
EOP	Exterior Orientation Parameters
GNSS	Global Navigation Satellite System
GPS	Global Positioning System
GCP	Ground Control Points
IMU	Inertial Measurement Unit
INS	Inertial Navigation System
ISO	Integrated Sensor Orientation
IOP	Interior Orientation Parameters
ICC	Intra-Class Correlation

ITM	Irish Transverse Mercator
KNN	K-Nearest Neighbours
MAE	Mean Absolute Error
NED	North-East-Down
ORB	Oriented FAST and rotated BRIEF
PPK	Post-Processed Kinematic
PIL	Python Imaging Library
RF	Random Forest
RANSAC	Random Sample Consensus
RFM	Rational Functional Models
RPAS	Remotely Piloted Airborne Systems
RMSE	Root Mean Square Error
SIFT	Scale-Invariant Feature Transform
SVD	Singular Value Decomposition
SURF	Speeded Up Robust Features (SURF)
SfM	Structure-from-Motion
SVM	Support Vector Machine
SDG	Sustainable Development Goal
TSS	Total Suspended Solids
WFD	Water Framework Directive
dt	Tilt displacement
3D	Three-dimensional
2D	Two-dimensional

Table of Contents

Acknowledgements i

Abstract iii

Acronyms v

1 Introduction **1**

1.1 Water Quality Monitoring 2

1.1.1 Surface Water Bodies and Regulatory Requirement in Ireland 3

1.1.2 In-Situ Water Monitoring 5

1.2 Linking Remote Sensing Concepts with Water Quality Monitoring Needs 7

1.2.1 How is Scale and Time Relevant for Water Quality Monitoring? 7

1.3 What Platforms can Provide the Required Spatial and Temporal Resolution? 10

1.3.1 Satellites - Trading Spatial for Temporal Resolution 10

1.3.2 Flying Lower - the Role of Airborne Remote Sensing 13

1.3.3 The Advent of New Lightweight Tech - Drone Photogrammetry 15

1.4 Can Low-cost Drones Play a Role in Water Quality Monitoring? . 17

1.4.1 Definition of a Low-cost Drone 17

1.4.2 Categories and Classification 18

1.4.3 Work to Date: Low-Cost Drones for Monitoring Water Quality 21

1.5 Gaps in Current Knowledge for Mapping Water Bodies with Drones 23

1.6 Research objectives 26

1.6.1 Objective 1 26
1.6.2 Objective 2 26
1.6.3 Objective 3 26
1.6.4 Objective 4 27
1.7 Research Assumptions 27
1.7.1 Assumption 1 27
1.7.2 Assumption 2 27
1.7.3 Assumption 3 28
1.7.4 Assumption 4 29
1.8 Terminologies for Drone Image Outputs 29
1.9 Thesis Structure 30
1.10 Publications 32

2 Current State of the Art - Literature Review 33
2.1 Introduction 33
2.2 Objective 1- Benchmark and Test DG 34
2.2.1 The Role of DG in Research and Industry 34
2.2.2 Concept of Direct Georeferencing 36
2.2.3 Interior Orientation Parameters 37
2.2.4 Exterior Orientation Parameters 39
2.2.5 Pros and Cons of the DG Method 39
2.2.6 DG, Drones and Water: the Current State of the Field 40
2.2.7 A Possible Solution 41
2.3 Objective 2 - Analyse Errors Associated with Direct Georeferencing 41
2.3.1 History of Navigational Sensors 41
2.3.2 Inertial Measurements Units - the IMU 42
2.3.3 Satellite Positioning - GNSS 48
2.3.4 Navigational Sensors - Influence of Errors on Accuracy . . . 49
2.3.5 Drone Sensor 50
2.3.6 Sensor Mount 51

2.4 Objective 3 - Develop a Method that can Combine Bundle Adjustment and Direct Georeferencing 54
2.4.1 Relevant Photogrammetric Principles 54
2.4.2 Safety in Numbers: the Bundle Adjustment 56
2.4.3 Workflow and Key Components of Bundle Adjustment . . . 56
2.4.4 Integrated Sensor Orientation - ISO 60
2.5 Objective 4 - Automated Image Registration Model 61
2.5.1 Definition of Image Registration 61
2.5.2 Concept of Homography 63
2.5.3 Homography Estimation 66
2.5.4 Machine Learning 66
2.5.5 ML Method 1: K-Nearest Neighbours 66
2.5.6 ML Method 2: Random Forest 67
2.5.7 ML Method 3: Support Vector Machine 69
2.6 Conclusion 71

3 Theoretical Analysis of the Positional Orientation (POSE) Errors 73
3.1 Introduction 74
3.2 Important Assumptions Around the Error Budget 75
3.2.1 GNSS and IMU Errors 75
3.2.2 Sensor Rotational Angles Influence 76
3.3 Design and Development of the Simulator 77
3.3.1 Calculations based on the Collinearity Equations 77
3.3.2 Parameters for the Simulation 78
3.3.3 Implementation of the Simulation in Python 79
3.4 Results of the Theoretical Analysis 81
3.4.1 Test 1: Influence of sensor Rotation Angles on Reconstructed 2D Image 81
3.4.2 Image Skewing due to Sensor Rotation Angles 82
3.4.3 Test 2: Introducing GNSS Error along with Sensor Rotation Angle Influence 85

3.4.4 Test 3: Introducing IMU Error along with Sensor Rotation Angle Influence . . . 86
3.4.5 Test 4: Theoretical Simulation of Combined Effects of Sensor Rotational Angle Influence and GNSS/IMU Error . . . 87
3.5 Discussion . . . 89
3.6 Conclusion . . . 90

4 Developing an Analytical Rectification Method for Featureless Terrain - ARMFET 92
4.1 Introduction . . . 93
4.2 Errors Associated with Direct Georeferencing . . . 94
4.2.1 Error 1 - Ground Principal Point Offset . . . 95
4.2.2 Error 2 - Tilt Displacement . . . 97
4.2.3 Error 3: Effects of Scale Variations . . . 99
4.3 Difficulties of Using GCPs in Improving Accuracy in Water Bodies 100
4.4 Experimental Design . . . 101
4.5 Drone and GNSS Datasets - Planning and Capture . . . 101
4.5.1 Study Area . . . 102
4.5.2 Sensor and Platform . . . 103
4.5.3 Field Survey . . . 105
4.5.4 Additional data . . . 106
4.6 Methods . . . 107
4.6.1 Method 1: Benchmark Dataset Using Bundle Adjustment . 109
4.6.2 Method 2: Image Pre-processing for Direct Georeferencing 110
4.6.3 Method 3: Direct Georeferencing . . . 110
4.6.4 ARMFET - Analytical Rectification Method For Featureless Terrain . . . 114
4.7 Results and Analysis . . . 119
4.7.1 Analysis of the Attitude Angles . . . 119
4.7.2 Effect of Wind Speed on Attitude . . . 120
4.7.3 Effect of Wind Direction on Attitude . . . 123

4.7.4 Comparison of Omega/Phi Angles Against Benchmark Data 125
4.7.5 Evaluation of the Traditional DG method 127
4.7.6 Accuracy Assessment of the ARMFET Approach 129
4.8 Discussion 131
4.9 Conclusion 132

5 ADGEO - An Assisted Direct Georeferencing Approach 134
5.1 Introduction 135
5.1.1 Overview and Assumptions of the ADGEO Method 137
5.2 Data 138
5.2.1 Overview of the Method in Generating the Synthetic Data . 138
5.2.2 Description of the Simulated Attitude Data 141
5.2.3 Validation Dataset 145
5.3 Method 145
5.3.1 Step 1: The Shore - Calculation of Offset Errors 147
5.3.2 Step 2: The Water - Prediction of Offset Errors 149
5.4 Results and Analysis 152
5.4.1 Theoretical Analysis 1: Low Variability Attitude Measurement 152
5.4.2 Theoretical Analysis 2: High variability Attitude Measurement 155
5.4.3 Sensitivity Analysis 157
5.5 Experimental Results 158
5.5.1 Description of the Two Scenarios 158
5.5.2 Planimetric Accuracy 160
5.5.3 Inter-Rater Reliability of the Two Scenarios 161
5.5.4 Influence of Overlapping Percentage on the ADGEO Method 162
5.5.5 Example Results of Images Reconstructed Through Traditional DG and ADGEO Methods 164
5.6 Discussion 168

5.6.1 Accuracy Assessment of the ADGEO Method 168
5.6.2 Planimetric Accuracy 168
5.6.3 Influence of Flight Parameters 170
5.6.4 Reliability of the ADGEO Method 171
5.6.5 Sensitivity Analysis 172
5.6.6 Sources of Errors and Limitations 172
5.7 Conclusion 173

6 AirMAP – An Automated Image Registration Model for Mapping Water Bodies using Multi-Sensor Drone Data 175
6.1 Introduction 176
6.2 Data 178
6.2.1 Description of the Training, Validation and Testing Dataset 178
6.2.2 Statistical Overview of the Datasets 181
6.3 Methods 184
6.3.1 Data Preparation for the ML Model 185
6.3.2 Training and Assessment of the ML model 190
6.3.3 Hyperparameter Selection 191
6.3.4 Selection of ML Model 191
6.3.5 Geometric transformation of the model 191
6.3.6 Evaluation of the Trained Model 192
6.4 Results 193
6.4.1 Analysis of Feature Detectors 193
6.4.2 Analysis of the RANSAC threshold 194
6.4.3 Evaluation of the ML Models on Validation Dataset 195
6.4.4 Accuracy Assessment on Test Data 196
6.5 Discussion 202
6.5.1 Data Quality 202
6.5.2 Evaluation of the ML Model 203
6.5.3 Accuracy Assessment of the AirMAP Method 204
6.5.4 Applicability of the AirMAP Model 206

6.5.5 Limitations of the AirMAP Model 207
6.6 Conclusion 208

7 Conclusions and Future Works **209**
7.1 Thesis Summary 210
7.1.1 Objective 1: Benchmark and Test the Accuracy of the DG Method 210
7.1.2 Objective 2: To Analyse the associated errors in the images derived using the DG method and propose an analytical photogrammetric method to improve them 210
7.1.3 Objective 3: To develop a method that integrates BA and DG in a single workflow by using the features from the shore as a reference to enhance the accuracy of drone imagery over water bodies 211
7.1.4 Objective 4: To develop a method that aims to improve accuracy, efficiency, and scalability for generating orthoimagery for larger water bodies 211
7.2 Main Contributions to the Field of Mapping Water Bodies with Low-cost Drones 212
7.2.1 Benchmarking the DG Method 212
7.2.2 Developing an Analytical Photogrammetric Method 213
7.2.3 Developing a Method that Exploits the Shore 213
7.2.4 Scaling for Mapping Larger Water Bodies 214
7.3 Future Work 215
7.3.1 Additional Data Source 215
7.3.2 Algorithm Improvements 216
7.4 Final Remarks 217

Bibliography **218**

Appendices **244**

List of Figures

1.1 The ecological status of Irish lakes 4
1.2 Spatial distribution of Phosphorus measurements across Irish lakes 6
1.3 An experiment of water turbidity maps derived from three types of drone imagery 10
1.4 An example of a drone dataset over Blessington Lake showing how difficult it is to collect tie points over water 24

2.1 Illustration of the DG concept 37
2.2 An Image representing the differences between the ECEF and NED system frame 44
2.3 A graphic showing the sensor frame with the centre being the perspective centre 45
2.4 Illustration of the orientation of a rigid body for a drone in terms of initial position, Roll, Pitch and Yaw 48
2.5 A graphic showing examples of drone sensors 51
2.6 Comparative illustrations of a drone stabilized by gimbal and without gimbal 53
2.7 An graphic representing the standard photogrammetry approach . 55
2.8 A workflow of the BA method which consist of a series of steps to refine the EOPs 57
2.9 Results from Pix4D Mapping software that utilizes the BA technique 59
2.10 Illustration of the ISO method 60
2.11 An image showing the concept of image registration technique . . 62
2.12 An illustration of the initial points correspondence detected between the target and the reference image. 65

2.13 A demonstration of the true point correspondences, where the bad matches have been removed through a filtering algorithm. 65
2.14 Example illustration of KNN where three different 'K' values have been explored 67
2.15 Example illustration of RF where decision trees are used to predict a new data point 69
2.16 Example illustration of SVM where a hyperplane separates data points into different classes 71

3.1 A graphic showing the sensor rotational angles 77
3.2 A theoretical accuracy assessment for the sensor rotational angle influence on a projected point 82
3.3 An illustration of the orientation effects in the X and Y coordinates 84
3.4 A theoretical accuracy assessment for the influence of rotational angles and GNSS error on a terrain point 86
3.5 A theoretical accuracy assessment for all three previous tests . . . 87
3.6 A stacked bar graph showing the reelvant contributions of errors for GNSS, IMU and rotational angle influence in Pitch/Roll 88

4.1 Illustration of the principle of tilt angle 97
4.2 An image representing the principle of tilt displacement error . . . 99
4.3 An illustration explaining the scale variation effect due to tilt . . . 100
4.4 A map showing the location of the study area at Enfield 102
4.5 An image of the Parrot Bluegrass with (a) the Sequoia sensor visible underneath and (b) the sunshine sensor 104
4.6 An image showing a sample grid mission flight plan for the first drone survey across the open field in Enfield 105
4.7 Distribution of 30 GCPs across the open field 106
4.8 A flow diagram leading from the traditional DG process of reconstructing a 2D surface to the application of the ARMFET novel correction method 108

4.9 An image showing the complete transformation matrix where the intrinsic and the extrinsic parameters are combined 114
4.10 An illustration of the workflow involved in rectifying images via analytical photogrammetry 115
4.11 An illustration showing how images are rectified using the ground coordinate from a tilted image and the ground coordinate from a vertical image 118
4.12 Attitude angles in Pitch (brown) and Roll (black) for 72 images captured by the Parrot Bluegrass over Enfield, Co. Kildare 120
4.13 Comparison of attitude angles measured under different wind speed conditions 122
4.14 An image showing a flight path where it is away from the wind direction 124
4.15 An image showing the effect of wind direction on the Pitch angle of the drone 124
4.16 A graph showing the (ω) angle residual error for Traditional DG and BA with no GCP 126
4.17 A graph showing the (ϕ) angle residual error for DG (Green) and BA with no GCP (Black) 127
4.18 Analysis of MAE for positional accuracy using DG before the proposed correction and compares the result to BA with GCPs and BA with no GCPs 128
4.19 Positional accuracy for Direct Georeferencing compared with corresponding Pitch angle 129
4.20 Comparison of the positional accuracy for the initial result for DG and after the proposed correction method has been applied 130

5.1 The flight plan for the synthetic data. 140
5.2 A graph showing the Pitch angles and standard deviation represented as error bars for the low variability simulated data. 142

5.3 A graph showing the Roll angles and standard deviation represented as error bars for the low variability simulated data. 143
5.4 A graph showing the Pitch angles and standard deviation represented as error bars for the high variability scenario 144
5.5 A graph showing the Roll angles and standard deviation represented as error bars for the high variability scenario 144
5.6 A flow diagram showing the ADGEO process of improving the accuracy by combining BA and DG 146
5.7 An illustration showing the steps and their mathematical equations used from the image projection 147
5.8 An image showing the image projection process with the offset error calculated between BA and DA 151
5.9 Initial results for the low variability scenario of the reconstructed 2D153
5.10 ADGEO results for the low variability scenario of the reconstructed 2D images 153
5.11 Assessment of the model's accuracy under low variability attitude measurement. 154
5.12 An illustration of initial results of the reconstructed images using the traditional DG approach 156
5.13 An image of the initial results of the reconstructed images using the ADGEO method 156
5.14 Assessment of the model's accuracy under High variability attitude measurement. 157
5.15 An illustration for Scenario 1- ADGEO 159
5.16 An illustration for Scenario 2 - ADGEO 160
5.17 A graph showing the accuracy of the ADGEO method for Scenario 1 and 2 161
5.18 Example results of selected orthophotos and their MAE via traditional DG and ADGEO method 167

6.1 An image showing the distribution of Pitch angles for the Sequoia dataset 182
6.2 An image showing the distribution of roll angles for the Sequoia dataset 182
6.3 An image showing the distribution of Pitch angles for the DJIFC6310 dataset 183
6.4 A graph showing the distribution of Roll angles for the DJI FC6310 dataset 184
6.5 Illustration of the novel AirMAP approach 185
6.6 A graph showing the accuracy Assessment of the Sequoia dataset . 197
6.7 A graph showing the accuracy Assessment of the DJI FC6310 dataset 197
6.8 Example results of selected reconstructed images and their MAE via traditional DG and AirMap 201

List of Tables

1.1 Comparison of Satellite, Airborne and Drone Images for Regular, High Spatial Resolution Monitoring. 16
1.2 Market Study of Drones Equipped with Low-cost Sensors 20
1.3 Water Studies Utilising Low-Cost and High-End Drones in Scientific Literature 22

2.1 Pros and Cons of the DG Method 40
2.2 Pros and Cons of Bundle Adjustment 59

3.1 Detail Description of the Parameters for the Theoretical Simulation. 79

4.1 Detailed Description of the Parrot Sequoia Sensor 104
4.2 Environmental and Flight Parameters for the Field Surveys - Enfield 106
4.3 Drone Surveys Over Lough Egish and Blessington Lake 107
4.4 Analysis of Mean Pitch and Roll Values Under Varying Wind Speed 122

5.1 The Parameters Used for Generating the Synthetic Images for the Grid Survey in Figure 5.1. 140
5.2 Statistical Analysis of the Simulated Attitude Data 141
5.3 Sensitivity analysis of the input variables for the ADGEO method 158
5.4 Statistical Analysis Showing Mean Difference, Standard Deviation Difference, and Reliability Analysis Between Scenario 1 and 2 . . . 162
5.5 Analysis on the Influence of Overlapping Percentages on ADGEO . 163

6.1 A detailed Description of the Characteristics and Sources of the Dataset. 180

6.2 Analysis of Various Feature Detectors Showing the Precision Percentage and Average Number of Keypoints Detected. 193
6.3 Accuracy Assessment of the Various Thresholds Explored and their Corresponding Average Number of Good Matches Detected 195
6.4 Accuracy Assessment of the ML Algorithms 196

Chapter 1

Introduction

Understanding the issues that influence the accuracy of images created by low-cost drones are essential for exploring the potential of photogrammetric tools for monitoring water quality. This chapter introduces the reader to the motivation behind this research and offers a thorough overview of the knowledge gap concerning the use of low-cost drones. The background of existing methods used for water quality monitoring is provided to illustrate the challenges associated with the current methods.

This thesis makes four key contributions to the body of knowledge. First, a theoretical analysis of the potential sources of error that limit the accuracy of drone imagery over water bodies is examined, and an error budget is defined. Second, the understandings gleaned during the theoretical analysis are applied in the development of an analytical photogrammetric approach that enhances the accuracy of the drone imagery by correcting errors arising from the sensor rotational angles. The third contribution augments the traditional direct geogreferencing techniques by incorporating sparse shore features as a reference to improve the accuracy of the drone imagery. The fourth and final contribution explores the potential of machine learning to develop a more scalable and generalizable approach that can be used without a requirement for any supporting external data.

This chapter will first review important issues concerning water quality monitoring in section 1.1. The key concepts of remote sensing as a tool for monitoring water quality are then established in Section 1.2. The evolution of satellite remote sensing for water quality monitoring and its associated challenges are detailed in Section 1.3.1. This will be followed by an introduction of the role of airborne remote sensing in Section 1.3.2 and Section 1.3.3 will provide the necessary background information on drone mapping. This will reinforce the potential benefits that accrue from using drones as an alternative to 'bridge the gap' between the more costly satellite and airborne methods from Section 1.3.3.1. The discussion then leads into an overview of low-cost drones and their role in water quality monitoring in section 1.4 and will then highlight the gaps in the current knowledge of mapping water bodies with drones in section 1.5. The research aim and objectives that have been identified to fill this research gap are provided in Section 1.6, and the underlying research assumptions that enable this research are explained in Section 1.7. The key terms used for the different image outputs is presented in Section 1.8. This chapter concludes by outlining the thesis structure and listing all existing publications that have arisen from the thesis in Sections 1.9 and 1.10, respectively.

1.1 Water Quality Monitoring

Water is an essential commodity that supports life on Earth and serves as a habitat for aquatic animals and plants, is vital for many recreational activities and important for many farming and industrial activities (Trodd and O'Boyle, 2021; Ahmed et al., 2019). Therefore, efficient and timely monitoring of water as a resource is essential and this has been recognized in the development of the UN Sustainable Development Goals (SDGs) (United Nations, 2015), particularly SDG 6: Clean Water and Sanitation. Many water resources are threatened by pollution from a range of anthropogenic activities such as agriculture, discharge of untreated urban sewers and industrial waste, and urban runoff (Kupssinskü et al., 2020). In Ireland, one of the main problems that affects water quality is the

widespread of nutrients (such as Chlorophyll-a (Chl-a), Nitrogen, and Phosphorus) in surface waters like lakes and rivers. This leads to eutrophication, which is the elevation of nutrients in surface waters that causes algae to bloom (O'Boyle et al., 2019). The Environmental Protection Agency (EPA) 2022 report on water quality in Ireland suggest that nearly half (46%) of the water surfaces in Ireland are in unsatisfactory condition (Trodd et al., 2022). This report also indicates that rather than improving to meet targets for SDG 6, the level of these harmful nutrients is increasing in many Irish waters. In parallel, the planned expansion in the Irish agricultural and dairy sectors under Food Wise 2025 (DAFM, 2015) can be expected to increase the application of these harmful nutrients. Also, climate change has resulted in more frequent storms and heavier rainfall, which tend to impact water quality, putting increased strain on Ireland's ability to improve water quality.

Water quality monitoring is therefore an essential tool for assessing national water status and enabling efficient pollution management. To be able to restore polluted waters to a satisfactory standard and maintain the quality of waters that are already in a good state, continuous monitoring is essential. This typically involves continuous measurement of various water quality parameters at frequent intervals.

1.1.1 Surface Water Bodies and Regulatory Requirement in Ireland

Managing and regulating water resources in Europe is currently guided by the EU Water Framework Directive (WFD) (2000/60/EC) (Dalton, 2018). This directive aims to protect and manage water resources in Europe. In Ireland, a recent EPA inventory (Trodd and O'Boyle, 2021) shows that there are approximately 12,000 lakes and 14,000km^2 of transitional waters (a term used to describe lagoons and estuaries) and coastal waters. Importantly, the WFD mandates that both lakes over 50ha in surface area, as well as smaller lakes located in protected areas,

must be monitored. Therefore, in Ireland, 812 lakes fall under the WFD (Delaney et al., 2023). However, only 224 of these water bodies were monitored during the period 2019-2021, representing only 27% (Delaney et al., 2023). This means that the majority of Irish lakes are not currently being monitored. Of those lakes with available data, the ecological status (an assessment of the overall health and condition in terms of biological quality) reported by EPA (Trodd et al., 2022) was not promising: these were classed as High - 31%, Good - 38%, Moderate - 21%, Poor - 10%, and Bad - 1% as seen in Figure 1.1a. Overall, 69% of the monitored lakes are in satisfactory condition (high and good status), leaving 31% in poor condition (moderate, poor, and bad). According to these findings, the main problem contributing to this poor ecological water status is recognised as the presence of too many harmful nutrients, which has resulted in a 5% decrease in the number of lakes in satisfactory condition. Figure 1.1b shows the change in ecological status in terms of Phosphorus concentrations.

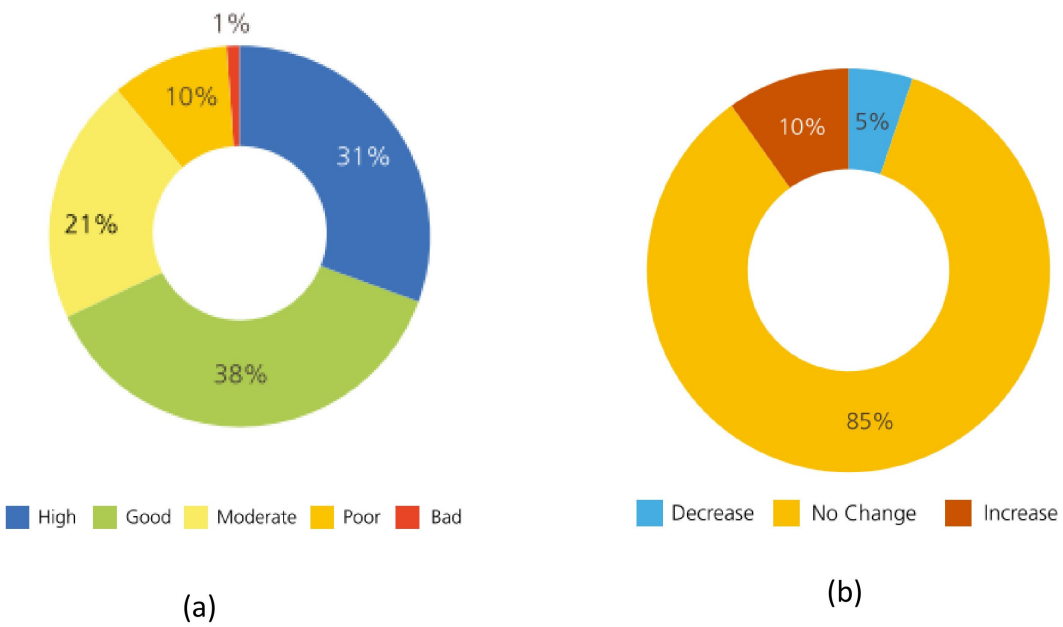

Figure 1.1: The ecological status of Irish lakes from (a) current classification of ecological status (b) the change in nutrient status for one harmful nutrient (in this case Phosphorus) of lakes in Ireland for the period of 2016-2021.
Source: (Trodd et al., 2022)

In Ireland, water bodies are typically monitored through in-situ water sampling method. Notably, this method is recognised as the primary tool for monitoring water quality globally. In-situ water sampling is a well-established method that plays a pivotal role in monitoring water bodies. Therefore, in the following section, a review of the method will be carried out to understand how it works and its limitations.

1.1.2 In-Situ Water Monitoring

In-situ water sampling typically involves at least two people tasked with collecting water samples from the water body. These water samples are stored in containers and are taken to the laboratory for analysis. It usually takes between 2 hours to 1 day to complete the laboratory analyses (Delaney et al., 2023). Figure 1.2 illustrates a spatial distribution of the in-situ water sampling by the EPA. While this method is accurate, studies have shown many limitations with this approach. Firstly, field personnel may be restricted by the lack of accessibility to water bodies, with some lakes removed from Ireland's WFD programme because of accessibility issues (Delaney et al., 2023). Furthermore, this approach is time-consuming (Gholizadeh et al., 2016), labour intensive (Dlamini et al., 2016; Delaney et al., 2023), costly (Keller et al., 2018) and is not suitable for frequent or regular monitoring. In Ireland, for example, according to Delaney et al. (2023), phytoplankton in lakes is only monitored twice a year, and physico-chemicals (an assessment of the nutrient conditions and oxygenation conditions) in lakes is only monitored six to eight times a year for lakes within the operational monitoring program. Lastly and most importantly, the required spatial coverage of the water quality cannot be achieved (Gholizadeh et al., 2016; Delaney et al., 2023) because water sampling is carried out at single or multiple points in the lake, which does not represent the entire water body as illustrated in Figure 1.2 with only 2 sampling points for Lough Egish, Co. Monaghan. Water quality is typically spatially heterogeneous, i.e. it varies across the water surface (Li et al., 2021). Therefore, it requires a sufficient number of sampling points distributed

across the water body. According to United Nations Water (2017), a minimum of four evenly distributed sampling points is required. Thus, the more sampling points taken, the better the spatial representation of water quality.

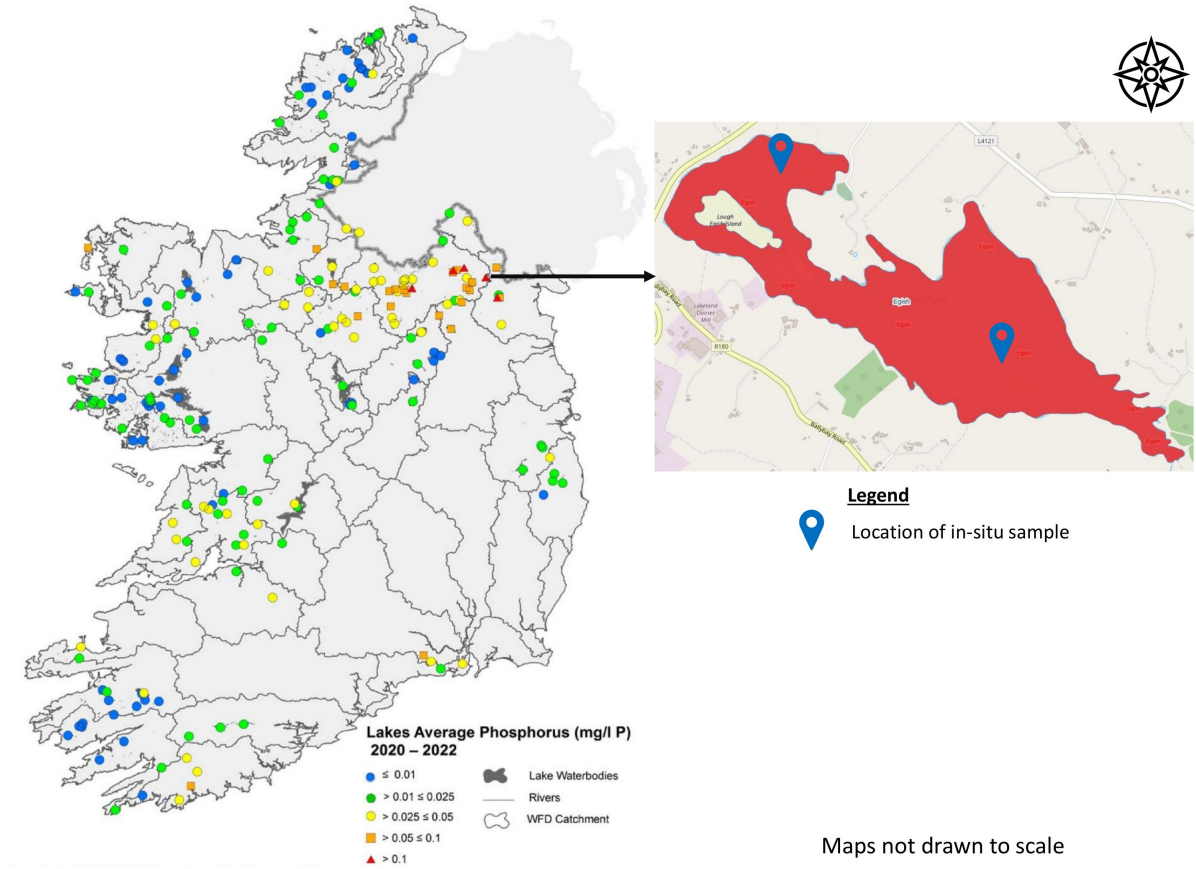

Figure 1.2: This map illustrates the spatial distribution of Phosphorus measurements across Irish lakes based on the in-situ water sampling approach. The main image (left) presents a general classification based on single or multiple points, and is exemplified for the image to the right (Lough Egish). This is important to demonstrate that these point samples necessarily do not represent the entire water body and are a key justification for the method proposed in this thesis. Source: (EPA, 2023)

Due to the sparse spatial distribution and low sampling frequency associated with this method, water bodies are not monitored sufficiently to capture the lake-wide distribution or the temporal dynamics of the water quality. Water quality parameters, particularly harmful algal blooms (HAB), can spread rapidly over short time periods, ranging from hours to days (Delaney et al., 2023). Traditional water quality monitoring methods could therefore benefit from adopting the type of synoptic approach typified by remote sensing to overcome these limitations (Zheng and DiGiacomo, 2017). This could revolutionise the process under key

categories such as scale and time. The subsequent section will review the relevant remote sensing concepts for ensuring effective water quality monitoring.

1.2 Linking Remote Sensing Concepts with Water Quality Monitoring Needs

This section discusses two key concepts in remote sensing and their potential contribution to providing detailed, timely, and accurate water quality information. Section 1.2.1 will critique these in terms of scale and time, and subsequent sections will review various remote sensing methods in light of these two key concepts.

1.2.1 How is Scale and Time Relevant for Water Quality Monitoring?

The importance of scale (spatial resolution) is an important consideration when monitoring the surface of the Earth for diverse fields, such as ecology, water resource management, forestry, agriculture and land use (Richards, 2009). Over the last two decades, advances in remote sensing technology have achieved a step-change in the potential ways of collecting data at different scales (McEliece et al., 2020).

Scale in remote sensing is the window of perception through which the Earth's surface can be viewed and all descriptions of the Earth's surfaces are expressed through a certain scale (Wu and Li, 2009). This concept addresses both the level of detail and also the size of the area observable within a dataset or image. When studying the Earth's surface, scale is an important basis for research. Thus, the investigations we make from the Earth's surface cannot be disengaged from a scale (Warner et al., 2008). Further, gathering data from the Earth's surface is possible across all scales. However, the data obtained changes in relation to the size of the scale, leading to different results. Importantly, there is the need to match the

scale of acquisition to the scale of the phenomena under investigation. This has been recognised in many remote sensing studies where they demonstrated the importance of scale in investigating a spatial problem (Pugnaire and Valladares, 2007; Utlu and Özdemir, 2020; Marceau and Hay, 1999). For example, according to Utlu and Özdemir (2020), they found that flood modelling that uses high spatial resolution images produces more accurate results. Similarly, analysis from Roth et al. (2015) and Yu et al. (2020) established that finer scales (higher spatial resolution images) improve plant species and land cover classification accuracy, respectively. These findings reinforce how high spatial resolution significantly influences both classification accuracy and spatial modelling outcomes.

In parallel with scale, the concept of time is another important phenomenon that helps to reconstruct the past and explore how processes develop over a period (Richards, 2009). It serves as a lens through which the dynamics of natural systems can be observed and analysed. For environmental monitoring, time is essential to understand the sequence of events and is an important component that needs significant attention. Time considerations in environmental monitoring can be characterized by sequence, duration, change, temporal interval, past, present, and future (Richards, 2009). When monitoring the Earth using remotely sensed images, time is typically defined by the sensing platform's temporal resolution (i.e. the revisit cycle), whether from satellite, aeroplane, helicopter, or drone (Miller et al., 2005).

In the context of water quality monitoring, studies suggest that methods that incorporate the concepts of both scale and time could be of benefit (Wu et al., 2023; Delaney et al., 2023). Spatial resolution significantly impacts the level of detail information that is obtained, thus influencing the accuracy of the monitored water quality parameter (Windle and Silsbe, 2021; Murray et al., 2022). For instance, a water quality monitoring approach that uses very high spatial resolution imagery will enable the detection and measurement of small changes

in water quality. This can be useful to identify specific pollution sources. For example, in Tamás Fráter et al. (2015), they demonstrated the potential for high spatial resolution imagery to help monitor the growth of algae, which is often unnoticed using lower spatial resolution imagery. Similarly, higher temporal resolution imagery has the potential to track the evolution of water quality over time (Delaney et al., 2023). These studies suggest that with the application of higher spatial and temporal resolution imagery, water pollution can be detected early on. Subsequently, the right management decisions can be taken to remedy the situation based on the extent and dynamics of this pollution.

To demonstrate the importance of considering the spatial resolution of the images for water quality monitoring, three datasets with different spatial resolutions as shown in Figure 1.3 were created. This comparison shows water turbidity maps generated using a standard band ratio described in (Ehmann et al., 2019) and classifies the level of suspended sediments in water which is an indication of how clear the water is. The experiment compared water turbidity maps derived from three image sources: very high spatial resolution (drone), moderate resolution (Sentinel-2), and low resolution (Landsat 8). The results highlight the ability of very high spatial resolution drone imagery to better delineate areas of different turbidity and also improve the performance for pixels at the shoreline.

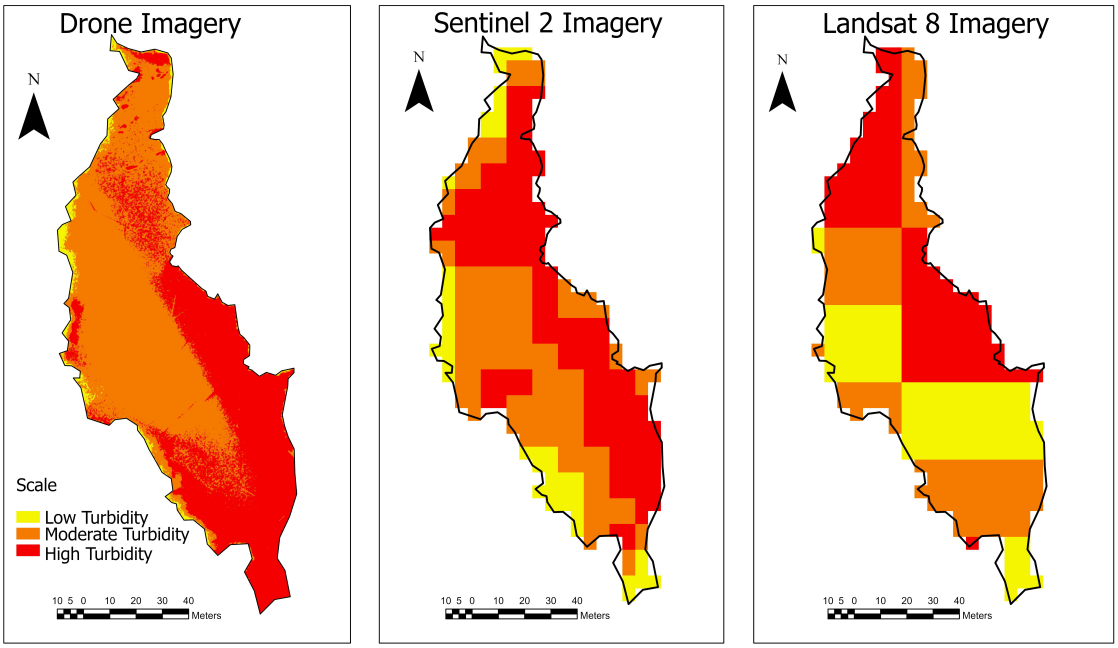

Figure 1.3: An Example from Egya lagoon, Ghana showing water turbidity maps derived from drone imagery (Very High-Resolution - 0.10m), Sentinel 2 image (Moderate Resolution - 10m) and Landsat 8 image (Low Resolution - 30m).

1.3 What Platforms can Provide the Required Spatial and Temporal Resolution?

Remote sensing consists of acquiring images across specific spectral bands in the optical, infrared, and microwave regions of the electromagnetic spectrum (Miller et al., 2005). One active research area within this field is water quality monitoring and it is important to consider the strengths and weaknesses of each platform.

1.3.1 Satellites - Trading Spatial for Temporal Resolution

Many water quality parameters, including Chl-a, total suspended sediments, and turbidity, have been detected using satellite images. The successful launch of Landsat 1 by NASA in 1972 was a disruptive technology that revolutionised how scientists and researchers monitor the Earth. The earliest records of using satellite data for monitoring water quality come from studies by Strong (1974);Scarpace et al. (1979);Carpenter and Carpenter (1983) and Blackwell and Boland (1979).These

studies laid the foundation for the use of satellite imagery in water quality assessment. During these early periods, the primary limitations of satellite images were the frequency of satellite overpasses (temporal resolution), accessibility, cloud cover, and spatial resolution. Landsat 1 had an 18-day revisit cycle, meaning that potential 20 images could be acquired for water quality monitoring per year. However, literature has shown that the probability of acquiring cloud-free data is also influenced by region and month, which can affect its availability (Corbane et al., 2020; Robinson et al., 2019; Wu et al., 2021). In particular, Ireland's average cloud cover of 100% for over 50% of the year (Dwyer, 2012; Met Éireann, 2023) reduced accessibility and applicability to, at best, only 10 images per year. As a result, the general applicability of continuous water quality monitoring is significantly reduced. In addition, the Landsat 1 satellite imagery had a spatial resolution of 80m (USGS, 2017). In remote sensing applications, this is considered as low spatial resolution, which means that Landsat 1 imagery would not be suitable to provide the level of detail necessary to assess small-scale water pollution events. Following on, Landsat 2 carried the same sensor as Landsat 1 and had the same 18-day revisit period. Consequently, it faced the same limitations as Landsat 1. This meant that changes in water pollution could only be sensed at 80m, making monitoring smaller variations impossible. Additionally, the 18-day temporal resolution hampered their ability to track rapid events like algal blooms, which can occur over a few hours or days. Landsat 4's launch in 1982 marked an improvement with a 30m resolution and a revisit period of 16 days, yet it encountered the same setback of low spatial resolution and longer revisit cycle.

The advent of medium-resolution satellites like SPOT 1, 2, and 3 in the mid-1980s to early 1990s provided better spatial resolution (10m panchromatic and 20m multispectral) but with longer revisit periods of 26 days (ESA, 2023a). Although the improved spatial resolution allowed for capturing more detailed imagery compared to the previous satellites, the limited revisit cycle, coupled with

cloud cover, reduced the overall applicability of these satellite images. In the past two decades, there has been a significant improvement with satellites like Landsat 8 and Sentinel 2, offering improved spatial resolution and revisit cycles. The Landsat 8 has a 30m spatial resolution and a revisit cycle of 16 days, while the Sentinel 2 has a spatial resolution of 10m and a revisit cycle of 5 days. However, like the previous satellites, they all struggle to provide finer detail (higher spatial resolution) and higher temporal frequency needed for effective small-scale and intra-seasonal water pollution management (Gholizadeh et al., 2016).

Additionally, several high-resolution satellites imagery provide both high spatial and tempotal resolution. For example, SPOT 6 and 7 provide a spatial resolution of 1.5m (Panchromatic) and 6m (Multispectral) and a revisit capability of 1-3 days (Airbus, 2018). Similarly, the Digital Globe Worldview 2 and Worldview-3 provide 1.64m (8-band multi-spectral) and 1.24m (Visible Near Infrared bands) spatial resolution and 11- days and 1-day revisit cycles, respectively (ESA, 2023b). These high-resolution satellite images capture finer details and enable frequent data collection. They have state-of-the-art technology that can monitor water quality at a smaller scale and help detect water pollution patterns. As with all satellite images, cloud cover can affect the availability of cloud-free images. However, the high revisit cycle mitigates the impact of cloud cover on the availability of usable imagery. This means that a good percentage of images will be cloud cover-free.

However, the major limitation is that these high resolution satellite imagery are commercial. They are very expensive to use and are operated for profit, so users have to pay to access the data. This limits their accessibility to individuals, organisations and the scientific community. As a result, these satellite images are less commonly used in high frequency water quality monitoring due to resource constraints. This is evident in a review of water quality studies where they found that only a limited number of commercial satellites were employed in water quality

assessments as compared to non-commercial satellites (Gholizadeh et al., 2016). Given the limitations outlined for satellite imagery, the next section will explore the potential of airborne remote sensing as an alternative approach to water quality monitoring.

1.3.2 Flying Lower - the Role of Airborne Remote Sensing

Airborne remote sensing is the process of collecting information about the earth's surface from airborne platforms such as aircraft or helicopters. It involves mounting sensors on these airborne platforms, and a major strength is that it operates below the cloud and the Earth's atmosphere (Adjovu et al., 2023). One of the earliest remote sensing studies to employ the use of piloted aircraft equipped with a multispectral sensors to map the distribution of algal blooms was carried out by Strong (1974). Following this success and subsequent advances in airborne remote sensing technology, many other studies (Ledrew and Franklin, 1983; Engelhardt, 1999; Mueksch, 1995) began to emerge. For example, Ledrew and Franklin (1983) conducted a study using piloted aircraft with a RGB sensor to study effluent plumes and this early study further demonstrated that aerial photos could be used to monitor water bodies. Similarly, other studies like Engelhardt (1999) and Mueksch (1995) also successfully used piloted aircraft to monitor oil spills and Chl-a concentration, respectively in water bodies.

In parallel with technological advances in the 1990s and early 2000s, airborne remote sensing benefited from these sensor improvements. Well-established sensors common in the literature include the Airborne Visible Infrared Imaging Spectrometer (AVIRIS), Compact Airborne Spectrographic Imager (CASI-1500), Airborne Prism Experiment (APEX) and Hyperspectral Digital Imagery Collection Experiment (HYDICE). Over the years, these sensors have been used to assess different water quality parameters. For example, in Lunetta et al. (2009), AVIRIS hyperspectral imagery was acquired from the NASA Earth Resources 2 (ER-2) aircraft to monitor Chl-a, Chromophoric Dissolved Organic Matter (CDOM), and

Total Suspended Solids (TSS) in the Neuse River and Pamlico Sound Estuaries in the USA. Similar airborne hyperspectral sensors, such as APEX, have also provided opportunities for operational monitoring of water bodies. APEX, which was developed by a Swiss-Belgian consortium (VITO) on behalf of the European Space Agency (ESA), was used to measure Chl-a, TSS, and CDOM parameters for coastal waters in Belgium (Knaeps et al., 2009).

Airborne remote sensing provides very high spatial resolution images ranging from 80cm to 5m (Gholizadeh et al., 2016). Additionally, airborne platforms operate below the cloud cover (Cahalane et al., 2017), and so provide cloud-free data. This largely removes the atmospheric component that influences the quality of spectral measurements made by satellite. Typically, the spatial resolution of airborne imagery provides the necessary finer details for examining the extent and spatial dynamics of water pollution (Lunetta et al., 2009). However, this approach has several setbacks, the primary one being the high cost of the sensors and the high operational costs associated with pilots and suitable piloted aircraft. Although one study by Cahalane et al. (2017) has explored the option of using lower-cost sensors in light, piloted aircraft. However, methods requiring multiple crew members onboard and a dedicated aircraft is unsuitable for a repeat- survey methodology for continuous water quality monitoring. As previously explained, continuous water quality monitoring is essential because the evolution of water pollution events can take a few hours or days to occur (Delaney et al., 2023), making airborne remote sensing an economically impractical approach. Drones have emerged as a potential alternative to employ a more cost-effective and reactive aerial survey methodology (Nex et al., 2022). Therefore, the subsequent sections will provide an overview of drone photogrammetry and its potential as a water monitoring tool.

1.3.3 The Advent of New Lightweight Tech - Drone Photogrammetry

Remotely Piloted Airborne Systems (RPAS), also popularly known as drones, can be described as any aircraft without an onboard pilot which can fly autonomously or be piloted remotely and utilize onboard sensors such as GNSS, IMU and sensors (Gevaert, 2018; Rehak, 2017; Cabreira et al., 2019). Drones were primarily developed for military purposes, but their use for civilian applications has grown significantly in recent years (Rehak, 2017). Topographic surveys using photographs are one of the most widely used civilian applications in diverse fields (Nex et al., 2022). Drones have emerged as an important piece of survey equipment for geomatics professionals across various industries and organisations worldwide. Drones now serve as the middle ground between aerial surveying with piloted aircraft and traditional terrestrial surveying using total stations, GNSS, or laser scanners (Prior et al., 2020b). The underlying principle of drone surveys is similar to traditional aerial photogrammetry where the goal is to capture and then utilize overlapping images to reconstruct the geometry and texture of any scene (Nex et al., 2022). These overlapping images can be used to create many typical survey outputs, such as high-resolution 3D models (Bouziani et al., 2021b), point clouds (Bouziani et al., 2021a), and orthomosaics (Stöcker, 2021).

1.3.3.1 Benefits of Drone Mapping

The surge in drone applications over the last decade can be attributed to the improvement in battery time and quality, lightweight materials and sensors, the widespread availability of affordable, off-the-shelf drone systems and advances in image processing techniques (Gevaert, 2018). Drones provide very-high spatial resolution (1cm-10cm) datasets, operate below the cloud cover (Cahalane et al., 2017) similar to light aircraft, and so provide cloud-free data. Just as importantly, they can often be operated by a single pilot, are lightweight and easily portable and therefore can access remote areas for repeat surveys. They also produce datasets in near real-time, which helps in continuous water monitoring.

Drones can provide very fine details at regular intervals at a low cost, unlike commercial satellite and airborne platforms, which are often expensive or not of sufficient spatial resolution (Su and Chou, 2015). With increased temporal resolution enabled by drones (multiple times each day, any time of day), monitoring and rapid response to water pollution outbreaks is possible (Wu et al., 2019; Castro et al., 2020). This helps provides an understanding of the stages of the outbreaks (Kubiak et al., 2016) that would not be possible using satellite or airborne images alone. Table 1.1 provides a comparison of satellite, airborne and drone imagery.

Table 1.1: Comparison of Satellite, Airborne and Drone Images for Regular, High Spatial Resolution Monitoring.

Parameters	**Satellite**	**Airborne**	**Drone**
Revisit cycle	High temporal: 1 day Low temporal: 16 days	Anytime	Anytime
Spatial resolution	High resolution: ≤ 5m Medium resolution: 10m Low resolution: ≥30m	Very high resolution: ≤1m	Very high resolution: ≤ 20cm
Cloud free	Obscured with cloud	Cloud free	Cloud free
Cost	High resolution: commercial Medium/Low resolution: free	Expensive	Low - cost

In addition to their well-established terrestrial applications, drones are also suitable for water quality monitoring, and over the years, their application in mapping the distribution of water quality parameters has increased. Specifically, low-cost drones have become a better alternative to high-end drones and have seen an increase in their application over water in recent years (Knaeps et al., 2019). Therefore, the subsequent section will review low-cost drones to understand their potential role in water quality monitoring.

1.4 Can Low-cost Drones Play a Role in Water Quality Monitoring?

In this section, the concept of low-cost drones adopted in this thesis will be explained in greater detail. It will define the main criteria for describing or defining a low-cost drone. This section also contains a review of recent advances in low-cost drones to help emphasise the pace of rapid development. Lastly, it explores the work to date of these low-cost drones for water quality monitoring.

1.4.1 Definition of a Low-cost Drone

In drone photogrammetry, the off-the-shelf (i.e. available immediately to be purchased and does not need any customization or special ordering) market offers an extensive range of low-cost drones. In the last decade, there has been increased innovation and investment in low-cost drone technology, leading to affordable, smaller platforms, more efficient flight and a variety of sensors for obtaining reliable information about the Earth's surfaces (Rambat, 2011). Consequently, interest in low-cost drones has increased in the scientific community, including an increase in use for remote sensing applications (Song et al., 2016). For example, several studies have been conducted using these low-cost drones to monitor and map seaweed habitats (Kellaris et al., 2019), malaria habitats (Hardy et al., 2017), measure tree characteristics (Bossoukpe et al., 2021), map forests (Williams et al., 2022), map weeds (Mattivi et al., 2021), and map ecosystems and features (Kabiri, 2020).

In educational institutions and research centres, budget constraints often limit the adoption and application of cutting-edge technologies such as high-end drones. One of the main advantages of these low-cost drones is their affordability (Bikov et al., 2022). These low-cost drones are invaluable tools, allowing researchers to explore various applications and innovate without incurring a significant financial burden. Furthermore, low-cost drones offer opportunities for effective

environmental monitoring by allowing local communities, NGOs, and volunteer groups or citizen scientists to acquire such platforms. Due to their affordability and accessibility, it can be assumed that these low-cost drones will continue to be popular and as technology improves, they will incorporate more advanced features while still maintaining a relatively low price (Bikov et al., 2022).

Generally, low-cost drones can be categorized into two types: semi-professional-grade and consumer-grade (Stöcker, 2021), each differing significantly in terms of their intended purpose, features, capabilities, and price. In this thesis, semi-professional grade drones are referred to as drones that are specifically designed for professional use such as high accuracy topographic surveys. This category offer a certain level of spatial accuracy for derivative datasets, ranging from 1 to 3 meters, though not reaching the highest achievable of centimetre-level accuracy. On the other hand, consumer-grade drones can be considered as those that are designed for general-purpose use, such as recreation, photography, videography, and racing. They typically feature basic Global Navigation Satellite System (GNSS) modules and Inertial Measurement Units (IMUs) for navigation, which are not adequate for professional applications. Therefore, in this thesis, the term "low-cost drones" is used subsequently to refer to semi-professional grade drones.

1.4.2 Categories and Classification

In the context of this thesis, a low-cost drone is defined by two key criteria: the imaging device and the navigational sensor(s). These criteria were chosen as they can be considered to be the most significant factors influencing the overall cost of any drone. Other criteria, such as flight time, type of motor/rotor blade and battery capacity, were not considered as they are deemed by the researcher to have a lesser impact on the overall cost. These two components are explored in more detail in 1.4.2.1, 1.4.2.2 and 1.4.2.3.

1.4.2.1 Imaging Device

The imaging device or sensor is the tool - fundamental for the application of a remote sensing methodology - that enables the collection of information about the Earth's surface (Wolf et al., 2014; Aber et al., 2019). Examples of imaging devices include visible-only, multispectral, hyperspectral, and microwave sensors. These sensors capture data across many parts of the electromagnetic spectrum, including ultraviolet, visible, and infrared wavelengths.

Typically, the quality and capabilities of the imaging device are the major influence that determine the price of a drone (Rambat, 2011). For instance, the greater the number of spectral bands that the sensor can detect, the more useful the information it can capture, consequently affecting the price. Additionally, higher spatial resolution sensors also influence the price of a drone because this generally improves the ability to detect smaller features in an image. For example, if one drone sensor has 48 mp resolution while the other has 24 mp, say at the same height of 120 meters, the latter can capture data at 5 cm per pixel while the former can only capture data at 10 cm per pixel. Therefore, all other factors being equal, a drone sensor with a higher spatial or spectral resolution will be more expensive than one with a lower resolution.

1.4.2.2 Navigational Sensors

The type and quality of navigational sensors (GNSS/IMU) onboard a drone are also an important contributor to the price (Rambat, 2011). The navigational sensors are used to measure and record the 3D position and orientation of the drone during surveys (Stam, 2010). Drones equipped with high-precision navigational sensors are generally more expensive due to their enhanced accuracy in capturing data. For example, a market survey reveals that the DJI Phantom 4 Pro V2.0 drone costs €1,699 while the DJI Phantom 4 RTK (Real Time Kinematics) drone costs €6,950 as of November 2023 (DJI, 2023). The only appreciable difference in specifications between them is the accuracy of the GNSS. The former utilises a

standard GNSS while the latter employs a high-precision RTK differential GNSS system. The high-end Phantom 4 RTK drone can provide a centimetre level accuracy while the low-cost non-RTK equivalent is only able to provide an accuracy ranging from 1 -3m.

1.4.2.3 Market Survey

The drones of relevance to this thesis can range in price from a thousand euros to five thousand euros, depending on their features and capabilities. In Table 1.2, a market survey on a range of drones with low-cost sensors that are widely used in research have been listed along with their corresponding prices.

Table 1.2: Market Study of Drones Equipped with Low-cost Sensors

Drone Model	Price	Sensor	Accuracy IMU	Accuracy GNSS	Price Source	Date Published
Parrot Bluegrass Quadcopter with Sequoia sensor	€4750	MS	0.5 ^{o}	1.5m	Link 1	2024
PARROT DISCO-PRO AG with Sequoia sensor	€4,276	MS	0.5 ^{o}	1.5m	Link 2	2024
Sequoia sensor+ mounted on DJI Phantom 4	€4,231	MS	0.5 ^{o}	1.5m	Link 3	2024
MicaSense Altum-PT sensor mounted on DJI Mavic Air 2	€1,950	MS	0.2 ^{o}	1.5m	Link 4	2024
Micasense RedEdgeM mounted on DJI Phantom 4	€4,673	MS	0.2 ^{o}	1.5m	Link 6	2024
Micasense RedEdge-MX mounted on DJI Phantom 4	€4,030	MS	0.2 ^{o}	1.5m	Link 7	2024
Phantom 4 Pro with RGB sensor	€1,699	RGB	0.05 ^{o}	1.0m	Link 8	2023
DJI Air 3 with RGB sensor	€1,119	RGB	0.05 ^{o}	1.5m	Link 9	2023

Note: The prices are based on company quotations accessible at the links provided in the table. MS is Multispectral.

1.4.3 Work to Date: Low-Cost Drones for Monitoring Water Quality

To date, the application of low-cost drones for water quality monitoring trails behind that of their widespread use in terrestrial environments (Knaeps et al., 2019). This is because the issues that must be considered when mapping water bodies using low-cost drones are much less understood, and these pose many challenges to enabling the accurate collection and processing of drone imagery (Román et al., 2023). Despite these issues, there has been a gradual increasing trend in the use of low-cost drones for water quality monitoring. This increase signifies a growing recognition of this technology's potential benefits for rapid, regular and accurate water quality monitoring.

To demonstrate the gradual adoption of low-cost drones in water quality monitoring, a comprehensive literature search was conducted, as shown in Table 1.3. A selection of the most relevant academic databases were thoroughly examined, including Scopus, ScienceDirect, Web of Science, and also specialist journals focused on remote sensing and photogrammetry not included in those databases. This extensive search yielded a total of seventeen studies using drones for water quality monitoring from 2015 to 2023. Of these, thirteen studies employed low-cost drones, while only four utilized high-end drones. These findings suggest that the cost-effectiveness of low-cost drones is encouraging scientists to adopt the low-cost technology as a more attractive option for water quality monitoring.

Table 1.3: Water Studies Utilising Low-Cost and High-End Drones in Scientific Literature

Water quality parameter	Low-cost drones		High-end drones	
	Sensor	Studies	Sensor	Studies
Chl- a	Micasense RedEdge-M	Román et al. (2023); Wu et al. (2023)	DJI P4 Multispectral	Xiao et al. (2022); Lo et al. (2023); Zhao et al. (2022)
	Canon Powershot S110 NIR	Su and Chou (2015)		
	DJI FC6310 sensor	Cheng et al. (2020)		
	Micasense RedEdge-M	De Keukelaere et al. (2023)		
	Micasense RedEdge	Adelson (2020); Arango and Nairn (2019)		
	Parrot Sequoia	Maravilla et al. (2019)		
	SenseFly, Swinglet - Canon ELPH 110HS	Kupssinskü et al. (2020)		
	Parrot Sequoia	Román et al. (2023); Arango and Nairn (2019); Prior et al. (2020a)		
	Micasense RedEdge	Ying et al. (2021)		
Turbidity	Parrot Sequoia	Prior et al. (2020b)		
	Micasense RedEdge	Ying et al. (2021)		

1.5 Gaps in Current Knowledge for Mapping Water Bodies with Drones

Drone photogrammetry is the process of using overlapping drone images to create detailed and accurate orthomosaics, Digital Surface Models (DSM), and 3D models. With regards to image processing, drone photogrammetry has benefited from a fast automation process using structure-from-motion technology (SfM) (Granshaw, 2018), which is a traditional and widely used method for reconstructing a 3D surface by identifying tie points between these overlapping images (Losè et al., 2020; González-Jaramillo et al., 2019; Vitti et al., 2019; Iglhaut et al., 2019). The SfM process starts with extracting and matching tie points from overlapping images using algorithms such as the Scale-Invariant Feature Transform (SIFT) - a widely used feature detection algorithm for identifying tie points (key points). When sufficient tie points have been gathered, a Bundle Adjustment (BA) is performed to calibrate the sensor and refine its position and orientation. In this step, the user can often completely rely on the GNSS and the IMU onboard or manually add Ground Control Points (GCPs) to improve the accuracy (Chiabrando et al., 2019). The next step is to reproduce a sparse 3D point cloud of the surface. The final step is to generate the DSM and the orthomosaic.

However, in drone photogrammetry, the main impediment encountered when mapping water bodies is the absence of, or limited amount of ground features that can act as tie points for this surface reconstruction (Román et al., 2023; De Keukelaere et al., 2023). With the BA method being dependent on tie point collection, it is impossible to apply this method for images captured over water and so generally fails during surface reconstruction. This is because water can be considered as featureless terrain due to its dynamic nature and homogeneous appearance (Knaeps et al., 2019).

To illustrate this fundamental problem, an experiment was conducted on a set of drone images captured over water as shown in Figure 1.4. During this experiment, the SIFT algorithm was applied to this drone imagery. The result revealed that no tie points were detected on the water surface. Further evidence supporting this observation is found in Maravilla et al. (2019) and Roman et al. (2024), where the BA method was employed to create a mosaic of drone datasets over a lake. Their results mirrored those of the experiment, with 31% (Maravilla et al., 2019) and 86% (Roman et al., 2024) of the images being unable to be processed. Specifically, only images with a significant ground area of the shore in view could be processed, resulting in a hole in the final orthomosaic (Maravilla et al., 2019).

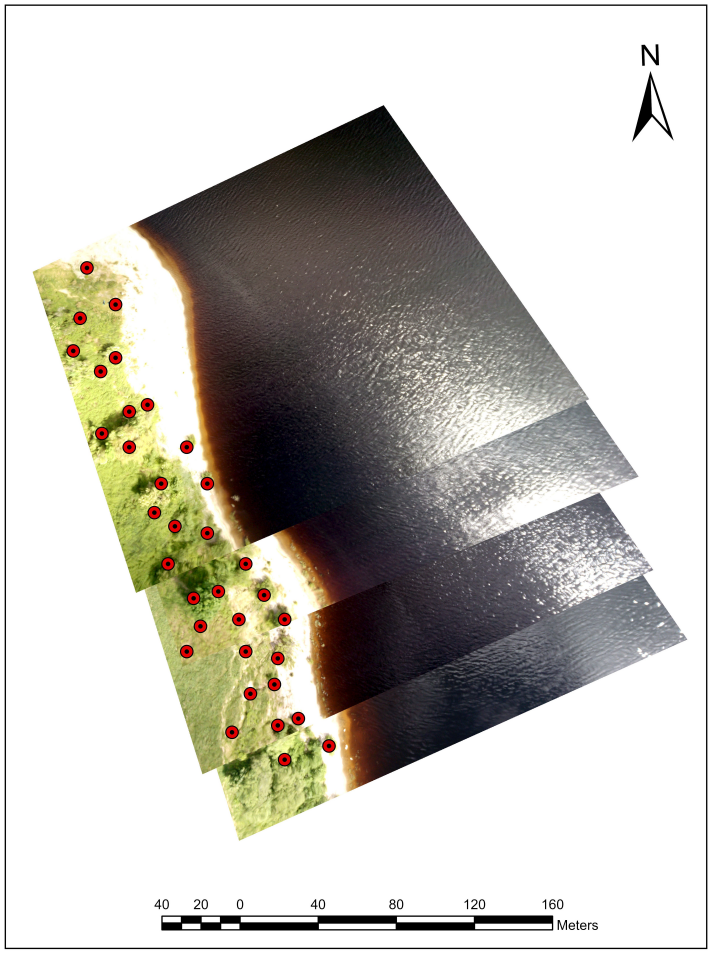

Figure 1.4: An example of a drone dataset over Blessington Lake in County Wicklow. This image illustrates how difficult it is to collect tie points over water compared to the terrestrial area.

In trying to solve this problem, photogrammetrists have favoured the Direct Georeferencing (DG) approach to derive the Exterior Orientation Parameters (EOP), which are the determination of the sensor's position and orientation required to project a point from a 3D world onto a 2D image plane (Román et al., 2023; Knaeps et al., 2019; Windle and Silsbe, 2021; Lo et al., 2023). DG can be described as a method that measures the position and orientation of an airborne sensor and uses it to directly determine the EOPs without any additional measurement, i.e. GCPs (Lo et al., 2015; Ekaso et al., 2020). In the DG method, the GNSS, which is for positioning and the IMU, which is for angular measurement, work together to determine the sensor's position and orientation (Bagherbandi et al., 2022; Yastikli and Jacobsen, 2005). These two devices make it possible to georeference an image directly. As of the time of this study, the DG method is still the only practical solution for deriving EOPs that can be used to reconstruct images over water.

Studies by Bláha et al. (2012) and Ip et al. (2007) have demonstrated that the DG approach is only successful in image reconstruction with high-end drones equipped with highly accurate RTK GNSS and IMU or Post-Processing Kinematic (PPK) modules. High-end drones are essential as the accuracy and reliability of the DG method is limited by the accuracy of the IMU and GNSS onboard the drone (Jacobsen, 2002). These high-end drones feature more advanced technology compared to low-cost drones, enabling them to produce accurate and reliable orientation and position measurements. Despite their efficiency in producing accurate EOP measurements, as previously argued in this thesis, high-end drones are not widely used due to their high cost. Therefore, it is difficult for individuals, organizations, and institutions to afford them, hence limiting their applicability. As low-cost drones become more prevalent in water quality monitoring, the need for methods or techniques that correct errors associated with drone imagery derived from DG becomes increasingly important. To date, no methods involving low-cost drones have been investigated to (i) understand their suitability, (ii) the

associated errors have never been quantified and (iii) there have been no attempts to improve accuracy. There is, therefore, a clear need for a study that will focus on these three issues.

1.6 Research objectives

The aim of this thesis is to explore and enhance the photogrammetric methods that can be employed to map water bodies using low-cost drones. To achieve this aim, this thesis incorporates four objectives that further the body of knowledge in the field of photogrammetry. This section summarizes these four objectives and all relate to low-cost drones.

1.6.1 Objective 1

The first objective of this thesis is to benchmark and test the accuracy of drone imagery of water bodies generated using the DG method. This will establish a benchmark for comparison with subsequent methods and tests. This objective will theoretically test the accuracy of EOPs derived from the DG method using the standard photogrammetric collinearity equations in Chapter 3 and will be validate further using real-world data in Chapter 4.

1.6.2 Objective 2

The second objective of this thesis is to analyse the associated errors in the images derived using the DG method and propose an analytical photogrammetric method to improve them.

1.6.3 Objective 3

The third objective of this thesis is to develop a method that can combine BA and DG by using the features from the shore as a reference to improve the accuracy of drone imagery over water. This objective will theoretically test and validate the method using real-world data in Chapter 5.

1.6.4 Objective 4

The last objective of this thesis is to develop a method that aims to improve accuracy, efficiency, and scalability for mapping water bodies. This will explore image registration techniques coupled with machine learning in Chapter 6.

1.7 Research Assumptions

A number of assumptions have been made in this thesis to facilitate work on the objectives listed in section 1.6. The sections below detail each of these underlying assumptions.

1.7.1 Assumption 1

One of the key assumptions of this thesis, and one that underpins all subsequent methods, is that the surface of a water body can be approximated as flat, i.e., a surface that is nearly planar. While this may not always be the case in practice, especially for the sea where strong winds can generate significant wave action, almost all inland waters can be considered relatively stable. Therefore, this assumption discounts swell, waves, and any other water disturbances. This assumption aids in establishing the relationship between the images captured by the drone when projected to the ground plane. Therefore, all the photogrammetric methods developed in this thesis adhere to this assumption.

1.7.2 Assumption 2

Another key assumption for this thesis is that water can be considered as an exclusively featureless terrain. Featureless terrain can be described as any terrain without ground features (Taha et al., 2022). A ground feature could be described as any distinctive and identifiable element present on the earth's surface that can be used as a reference point. These features are typically static and provide spatial information that aids in mapping, navigation and robotics applications. In the field of photogrammetry, examples of featureless terrain that pose challenges

during the traditional photogrammetric process include water, bare soil/sand, and ice sheets.

In this thesis, water as a featureless terrain is explained in two broad contexts: (i) a terrain without any identifiable features and (ii) a terrain with limited features. The first category represents the normal state of almost all water bodies – i.e. they lack features. In the second category, it is certainly true to say that there may be identifiable features over the water surface in certain instances. However, this thesis argues that these are not enough to make it a feature-rich terrain suitable for image reconstruction through traditional photogrammetric techniques. For example, an image of a body of water may contain high levels of suspended solids such as leaves, tree logs and plastics. However, these suspended solids are not reliable features for image reconstruction due to two primary reasons. Firstly, these suspended solids can move in the water due to currents, wind or other hydrographic causes, hence affecting the tie point matching. This causes more mismatches of the identified tie points in the matching process and this will affect the accuracy and quality of the image reconstruction. Additionally, these features are rare, not well distributed spatially, and therefore insufficient to properly reconstruct images. During a typical BA process, at least 100-5000 keypoints must be identified in each image (Mousavi et al., 2021). Hence, throughout this study, a key assumption that is made is that water should be considered an exclusive featureless terrain, even when there are suspended solids.

1.7.3 Assumption 3

The aim of objective one is to theoretically test the accuracy of EOPs derived from the DG method using the standard photogrammetric collinearity equations. This analysis relies on the assumption that the specified manufacturers' accuracies for GPS and IMU are suitably defined for the proposed theoretical method. This assumption considers a standard condition where the GPS and IMU are capable of measuring position and angular changes within the specified tolerances.

Additionally, all other variable factors that might influence the accuracy, such as signal quality, interference and satellite geometry for GPS and constant bias, temperature effects and calibration errors for IMU, can be discounted.

1.7.4 Assumption 4

This thesis focused on developing methods for drones without self-leveling gimbals. While the methods in this thesis are primarily targeted for such drones, it will be shown that they can be adapted for drones with gimbals as well. Drones without gimbals were chosen as the target for this research because they are particularly susceptible to orientation influence and can best benefit from this approach.

1.8 Terminologies for Drone Image Outputs

This section introduces the key terms used for the different image outputs presented in later chapters to ensure clarity throughout the thesis.

1. **Reconstructed 2D images** – These are generated by projecting 3D objects onto a 2D plane, representing the initial results of the DG approach before any corrections. These images may not necessarily be georeferenced, meaning their coordinates could be arbitrary, like the theoretical analysis in Chapter 3 or based on a real-world coordinate system, as demonstrated in Chapter 4. When combined into a single image, they become a mosaicked image.

2. **Orthoimages** – Orthoimages are images that have been geometrically corrected (orthorectified) to remove distortions caused by terrain relief, sensor tilt and image displacement, and scale variations (Shariat et al., 2008; Faraji et al., 2016). They are georeferenced, meaning each pixel corresponds to a specific location on the Earth's surface with an accurate scale and spatial alignment. Their geometric integrity allows them to be used as base maps for accurate measurements. In some instances, an image captured at nadir

(straight down) over a flat surface can be directly considered an orthoimage (Wolf et al., 2014). This thesis specifically focuses on producing orthoimages through novel methods developed in Chapters 4, 5, and 6. Therefore, after applying these methods to the reconstructed 2D images, the resulting product will be referred to as an orthoimage.

3. **Orthomosaic** – These are orthoimages that have been mosaicked into a single image. They are obtained by edge matching and colour balancing the orthoimages to create a seamless image (Wolf et al., 2014). This image represents the final output in mapping water bodies, where orthoimages over the water are combined to create a single image of the area.

1.9 Thesis Structure

This thesis is further divided into six chapters with the following structure:

Chapter 2: Current State of the Art - Literature Review

This chapter investigates the four research objectives listed in Section 1.6. It begins by introducing the concept of DG in more detail and investigates the work to date in this area. This chapter further reviews the navigational sensors essential to the DG method. Lastly, it reviews the standard photogrammetric principle and investigates how image registration and ML techniques could be employed for mapping water bodies.

Chapter 3: Theoretical Analysis of the Positional Orientation (POSE) Errors - Objective 1

This chapter describes the error sources that limit the accuracy of the drone imagery, namely; GNSS and IMU errors and sensor rotation angle influence. It further quantifies and analyses the error sources using the standard photogrammetric collinearity equations and a series of simulated tests in Python.

Chapter 4: Developing An Analytical Rectification Method for Featureless Terrain - Objective 2

This chapter investigates how the error sources described in chapter 3 can be corrected through analytical photogrammetry. The DG method was explored in this chapter, and the results were compared to the novel analytical photogrammetric method developed. This method was developed to remove image displacement, tilt displacement and scale variation errors.

Chapter 5: Assisted Direct Georeferencing Approach - Objective 3

This chapter was an improvement on the method developed in Chapter 4. This chapter presented a new methodological process that explores the potential of using the shore as a reference to improve the accuracy of drone images over the water. The assessment was conducted in two parts: theoretical and experimental assessments. The developed method was also tested under different real-world scenarios.

Chapter 6: Automated Image Registration Model for Mapping Water Bodies - Objective 4

The final methods chapter presents a new approach for mapping over water using image registration techniques and a machine learning approach. The potential of the method lies in its scalability, and its capability to map water surfaces at different geographic scales and is an improvement on the Chapter 5 method because no shore is needed. A series of drone datasets were used to train, validate and test the method.

Chapter 7: Conclusion

This chapter summarizes and syntheses the results of the individual chapters. It emphasized all the contributions and remaining gaps that could be filled. Finally, it highlights the challenges encountered during the research process and concludes with final remarks.

1.10 Publications

1. Essel, B.; McDonald, J.; Bolger, M.; Cahalane, C. (2022) Initial Study Assessing the Suitability of Drones with Low-Cost GNSS And IMU for Mapping over Featureless Terrain using Direct Georeferencing. In: ISPRS eds. International Archives of the Photogrammetry, Remote Sensing and Spatial Information Sciences, Volume XLIII-B2-2022 XXIV ISPRS Congress Nice, France, pp.37-44

2. Essel, B., Bolger, M., McDonald, J., Cahalane, C. (2023) Developing a Theoretical Assessment Method for an Assisted Direct Georeferencing Approach To Improve Accuracy When Mapping Over Water: the Concept, Potential and Limitations. International Archives of the Photogrammetry, Remote Sensing and Spatial Information Sciences - ISPRS Archives. 48(1/W1-2023), 139–144.

Chapter 2

Current State of the Art - Literature Review

2.1 Introduction

As explained in the previous chapter, the main aim of the thesis is to explore and improve the traditional photogrammetric approach for mapping water bodies using low-cost drones. This chapter is, therefore, divided according to the relevant objectives that must be met to achieve that aim. Section 2.2 will review the concepts and methodologies relevant to achieving Objective 1, i.e. the benchmarking. It will start with explanation on the role of DG in research and industry in Section 2.2.1. It will further review the concepts of DG in Section 2.2.2, and followed by an explanation on the Interior and Exterior Orientation Parameters in Section 2.2.3. The second objective will be introduced in Section 2.3 by reviewing the impact of navigational errors on DG. This will involve reviewing the IMU and GNSS in Section 2.3.2 and 2.3.3 respectively, and the considerations arising from the type of sensor, which is one of the fundamental components in photogrammetry, will be explained in Section 2.3.5. Section 2.4 will review concepts and methodologies relevant to achieving Objective 3, i.e. combining the BA and the DG methods. This will involve a review of the standard photogrammetric method in Section 2.4.1. This will explain the BA process in section 2.4.2. The final objective which is developing a scalable method will be explored in

Section 2.5, and will encompass an exploration of the key concepts influencing image registration and detail the types of machine learning algorithms employed in Chapter 6.

2.2 Objective 1- Benchmark and Test DG

The first objective of this thesis is to benchmark and test the accuracy of drone imagery of water bodies generated using the DG method. This section details the DG method in great detail, covering the two sets of parameters required for image reconstruction. It also reviews the current state of the DG method for mapping water bodies and proposes a solution to address the gap identified in the literature.

2.2.1 The Role of DG in Research and Industry

The concept of DG emerged in the 1990s as researchers delved into the potential of utilizing GPS-aided inertial navigation systems (INS) for photogrammetric applications. According to a study by Hutton and Mostafa (2005), some of the earliest tests of DG mounted a Litton LTN-90 INS on a Zeiss RMK film camera. While the results were not entirely accurate, they provided the proof of concept and laid the foundation for further exploration. Subsequent research reinforced the feasibility of the DG method, paving the way for commercial development and in 1996, Applanix, a Canadian company, unveiled the POS DG 510, the first commercially available DG system (Hutton and Mostafa, 2005).

The emergence of commercial DG systems spurred research at academic institutions, such as Cramer (1999) from the University of Stuttgart and Colomina (2000) from the Cartographic Institute of Catalonia, to investigate the full potential of this emerging technology. In the early stages of DG development, the primary question was whether the IMU and GPS could provide sufficiently accurate attitude and position information for DG. Notable studies, such as those by

Cramer et al. (2000); Cramer (1999); Jacobsen (2002); Grejner-Brzezinska (2001); Yastikli et al. (2002) and Wegmann (2002); Mostafa and Hutton (2001), demonstrated the potential of DG as a viable alternative to the traditional BA method. Importantly, the European Organization for Experimental Photogrammetric Research (OEEPE) - now the European Spatial Data Research Group (EuroSDR) conducted a groundbreaking study in 2002 that provided comprehensive information about the DG process and the necessary system calibration required to encourage adoption by research and industry (Heipke et al., 2002). This study encompassed a series of investigations comparing the accuracy of DG with the BA method, developing new system calibration methods for DG, and thoroughly exploring the Integrated Sensor Orientation (ISO) method.

Many years after the OEEPE Workshop proceedings and report, the DG method has become an established technique employed by both industry and the research community (Mostafa et al., 2010). In parallel with substantial technological advancements on IMU and GNSS systems, innovations in the development of navigational systems have enhanced the performance of the DG method. It has evolved from its initial application with film and digital cameras to encompass other common sensors such as multispectral sensors, hyperspectral sensors, and push-broom scanners. For example, several studies have employed this method in diverse applications such as wildfire monitoring (Maria and Santana, 2021), topographic mapping (Syetiawan et al., 2020), disaster mapping (Chiabrando et al., 2019), and many more.

One area of DG that has not received sufficient attention is its potential for use with low-cost drones and specifically - when mapping water bodies. To date, no studies have been carried out to improve the accuracy of drone imagery derived through DG. In fact, no studies have even explored or analyzed the errors associated with using the DG method for low-cost drones for water bodies. Therefore, this thesis aims to advance the DG method by exploring and developing novel

techniques that can improve the performance of low-cost drones in mapping water bodies. This represents one of the major contributions of this work.

2.2.2 Concept of Direct Georeferencing

DG is the process of directly obtaining the EOPs from the navigation sensor onboard the aerial platform (Mitishita et al., 2016; Pfeifer et al., 2012). It can also be defined as the process of accurately positioning and aligning aerial images to a specific location on the Earth's surface without the use of GCPs (Correia et al., 2022). This term will be used for both processes in this thesis. The DG method is not a novel approach; it has been explored since the 1990s. A strength of this method is that it completely avoids the requirement for a parallel ground survey installing and recording ground targets and also bypasses the Bundle Adjustment stage, providing significant time savings (Cramer, 1999). The sensor's position is measured in 3D (X, Y, and Z) from the projection centre, while the orientation of the sensor is measured in three axes: Roll, Pitch, and Yaw. Figure 2.1 provides an overview of the DG process, where both the intrinsic parameters of the sensor i.e. the Interior Orientation Parameters (IOP) and the EOPs are combined. Combining these two parameters makes it possible to project a point (P) from the ground onto an image. One weakness of the DG approach is that accuracy of point P is constrained by the accuracy tolerances of IMU and GNSS sensors onboard the drone that record Pitch, Roll and Yaw, and 3D position respectively (Jacobsen, 2005; Rehak, 2017).

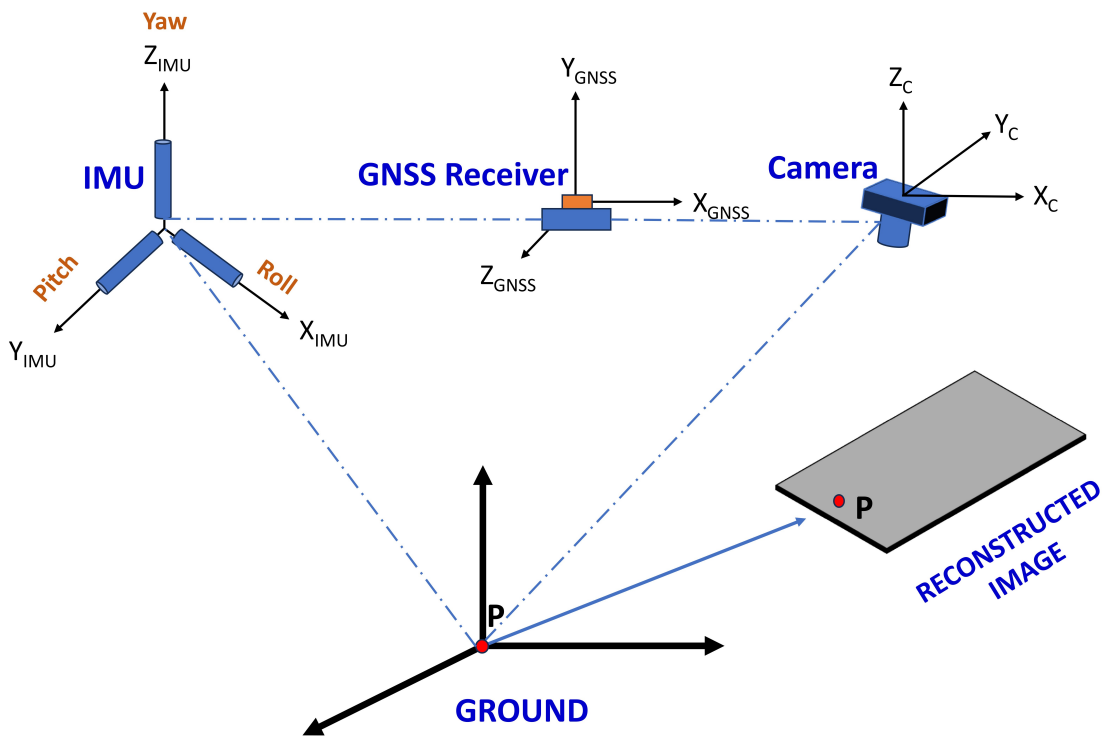

Figure 2.1: Illustration of the DG concept demonstrating how a point on the ground (P) is projected from 3D space onto a 2D coordinate system (the 2D image) by combining both the IOP (sensor) and the EOP (IMU and GNSS).

2.2.3 Interior Orientation Parameters

The term Interior Orientation Parameters (IOP), also known as intrinsic parameters - or 'what is going on inside the sensor' - refer to all of the essential parameters required for modelling the sensor's geometry and the physics of the interaction of the rays of light with that sensor (Förstner and Wrobel, 2016b). Sensors which have fixed IOPs can be described as metric sensors. These sensors are generally employed for high-accuracy topographic surveys, and examples include the list of sensors outlined in Section 1.4.3. Conversely, sensors without fixed or stable intrinsic parameters can be described as non-metric sensors. For example, these sensors include a Digital Single-lens Reflex Camera (DSLR), camcorders, smartphone cameras and Closed-circuit Television cameras (CCTV) (Wolf et al., 2014).

The IOPs that can be determined for a metric sensor can be described as follows:

1. Focal length: It is defined as the distance from the sensor's optical centre to the image sensor. This is usually measured in millimetres (Förstner and Wrobel, 2016b).

2. Principal point: It refers to the geometric centre of the photograph where the X and Y axes intersect. It represents the centre of the image and is used to locate image points relative to the sensor (Förstner and Wrobel, 2016b; Aber et al., 2019).

3. Radial lens distortion: These parameters quantify the amount of radial distortion in the image. This occurs along radial lines from the principal point (Wolf et al., 2014). Radial distortion causes straight lines to appear curved, and the distortion increases with distance from the principal point. They are typically presented as (k1, k2, k3) (Li-Chee-Ming et al., 2012)

4. Tangential lens distortion: These parameters quantify the amount of tangential distortion in the image. Tangential distortion causes straight lines to appear displaced from their ideal positions. They are presented as (p1, p2) (Wolf et al., 2014).

5. Pixel Size: The physical size of each pixel on the image sensor or film plane, typically measured in millimetres (Wolf et al., 2014).

Accurately determining these IOPs is important for many photogrammetric applications, and these are usually constant or fixed (either at manufacture or by the operator before each flight) and are predominantly determined by calibrating the sensor (Wolf et al., 2014) either through laboratory calibration or by the user through calibration targets such as a checkerboard or the BA process (Aber et al., 2019). Generally, the calibration state of sensors can be broadly distinguished into three types: (1) a calibrated sensor – where the IOPs of the sensor are completely and accurately known (2) a partially calibrated sensor – some of the IOPs are identified following the calibration process and (3) an uncalibrated

sensor – this is where the IOPs of the sensor are completely unknown (Förstner and Wrobel, 2016b).

2.2.4 Exterior Orientation Parameters

EOPs describe the spatial relationship between the sensor and the scene being photographed (Aber et al., 2019) - they explain where the sensor is (three-dimensional (3D) position - XYZ) and where it is pointing (the direction). It is also commonly referred to in photogrammetry and computer vision as the Position and Orientation (POSE). These EOPs are important for accurately reconstructing 3D scenes and surfaces from two-dimensional (2D) images. The process includes determining the position of the sensor in XYZ and the sensor's orientation in terms of Roll, Pitch and Yaw during image acquisition (Wolf et al., 2014). Accurate determination of the EOPs is a fundamental task in the photogrammetric workflow, enabling accurate measurements (Jacobsen, 2005; Han et al., 2011; Grussenmeyer and Al Khalil, 2002).

Two approaches are commonly employed for computing EOPs: direct and indirect determination (Ip et al., 2007). The first approach is commonly referred to as Direct Georeferencing (DG), while the second approach is called the Bundle Adjustment (BA) method. These two methods are suited for different applications and scenarios. For instance, a project demanding extremely high accuracy will require the BA method, while projects over featureless terrain or those that require rapid and immediate processing of images such as in emergencies like earthquakes can benefit from the DG method.

2.2.5 Pros and Cons of the DG Method

While exploring DG as a method, it is essential to evaluate its advantages and disadvantages critically. To provide a comprehensive overview, Table 2.1 outlines the pros and cons of the DG method. This table aims to offer a comparative analysis of the strengths and limitations associated with DG. In summary, the

use of the DG method provides the practical means to map a featureless terrain, albeit its accuracy is constrained by the performance of the integrated IMU/GNSS system. Thus, low accuracy for applications that use low-cost drones.

Table 2.1: Pros and Cons of the DG Method

Pros	Cons
Not dependent on GCPs	Requires rigorous system calibration such as boresight adjustment (is the process of determining the misalignment between the camera and the IMU) and lever arm offsets (is the process of determining the offset between GNSS and the camera)
Computationally less expensive, making it easy and fast to use	Accuracy constrained by IMU and GPS limitations.
Useful for areas with difficult access	Low accuracy for applications that use low-cost drones.
Can be used for standard mapping applications	Potential accuracy degradation in dynamic or vibrating platforms.
Reduces data acquisition time since a high overlap percentage isn't needed	Small errors in the navigation sensors at altitude are converted to large errors on the ground
Enables quick image processing for emergency applications	
Can be used for applications in challenging terrains such as featureless terrain where traditional methods cannot work	

2.2.6 DG, Drones and Water: the Current State of the Field

No research has been carried out to benchmark the accuracy of drone images of water bodies generated using the DG method. However, some research has been conducted to create mosaics of images from the DG method (Román et al., 2023; Lo et al., 2023; De Keukelaere et al., 2023; Windle and Silsbe, 2021). For example, De Keukelaere et al. (2023) produced a mosaicked image over several lakes across Europe, which was used to map water turbidity and Chlorophyll-a. This study utilized the DG approach by using a commercial VITO MapEO water software. This software projected the acquired drone images onto the ground plane and then radiometrically corrected the images to produce a final water quality map.

Similar studies have also been performed by Lo et al. (2023), which generated a mosaicked image of a medium-sized lake in China. This study aimed to measure the distribution of Chl-a, Total Phosphorus, Ammonia Nitrogen, and Electrical Conductivity using the mosaicked image. This was derived using a Python script that also projected the images onto the ground plane. A major issue is that neither of these studies provided an analysis of the accuracy of the reconstructed 2D images derived from the DG method. This thesis argues that benchmarking the accuracy of the reconstructed 2D images derived from the DG method is essential to assess the performance and establish an approach for comparison with methods that seek to improve the DG method. Additionally, it is important to assess the accuracy under different environmental conditions, such as in calm and strong winds. However, as at now, there is still no theoretical or real-world tests to determine the accuracy of reconstructed 2D images obtained from low-cost drones.

2.2.7 A Possible Solution

Benchmarking and testing the accuracy of reconstructed 2D images obtained from low-cost drones requires developing a simulator for theoretical tests and validate with real-world data. Because water bodies make it difficult to install fixed targets, the first objective of this thesis is to approximate a water environment to carry out the initial theoretical accuracy assessment.

2.3 Objective 2 - Analyse Errors Associated with Direct Georeferencing

2.3.1 History of Navigational Sensors

Throughout history, navigation systems have played a pivotal role in various fields, including exploration, military operations, construction, surveying, and many more (Stam, 2010). For instance, these systems enabled 15th-century ex-

plorers to identify new regions of the Earth (Chrysochou, 2016), and they continue to guide us in our daily lives, helping us navigate to shops and other destinations. Throughout history, the methods of navigation has changed. These explorers made progress in navigation through the use of instruments such as the compass, the cross-staff, and the astrolabe (Chrysochou, 2016). From the 19th to the 20th century, there have been great advances in navigational tools (Tazartes, 2014). Two of the most widely used and standardized navigational techniques in use currently are GNSS and IMU (Wolf et al., 2014). In the early 1980s, these devices were integrated into airborne platforms, such as helicopters, for aerial surveying applications (Hutton and Mostafa, 2005). This integration was a groundbreaking advancement in mapping, which improved the speed at which high-resolution maps of the Earth's surface could be produced.

However, these devices were bulky, averaging around 30 pounds in weight but since the early 2000s, these devices have significantly reduced in size, opening up the possibility of incorporating them into drones (Rehak et al., 2013). This innovation in the drone market has also been the prompt for developing smaller and more affordable IMU and GNSS systems.

The IMU and GNSS are considered essential for acquiring navigational data from a drone (Mostafa and Abdelhafiz, 2017). In aerial surveying, these two devices are always used together. As a result, knowing only the location of the sensor during image capture is insufficient. Rather, it is equally important to understand the sensor's orientation during image capture.

2.3.2 Inertial Measurements Units - the IMU

IMUs are devices used to measure a drone's attitude or orientation (Correia et al., 2022). An IMU typically consist of three main parts: the accelerometer, the gyroscope and the magnetometer. These devices work together to provide an accurate attitude measurement of the drone. A typical IMU device contains three

accelerometers used to measure the acceleration in the X, Y, and Z directions (Stam, 2010). These accelerometers measure changes in velocity and can determine the direction and magnitude of accelerative forces acting on the drone. The gyroscopes measure angular velocity and aid in establishing the object's orientation. The magnetometer helps measure the direction of the magnetic field. IMUs combine the data from the accelerometer, gyroscope and magnetometer to calculate the drone's position, velocity, orientation and the direction of the magnetic field (Stam, 2010).

In simpler terms, the IMU defines the relationship between the navigation coordinate system and the body coordinate system (Rehak, 2017). Importantly, the IMU measures the drone's orientation around three axes in a right-handed coordinate system. Typically, an IMU has six degrees of freedom (DOF), but when a magnetometer is included, it measures nine DOF (Alatise and Hancke, 2017). Therefore, the rotation angles of the drone can be measured in Roll, Pitch, and Yaw. These three angles form part of the six EOPs. Roll, Pitch, and Yaw angles describe the three rotational angles from the orientation of a rigid body relative to a fixed reference frame known as the navigation coordinate system (Bäumker et al., 2002). Since direct georeferencing of airborne imagery involves projecting a point from a 3D world onto a 2D image, it will require the use of these different coordinate frames (Li et al., 2017). The subsection below provides a detailed explanation of the fundamental reference frames in photogrammetry.

2.3.2.1 Coordinate System 1 - the Navigation frame

The navigational coordinate system is a fixed reference frame used to define the position and orientation of an object in space (Rehak, 2017). It serves as the reference frame against which the orientation of an object is measured with different ways of representing navigational coordinate systems, including the North-East-Down (NED) frame and the Earth-Centered Earth-Fixed Coordinates (ECEF) system. The ECEF frame is a global reference frame with its origin at the Earth's

centre and three orthogonal axes fixed to the Earth. As shown in Figure 2.2, the Z-axis (Ez) points to the North Pole, the X-axis (Ex) points to the intersection of the Prime Meridian and the equator, and the Y-axis (Ey) completes the right-handed system. A NED system frame on the other hand is a local reference frame that uses Cartesian coordinates, where X (Nx) is North, Y (Ny) is East, and Z (Nz) is down to represent position relative to a local origin. The NED system frame is defined such that the North and East axes lie within a plane that is at a tangent to the Earth's surface, assuming the WGS84 ellipsoid model of the Earth.

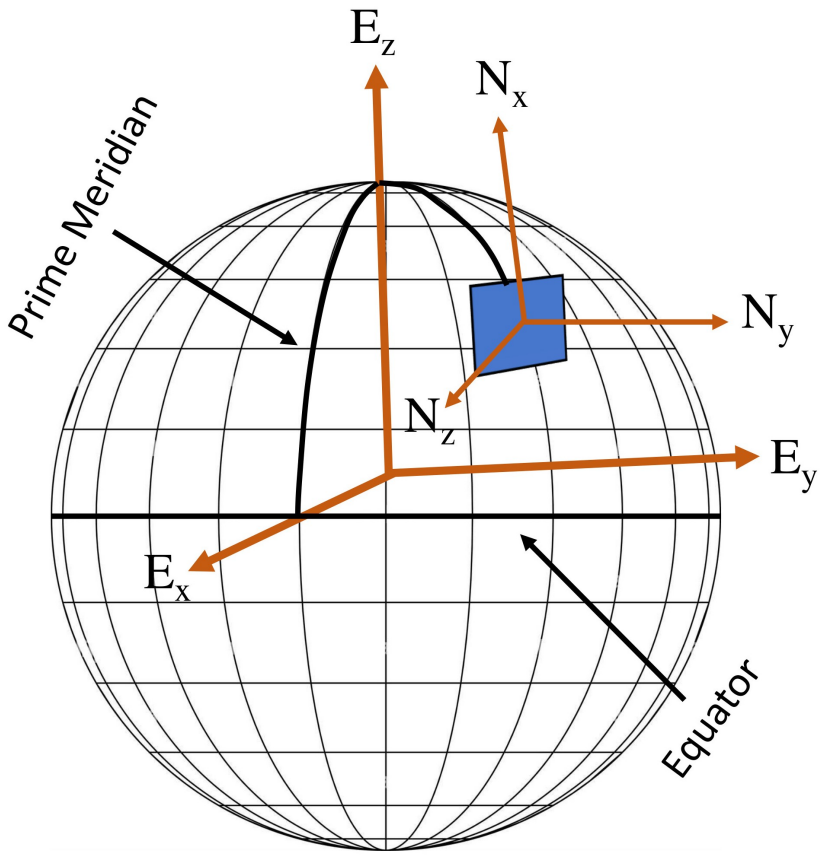

Figure 2.2: An image representing of the differences between the ECEF and NED system frame - these are the first coordinate systems involved and represent the Navigation Frame.

2.3.2.2 Coordinate System 2 - the sensor Frame

The sensor frame (c) refers to a frame of reference specifically associated with the sensor. In the context of photogrammetry, the sensor frame system is essential for accurately describing the spatial properties of images and scenes captured by

a sensor (Förstner and Wrobel, 2016b). The origin of the sensor frame is located at the perspective centre, the point where the optical axis intersects the image plane as shown in 2.3. The x-axis and y-axis of the sensor frame align parallel to the corresponding axes of the image coordinate system (Rehak, 2017).

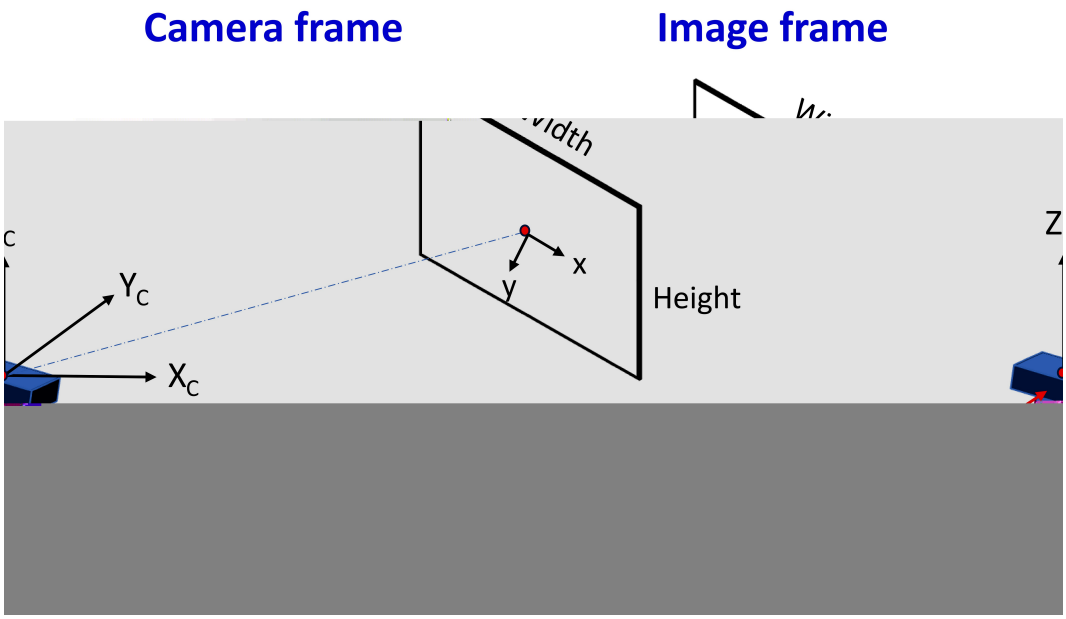

Figure 2.3: A graphic showing the sensor frame with the centre being the perspective centre: the point within the sensor lens through which light rays converge to form the image

2.3.2.3 Coordinate System 3 - the Body frame

When a sensor is fixed to a rigid body (such as a drone), the drone's centre of mass is typically chosen as the origin of the rigid body. The Z-axis points upwards, the X-axis points forward in the direction of motion or travel, and the Y-axis points to the right of the object, perpendicular to the direction of motion, to form a right-handed system, as shown in Figure 2.4a.

The Roll angle, also known as the tilt angle, describes the rotation of a body around the X-axis relative to the reference frame (Gustavsson, 2015; Förstner and Wrobel, 2016a; Yan, 2017; Khaghani and Skaloud, 2016). In other words, as the drone banks left or right, it is described as the Roll angle. Thus, a positive Roll

angle indicates that the sensor is tilted (or banked) to the right, while a negative Roll angle indicates that it is tilted to the left.

The Pitch angle defines the rotation of the drone around its Y-axis. In a standard orientation, the Pitch angle can be visualized as the angle between the longitudinal axis (running from nose to tail) and the horizontal plane (Rehak, 2017). A positive Pitch angle indicates that the nose of the drone is pointing upwards, while a negative Pitch angle indicates that the nose is pointing downwards. For example, Figure 2.4c shows an image of a drone Pitching down.

The final angle is the Yaw angle, which defines the rotation of a body around the z-axis (Bäumker et al., 2002). The Yaw angle typically aligns with the drone's direction of travel and points upwards, as shown in Figure 2.4d. A positive Yaw angle indicates that the body is rotated clockwise, while a negative Yaw angle indicates that it is rotated counterclockwise. Typically, the range of these angles is -180 degrees to +180 degrees for Roll, -90 degrees to +90 degrees for Pitch, and 0 to 360 degrees for Yaw.

In photogrammetry and computer vision, the representation of these rotation angles can be accomplished primarily through three methods: Euler angles, quaternions, and direct cosine matrices (Narkhede et al., 2019; Ellum, 2009; Alatise and Hancke, 2017). Besides these three, other methods can also be employed to represent rotation angles, namely the axis-angle representation (Alatise and Hancke, 2017) and Rodrigues parameters (Ellum, 2009). Euler angles are a set of three angles that describe the orientation of a rigid body in three-dimensional space. Consequently, they are defined by a sequence of three rotations about three distinct axes. The Roll, Pitch, and Yaw angles using a right-front-up body constitute the most commonly used sequences in photogrammetry (Ellum, 2009). This order of rotation is crucial for defining the position of a rigid body and is typically referred to as the "Euler angle sequence" (Ellum, 2009). One primary limitation

of Euler angles is their susceptibility to gimbal lock. This phenomenon occurs when two of the rotation axes become aligned, resulting in a loss of one degree of freedom and restricting the system's ability to represent certain orientations (Toso et al., 2015).

An alternative is the application of quaternions which are a mathematical representation of rotations in three-dimensional space. Quaternions offer a compact four-dimensional representation of attitude, using both a scalar and a vector component (Ellum, 2009). The scalar component captures the magnitude of the rotation, while the vector component represents the axis of rotation. Unlike Euler angles, quaternions have been found to be efficient and do not suffer from gimbal lock (Ellum, 2009). However, quaternions don't provide a clear and intuitive way to interpret and communicate rotations (Bernardes and Viollet, 2022), are computationally complex (Toso et al., 2015), and more difficult to visualize than Euler angles (Toso et al., 2015). Euler angles have a direct physical interpretation, aligning with how humans perceive and describe rotations in everyday terms. For example, Roll, Pitch, and Yaw correspond to familiar movements like tilting, nodding, and turning, which makes it easy to understand and communicate the rotation of a rigid body.

In this thesis, the Euler angle representation is used in all subsequent analysis and development of methods where rotational angles were used. This is due to its simplicity in representation and analysis and its ease of understanding and visualization (Nolze, 2006). Most importantly, Euler angle representation in the three axes makes it easier to visualize, animate rotations and simulations, as well as theoretical assessment and the development of methods where EOPs are used, which are important in photogrammetry and computer vision.

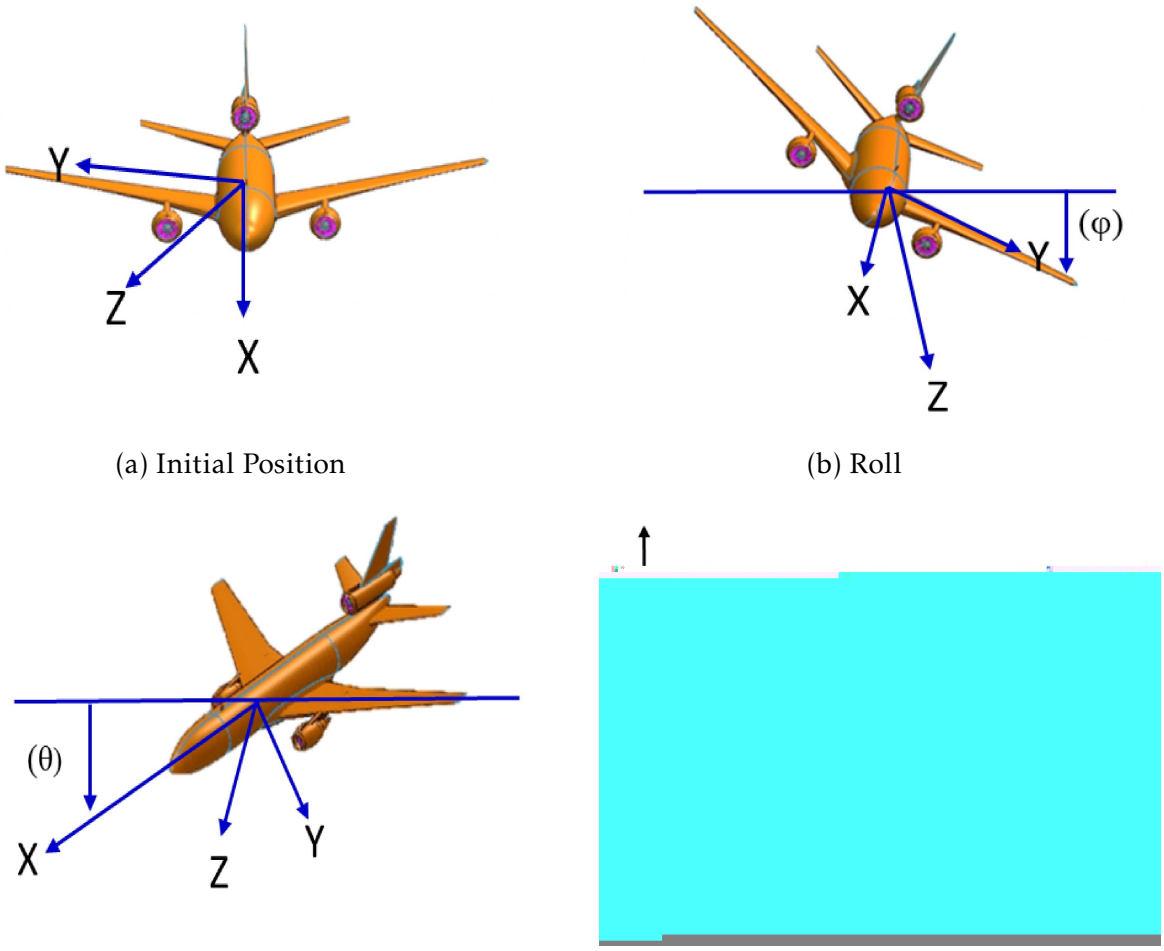

(a) Initial Position

(b) Roll

(c) Pitch

(d) Yaw

Figure 2.4: Illustration of the orientation of a rigid body (drone) where (a) is the initial position of a drone, (b) is where the drone is tilted on the right wing down (i.e. Roll), (c) is where the nose of the drone is Pitched down (i.e. Pitch) and (d) where the drone is turned to the right (i.e. Yaw).

2.3.3 Satellite Positioning - GNSS

GNSS is a satellite-based navigation system that provides location worldwide (Wolf et al., 2014). These locations are derived from a set of satellites orbiting around the Earth, based on the principle that the receiver is within a line of sight for at least four satellites (Stam, 2010). Each satellite transmits a signal that includes its position and a precise time stamp. The receiver calculates the distance to each satellite by measuring the time it takes for the signal to arrive. Once the distances to the satellites are known, the receiver can calculate its own position in X, Y, and Z using trilateration (Stam, 2010).

GNSS devices provide varying accuracy, ranging from centimetres to meters, depending on the type of device (Rehak, 2017; Kraus, 2007). RTK and Differential GPS (DGPS) technology offer very high accuracy by utilizing reference stations to correct satellite signal errors caused by atmospheric conditions and other factors (Rehak, 2017). According to Stam (2010), there are three different grades of GNSS devices: industry/survey-grade, professional-grade, and consumer-grade devices.

Survey-grade drones employ RTK or DGPS systems and typically achieve an accuracy of less than 5cm in XY and 10cm in Z. Professional-grade drones often use the single-point positioning technique to derive locations, rendering them unable to utilize reference stations for signal and atmospheric interference correction.

Consumer-grade drones come with low-quality antennas that do not provide the signal quality and reception of professional and survey-grade drones. They are more susceptible to signal interference, which affects the calculations of GPS positions.

2.3.4 Navigational Sensors - Influence of Errors on Accuracy

The effects of errors in navigational sensors can significantly affect the accuracy and reliability of reconstructed 2D images created through DG. All navigational sensors have error tolerances; however, drones equipped with low-cost navigational sensors unsurprisingly have larger tolerances (Hajiyev et al., 2015). In standard photogrammetric methods over terrestrial regions, these errors are minimized through the BA process or through the incorporation of GCPS as they help accurately calibrate the sensor and refine the EOPs. During DG, there are several sources of errors such as sensor model error, calibration errors, errors due to varying topography or elevation, GNSS positional errors, and IMU angular errors (Heipke et al., 2002). This thesis focuses on GNSS and IMU errors because the

DG method relies heavily on these sensors and therefore, quantifying their effects on reconstructed 2D image is essential. Studies suggest that GNSS position errors translate to equivalent position errors on the ground, while IMU errors lead to positional errors that increase in magnitude with the drone's flight height (Brown et al., 2007). Ultimately, each of these errors translate into positional inaccuracies in the reconstructed 2D image produced by the DG method.

To the best of the authors' knowledge, no assessment has been conducted to quantify the influence of errors in navigational sensors for low-cost drones when using the DG approach. The impact of navigational sensor errors on low-cost drones for mapping water bodies further introduces specific challenges that must be addressed.

2.3.5 Drone Sensor

Apart from the navigational sensors described above in Sections 2.3.2 and 2.3.3, the optical sensor is another fundamental component that influences the accuracy of the survey. Recent advancements in sensors for drone photogrammetry have significantly increased the use of drones. Technological advancements have enabled the design of smaller sensors, with weights ranging from 20 grams to 800 grams (Wolf et al., 2014).

There are several sensors that can be used for drone photogrammetry, including RGB cameras,oferamer7(t4rg 0 0 1(ey)100(.)-526(Recen)5(t)-326(aWf)9(oush-b)5(as401

sor remains level and focused on the target area (Wu et al., 2019). This device is particularly valuable when strong winds or wind gusts are present during the survey. Self-levelling gimbal ensures that the tilting of the sensor is minimized, resulting in near-vertical imagery (Wolf et al., 2014).

On the other hand, some sensors are not mounted on a self-leveling gimbal (Aber et al., 2019). Such sensors are normally affected by vibrations from the platform they are mounted on. When sensors are exposed to excessive vibrations without a self-levelling gimbal, the sensor's optical axis struggles to remain vertical, causing significant tilt in the images. Currently, there are many low-cost drones in which the sensors are not mounted on self-leveling gimbals. For example, drones like the Parrot Bluegrass, Parrot Disco AG, and fixed wing drones such as the sensefly eBee series all lack a self-leveling gimbal. Typically, fixed-wing drones do not have gimbals for stabilizing sensors as many multi-rotor drones do, as the design and flight characteristics of fixed-wing drones differ from those of multi-rotor drones, affecting how sensors are mounted and stabilized. In most fixed-wing drone designs, sensors are usually mounted in a fixed position inside the aerial platform to minimise drag.

Similarly, there are sensors onboard multi-rotor drones that do not have self-leveling gimbals. For instance, the most widely used multispectral sensors, such as the Parrot Sequoia and all the MicaSense series sensors, do not have self-levelling gimbals. While self-levelling gimbals are not inherently required for these sensors, gimbal devices can be installed on the drone to stabilize the sensor further. These installations come at an additional cost of several hundred euros. Additionally, manually installing a sensor on a gimbal can be a more complex process (Rehak, 2017), especially for users unfamiliar with the specific requirements and adjustments needed for proper integration and often voids a manufacturer's warranty or insurance premium. Consequently, these installations often require technical experts to ensure the sensor's proper functioning. Most im-

EOPs for generating orthoimagery.

2.4.2 Safety in Numbers: the Bundle Adjustment

Since the early 1980s, the BA method has become the standard technique for computing EOPs and for subsequent 3D image reconstruction (Defrise and Grangeat, 2010). BA is a mathematical optimization technique used to refine the 3D coordinates of points and the EOPs of sensors in photogrammetry (Triggs et al., 2000). It is an iterative process that minimizes the reprojection error, which is the difference between the observed image locations of points and the predicted image locations of points based on the current estimates of the 3D coordinates and sensor parameters (Defrise and Grangeat, 2010; Förstner and Wrobel, 2016b; Triggs et al., 2000). BA is important because it corrects for sensor POSE inaccuracies, subsequently improving the EOP's accuracy and image reconstruction. It can also be used to compensate for errors made during the initial sensor calibration and to reduce the effects of noise in the data.

2.4.3 Workflow and Key Components of Bundle Adjustment

The processes involved in computing the EOPs via BA consist of the following steps as illustrated in Figure 2.8: Feature extraction and matching, initial reconstruction, reprojection error calculation, objective function formulation, nonlinear optimization, simultaneous parameter update, refined reconstruction and output.

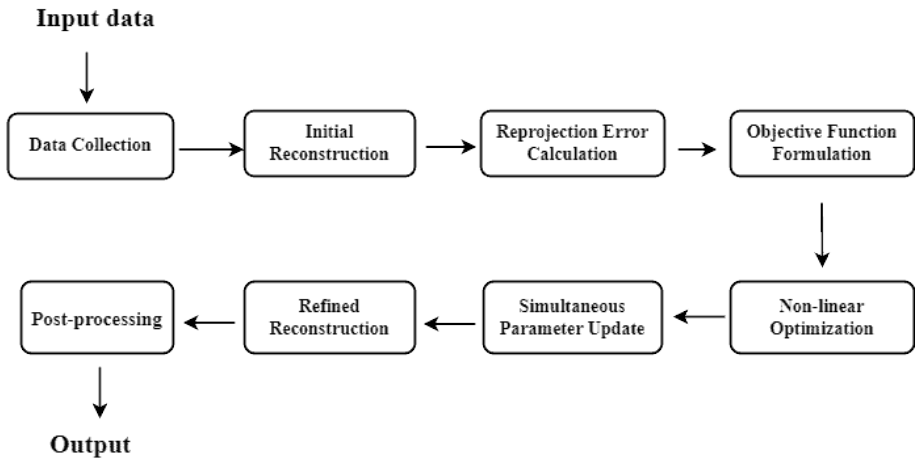

Figure 2.8: A workflow of the BA method which consist of a series of steps to refine the EOPs.
Source: (Kumar and Simic, 2024)

1. **Feature extraction and matching**: To estimate the EOPs, distinctive features are identified in multiple images and matched with similar ones identified in other images- these are called matching points (Verykokou and Ioannidis, 2018). These matching points are then further filtered using techniques such as Random Sample Consensus (RANSAC) to remove the outliers.

2. **Initial reconstruction**: This step creates an initial 3D reconstruction of a surface using techniques like SfM technology as explained in Section 1.5. This initial reconstruction provides an initial guess of the EOPs and the 3D scene structure. This initial estimate often has errors, but importantly provides the initial approximations for the BA process when refining the EOPs.

3. **Reprojection error calculation**: This step computes the reprojection error for each image, thus calculating the residuals by comparing the observed image features (from step 2) with their corresponding projections from the structure-based projection positions (Granshaw, 1980). Usually, it quantifies the overall error in the current reconstruction by summing the squared errors.

4. **Non-linear optimization and Simultaneous Update**: This step aims to minimize this cost function by adjusting the 3D points and sensor parameters (Granshaw, 1980). Non-linear optimization techniques, such as Gauss-Newton or Levenberg-Marquardt algorithms, are applied to minimize the cost function iteratively. Afterward, simultaneous updates are applied to update the EOPs from Step 2 based on the optimization results obtained from the non-linear optimization.

5. **Refined Reconstruction and Output**: In this step, the results obtained from step 4 can be further refined and iterated. This iteration can involve replacing the feature correspondences, adjusting input parameters, or applying additional constraints to improve the accuracy of the EOPs and the reconstructed surface (Verykokou and Ioannidis, 2018). The outputs from the BA represent the most accurate and consistent representation of the EOPs and the reconstructed 3D scene. The output is therefore suitable for various high accuracy applications such as topographic mapping and engineering surveys.

Figure 2.9 shows the process of BA from multiple stereo images, and Table 2.2 outlines the pros and cons of the BA method.

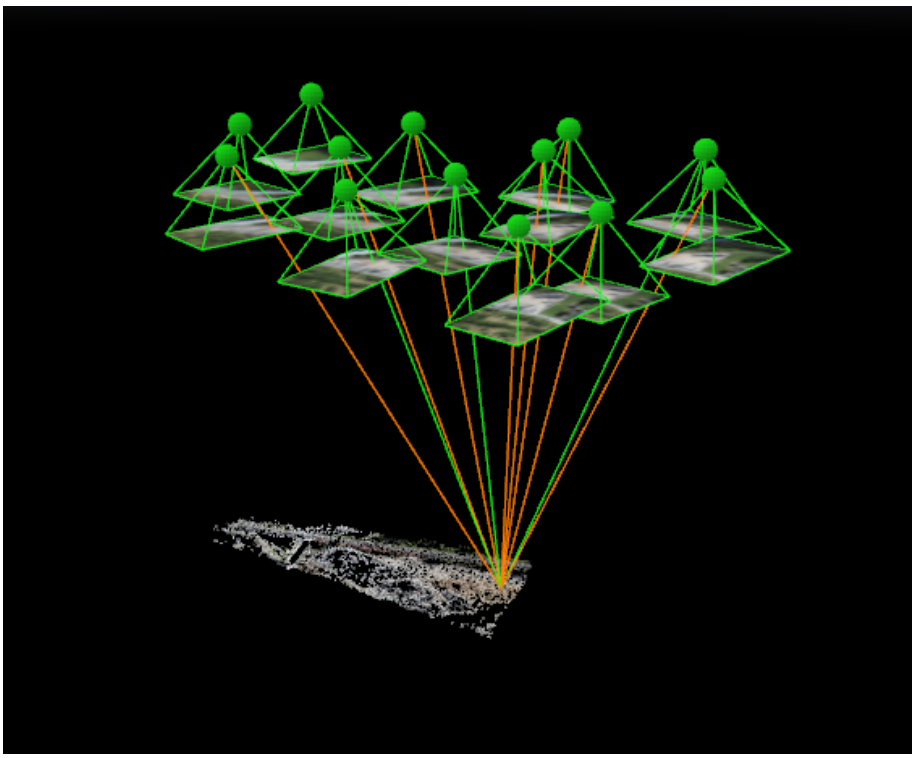

Figure 2.9: Results from Pix4D Mapping software - a widely used drone image processing software that utilizes the BA technique. This process is based on finding common points between overlapping images that are used to refine and improve the estimation of the EOPs for each image.
Source: (PIX4D, 2019)

Table 2.2: Pros and Cons of Bundle Adjustment

Pros	Cons
Accuracy: It corrects for inaccuracies in the sensor pose, hence enhancing the accuracy of the image reconstruction	Featureless terrain: it is nearly impossible to apply BA in featureless terrain due to the absence of tie points.
Consistency: It ensures internal consistency among all sensor poses and 3D points.	Computationally expensive: Bundle adjustment can be computationally intensive, especially for large datasets.
Robust: It is robust to outliers and noise in the data.	Emergency Response: The optimization process requires substantial processing time, making emergency or real-time applications impractical.
Large Datasets: BA can handle large datasets with numerous images with different viewing angles.	Sensitivity to initial estimates: BA requires accurate initial estimates of the 3D coordinates and sensor parameters. If the initial estimates are not accurate, it may lead to convergence issues.

2.4.4 Integrated Sensor Orientation - ISO

As described in Sections 2.2.2 and 2.4.2, the DG method uses GNSS and IMU to determine the EOPs directly, while BA relies on tie points and Ground Control Points (GCPs) to determine the EOPs. Recognizing the benefits of both approaches, photogrammetrists have explored another method called Integrated Sensor Orientation (ISO) for surveying and mapping (Heipke et al., 2002). This technique leverages the DG method's ability to provide an initial approximation of EOPs, allowing the BA method to function with only a limited number of tie points in overlapping images (Rehak, 2017; Heipke et al., 2002). Additionally, ISO eliminates the need for extensive GCPs by distributing only a sparse network of these targets around the edges of the survey area (Khoshelham, 2009). This approach reduces computational time while improving the accuracy of the resulting orthoimagery (Ip, 2005). The ISO method has been primarily used in areas with limited or no ground features like forests, deserts, and snow-covered regions (Ip, 2005; Tanathong and Lee, 2014). Emergency response situations involving forest fires, floods, and earthquakes also benefit from ISO (Ip et al., 2007). Figure 2.10 shows the ISO method and how it utilises limited GCPs and tie points.

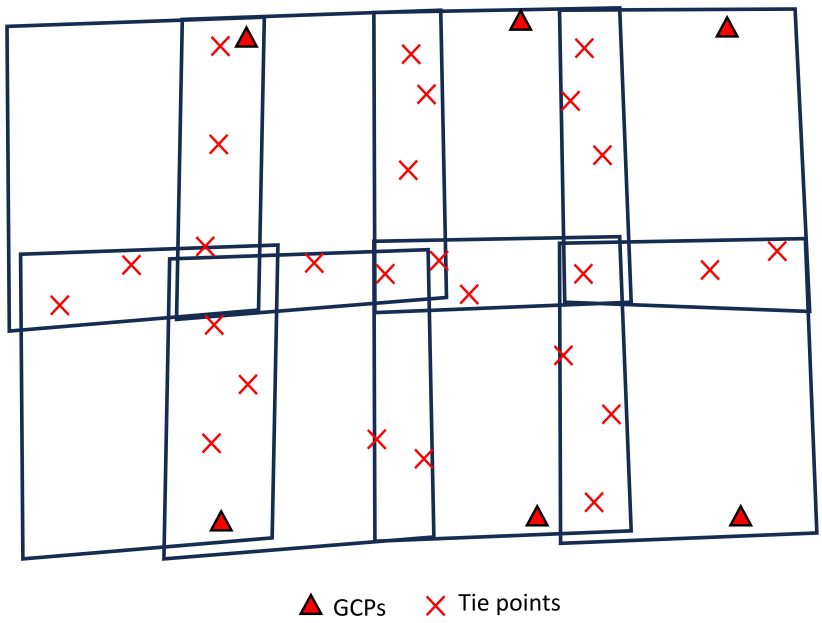

Figure 2.10: Illustration of the ISO method where it minimises the use of GCPs and tie points. Utilizing blocks of images makes it possible to leverage the benefits of DG and BA.

Motivated by the potential capabilities of the ISO method in areas with limited or no ground features, this thesis investigates whether ISO can be directly applied or requires adaptation for mapping water bodies. The presence of adjacent landmasses around water bodies suggests the ISO method could potentially be implemented for mapping water bodies. Therefore, it is essential to explore whether applying ISO with low-cost drones can achieve comparable accuracy to the standard photogrammetry technique - BA.

2.5 Objective 4 - Automated Image Registration Model

This section reviews key image registration theory and terminology necessary for understanding the model developed in Chapter 6. It explains image registration and homography concepts, as well as the machine learning techniques used for training and validating the model.

2.5.1 Definition of Image Registration

Image registration is an important process in photogrammetry that involves geometrically aligning two or more images of the same scene taken under different conditions, such as different viewing angles (Ye et al., 2020). It is the process of registering one or more images onto another image, typically onto a referenced image (Scheffler et al., 2017). One of the goals of this process is to find the optimal spatial transformation that aligns the target image with the reference image, as shown in Figure 2.11, enabling accurate analysis and comparison of features in the images. It corrects misalignment by eliminating significant differences in rotation, translation and scale. (Ye et al., 2020).

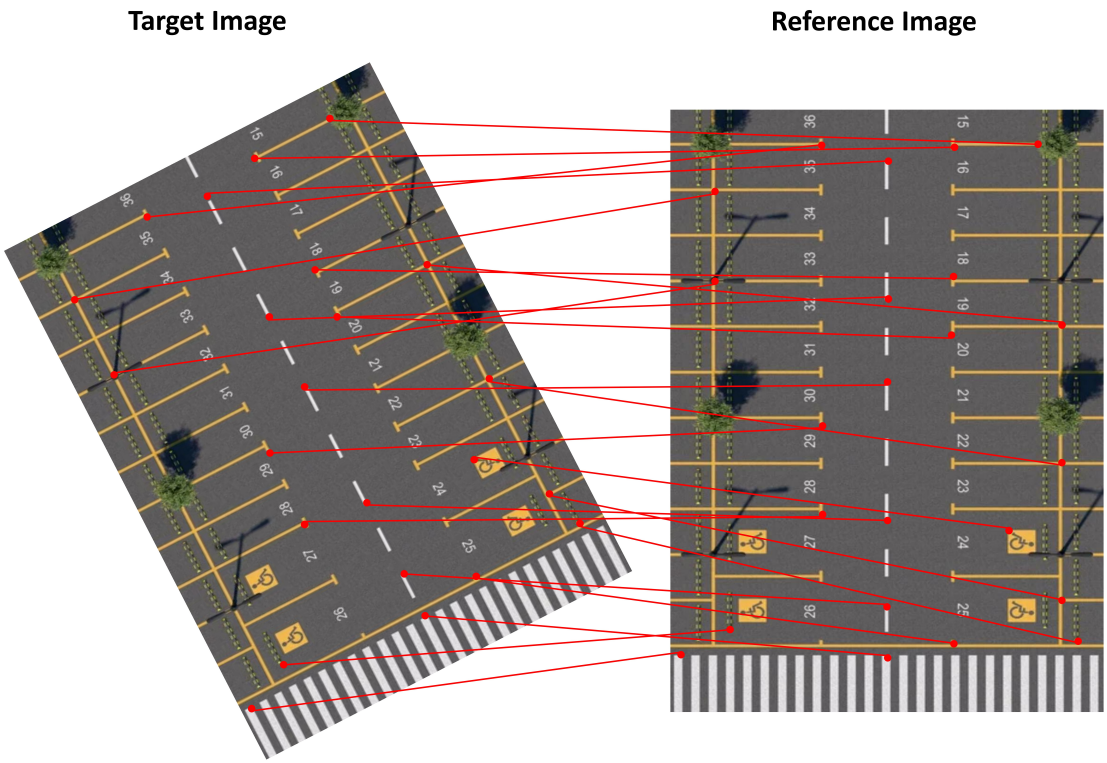

Figure 2.11: An illustration of the concept of image registration where a spatial transformation is determined to map a target image onto a reference image. This illustration shows that both images are of the same scene; however, the target image has a different orientation from the reference image. The image registration technique works by transforming the target image to align with the reference image

According to photogrammetric literature, image registration methods can be categorized into two main categories: region-based/ gray-based registration and feature-based registration (Yang et al., 2019; Zhao et al., 2020; Ye et al., 2020). The region-based registration involves comparing the pixels in a small window on one image with the same-sized window on another image. It then calculates a similarity measure, which is directly derived from the pixel intensity in the corresponding windows. Feature-based registration, on the other hand, extracts points or features to establish the geometric relationship between the target and reference images. A typical feature-based image registration method consists of two important steps: image matching and image warping. The first step identifies corresponding points between the target and reference images, while the second step calculates the homography transformation matrix that is employed to transform the target image (Ihmeida and Wei, 2021).

According to Zhao et al. (2020), the feature-based method has the advantage of easy extraction of points/features, requires less run time and exhibits high robustness for image registration when compared to the region-based method. Furthermore, the feature-based registration methods have demonstrated the capability for handling non-linear deformations and complex image transformations. This capability is particularly important when dealing with images that undergo significant changes arising from factors such as significant variation in the viewing angle of the sensor and perspective distortion that might be encountered for oblique imagery. A limitation of the feature-based method is that it requires a sufficient number of repeatable features extracted from both images.

In Chapter 6, the feature-based method will be employed to determine the relationship between target and reference images. This method is chosen because the training datasets that will be used in Chapter 6 contain a significant number of images captured from varying viewing angles, some of which require complex image transformations.

2.5.2 Concept of Homography

Homography is a mathematical concept that represents a transformation parameter that finds and maps points in one image to corresponding points in another image, given that both images are of the same planar surface (Hussnain, 2020; Tzanidou et al., 2015). Estimating a 2D homography from a pair of images is one of the fundamental principles of computer vision (Fristedt, 2017). In photogrammetry and computer vision, homography estimation is a technique used to establish this mathematical relationship between the two images of the same scene but taken from different viewpoints. The homography can be calculated by finding a set of corresponding points between two images and then fitting a mathematical model to these points. These corresponding points' accuracy directly influences the homography estimation's accuracy (Zeng et al., 2019). The

general approach for estimating the homography using the feature-based method that has been chosen for this thesis can be described in two main steps: correspondence detection and homography estimation.

2.5.2.1 Point Correspondence Detection

The first step in estimating the homography is to identify correspondences. Correspondence detection involves finding identical tie points/keypoints between the target and reference images. In recent years, the widespread adoption of varying image-capturing devices has spurred an increase in the use of different feature detection algorithms (Salahat and Qasaimeh, 2017). This has necessitated the development of automated algorithms for robust correspondence determination called feature detectors. Some of the most widely used feature detectors are Scale-Invariant Feature Transform (SIFT), Speeded Up Robust Features (SURF), Oriented FAST and rotated BRIEF (ORB) and Accelerated-KAZE (AKANZE) (Bouchiha and Besbes, 2015; Ye et al., 2020). Though several feature detectors exist, according to Salahat and Qasaimeh (2017), there is no ideal detector for all applications. This is due to the diversity of computer vision applications and the varying sensors and image conditions, making it impossible to have one ideal detector.

In general, point correspondences are first described by encoding their local or global features, which allows them to be uniquely identified across images. Next, a matcher is applied, which aims to remove outliers in the key points detected. Removing outliers is important because the initial points detected may contain incorrect matches. Algorithms like Random Sample Consensus (RANSAC) can subsequently be applied to reduce the matching error where points are incorrectly paired (Wang et al., 2018). For illustrative purposes, Figure 2.12 and 2.13 shows the initial point correspondences and the true point correspondences after the application of the RANSAC algorithm, respectively, for an image taken from a drone. The initial point correspondence, as illustrated in Figure 2.12, typ-

ically includes a lot of matching errors, which tends to affect the estimation of the homography matrix.

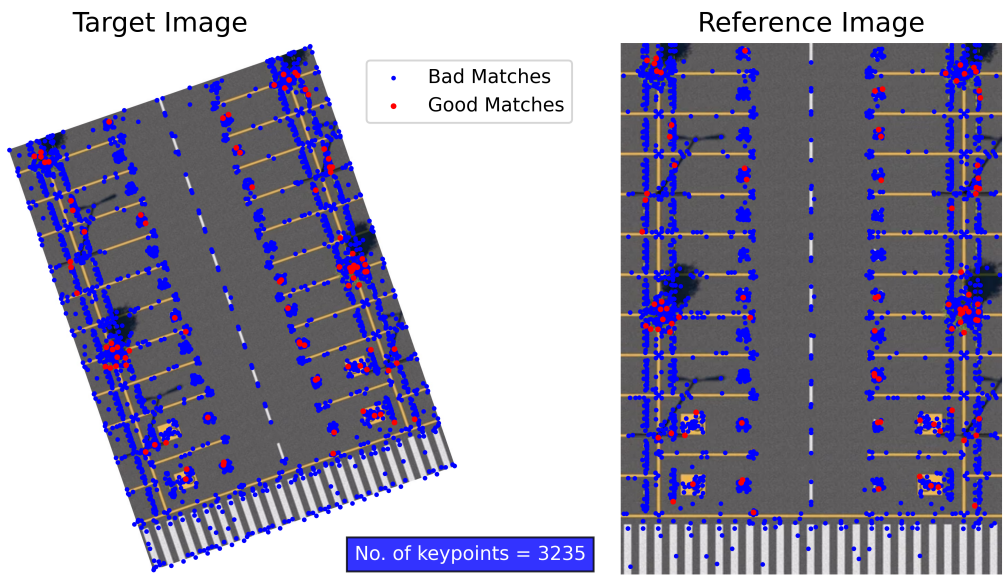

Figure 2.12: An illustration of the initial points correspondence detected between the target and the reference image. This initial result contains a lot of mismatches that affect the accuracy of the estimated homography matrix.

These errors present can then be filtered to produce the true correspondence as seen in Figure 2.13.

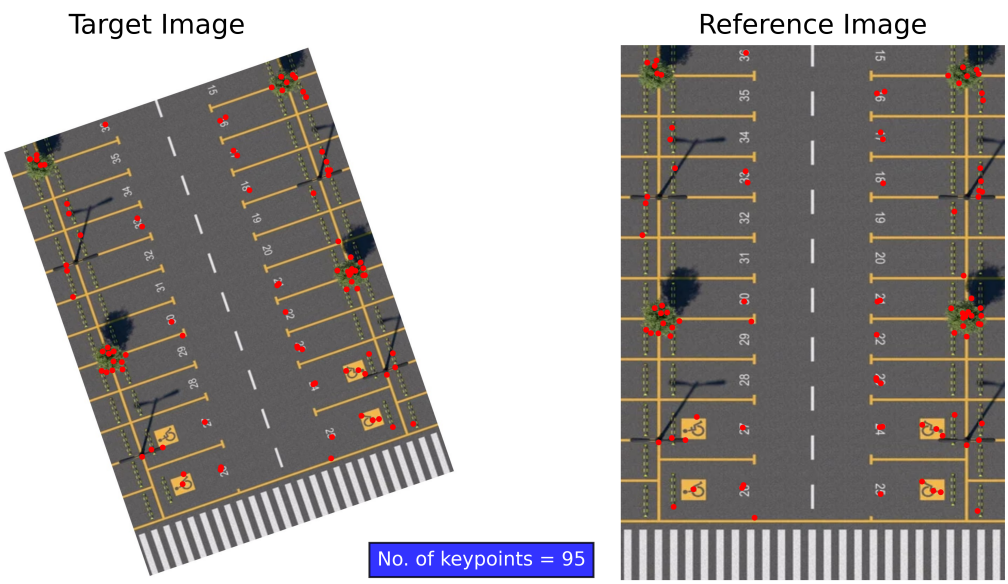

Figure 2.13: A demonstration of the true point correspondences, where the bad matches have been removed through a filtering algorithm. This improves the estimation of the homography matrix that will accurately describe the true relationship between the target and the reference image.

2.5.3 Homography Estimation

After identifying a set of true correspondences, the homography parameters are computed using algorithms such as the Direct Linear Transform (DLT) method (Fristedt, 2017). The selection of the optimal method will contribute to the accuracy and reliability of the resulting homography estimation. Therefore, the successful computation of the homography parameters can be used to register the target image accurately to conform to the reference image.

2.5.4 Machine Learning

The ML techniques examined in this study include K-Nearest Neighbours (KNN) in Section 2.5.5, Random Forest (RF) in Section 2.5.6 and Support Vector Machine (SVM) in Section 2.5.7

2.5.5 ML Method 1: K-Nearest Neighbours

The K-Nearest Neighbours (KNN) algorithm is a supervised machine learning algorithm that can be used to solve both classification and regression problems (Sathishkumar and Cho, 2020). In this study, the ML task of estimating the homography parameters is considered a regression problem. The KNN operates on the assumption that similar things exist in close proximity (Boateng et al., 2020), and this similarity plays an important role. The KNN algorithm makes predictions by finding the closest matches to a new data point within its training data. The labels of these nearest neighbors are then used to predict the label of the new data point (Srivastava, 2020). In this approach, the entire training data is stored and when a prediction is required, the k-most similar records from the training dataset are located. Then, based on these neighbours, a prediction is made.

This approach is often regarded as a form of "lazy learning" since no computation is performed until a prediction is requested. To effectively employ the KNN algorithm, an appropriate value for 'k' must be determined. The accuracy of the predictions significantly depends on this selection (Meersman et al., 2003). The

'k' value plays an important role in defining the number of neighbours considered during the prediction process. The optimal 'k' value can be determined by running the algorithm multiple times with varying 'k' values to identify the configuration that produces the most accurate predictions. The choice of 'k' can be influenced by the characteristics of the training data. For instance, if the training data contains outliers in Pitch and Roll, a higher 'k' value might be beneficial. Conversely, if the training data exhibits a high correlation, a lower 'k' value would be more suitable (Meersman et al., 2003). Figure 2.14 provides an illustration of an example of how the KNN algorithm works.

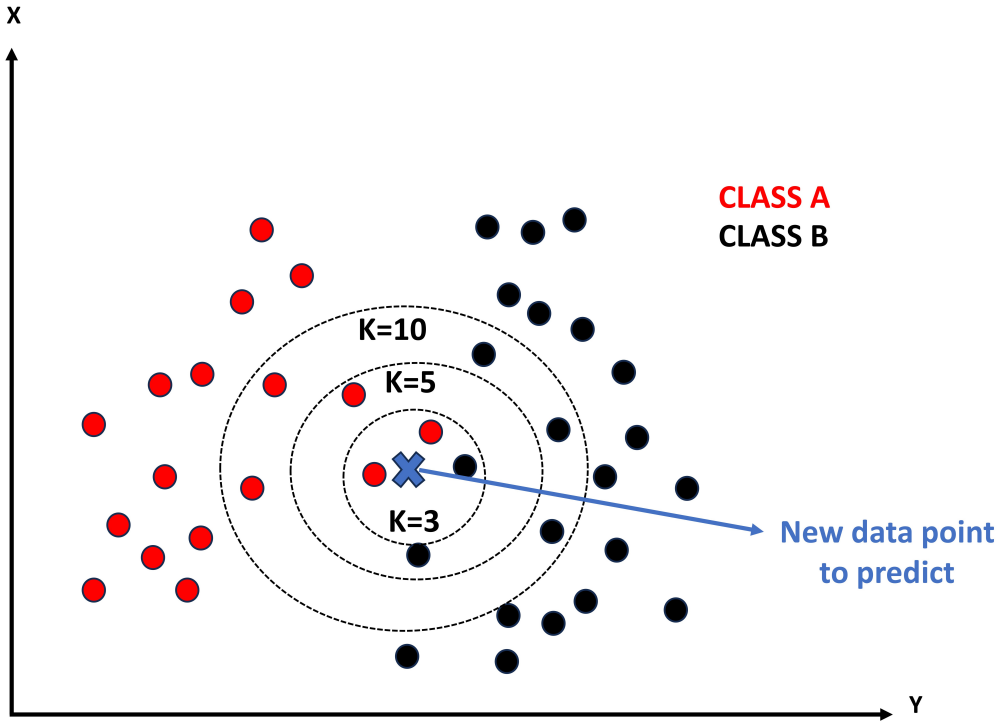

Figure 2.14: Example illustration of KNN where three different 'K' values have been explored. In predicting a new data point, the similar neighbours close to the new data point are used to make predictions.

2.5.6 ML Method 2: Random Forest

Random Forest (RF) is also a supervised machine learning technique that can be used for both classification and regression problems. It operates on the principles of ensemble learning, which involves combining multiple classifiers to improve the predictive accuracy that can be used to address complex problems in remote

sensing (O'Hara, 2019) such as classification mapping of coastal dune habitats (Cruz et al., 2023b), estimating chl-a concentration (Kupssinskü et al., 2020), and land cover classification (Magee, 2023).

The RF algorithm contains several decision trees, each trained on a distinct subset of the original dataset (Ahmed et al., 2019). Rather than relying on a single decision tree output, RF aggregates results from each tree and ultimately generates the final output based on a majority vote from individual predictions (Magee, 2023). Generally, the greater number of trees in the forest leads to higher accuracy and prevents the problem of overfitting, which ensures the model can be applied in other scenarios and environments (Magee, 2023).

The RF algorithm operates by randomly sampling the training data. Thus, it creates multiple datasets by sampling with replacements from the original training dataset. Each of these individual datasets is commonly known as "bootstrap samples." A random subset of features is considered for splitting at each node within each decision tree. Following this, the algorithm builds a decision tree for each bootstrap sample, obtaining predictions from each tree. Voting is then performed to aggregate predicted results, and the most frequently voted prediction is selected as the final output (Ahmed et al., 2019).

Given that RF combines multiple trees, variations in the individual decision tree predictions are expected. However, the collective predictions from all trees contribute to the correct output. To optimize the performance of the algorithm, two key principles should be considered: first, the inclusion of actual values in the feature variable facilitates accurate predictions, and second, predictions from each tree should have low correlations.

As highlighted by Pont (2021), important reasons for using RF include less training time as compared to other algorithms, high prediction accuracy even for large

datasets and the ability to maintain accuracy even when a significant portion of data is missing. Figure 2.15 illustrates how the RF algorithm works.

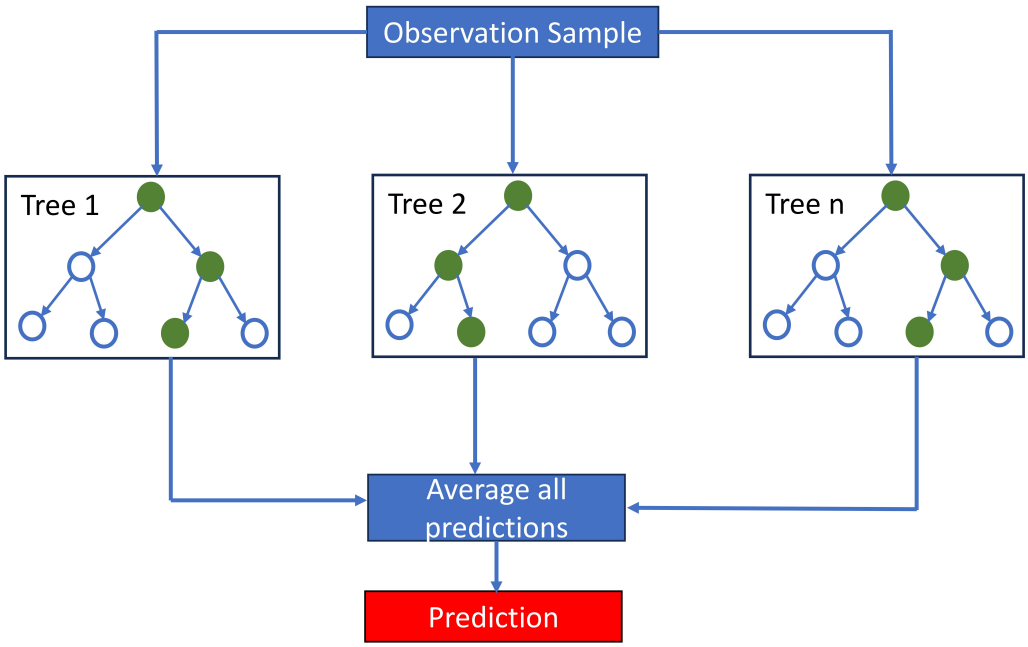

Figure 2.15: Example illustration of RF where decision trees are used to predict a new data point. In predicting, a decision from each tree is averaged to make the final prediction.

2.5.7 ML Method 3: Support Vector Machine

A Support Vector Machine (SVM) is a supervised ML algorithm, which similar to RF, can also be used for both classification and regression tasks. Its primary aim is to establish an optimal decision boundary, referred to as a hyperplane, capable of segregating an n-dimensional space into distinct classes (Kotsiantis, 2007). The hyperplane is a mathematical concept that can be visualized as a line or plane in a high-dimensional space. This facilitates the accurate categorization of new data points in the future. Hyperplanes as shown in Figure 2.16 function as classification guides, that help to delineate data points into distinct categories based on their position relative to the hyperplane. Further, the dimension of the hyperplane depends upon the number of features, thus the number of features in the dataset directly influences the dimensionality of the hyperplane (Corrigan, 2018).

SVMs are broadly categorized into simple or linear SVMs and kernel or non-linear SVMs (Corrigan, 2018). A linear SVM determines the optimal hyperplane directly within the original feature space in scenarios where the data is linearly separable. Conversely, when dealing with non-linearly separable data, a kernel SVM employs kernel functions to transform the data into a higher-dimensional space, thereby enabling the identification of a suitable hyperplane.

The SVMs work by finding a hyperplane that maximizes the separation between data points of different classes in the high-dimensional space (Boateng et al., 2020). The data points that are found close to the hyperplane are called the support vectors. These support vectors are considered the most important points in the data set because they directly define the positioning of the hyperplane.

SVMs are a powerful and versatile machine learning algorithm with several advantages. As explained by Magee (2023) for satellite data classification, SVMs are particularly effective when applied to high-dimensional data. Further, they can effectively separate non-linearly separable data points, making them applicable to problems that other algorithms may struggle to address. Additionally, SVMs exhibit robustness to noise, ensuring optimal performance even when the data is not cleaned properly. Lastly, their scalability allows them to handle problems involving many data points. Figure 2.16 shows how SVM algorithm works.

Figure 2.16: Example illustration of SVM where a hyperplane separates data points into different classes. The data points close to the hyperplane, called the support vectors, are used to make predictions.

2.6 Conclusion

The increasing adoption of low-cost drones presents opportunities for research institutions, NGOs, local communities, and volunteer groups to engage in environmental monitoring. However, its application for mapping water bodies remains largely unexplored. This can be attributed to the fact that the traditional BA method fails to determine the EOPs.

On the other hand, the DG method, as explained in section 2.2.2, allows for direct determination of the EOPs using the GNSS and IMU. However, one of the main drawbacks of this method, as shown in Table 2.1, is its low accuracy when using low-cost drones, especially in featureless terrain. Additionally, as explained in section 2.3.2, the GNSS and IMU were identified to have an influence on the

accuracy of reconstructed 2D image. This closer examination helped to propose a solution that will be explored in Chapter 3. This chapter further examined the two common sensor mounting methods for drones. Through this literature review, it was found that sensors not mounted on self-levelling gimbals are much more susceptible to platform instability, potentially affecting the accuracy of the reconstructed 2D image.

This chapter also examined the ISO method in great detail and identified areas requiring further investigation. Specifically, it explored whether the ISO method can be used or adapted to map water bodies, and this will be explored in the following chapters. Finally, the literature review explored image registration techniques and ML algorithms in relation to achieving the fourth objective which will be explored in Chapter 6.

Chapter 3

Theoretical Analysis of the Positional Orientation (POSE) Errors

The first objective of this thesis is to benchmark and test the accuracy of reconstructed 2D images of water bodies generated using the DG method. This chapter focuses on investigating the effects of navigational sensor errors on the DG method and how they contribute to the final accuracy of the reconstructed 2D image. This follows from the findings from the literature review that there has been no research to quantify the accuracy of the reconstructed 2D image under certain navigational errors using a low-cost drone. This chapter performs a theoretical assessment using standard collinearity equations and develops a series of simulations to further assess the contribution of both systematic and random errors. The theoretical findings from this chapter will be further validated in Chapter 4 by using real-world drone imagery and will act as the benchmark dataset for many subsequent tests throughout this thesis.

The motivation for this chapter is introduced in Section 3.1, and the important assumptions for the theoretical analysis are presented in Section 3.2. The design and development of the simulator for the theoretical analysis are presented in Section 3.3. The results of the theoretical analysis are detailed in Section 3.4, and the discussion is presented in Section 3.5.

3.1 Introduction

As explained in Chapter 2, the DG method is based on the combination of GNSS for positioning and IMU for angular measurement. These two devices make it possible to estimate the EOPs. However, the accuracy and reliability of the DG method are limited or constrained by the accuracy of the IMU and GNSS onboard the drone (Khaghani and Skaloud, 2016). Generally, errors during DG can be categorized as errors of the intrinsic or IOPs and errors of the extrinsic or EOPs (Yuan and Zhang, 2008). Errors in IOPs refer to systematic errors within the sensor systems, while errors in EOPs encompass both random and systematic errors related to the external factors affecting the measurements.

One of the main aims of this chapter is to determine the effects of these errors in the measurement of position or orientation from the navigational sensors and quantify their impact on the accuracy of a reconstructed 2D image. In this chapter, the errors that will be considered are GNSS/IMU errors and sensor rotation angles. The sensor rotation angles themselves are not errors, but the error lies in the perturbation or deviation of these measured values from the ideal nadir orientation of the sensor. Thus, these measured angles also contribute to errors in a reconstructed 2D image when the sensor's orientation is not nadir/vertical.

This is the first study to carry out a theoretical analysis of errors in IMU/GNSS measurements and sensor rotation angles for low-cost drones, which will enable a comprehensive understanding of their sources, characteristics, and propagation mechanisms. By modelling and understanding these errors, methods can then be developed in subsequent chapters that will help to improve the accuracy of the reconstructed 2D image through the identification of error patterns and the development of compensation techniques to mitigate the impact of GNSS and IMU errors on drone datasets. The mathematical principle behind each of these errors can be best understood and quantified in an initial study through theoretical analysis. An error simulation for a low-cost drone using the DG method will be

presented in this chapter and used as the benchmark for all subsequent analyses.

3.2 Important Assumptions Around the Error Budget

To understand and quantify potential errors throughout the image reconstruction process, an error budget was required. This budget quantifies the potential errors and is important for the theoretical analysis. However, developing an error budget for the theoretical analysis demands an understanding of the underlying assumptions required to meet this objective. Therefore, this section explains the fundamental assumptions underpinning the theoretical analysis.

3.2.1 GNSS and IMU Errors

As detailed in Section 2.3.3. the GNSS receiver aboard the drone measures the 3D location of the sensor when any images are captured. Therefore, any positional errors in the GNSS receiver will translate into errors in the sensor centre coordinates. According to Nowakowski et al. (2023), GNSS accuracy is influenced by factors such as signal quality, atmospheric conditions, interference, and satellite geometry. However, in this thesis, we first make an assumption that many of these inflences are too variable for reliable prediction and that a theoretical assessment can be developed by using the manufacturer's specified accuracies. While it is possible to use software or theoretically model many sources of error (Suo et al., 2020), doing so comprehensively for all possible environmental and atmospheric scenarios is impractical. The manufacturer's specified accuracy typically propose that in common or ideal conditions, the GNSS device should be able to determine your location within a specified tolerance. The manufacturer's accuracy rating is also predicated on the assumption of having a clear line of sight to multiple GNSS satellites and minimal interference from obstacles (Parrot, 2017).

Section 2.3.2 also explained that the IMU typically consist of gyroscopes and accelerometers, and these devices influence the accuracy of the attitude measurements. According to Jen et al. (2023), the accuracy of the IMU can be influenced by factors such as constant bias, bias instability, temperature effects and calibration errors. However, in this thesis, we once again assume that the specified manufacturer's accuracy is suitable for developing this theoretical assessment. This assumption means that under standard conditions, the IMU should be capable of measuring angular changes within the specified tolerance. All other random factors that might affect the accuracy of that measurement are not considered.

3.2.2 Sensor Rotational Angles Influence

The drone's IMU measures the sensor's orientation in three axes: X, Y, and Z, corresponding to the Roll, Pitch, and Yaw angles, respectively. According to Wolf et al. (2014), tilting the sensor away from the ideal vertical (nadir) position introduces tilt distortion in the image. This distortion affects the positional accuracy of points in the reconstructed 2D image. Consequently, larger sensor tilts lead to more pronounced tilt effects. In this thesis, the "sensor rotational angles influence" is specifically referred to as the deviation from the nadir position measured by the IMU. Figure 3.1 illustrate the sensor rotational angles.

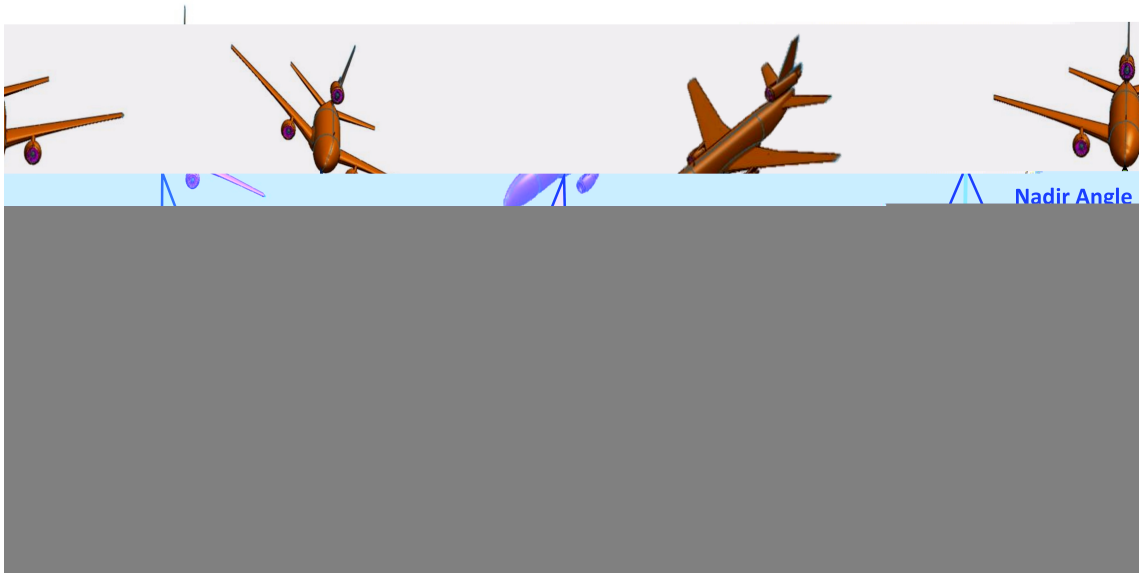

Figure 3.1: Illustration of the sensor rotational angles: the left image shows the ideal sensor position, pointing directly at the ground, the middle image demonstrates a tilted sensor due to drone Rolling and the right image shows a sensor tilted away from the nadir due to drone Pitching.

3.3 Design and Development of the Simulator

3.3.1 Calculations based on the Collinearity Equations

One of the focuses of the first objective of this thesis is to theoretically determine the relationship between measurement errors in the navigational plane and the resulting accuracy in a reconstructed 2D image. A theoretical analysis was carried out to simulate the influence of each of the error types detailed in Section 3.2 using the standard collinearity equations. These equations are fundamental in photogrammetry as they form the basis of projecting a point from the world coordinate onto the image coordinate (Förstner and Wrobel, 2016b). These equations assume a condition where the exposure station of a photograph, an object point, and its photo image all lie along a straight line (Wolf et al., 2014). The collinearity equations were chosen as the basis for this simulation because the theoretical accuracy of DG based on collinearity equations is often better than space intersection (Yuan and Zhang, 2008) because, in space intersection, the location of an object in space is calculated by intersecting two rays from the sensor.

Therefore, any errors in the image points and exterior orientation elements will directly affect the projection coefficients of the points and, therefore, the final location of the object.

Therefore, the mathematics underpinning the collinearity equations can be represented in the Equation (3.1) and (3.2) as explained in Wolf et al. (2014). The $\boldsymbol{x_a}$ and $\boldsymbol{y_a}$ are defined as the photo coordinates for image point a. Thus in order to simulate any point A, the $\boldsymbol{X_A}$, $\boldsymbol{Y_A}$ and $\boldsymbol{Z_A}$ which are defined as the object space coordinates of point A, and $\boldsymbol{X_L}$, $\boldsymbol{Y_L}$ and $\boldsymbol{Z_L}$ which are defined as object space coordinates of the exposure station, the $\boldsymbol{m_{11}}$, $\boldsymbol{m_{12}}$, $\boldsymbol{m_{13}}$, $\boldsymbol{m_{21}}$, $\boldsymbol{m_{22}}$, $\boldsymbol{m_{23}}$, $\boldsymbol{m_{31}}$, $\boldsymbol{m_{32}}$, $\boldsymbol{m_{33}}$ which are defined as the functions of the three rotation angles, f as the focal length and $\boldsymbol{x_o}$, $\boldsymbol{y_o}$ as the coordinate of the principal point and must be combined and expressed as Equation (3.1) and (3.2).

$$x_a = x_o - f\left[\frac{m_{11}(X_A - X_L) + m_{12}(Y_A - Y_L) + m_{13}(Z_A - Z_L)}{m_{31}(X_A - X_L) + m_{32}(Y_A - Y_L) + m_{33}(Z_A - Z_L)}\right] \tag{3.1}$$

$$y_a = y_o - f\left[\frac{m_{21}(X_A - X_L) + m_{22}(Y_A - Y_L) + m_{23}(Z_A - Z_L)}{m_{31}(X_A - X_L) + m_{32}(Y_A - Y_L) + m_{33}(Z_A - Z_L)}\right] \tag{3.2}$$

3.3.2 Parameters for the Simulation

The simulation incorporates the parameters that best approximate a low-cost drone, such as the Parrot Bluegrass drone from Section 1.2. For example - the focal length and the GNSS/IMU tolerances were sourced directly from the Parrot Sequoia sensor specifications. This choice was deliberate, as the first objective of this thesis was to replicate any low-cost drone and the Parrot Bluegrass was selected because it met all the specific criteria outlined in Section 1.4.2. Further, in the context of the simulation, the parameters for the exposure station (the position and orientation of the sensor) coordinate and the object coordinate (the location of the object in space) were all arbitrary values. The term "arbitrary" implies that these coordinates were chosen without specific real-world data. They are hypothetical values that were used for the simulation. It was also assumed

that the aircraft was flying in the X direction. This means that the drone was moving forward on the horizontal axis, and the simulation was based on a single direction. This parameter was used because a change in the aircraft's direction will not affect the result. In this simulation, the theoretical analysis was carried out solely on the tilt angles, i.e. Pitch and Roll angles. This is because the Yaw angle represents the change in the aircraft's direction and does not influence the tilt angles. Table 3.1 gives a detailed description of each of the parameters used.

Table 3.1: Detail Description of the Parameters for the Theoretical Simulation.

Parameters	**Test 1: Sensor Rotation Angle**	**Test 2: GNSS and Sensor Rotation Angle**	**Test 3: IMU and Sensor Rotation Angle**	**Test 4: Combined Effects of GNSS/IMU Error and Sensor Rotation Angle**
Focal Length	3.98mm	3.98mm	3.98mm	3.98mm
Flying Height	120m	120m	120m	120m
Exposure Station Coordinate (X_L, Y_L,Z_L)	X_L= 110m Y_L = 100m Z_L = 0m	X_L= 110m Y_L = 100m Z_L = 0m	X_L= 110m Y_L = 100m Z_L = 0m	X_L= 110m Y_L = 100m Z_L = 0m
Object Coordinate (X_A,Y_A,Z_A)	X_A = 100m Y_A = 110m Z_A = 120m	X_A = 100m Y_A = 110m Z_A = 120m	X_A = 100m Y_A = 110m Z_A = 120m	X_A = 100m Y_A = 110m Z_A = 120m
GNSS and IMU Error	GNSS and IMU with infinite accuracy	GNSS XYZ error = ± 1.5m IMU with infinite accuracy	GNSS with infinite accuracy IMU error of 0.5^o for Roll and Pitch	GNSS XYZ error = ± 1.5m IMU error of 0.5^o for Roll and Pitch

3.3.3 Implementation of the Simulation in Python

The simulator was developed in the Python programming language. The Python script was developed incorporating libraries such as OpenCV (Bradski, 2000), Cameratransform (Gerum et al., 2019), NumPy (Harris et al., 2020) and Matplotlib (Hunter, 2007). The simulator consisted of two main components: (1) a

module for computing the X and Y coordinates of a point via collinearity equations, and (2) a module for projecting a planar image based on the parameters specified in Section 3.3.2.

The first module of the simulator was developed using the NumPy. NumPy is a fundamental library for numerical computing in Python (Harris et al., 2020). This package provided the necessary mathematical tools for the first component of the simulator. The NumPy library was used to implement the necessary mathematical operations to generate the collinearity equations. This involved constructing matrices to represent the equations, specifying coefficients and constants, and then applying appropriate NumPy functions to obtain the solution.

The second module of the simulator was developed using OpenCV. The OpenCV package played an important role in the simulation. OpenCV provides essential functions for image processing, manipulation, and analysis. In the context of the simulator, OpenCV facilitated the handling and transformation of images.

Cameratransform library used to project points from sensor space to the object space. This library offered the tools to define the optical sensor parameters, define the EOPs, and simulate the effects of different sensor orientations. By utilizing Cameratransform, the simulator could accurately project planar images based on the specified input parameters in Section 3.3.2.

Matplotlib was the final library used - it is a popular data visualization library. In developing the simulator, Matplolib was instrumental in creating graphical representations of the simulation results. It was utilized to visualize the attitude effects of the projected planar image in the X and Y directions as seen in Figure 3.3. It provided valuable insights into how any changes in orientation impacted the final projected images.

3.4 Results of the Theoretical Analysis

Having explained the assumptions and the theoretical and technical development of the simulator in the previous sections, this section will present the simulation results. This assessment was for the four tests in Table 3.1 and explored errors that may accrue from the (1) Sensor rotation angle, (2) a combination of GNSS and sensor rotation angle, (3) a combination of IMU and sensor rotation angle and (4) a combination of GNSS/IMU and sensor rotation angle.

3.4.1 Test 1: Influence of sensor Rotation Angles on Reconstructed 2D Image

The first test theoretically assessed the effects of sensor rotational angle on a terrain point. As mentioned in Chapter 2, the drone IMU records the angular measurement in the three axes. Hence, it is essential to understand the influence the angular measurement will have on the accuracy of the final reconstructed 2D image. To determine and compute the sensor rotation influence, the simulator used the collinearity equations in Equations (3.1) and (3.2) to model the errors. This was done by computing the projected points in X and Y from the sensor rotation angles, and compared them to a point projected from the nadir position. There was no calculation of errors in the Z direction because the synthetic data was generated from a planar surface, and therefore there were no associated errors. For the initial development of this simulation, it was assumed that GNSS and IMU have infinite accuracy- thus, they measure the true position and orientation without any error. In this case, the GNSS and IMU did not influence the overall accuracy. The first test only modelled the influence of sensor rotation angles on the projected points and from Figure 3.2, the effect of these rotation errors can be seen. The simulation suggested that for every one-degree change in Pitch/Roll a shift of 2.11m in the XY position of a projected point can be expected for a flying height of 120m. Calculations have been carried out for a range of values and these results can be found in Appendix Appendix A, where the sensor rotation

angles ranging from 1 ^{o} to 8 ^{o} have been calculated. The first test demonstrated that as the sensor rotation angle increases, the accuracy in the ground coordinate system decreases for a DG approach.

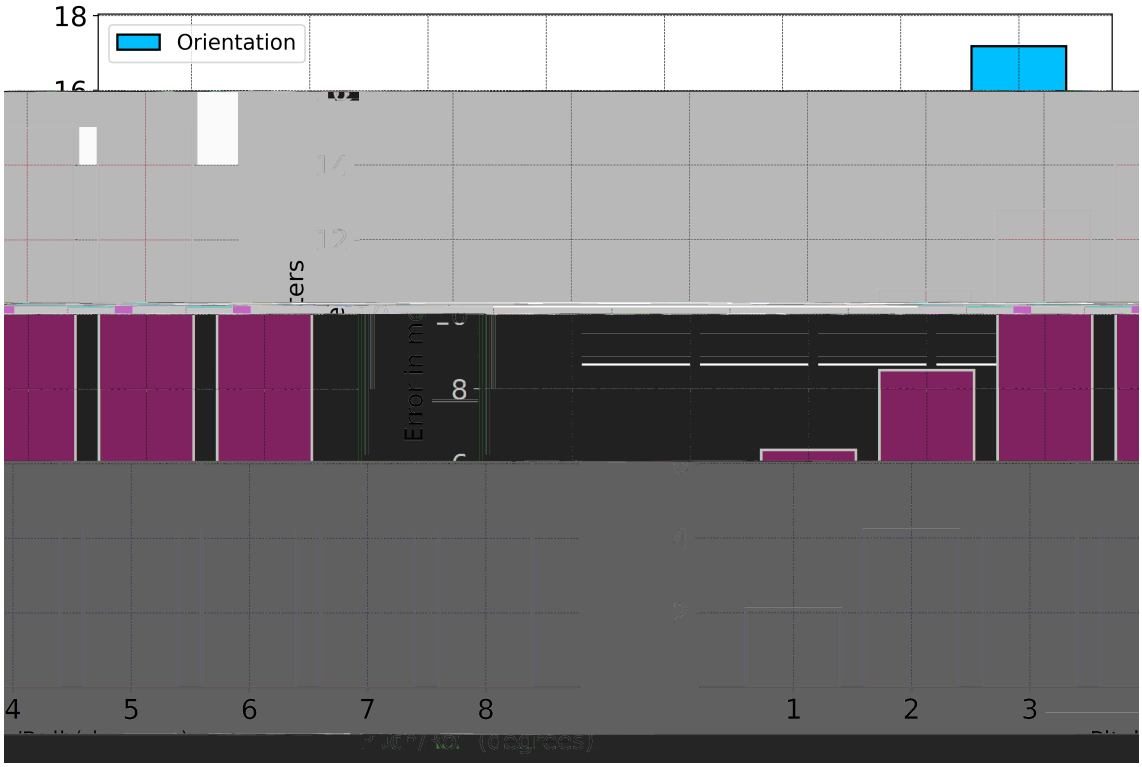

Figure 3.2: A theoretical accuracy assessment for the sensor rotational angle influence on a projected point for a drone flight at 120m - assuming a low-cost drone similar to the Parrot Bluegrass. The x-axis shows the degree changes in either Pitch or Roll, and the y-axis shows the mean absolute errors in meters

3.4.2 Image Skewing due to Sensor Rotation Angles

In addition, looking at the simulated test in Figure 3.3, further analysis can be drawn on the effect of sensor angles on the image footprint. For the purpose of better visualization of this effect, a more severe angle of 10 ^{o} was used. Figure 3.3a illustrates the footprint if the sensor was perfectly vertical during the image acquisition. This results shows that there are no tilt effects on images captured at nadir. Conversely, Figure 3.3b illustrates a situation where the sensor is Pitched (nose down) at 10 ^{o} while the Roll and Yaw are 0 ^{o} . The results from this illustration show that a rotation in the Pitch has a very small effect along the X-axis but much effect along the Y axis where the projected image transforms to a trapezoid-

like shape. Figure 3.3c illustrates a situation where the drone is Rolled (tilt in the wings) at 10° while the Pitch and Yaw are 0°. This result shows a minimal image displacement effect along the Y-axis but a more pronounced effect along the X-axis.

Overall, this simulation helps justify the conclusion that the orientation of the sensor will impact the positional accuracy of any point in a DG approach, in both the X and Y coordinates. The degree of the error will depend on how much the drone is Rolled or Pitched. Further, the findings give insights into the nuances of how different orientations impact the footprint of images over flat surfaces such as water bodies.

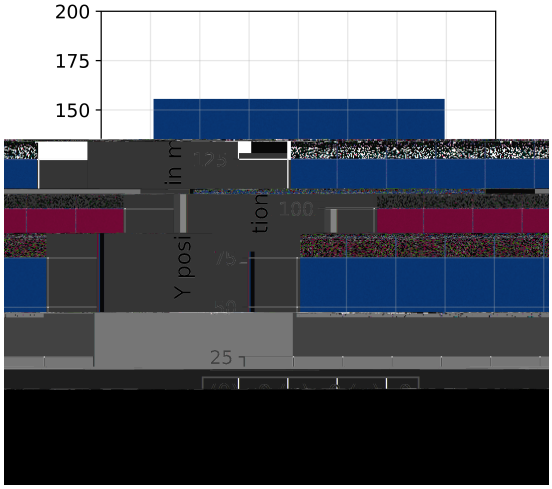

(a) No orientation effect

(b) Effect of Pitch

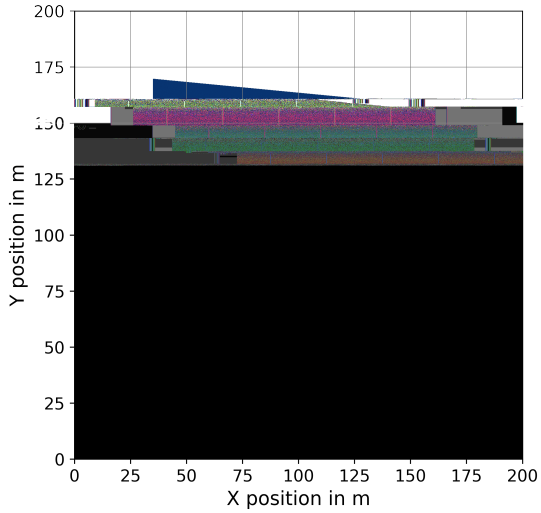

(c) Effect of Roll

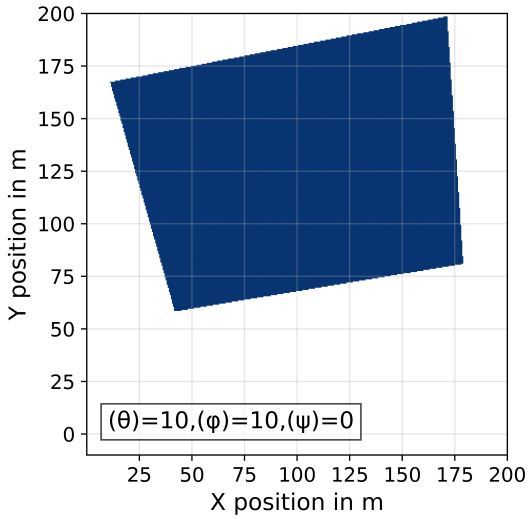

(d) Effect of both Pitch and Roll

Figure 3.3: An illustration of the orientation effects in the X and Y coordinates. Image (a) shows an image captured at nadir and, as a result, no orientation effect, (b) an image captured with angular measurement from Pitch while Roll and Yaw remain constant, (c) an image captured with angular measurement from Roll while Pitch and Yaw remain constant, and (d) an image captured with angular measurement from Pitch and Roll while Yaw remain constant

3.4.3 Test 2: Introducing GNSS Error along with Sensor Rotation Angle Influence

Errors in the measurement of the 3D position of the GNSS receiver also influence the errors on the ground coordinate. In this second simulation, it was now assumed that the ground coordinates were derived from a drone equipped with a GNSS receiver, which contains a constant error defined by the manufacturer tolerance. The IMU error influence was excluded from these tests, hence it was assumed it had an infinite accuracy. The simulation combined the GNSS error and the influence of the sensor rotation angle for a drone flight at 120m assuming a low-cost drone similar to the Parrot Bluegrass.

The findings obtained from Figure 3.4 highighted an important result in the relationship between the sensor rotation angle and GNSS accuracy, particularly regarding their impact on accuracy. It was observed that a one-degree change in Pitch or Roll when combined with a GNSS manufacturers accuracy tolerance of 1.5m resulted in a 3.61m shift in the XY position for the projected point for a drone flying at a height of 120m. This implies that when the effects of orientation errors and GNSS accuracy are combined, the positional accuracy of a point is further reduced and highlights how a low-cost GNSS will impact the planimetric accuracy of the DG method. Table 1 and 2 in Appendix Appendix A detail the changes in Pitch and Roll angles combined with GNSS accuracy and the corresponding errors.

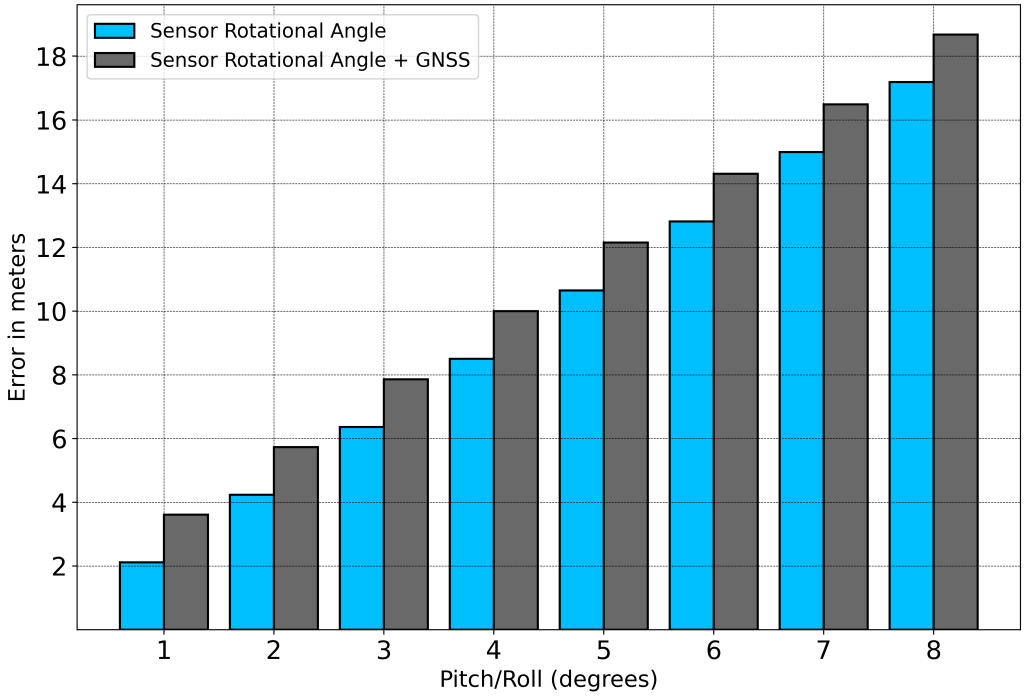

Figure 3.4: A theoretical accuracy assessment for the influence of rotational angles and GNSS error on a terrain point for a drone flight at 120m assuming a low-cost drone similar to the Parrot Bluegrass. The x-axis shows the degree changes in Pitch or Roll and the y-axis shows the mean absolute errors in meters with a constant 1.5m GNSS position error in XYZ. The intial tests showing the sensor orientation-only errors are in blue and the combined GNSS/sensor orientation error are in grey.

3.4.4 Test 3: Introducing IMU Error along with Sensor Rotation Angle Influence

This third simulation combines the IMU error and the sensor rotation influence. In this simulation, it is now assumed that the GNSS has an infinite accuracy and is excluded from the tests. This way, the results were not corrupted by any error influences other than those that were introduced using the IMU manufacturer's tolerances when combined with the sensor orientation error. From the result in Figure 3.5, it can be seen that the IMU accuracy of 0.5^{o} in Pitch/Roll will translate to an error of 1.4m in X and Y in the ground coordinate for a drone flying at a height of 120m. For example, a one-degree change in orientation will lead to an error of 3.51m in the planimetric. These results highlight the crucial role IMU plays in measuring the angular rotations of the sensor's position. As

a result, any errors in these IMU measurements directly affect the accuracy of the rotational angles in the exterior orientation. It also highlights that the GNSS is potentially the larger contributor to these errors among the two navigation sensors.

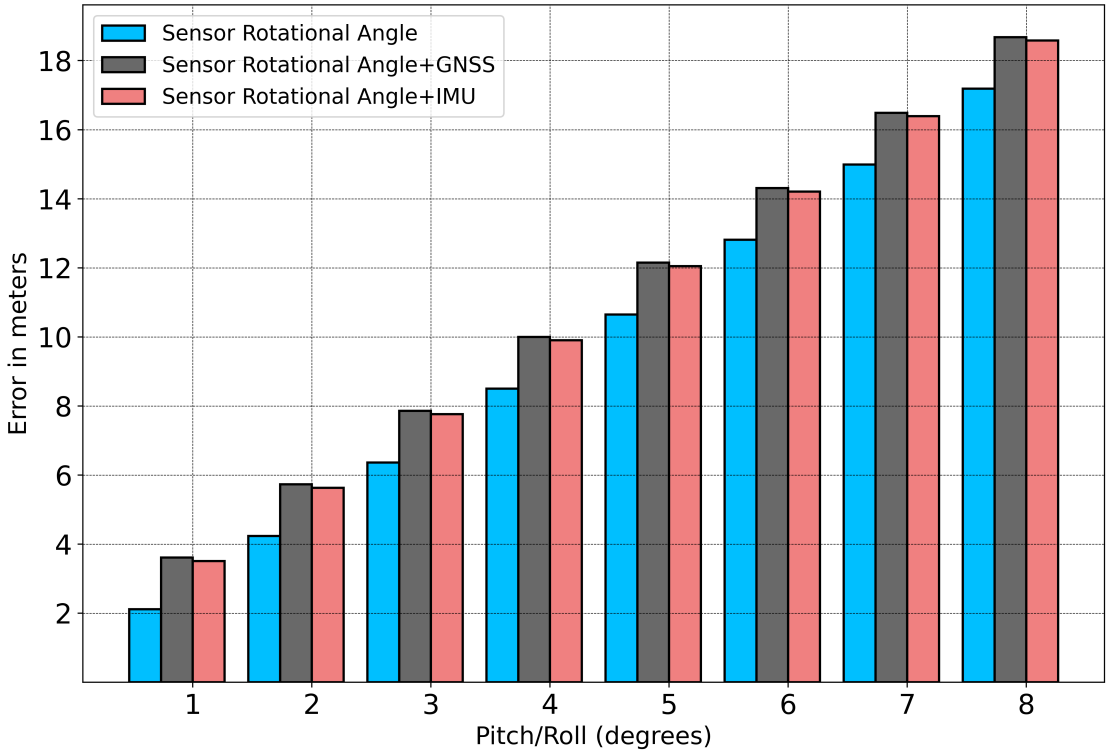

Figure 3.5: A theoretical accuracy assessment for all three previous tests for a drone flight at 120m assuming a low-cost drone similar to the Parrot Bluegrass - the influence of (i) orientation, (ii) orientation+GNSS 1.5m error and (iii) orientation+IMU 0.5 ^{o} error on a ground projected point. The x-axis shows the degree changes in Pitch or Roll and the y-axis shows the mean absolute errors in meters

3.4.5 Test 4: Theoretical Simulation of Combined Effects of Sensor Rotational Angle Influence and GNSS/IMU Error

The final theoretical simulation combines all the contributory error sources (GNSS, IMU and Sensor Rotational Angle). In this simulation, the orientation influence, the IMU and GNSS errors are evaluated together to ascertain how they influence the projected terrain point.

The simulation results in Figure 3.6 summarises the combined results of these tests, where a one-degree change in Pitch or Roll, when combined with expected

errors of 1.5m (manufacturer tolerance for GNSS accuracy) and a 0.5 ^{o} IMU accuracy (manufacturer tolerance), results in a potential error of 5m in the coordinates of a ground projected point for a drone flight at 120m assuming a low-cost drone similar to the Parrot Bluegrass. Clearly, these results demonstrate that errors originating from sensor rotation or angular elements are potentially more significant than errors arising from the IMU or GNSS. Summarising the results, a 1° change in the Pitch/Roll will result in a 2.11m shift for the point on the ground. In addition, the navigational errors, represented by the GNSS and IMU inaccuracies, contribute an additional error (or shift) of 2.9m to the ground point. This means that by default, using a low-cost drone will directly impact the accuracy for a DG approach. Detailed calculations combining the GNSS/IMU error and sensor rotation angles ranging from 1° to 8° can be found in Table 1 and 2 in Appendix A.

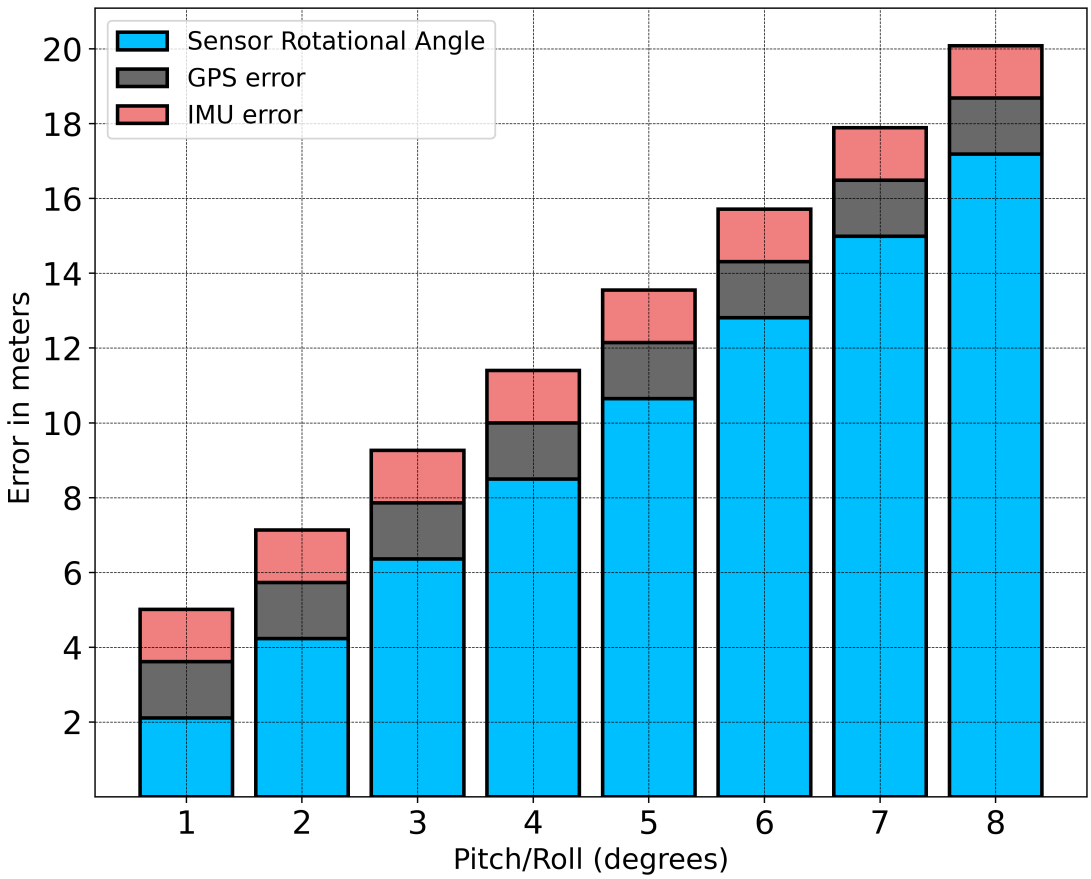

Figure 3.6: A stacked bar graph showing the the reelvant contributions of errors for GNSS, IMU and rotational angle influence in Pitch/Roll. The higher the rotational angle encountered (i.e. how much the drone pitches or rolls), the greater the error in meters for the projected ground point.

3.5 Discussion

Previous studies have shown that the positional accuracy of an object projected through DG is correlated with factors such as orientation, IMU and GNSS errors (Dreier et al., 2021; Heipke et al., 2002; Grejner-Brzezinska, 2001). In this study, the findings from the theoretical analysis have given the first insights into the influence that orientation, IMU, and GNSS errors have on the accuracy of the final image. This has also highlighted the disproportionate influence that the sensor rotation angles in Pitch and Roll has on subsequent image reconstruction. This influences the accuracy of a reconstructed 2D image and highlights the need for this study and the overall thesis, where low-cost drones do not have a reliable IMU. This confirms, reinforces and advances the work on traditional aerial platforms by Cramer et al. (2000), which highlighted the angular elements as the critical factor in a DG approach.

This investigation indicates that the angular elements, specifically orientation in Pitch and Roll, will also be crucial factors for consideration for mapping over water using DG. This means that any factors that will directly affect the angular measurement need to be minimised or compensated for by a drone operator. For example, high wind speed and high flight speed have all been found to contribute to high angular measurement. In Otsuka et al. (2018), it was also suggested that higher flight speed can increase the Pitch angle of multi-rotor drones. Strong winds can affect the drone's speed and flight path. Thus, flying upwind and downwind increases or decreases the flight speed, which affects the angular measurement. Downwind can be defined as the wind that blows in the direction of the drone and increases the speed of a rotary drone, while an upwind is the wind that blows against the direction of the drone and reduces the drone's speed (Soares, 2013).

Furthermore, this study has also highlighted how the accuracy of any image reconstruction relies on accurate estimation of sensor orientation (Pepe et al.,

2019). Another factor that impacts the positional accuracy is the accuracy of the GNSS/IMU. According to Stam (2010), errors due to GNSS/IMU accuracy will cause errors in accuracy of the same magnitude. Meanwhile, errors due to angular measurements will cause errors in accuracy of several meters per degree. This observation becomes particularly apparent in the aforementioned results, emphasizing the significant impact of sensor rotation influence on the accuracy of a projected point.

3.6 Conclusion

In this chapter, the error sources that limit the accuracy of a reconstructed 2D image have been introduced and discussed, namely GNSS and IMU errors and sensor rotation angle influence. Each of these factors were quantified and analysed using the standard photogrammetric collinearity equations and a series of simulated tests. There are limitations to this approach, for example the simulation was predicated on important assumptions that defined the GNSS/IMU accuracy using the specified manufacturer's accuracy and did not account for all other factors that might affect the accuracy. However, the results are an important initial step in this investigation and show real value, as it was found that a one-degree change in Pitch or Roll, when combined with a 1.5m GNSS error and a 0.5^{o} IMU error, results in an error of 5m in the planimetric coordinates. Moreover, these initial results revealed that the sensor rotation influence significantly contributed to the accuracy of the reconstructed 2D image compared to the GNSS and IMU errors. Overall, the theoretical error budget obtained by approximating a low-cost drone has highlighted the limitations of such systems when using the DG approach.

This chapter has shown the importance of correcting for sensor rotation angle and the significant contribution to the errors in a reconstructed 2D image. In the next chapter, the results from the simulated tests will be exploited to correct for specific errors resulting from the sensor rotation angle and navigation sensor

errors. This method will then be validated using real-world data.

In summary, this chapter provided the following contributions:

1. Provided insight into the contribution of sensor orientation to the accuracy of a reconstructed 2D image.
2. Quantified the contribution of navigational errors from low-cost drones on a reconstructed 2D image.
3. Provided an error budget through simulation for a low-cost drone.

Chapter 4

Developing an Analytical Rectification Method for Featureless Terrain - ARMFET

The second objective of this thesis is to analyse the associated errors in the images derived using the DG method and propose an analytical photogrammetric method to improve them. This phase of the research is a natural progression enabled by the simulated tests presented in the previous chapter and is essential to further our understanding by identifying and quantifying any errors associated with the traditional DG approach. By robustly assessing this process, novel photogrammetric methods can be developed to effectively improve the accuracy of reconstructed 2D images. This chapter will explore the performance and suitability of low-cost drones for DG in greater detail. Subsequently, the first, novel method developed in this thesis called **A**nalytical **R**ectification **M**ethod for **FE**atureless **T**errain - 'ARMFET' will be introduced in Section 4.6.4.

4.1 Introduction

As explained in the previous chapters, when mapping water bodies through the standard photogrammetric method, the main challenge is the almost complete absence of ground features that can act as tie points for image reconstruction. The identification of these ground features is a critical limitation as they serve as reference points, enabling 2D image reconstruction.

In trying to solve this problem, photogrammetrists generally must rely on the DG approach to derive the EOPs required to reconstruct drone images of water bodies (Knaeps et al., 2019; Román et al., 2023; Windle and Silsbe, 2021; Lo et al., 2023; Ip et al., 2007). These studies suggested that traditional DG is the only practical solution for reconstructing images over water. This is in stark contrast to the terrestrial environment, where the BA method can be used to refine the EOPs by using tie points identified in the overlapping drone images. Also, in many instances, ground targets can be placed, which improve accuracy. This is impractical for water surveys due to the difficulty of placing visible targets on the water surface that remain static throughout the GNSS measurement campaign and also during the flight. These therefore cannot be used by a low-cost drone to improve the accuracy after the survey of a water body. Hence, a DG approach for water bodies is possible for drones with highly accurate RTK GNSS and IMU (Bláha et al., 2012; Ip et al., 2007). As a result, there is a clear gap in the knowledge regarding the suitability and performance of low-cost drones when mapping water bodies. There is also a clear gap regarding the techniques that can be employed to optimise their performance for DG. This gap is particularly deserving of investigation given the growing popularity of these low-cost systems.

Hence in this chapter, the aim is to explore and propose photogrammetric methods that can be used to correct errors and improve the accuracy of reconstructed 2D images when mapping over water using DG.

In particular, the objectives of the part of the thesis are to:

1. Carry out a series of drone surveys and field campaigns to develop a catalogue of drone images suitable for further analysis.

2. Assess the accuracy of DG using low-cost drones to develop a second benchmark dataset for comparison with subsequent methods.

3. Develop an approach to improve rectification of drone images captured with low-cost drones for DG.

4.2 Errors Associated with Direct Georeferencing

In the field of photogrammetry, before one can accurately measure distances, areas and positions in an aerial photograph, one requires knowledge of the errors present in the image. According to Wolf et al. (2014) and Azim et al. (2019), image rectification is essential for removing errors from reconstructed 2D images. These errors are mainly caused by tilt, relief displacement and scale variation (Wolf et al., 2014). In principle, an aerial photograph is not a plan, except (i) where the terrain is perfectly flat, and (ii) the optical axis of the sensor is truly vertical/nadir. However, a key assumption that enables the methodology in this thesis is that when mapping over (relatively) flat terrain such as water, it is assumed that there will not be any appreciable change in the elevation of the water surface. However, it is still essential to correct for tilt and scale variation in tilted photographs. As demonstrated in Section 3.4.2, tilted photographs when projected onto the ground plane transforms to a trapezoid-like shape which exhibits tilts effects. This chapter will focus on three main types of problems/effects that need to be corrected in a tilted photograph captured over a flat terrain, namely; the (i) ground principal point offset, (ii) tilt displacement and (iii) scale variations. The subsequent sections in 4.2.1, 4.2.2 and 4.2.3 will explain in detail the errors associated with DG.

4.2.1 Error 1 - Ground Principal Point Offset

Despite the presence of an IMU, a sensor stabilising gimble, and other stabilizing equipment such as vibration isolation mounts or camera shock absorbers, in practice, it is often impossible to ensure that the optical axis of a drone sensor is truly vertical at the time of image capture (Förstner and Wrobel, 2016a; Wolf et al., 2014). Images from low-cost drones generally do not have self-stabilizing gimbals and are therefore most affected by tilt. In photogrammetry, different types of images can be captured during a survey, namely; nadir/near-nadir, low tilt, high tilt and oblique imagery. An agreed convention in the literature (Wolf et al., 2014) is that when the sensor axis is truly vertical or there is a small unintentional tilt ($< 1^o$), the image can be categorized as a nadir/near-nadir image. For low tilt images, the tilt of the sensor axis can be defined as equal to or not more than 3°. Images captured with the sensor axis unintentionally tilted more than 3° can be considered as high tilt. Further, images that are captured with the sensor axis intentionally inclined more than 5° can be classified as oblique images (Verykokou and Ioannidis, 2018). In image reconstruction, the procedures suitable for rectifying nadir/near-nadir images can also be applied for low tilted images without serious consequences, however, this cannot be extended to cover high tilt or oblique images because, in such images, the errors resulting from the tilt are pronounced.

Early work in this thesis identified a flaw in the very beginning of the DG approach for water bodies - high tilt of the sensor will result in a mismatch between the Ground Principal Point (defined henceforth as GPP) and the GPS coordinates of the drone. The principal point represents the central point of the image taken by the sensor at nadir and the GPP refers to the location on the ground that corresponds to the principal point of the sensor - these two should be identical. However, in tilted images, the principal point is different, or 'shifted' away from the centre of the image. The amount and direction of this shift tilt is dependent on the degree and the direction of the tilt. This is because, in that scenario, the

sensor optical axis no longer points point directly down at the ground when the sensor is tilted (either Roll or Pitch) but the GPS coordinates, on the other hand, represent the position of the drone in the real world which has not moved. This introduces a shift in the ground coordinate system due to changes in the perspective centre (principal point) of the sensor and GPS.

This mismatch is further illustrated in Figure 4.1. From the Figure, the image to the left illustrates the ideal scenario where there is no tilt, i.e. perfectly nadir. As a result, the Ground GPS point (GP) added during the geotagging process (each image is "stamped" with this GPS point also referred to as being "geotagged") and the GPP have the same XY coordinates. The image on the right in Figure 4.1 highlights one of the issues identified in this thesis - that there is a shift between the GPP and GP when the sensor tilts. This shift is proportional to the angle of tilt (either Roll or Pitch) of the drone and therefore, particularly prevalent in high tilt images. In a traditional BA approach, this problem is resolved through the iterative BA workflow described in Section 2.4.3. Similarly, in traditional DG approach over a terrestrial environment, this can be resolved by applying GCPs. However, both of these are impossible over water. Over flat terrain, this shift can be potentially calculated through analytical photogrammetry. Hence, as the second novel contribution of this thesis, a method is proposed to calculate and correct for this shift.

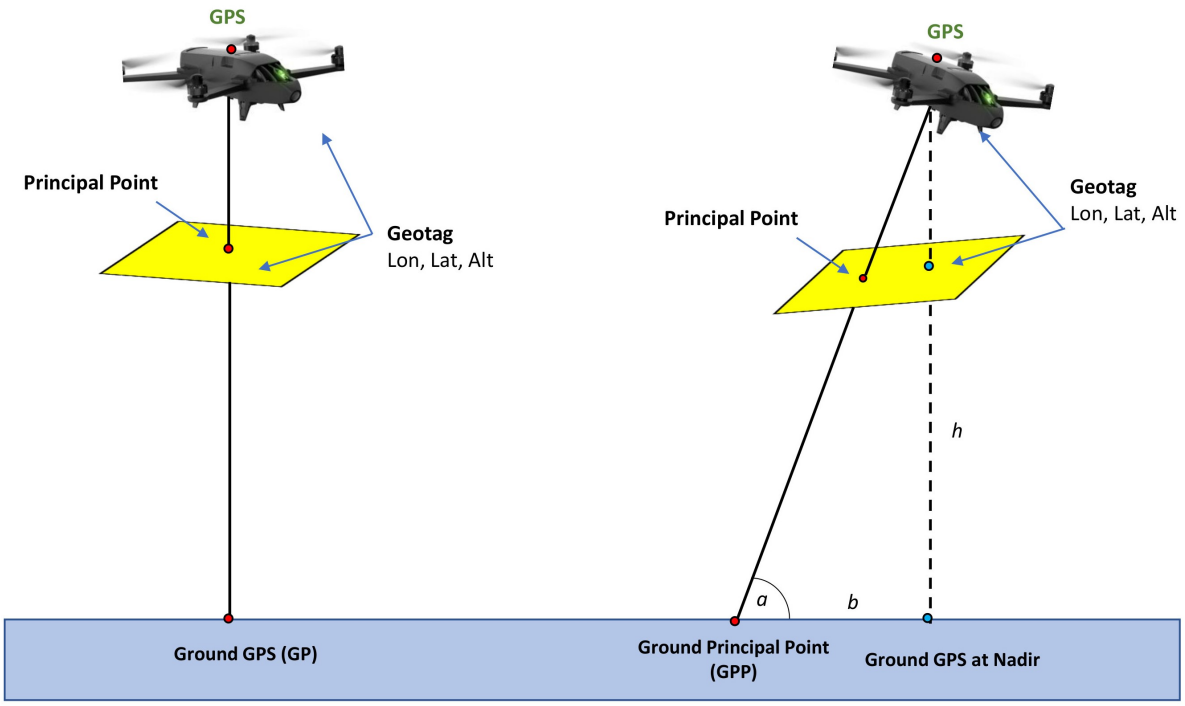

Figure 4.1: Illustration of the principle of tilt angle. The image (left) shows an image captured at nadir, where the XY coordinates of the Ground Principal Point (GPP) match with those of the ground GPS (GP). The image (right) shows the more common scenario where an image captured when the drone is tilted at an angle introduces a mismatch between the Ground Principal Point and the ground GPS.

4.2.2 Error 2 - Tilt Displacement

Tilt displacement is the change in an object's image position on a tilted photo from its theoretical position on a truly vertical photo (Wolf et al., 2014). The tilt of the sensor leads to the apparent displacements of objects from their actual positions in the real world and links back to the XY shift issue illustrated in Section 3.4.1. The tilt displacement error is different from the ground principal point offset because the latter moves the entire image in a particular direction while the former changes the position of an object in a tilted photo. This tilt is caused by the rotation of the sensor away from the vertical (Kraus, 2007). The magnitude of the error introduced by the tilt in the image depends upon the severity of the tilt and is subsequently referred to as a tilt displacement error. The tilt displacement also applies along both axes of the drone coordinate system.

Figure 4.2 illustrates the tilt displacement error. In this scenario, the principal point (P) refers to the geometric centre of the photograph where the X and Y axes intersect. The isocenter (i) is the midpoint between the Nadir and the Principal Point and Nadir is the point vertically beneath the sensor during image acquisition. In this illustration, point A can be considered as an arbitrary point captured over a flat ground plane in the ground coordinate system. Point a is the projected point of A in the image coordinate system when the sensor is at nadir, thereby creating a vertical photo. Point a' is the projected point A in the image coordinate system when the sensor is tilted at an angle and results in generating a tilted photo. Point a'' is the location of the point on the ground plane that would correspond to the point on the tilted photo (a'). The ground distance between point A and the corresponding point from the tilted photo onto the ground plane a'' is tilt displacement error *(dt)*.

The tilt displacement radiates from the isocenter of the photo and causes objects to be displaced radially towards the isocenter on the upper side of the tilted photo and radially outward on the lower side (Förstner and Wrobel, 2016a). In photogrammetry, if the amount and direction of tilt are known, then the photo can be rectified to its vertical equivalent (Schofield and Breach, 2007). In this chapter, an approach to calculate tilt displacement error via an analytical photogrammetry method is developed in section 4.6.4.2. This process is important and required for images that contain tilt.

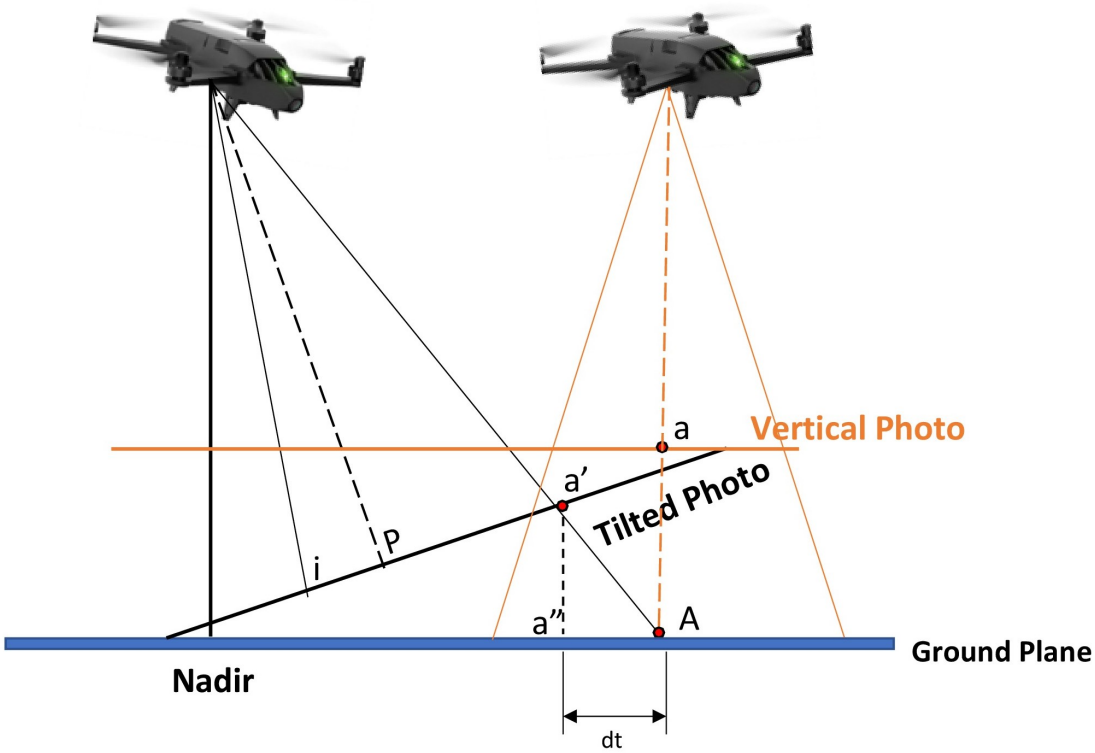

Figure 4.2: An image representing the principle of tilt displacement error. The image (left) shows an image taken when the drone is tilted at an angle which introduces tilt displacement error *(dt)*. The image (right) shows an image captured at nadir, as a result, there is no tilt displacement error.

4.2.3 Error 3: Effects of Scale Variations

Scale variation is another error that could be present in an aerial photograph. For vertical photographs over terrestrial areas, scale variation is caused by topographic relief. Whereas, in a tilted photograph, this scale variation is exacerbated by the combined effects of topographic relief and tilt. A key assumption underlying this thesis is that the study deals with imagery for a water body, represented as a uniform flat surface, and so the effects of topographic relief will not be considered further in the development of this methodology. However, the scale variation effect that needs to be considered is demonstrated in Figure 4.3. In this example, an experiment was conducted where a grid of square cells was overlaid on a vertical and tilted photographs on an area that best approximates a flat terrain. In this scenario, it can be seen in 4.3b that due to the tilt, the distance between C-D was less than the distance between A-B, yet both represent the same

real-world distance on the ground.

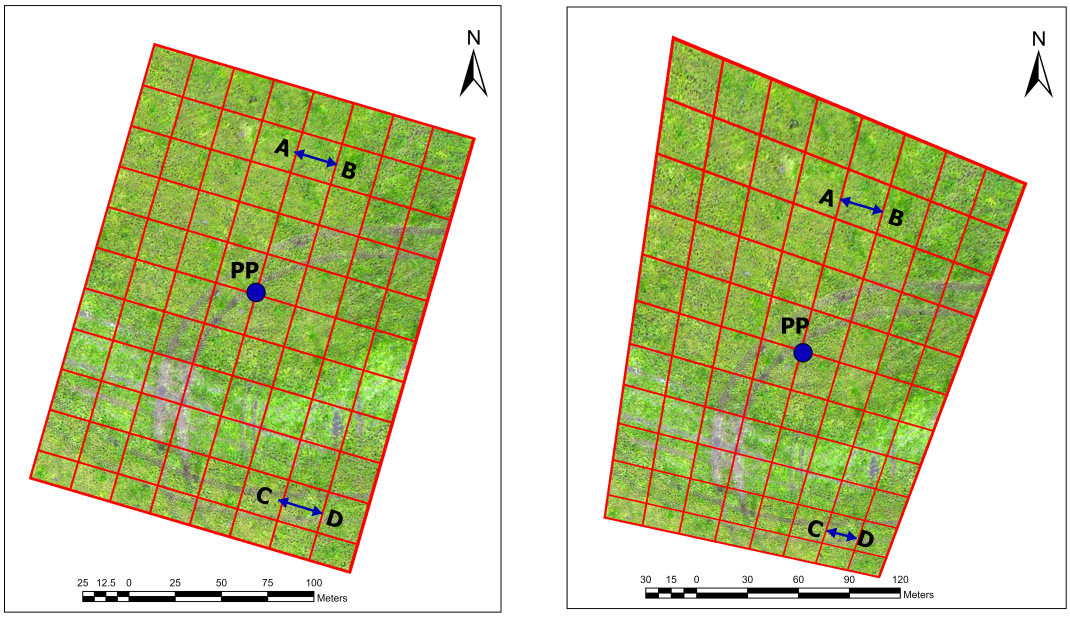

(a) Image captured at nadir

(b) Tilted photograph

Figure 4.3: An illustration explaining the scale variation effect due to tilt – where distance 'AB' is longer than distance 'CD', yet they are the same distance on the ground. However, for images captured at nadir, there is no scale variation effect.

4.3 Difficulties of Using GCPs in Improving Accuracy in Water Bodies

According to Wolf et al. (2014) and Behan (2004), the fundamental process of correcting for the ground principal point, tilt displacement and scale variations errors is performed through a process known as image rectification and this can be done by the use of GCPs. These GCPs could either be visible targets or naturally occurring, well distributed and identifiable features on the ground. However, as explained in section 4.1, one of the additional challenges when mapping water bodies is the near-impossibility of placing, fixing and recording the XYZ coordinates of stable targets over the water (Luan et al., 2012). When mapping water bodies, the image rectification step is often skipped due to this problem. This is evident in studies such as Knaeps et al. (2019); Román et al. (2023); Windle and Silsbe (2021); De Keukelaere et al. (2023) where no image rectification was performed, even though they used a drone without a self-levelling gimbal.

Therefore, the second objective of this thesis is to develop an improved approach to rectify images captured with low-cost drones over water and minimise each of these effects. This process will rely heavily on analytical photogrammetric principles and is entitled, **A**nalytical **R**ectification **M**ethod for **FE**atureless **T**errain - or 'ARMFET'.

4.4 Experimental Design

One of the fundamental research assumptions in this thesis is that the water surface can be considered perfectly planar, discounting small variations from swell or waves. To evaluate the proposed approach, a dataset over a large, flat, open terrain was required. This setup was necessary because placing or fixing visible targets over a water surface is too difficult and prone to error. This allowed for the best possible approximation of a 2D water body, facilitating accurate ground truth measurement where the ARMFET approach could be directly compared to the standard photogrammetric method (BA). In practice, this meant that the study area needed to have a low standard deviation in elevation. The main focus in this thesis is also to explore the suitability and performance of a low-cost drone. As such, a drone that meets the criteria described in Section 1.4.2 was selected. This was a fundamental requirement as the methods developed in the thesis were to optimise the performance of such drones.

4.5 Drone and GNSS Datasets - Planning and Capture

The following sections detail the study area (section 4.5.1), the sensor and platform (section 4.5.2) and the data used (section 4.5.3) during the development of this methodology.

4.5.1 Study Area

The study area chosen for this chapter was a flat, open field situated in Enfield, Co. Kildare, Ireland, approximately 20 kilometres from Maynooth University. The total area of the survey site covered 10.8 hectares. A site of this size provided adequate grounds to enable several flight lines and to alternate flight parameters for robust validation of the methodology. It also provided a large area which allowed GCPs to be placed at intervals of 60m and ensured that the GCPs were well distributed throughout the survey area. Also, it helped to ensure a sufficient number (> 4) of the GCPs could be identified in each image for the purposes of validation. The standard deviation in elevation across the whole test site was measured and identified as only 0.54m. This standard deviation suggests a relatively uniform and flat terrain within the study area. Figure 4.4 shows the location of the study area.

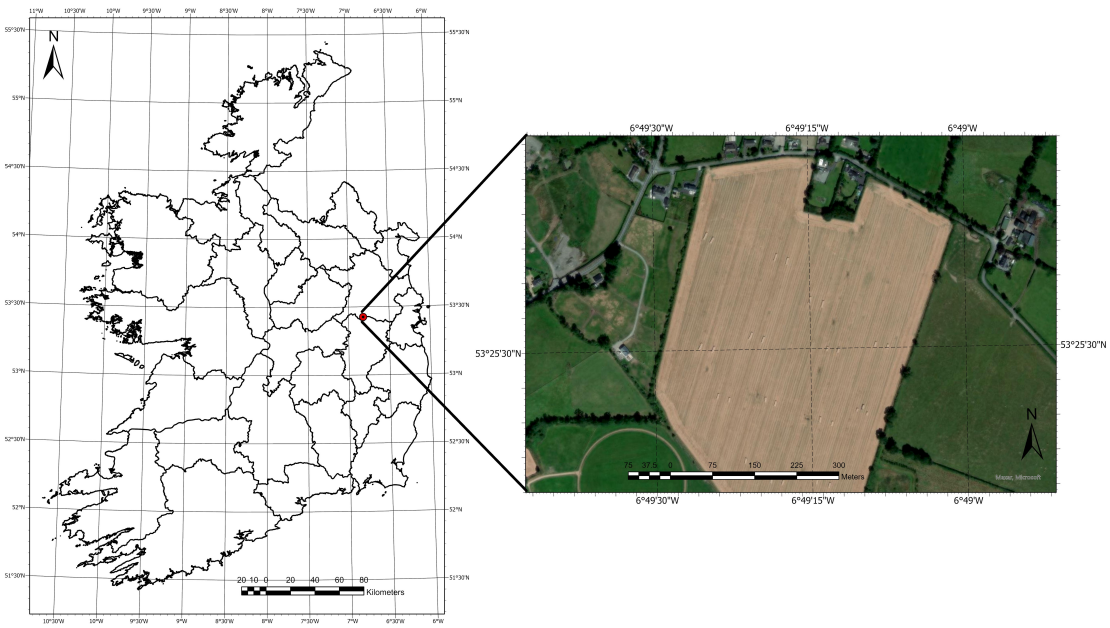

Figure 4.4: A map showing the location of the study area at Enfield: the image on the left shows a map of Ireland with the location of the field highlighted, and the right image shows an aerial view of the open field.

4.5.2 Sensor and Platform

A Bluegrass VTOL (Vertical Take-Off Landing) drone manufactured by Parrot was used to acquire the imagery and navigation data for each image over the test site. The Bluegrass has a Skycontroller to control the rotor inputs, a Sequoia multispectral sensor with four bands and a sunshine sensor to standardise the image reflectance during the survey (Parrot, 2017). The sunshine sensor records the ambient illumination from the sun and is also used in the radiometric calibration of the images. The Sequoia sensor also has two features of relevance to this study: an IMU and a GNSS. The GNSS helps in the precise geotagging of images, and the IMU helps measure the angular orientation of the sensor. According to the manufacturer's tolerances, the IMU on the Bluegrass has an accuracy of 0.5 ^{o} for Pitch and Roll and 1.0 ^{o} for Yaw (Sekrecka et al., 2020). The drone can record GNSS values to an accuracy of ± 1.5 m for the horizontal and vertical plane (Sekrecka et al., 2020), and it measures both the GPS and GLONASS constellations. Like many drones introduced in Chapter 1, Section 1.4.2.3, the sensor is not mounted on a self-levelling gimbal. To account for this, the Sequoia sensor is mounted beneath the Bluegrass but inclined at an angle of -15 ^{o} to account for the forward motion of the platform. This means that the sensor is perfectly vertical when the drone Pitches forward at approximately 15 ^{o} angle to begin forward flight. Figure 4.5 illustrates the Bluegrass drone equipped with a camera and a sunshine sensor. Table 4.1 gives a detailed description of the Parrot Sequoia specifications.

Table 4.1: Detailed Description of the Parrot Sequoia Sensor

Item	**Description**
Multispectral sensor	
sensor type	Global shutter
Bands	Green (530-570 nm), Red (640-680 nm), Red-edge (730-740 nm) Near Infrared (770-810 nm)
Focal Length	3.98 mm
Sensor size	3.75 μm
Image size	1280×960 pixel
sensor pixel	1.2 megapixel
Radiometric resolution	16-bits
Front-facing camera	
sensor type	Rolling shutter
Focal length	4.88 mm
Sensor size	1.34 μm

Source: (Parrot, 2017)

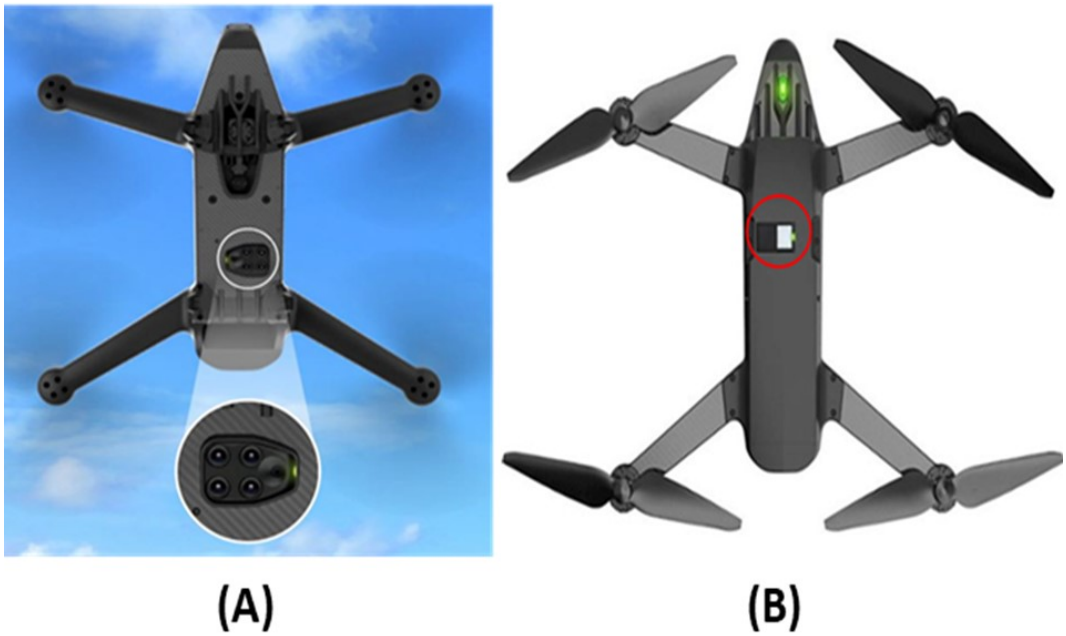

Figure 4.5: An image of the Parrot Bluegrass with (a) the Sequoia sensor visible underneath and (b) the sunshine sensor (highlighted in red) visible in a top-down view.

4.5.3 Field Survey

Flight paths for all drone surveys were predefined using the Pix4dCapture app as can be seen in Figure 4.6 – this app enables autonomous flight by allowing drones to fly following paths/waypoints with the pilot supervising operations. Three drone surveys were carried out as part of the initial survey at the Enfield test site, with the various flight and environmental parameters detailed in Table 4.2. A total of 30 GCPs were recorded using a Trimble 5800 dGPS receiver with a horizontal and vertical accuracy of ±50mm, as can be seen in Figure 4.7. The GCPs were recorded in the Irish Transverse Mercator (ITM) coordinate system.

Figure 4.6: An image showing a sample grid mission flight plan for the first drone survey across the open field in Enfield. The flight paths were defined using the Pix4D capture app, and the flight took approximately 8 mins.

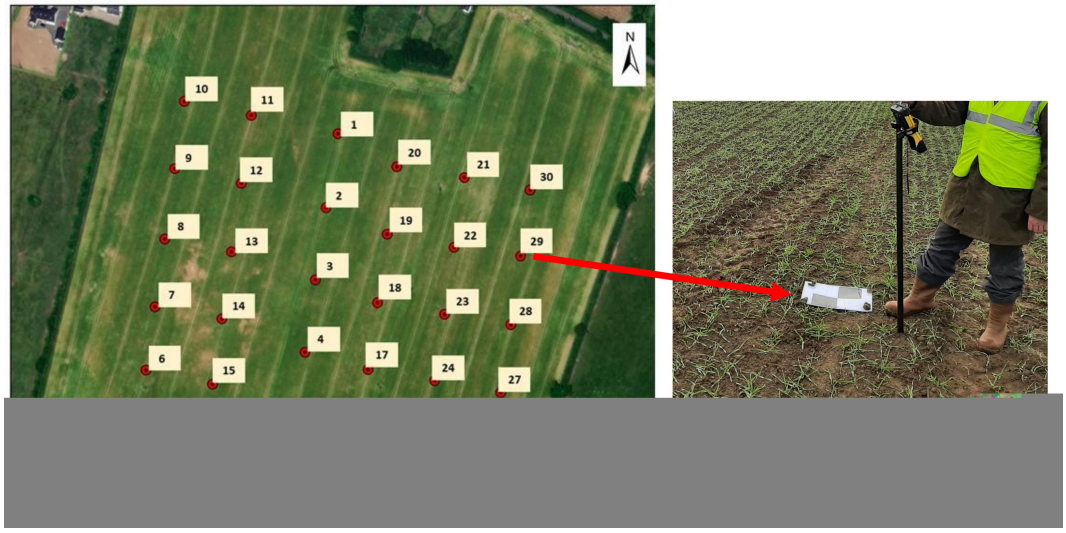

Figure 4.7: Distribution of 30 GCPs across the open field. An interval of approximately 60m between rows and columns was used. This ensured that a sufficient number (> 4) of GCPs were identifiable in each image.

Table 4.2: Environmental and Flight Parameters for the Field Surveys - Enfield

Parameters	**First survey**	**Second survey**	**Third survey**
Environment			
Temperature	6^oC	6^oC	6^oC
Wind speed	15km/h	15km/h	15km/h
Precipitation	0mm	0mm	0mm
Cloud cover	26%	50%	40%
Wind direction	NW to SE	NW to SE	NW to SE
Flight			
Altitude	120m	120m	100m
Overlap percentages	70% across track, 70% along track	70% across track, 70% along track	70% across track, 70% along track
Flight speed	12m/s to 14m/s	12m/s to 14m/s	10m/s to 12m/s
No. of flight lines	6	6	8
Flight direction	W to E	W to E	N to S
GSD	0.11m	0.11m	0.09m
No. of images captured	72	68	65

4.5.4 Additional data

Two additional drone surveys were conducted over water; two flights were carried out over Lough Egish, Co. Monaghan at 54 ^{o} 04'1.20" N and -6 ^{o} 47'60" W in December 2020. Three subsequent drone surveys over water were conducted at

Blessington Lake, Co. Wicklow at 53 ^{o} 10'12" N and -6 ^{o} 31'57" W in June 2021. These surveys were conducted in different seasons and under varying flight parameters and environmental factors. Table 4.3 details the flight parameters and the environmental factors during the survey. These datasets will be used for analysis in Section 4.7.2 and again in Chapters 5 and 6 as validation datasets.

Table 4.3: Drone Surveys Over Lough Egish and Blessington Lake

	Lough Egish		**Blessington Lake**		
Parameters	First survey	Second survey	First survey	Second survey	Third survey
Environment					
Temperature	6^oC	6^oC	12^oC	12^oC	12^oC
Wind speed	25km/h	25km/h	12.km/h	12.km/h	12.km/h
Precipitation	0mm	0mm	0mm	0mm	0mm
Cloud cover	26%	50%	20%	20%	20%
Wind direction	NW to SE	NW to SE	W to E	W to E	W to E
Flight					
Altitude	120m	80m	120m	120m	100m
Overlap percentages	70% across track, 70% along track	70% across track, 70% along track	70% across track, 70% along track	70% across track, 70% along track	50% across track, 50% along track
Flight speed	10.5m/s to 11m/s	9.37m/s to 10.5m/s	8.3m/s to 10m/s	8.3m/s to 10m/s	8.3m/s to 10m/s
No. of flight lines	6	4	4	5	7
Flight direction	N to S	N to S	W to E	W to E	S to N
GSD	0.11m	0.11m	0.07m	0.11m	0.94m
No. of images captured	54	28	44	58	36

4.6 Methods

This section explains the photogrammetric methods that were developed to improve the accuracy of the reconstructed 2D images obtained from the traditional DG method. The methods applied in this chapter are broadly grouped into four

categories. Methods 1 explains the steps involved in the image processing using the traditional BA method. Method 2 explains the pre-processing steps: primarily the extraction of navigation and auxiliary data and the sensor lens distortion corrections. Method 3 explains the steps employed in reconstructing images using the EOPs derived from the DG method. Method 4 is the another important contribution of this thesis, and it details the novel method developed to improve the accuracy of the reconstructed 2D images through the removal of associated errors in tilted images as detailed in Sections 4.6.4.1, 4.2.2 and 4.2.3 above. The workflow illustrated in Figure 4.8 explains the process (from Method 2 to 4) of projecting an image onto the ground plane through the application of correction methods and highlights the novel content.

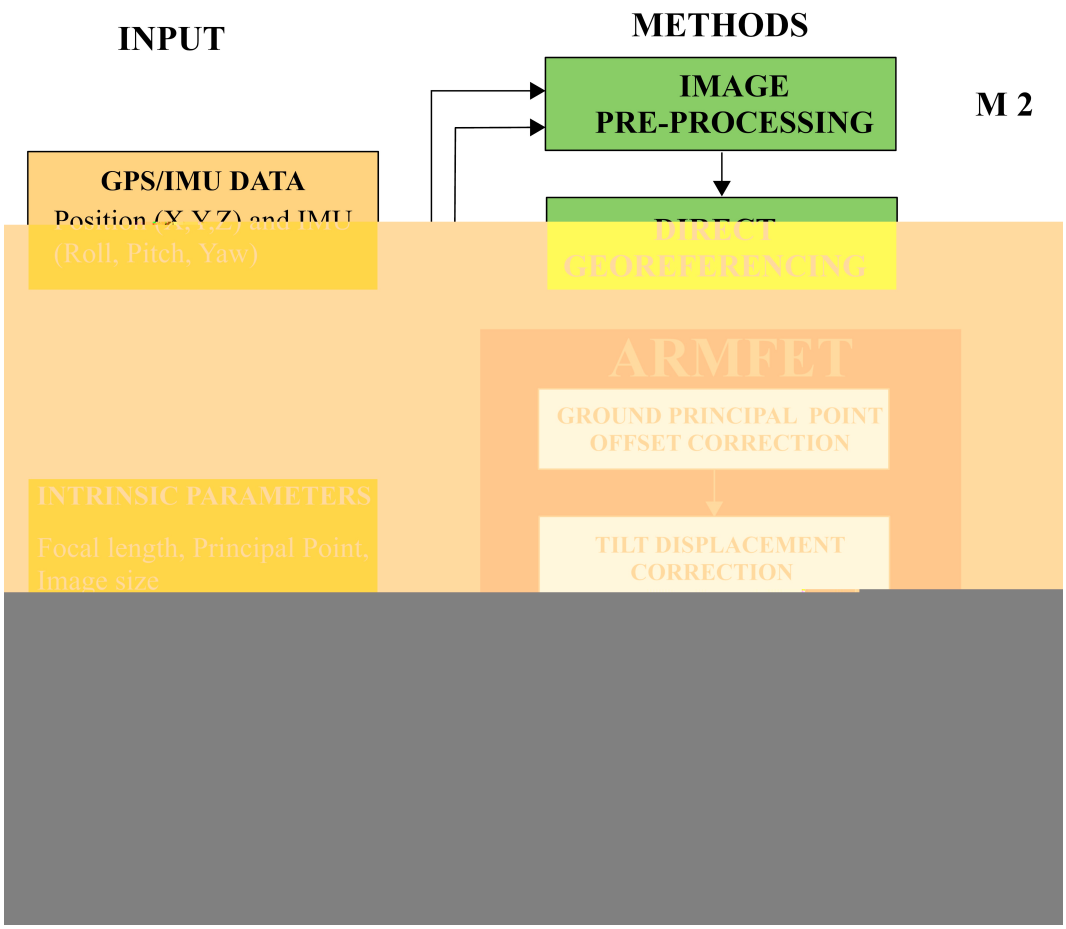

Figure 4.8: A flow diagram leading from the traditional DG process of reconstructing a 2D surface to the application of the novel correction methods developed in this thesis to minimize errors. The input variables are the parameters used for the reconstruction. ARMFET is the novel method proposed to improve the accuracy by removing the errors and its sequence in the process is highlighted in pink. The "M" denote method.

4.6.1 Method 1: Benchmark Dataset Using Bundle Adjustment

The traditional DG approach was used as the primary method for reconstructing the images over featureless terrain, while the BA approach was used as the benchmark data for comparing the performance of the traditional DG approach with each of the methodologies developed during this thesis.

The processing of the drone data was carried out using Pix4D software version 4.6.4. Two separate orthomosaics were generated using the traditional BA approach. The first orthomosaic was created without the utilization of GCPs and the accuracy of this orthomosaic was assessed using all 30 GCPs. This orthomosaic provided a baseline representation of the imagery without optimisation (i.e. no GCPs included in the processing). The second orthomosaic was generated and optimised during the BA approach using a set of 10 GCPs. The accuracy of this second orthomosaic was then validated using the remaining 20 GCPs.

The processing steps followed the typical SfM workflow, which encompassed several key stages as described in (Maravilla et al., 2019; Franzini et al., 2019; Teppati Losè et al., 2021). Firstly, image alignment and sensor calibration were performed to ensure accurate spatial registration of the images and precise calibration of the sensor parameters. Next, tie point extraction was carried out to identify and establish corresponding points across the images, aiding in the subsequent BA. This BA process refined the sensor positions, orientations, and 3D scene geometry, optimizing their alignment with the observed image features. Once the BA was completed, dense point clouds were generated, capturing detailed and dense 3D information of the scene. From the dense point clouds, DSM was then created, representing the elevation of the terrain and objects in the area. Finally, an orthomosaic was generated by combining each of the georeferenced images of the surveyed area.

4.6.2 Method 2: Image Pre-processing for Direct Georeferencing

4.6.2.1 Extraction of Navigation and Auxiliary data

DG requires the use of IOPs and EOPs to project a point in any 2D image onto the 3D ground plane. Each image captured also contains ancillary information which can help in the sensor lens distortion correction. A Python script was implemented to extract the ancillary information stored in the Exchangeable Image File Format (EXIF) data of each image. This included information such as the sensor size, focal length, image size, attitude angles (Pitch, Roll and Yaw), GPS position, GPS time-stamp, sensor aperture, shutter speed along with other related metadata.

4.6.2.2 Sensor Lens Distortion Correction

Sensor lens distortion correction is a crucial step in photogrammetry for applications that heavily depend on accurate measurements of objects. To ensure precise calibration, the Sequoia sensor calibration parameters were obtained from the EXIF data of the calibration certificates generated by the company laboratory. The images were corrected for radial and tangential distortion using K1, K2 and P1, P2 respectively. This was implemented using a Python script that utilized the sensor parameters.

4.6.3 Method 3: Direct Georeferencing

As explained in Chapter 1, the DG is the only practical means of deriving the EOPs for reconstructing 2D images over the water surface. This approach utilizes the IMU and GNSS sensor measurements to project an image onto the ground plane. The steps employed to project an image onto the ground plane are explained in the subsequent subsections and will establish the principles for discussing the proposed improvements in ARMFET.

4.6.3.1 Image Reconstruction

According to Wolf et al. (2014), most sensor models used in photogrammetry assume or employ the pinhole sensor model. The sensor function of capturing images, which involves taking points in the world and projecting them onto a 2D image plane, can then be simulated and implemented using these models. To project images captured by the drone onto the ground plane, it is necessary to utilise the IOPs and EOPs. These parameters allow us to compute a set of transformation matrices that project points through a series of coordinate systems. In particular, the projection process includes the following four coordinate systems: the World coordinate system (3D) >> the Sensor coordinate system (3D) >> the Image coordinate system (2D) >> and the Pixel coordinate system (2D). The extrinsic matrix models the 3D transformation from the world coordinate system to the sensor coordinate system, whereas the intrinsic matrix models the transformation from 3D points in the sensor coordinate system to points in the 2D pixel coordinate system.

I. Intrinsic Parameters

The reconstruction process begins with the sensor projection. It establishes the relationship between a point and its image which lies on a straight line that passes through the perspective centre. These intrinsic parameters describe the interior orientation of the sensor. They are parameters needed to model the geometry and the physics of the sensor such as focal length, principal point, sensor dimensions and any parameter used to model lens distortion. This transformation matrix (K) is represented as a 3*3 matrix as shown in Equation (4.1). The focal length is denoted as, f_x and f_y, in the x and y direction respectively, and the principal point is denoted as (C_x,C_y). Note that each of the parameters in Eq. (4.1) are given in pixels.

$$K = \begin{pmatrix} f_x & 0 & C_x \\ 0 & f_y & C_y \\ 0 & 0 & 1 \end{pmatrix} \tag{4.1}$$

II. Extrinsic Parameters

The extrinsic parameters define the POSE of the sensor during exposure in 6DOF. It contains six parameters; that is the spatial 3D position (X, Y, Z) of the projection centre and the attitude angles (Yaw (ψ), Pitch (θ), Roll (ϕ) around the sensor axis. The rotational angles vary with the motion of the sensor. However, two of the rotational angles (ϕ, θ) may be constant/exhibit minimal change over time if the sensor is mounted on a gimble. At any point during the flight, the transformation of points from the 3D world coordinate system to the 3D sensor coordinate system is modelled as a 4×4 transformation matrix. This can be achieved in two steps according to Förstner and Wrobel (2016a):

1. Rotation: The rotation is performed by three independent parameters where Yaw, Pitch and Roll are denoted as (ψ,Θ,ϕ) respectively as shown in Equation (4.2).

$$C_b^n = R_z(\psi).R_y(\theta).R_x(\varphi) \tag{4.2}$$

2. The translation parameters T are denoted as X,Y,Z in the world coordinate system through the projection centre O as seen in Equation (4.3). The Z denotes the point's position in 3D space.

$$Z = [XO,\ YO,\ ZO]^T \tag{4.3}$$

Adopting the equation from Bäumker et al. (2002), the extrinsic rotation matrix (M_{ext}) is given by Equation (4.4) below where tx,ty,tz are the translation point.

$$M_{ext} = \begin{pmatrix} R_{3\times3} & t_{3\times1} \\ 0_{1\times3} & 1_{1\times1} \end{pmatrix} = \begin{pmatrix} r_{11} & r_{31} & r_{13} & tx \\ r_{21} & r_{31} & r_{23} & ty \\ r_{31} & r_{32} & r_{33} & tz \\ 0 & 0 & 0 & 1 \end{pmatrix} \tag{4.4}$$

In the context of photogrammetry, it is also required to covert Pitch, Roll and Yaw into Omega (ω), Phi (ϕ) and Kappa (κ) respectively. This is because the Yaw, Pitch, and Roll angles are typically used to describe the orientation of a body (drone) relative to its navigation coordinate system (see Section 2.3.2.3), whereas the Omega, Phi, and Kappa (OPK) angles were used to describe the rotation between the image coordinate system and a projected coordinate system. The conversion is explained in Equation (4.5) and is further expanded in Equation (4.6) as a rotation matrix (C_B^E) and is defined using counter-clockwise rotation angles.

$$C_B^E = Rx(\omega).Ry(\phi).Rz(\kappa) \tag{4.5}$$

$$= \begin{pmatrix} 1 & 0 & 0 \\ 0 & \cos\omega & -\sin\omega \\ 0 & \sin\omega & \cos\omega \end{pmatrix} \begin{pmatrix} \cos\varphi & 0 & \sin\varphi \\ 0 & 1 & 0 \\ -\sin\varphi & 0 & \cos\varphi \end{pmatrix} \begin{pmatrix} \cos\kappa & -\sin\kappa & 0 \\ \sin\kappa & \cos\kappa & 0 \\ 0 & 0 & 1 \end{pmatrix} \tag{4.6}$$

$$= \begin{pmatrix} \cos\varphi\ \cos\theta & -\cos\varphi\ \sin\kappa & \sin\varphi \\ \cos\omega\ \sin\kappa + \sin\omega\sin\varphi\cos\kappa & \cos\omega\cos\kappa - \sin\omega\sin\varphi\sin\kappa & -\sin\omega\cos\varphi \\ \sin\omega\sin\kappa - \cos\omega\sin\varphi\cos\kappa & \sin\omega\ \cos\kappa + \cos\omega\ \sin\varphi\sin\kappa & \cos\omega\cos\varphi \end{pmatrix}$$

After computation of the rotation matrix, the Omega (ω), Phi (ϕ) and Kappa (κ) angles can be extracted using the System PATB formulas explained in Bäumker et al. (2002) which was developed by University of Stuttgart as shown in Equation (4.7).

$$\omega = \arctan2\left(\frac{-r_{23}}{r_{33}}\right), \varphi = \arcsin(r_{13}), \kappa = \arctan2\left(\frac{-r_{12}}{r_{11}}\right) \tag{4.7}$$

Finally, by combining the intrinsic and extrinsic parameters, a full transformation can be achieved, as shown in Figure 4.9. This transformation represents the complete mapping of any point or image from the 3D world coordinate system to the 2D pixel coordinate system, taking into account both the internal characteristics of the sensor (IOPs) and its position in the world (EOPs).

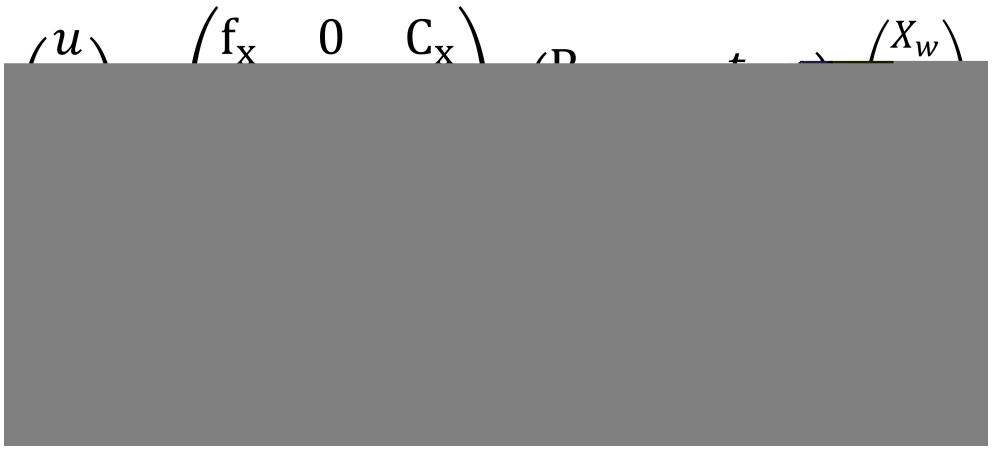

Figure 4.9: An image showing the complete transformation matrix where the intrinsic and the extrinsic parameters are combined. This complete the mapping process from world coordinate to pixel coordinate

4.6.4 ARMFET - Analytical Rectification Method For Featureless Terrain

In order to rectify reconstructed images over water, this thesis proposes a novel method called 'ARMFET'. In ARMFET, two key methods were developed and applied: (i) a ground principal point offset correction (see Section 4.2.1 and (ii) a tilt displacement correction that corrects error 2 and error 3 (see Sections 4.2.2 and 4.2.3). Each step of this process is illustrated in Figure 4.10. The goal is that at the end, a rectified image which can be considered equivalent to a vertical photograph is produced.

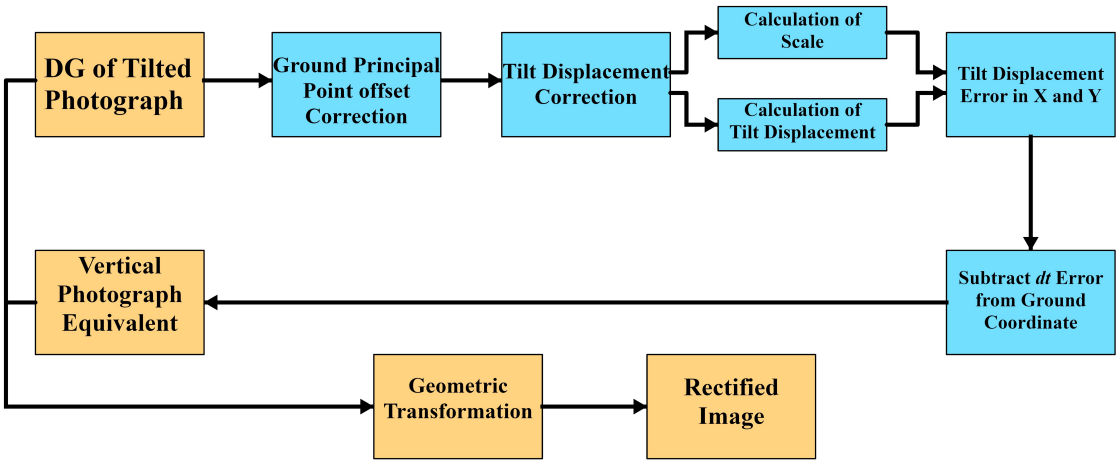

Figure 4.10: An illustration of the workflow involved in rectifying images via analytical photogrammetry. The blue colour shows the novel ARMFET components which was applied : the GPP correction method was developed in this thesis and the remaining components were derived from photogrammetric literature. The yellow colour shows all other steps that were applied to derive the rectified image.

4.6.4.1 Correction 1 - Ground Principal Point Offset

In correcting the first error source - (i) the ground principal; point offset due to tilt, ARMFET seeks to first calculate the shift in distance between GP and GPP on a flat terrain as depicted in Figure 4.1 in Section 4.2.1. In theory, the orientation of a sensor will impact the positional accuracy in both the X and Y coordinates. For example, the results from Chapter 3, Section 3.4.2 revealed that 1^oC tilt in Roll had a greater effect on the X coordinates and a smaller effect on the Y coordinate. Conversely, 1^oC change in Pitch had a greater effect on the Y coordinate and a smaller effect on the X coordinate. This shift can be mathematically calculated for flat terrain using the law of Sine rule, given that we already know (i) the flying height of the drone and (ii) the attitude from the IMU. The shift in X and Y coordinate is therefore calculated using Equation (4.8) and (4.9) respectively, where h is the flying height, b_x is denoted as the shift value in X direction between GP and GP' and b_y is the shift value in Y direction between GP and GP'. The value obtained is subsequently used to shift the image from the image centre. At the end of the process, the GP' is aligned with the GP.

$$b_x = h * \tan(\text{Pitch}) \tag{4.8}$$

$$b_y = h * \tan(\text{Roll}) \tag{4.9}$$

4.6.4.2 Correction 2 - Tilt Displacement

After the principal point correction, the image needs to be corrected for (ii) tilt displacement and (iii) scale variations. As explained in section 4.2.2, tilt displacement occurs due to the sensor axis not being level with the ground plane at the time of exposure. This can occur if the nose of the aircraft is slightly up or down (Pitch) or if a wing is tilted up or down (Roll). If the amount and direction of the tilt are known, then the photo can be rectified. In order to remove the tilt effect, the following steps were applied.

I. Calculation of Tilt Displacement

Firstly, the tilt displacement error in X and Y can be calculated adopting the equation from Schofield and Breach (2007). In equation (4.10) and (4.11), (x, y) denote the image coordinate of a random point measured about the fiducial axes, (x', y') represent the rotational effects in the image coordinate, f denotes focal length, H denotes flying height and Pitch and Roll are angles measured by the IMU.

$$x' = -x\cos(\text{Roll}) + y\sin(\text{Roll}) \tag{4.10}$$

$$y' = -x\sin(\text{Roll}) - y\cos(\text{Roll}) + \tan\left(\frac{\text{Pitch}}{2}\right) \tag{4.11}$$

After the calculation of the rotation effects in the image coordinate system, the tilt displacement error must then be converted to the ground distance. In this process, the scale of the photograph needs to be calculated. The scale can be calculated if the attitude angles and the flight height are known. In Equation (4.12)

and (4.14), K represent the scale of variation for an image on the lower side of a photograph, K' denote the scale of variation for an image on the upper side of a photograph, f denotes focal length, ia' denotes the distance between isocenter and random point a, H represent the flight height, θ denotes the Pitch angle and the (X,Y) represent the ground tilt displacement in x and y direction.

The scale of a photograph at a given point is therefore calculated as:

$$\mathrm{K} = \frac{\mathrm{f} + \mathrm{ia}' \sin\theta}{\mathrm{H}} \tag{4.12}$$

$$\mathrm{K}' = \frac{\mathrm{f} - \mathrm{ia}' \sin\theta}{\mathrm{H}} \tag{4.13}$$

This allows the ground distance for tilt displacement in X and Y to be calculated as:

$$X = \mathrm{K}x' \tag{4.14}$$

$$Y = \mathrm{K}y' \tag{4.15}$$

II. Geometric Transformation

After calculating the tilt displacement error in X and Y, a geometric transformation process was subsequently applied. This process removed (or eliminated) the tilt displacement (dt) error by transforming the tilted photograph to its vertical equivalent. In order to transform the image to its vertical equivalent, two separate/different ground points were first derived: the ground point from the tilted image and the ground point from its equivalent in vertical position. The first step calculated the tilt displacement in X and Y for at least four random points which are evenly distributed. This helped to avoid points being collinear which will affect the geometric transformation.The new ground coordinate point was then derived by adding the dt in X and Y to the corresponding generated ground coordinate point. The second step was to derive the ground coordinate for its

vertical position. This was derived by subtracting the dt in both X and Y from the measured ground coordinate. After these two points were mathematically derived, the image was rectified using these two different ground points. The last step was to apply an affine transformation to warp the image to its vertical equivalent. An affine transformation is a type of geometric transformation that preserves parallelism and is common for remote sensing applications (Shylaja and Sanil Shanker, 2022). It can be used to translate, rotate, scale, and shear an image. This can be seen in Figure 4.11 where the illustration explains how the non-rectified image is rectified from the derived ground coordinate points.

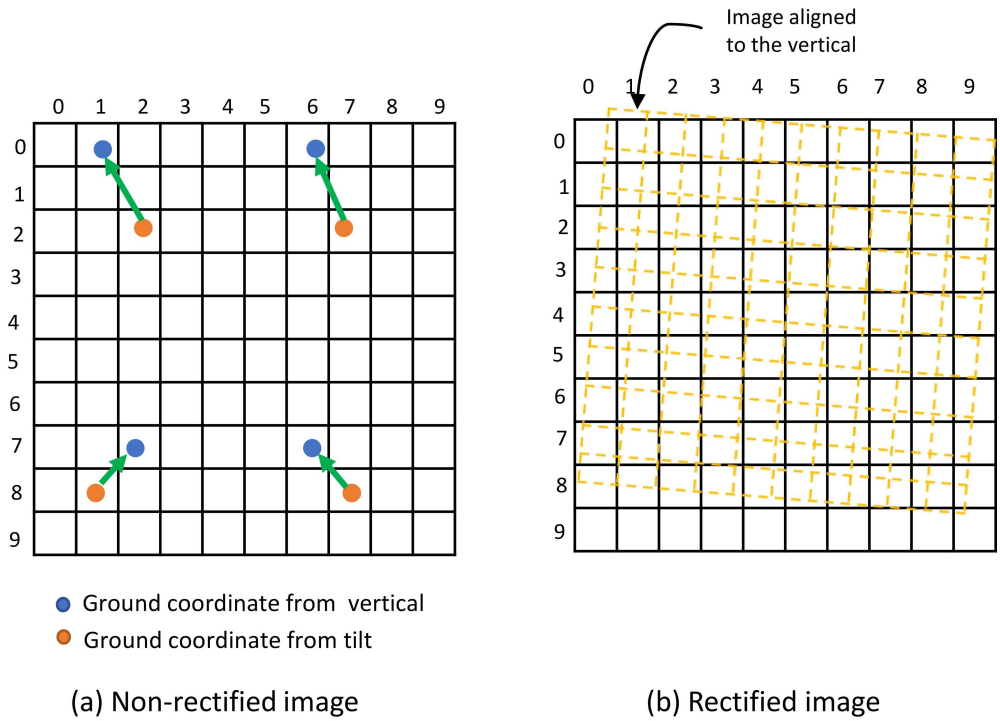

Figure 4.11: An illustration showing how images are rectified using the ground coordinate from a tilted image and the ground coordinate from a vertical image. Figure (a) shows the ground coordinate points obtained from the tilt and the ground coordinate obtained from the vertical. The image is aligned using these points through affine transformation to produce the yellow image in Figure (b).

4.7 Results and Analysis

This section presents the results obtained from the analysis. The first analysis was conducted by analysing the attitude angles obtained from the survey as shown in Section 4.7.1. Subsequent analyses were conducted on the effect of wind speed and wind direction on attitude in Section 4.7.2 and 4.7.3, exterior orientation analysis for DG in Section 4.7.4, evaluation of the traditional DG method in Section 4.7.5 and accuracy assessment of the ARMFET Approach in Section 4.7.6.

4.7.1 Analysis of the Attitude Angles

The evaluation of attitude angles helps assess how stable the platform was during the surveys. Also, as revealed in Chapter 3, Section 3.5, attitude angle was identified as the single most important factor influencing the accuracy of the reconstructed 2D image in DG.

From the Enfield drone survey, 72 images were captured and their ancillary data were extracted following the methodology described in section 4.6.2.1. The attitude angles measured from the Sequoia IMU were plotted to show the angular measurement over the entire survey as shown in Figure 4.12. From the result, the maximum angular measurement for Pitch and Roll were 18.49 ^{o} and 8.06 ^{o} respectively. The mean angular measurements for Pitch and Roll were 6.7^o and 5.5^o, respectively. To understand the degree of variation in the angular measurement, a standard deviation was also calculated. The standard deviation for the attitudes angles were 6.4^o, 1.5^o, 1.9^o for Pitch, Roll and Yaw respectively. Furthermore, analysis was conducted to group the images into four categories of aerial photographs defined by Wolf et al. (2014) : nadir/near-nadir, low tilt, high tilt and oblique imagery. The result revealed that 5.5% of the images captured were nadir/near-nadir images ($< 1^o$), 41.6% were low tilted images (greater than 1° equal but less than or equal to 3°) and 52.9% were high tilted images (more than 3°). This implies that most of the images acquired were impacted by the tilt displacement errors identified in Section 4.2.2 and therefore the methods proposed

in this thesis to remove the tilt effects from the images are applicable.

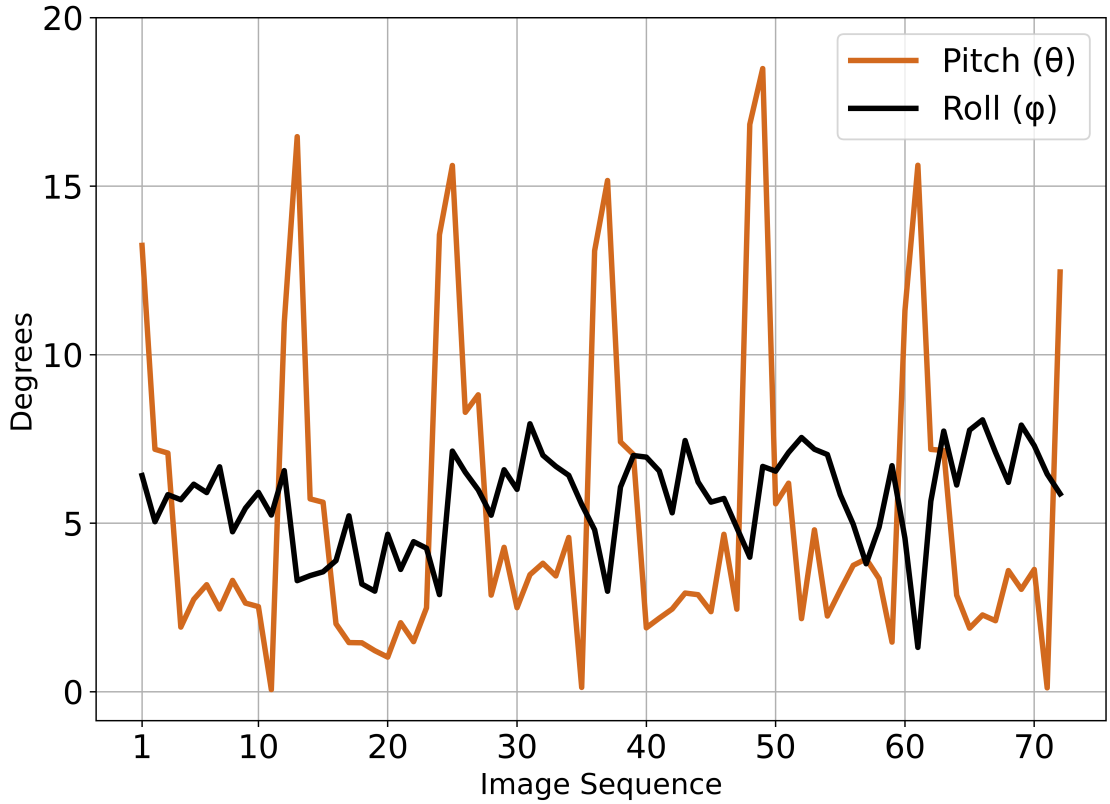

Figure 4.12: Attitude angles in Pitch (brown) and Roll (black) for 72 images captured by the Parrot Bluegrass over Enfield, Co. Kildare.

4.7.2 Effect of Wind Speed on Attitude

For further analysis, the additional data described in Section 4.5.4 was also included in the study of the influence of wind speed. This offered a greater range of wind speeds and different flight directions to identify trends in the data.

In the study conducted by Otarola et al. (2019), a relationship between wind speed and altitude above the surface was established. Specifically, it was determined that wind speed increases up to 0.25m/s per every 10m increase in flying altitude. The wind speed measurements gathered from the field surveys in this thesis were primarily obtained at ground level, hence the framework proposed by Otarola et al. (2019) has been used to extrapolate wind speeds that correspond to the different flight altitudes. The mean Pitch and Roll values were calculated for each survey as seen in Table 4.4. The results showed that the highest wind speed

recorded also produced the highest mean Pitch and Roll values. This is evident in Figure 4.13a and 4.13b where the high wind speed produced high Pitch values of up to 18.49 ^{o} . However, the relationship between the Pitch and Roll values was not linear. For example, a wind speed of 21 km/h produced a mean Pitch value that was higher than a wind speed of 22.8 km/h. This suggests that wind speed is not the only factor that can influence the attitude angles. For instance, the direction of the flight can also impact the attitude angles measured.

Another finding of this study was that the higher the wind speed, the more impact it has on the attitude measurement. This was evident when comparing the survey results for Figure 4.13a , which had a similar flight direction (meaning the impact of flight direction will not contribute to the attitude measurement). In this case, an increase in the wind speed resulted in a greater impact on the attitude measurement. Similarly, when comparing the first and second survey results from Blessington Lake which had the same wind speed and flight direction, the mean difference for the Pitch and Roll values was 1.8 and 0.9 degrees, respectively. This difference was not significant, suggesting that it could be due to random errors. These results suggest that a change in 1 km/h in wind speed results in an increase of 0.17^{o} in Pitch and 0.52^{o} in Roll for this type of drone. Additionally, it was found that gusts of winds can cause the images captured by the drone to be highly tilted. From the Figure 4.13a and 4.13b, it can be seen that almost all (95%) of the images captured were above 3°. Thus, it can be categorized using the Wolf et al. (2014) classification as a high-tilt image. On the other hand, about 45% of the images captured under low wind speed (Figure c,d,e and f) were under 3°, thus can broadly be described as low tilted images.

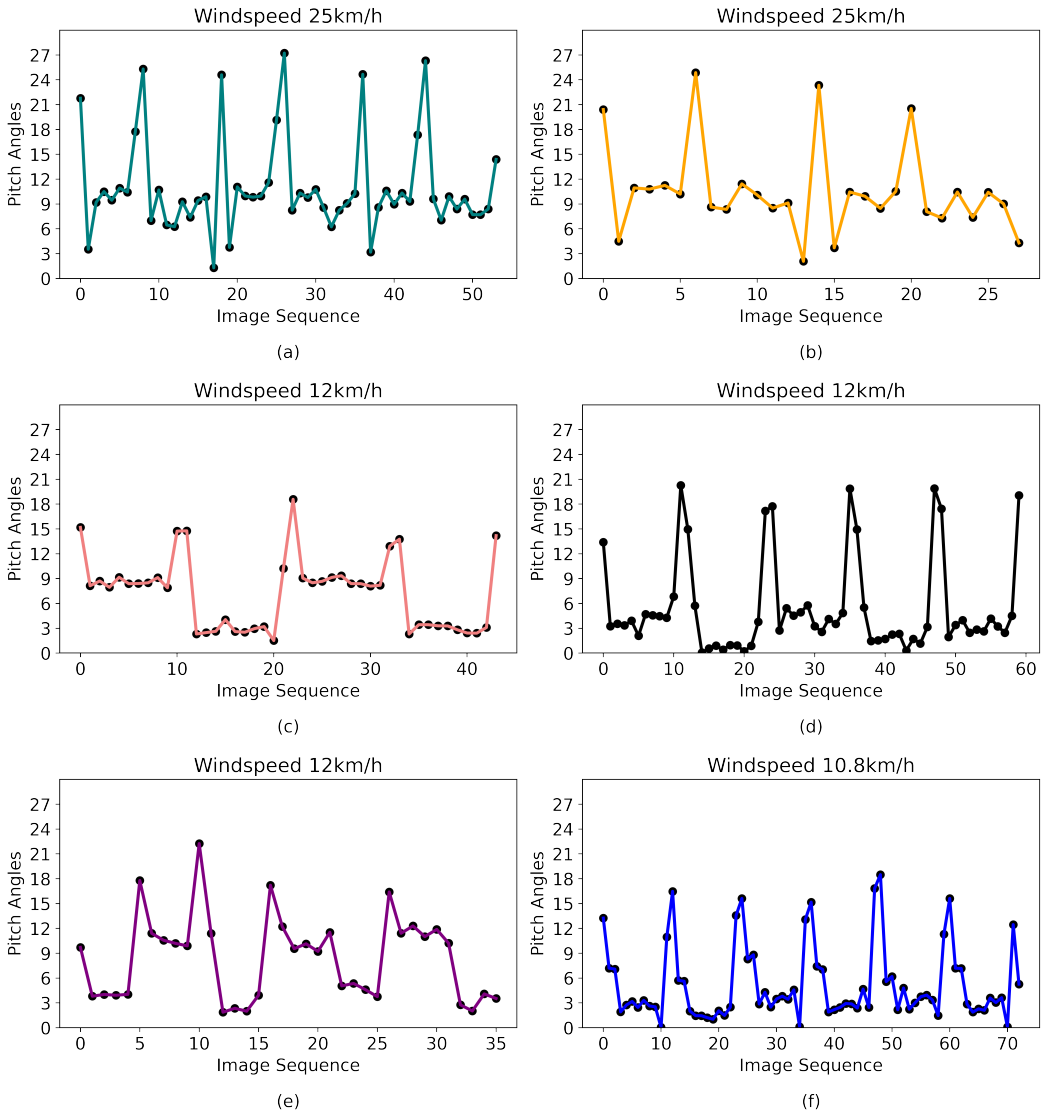

Figure 4.13: Comparison of attitude angles measured under different wind speed conditions. The Figure 4.13a, and 4.13b line graphs show attitude measurement under high wind speeds while 4.13c, 4.13d, 4.13e, and 4.13f line graphs shows attitude measurement under low wind speed.

Table 4.4: Analysis of Mean Pitch and Roll Values Under Varying Wind Speed

	Lough Egish		**Blessington Lake**			**Open Field**
Parameters	1st survey Wind-speed 34.9km/h	2nd survey Wind-speed 32km/h	1st survey Wind-speed 22.8km/h	2nd survey Wind-speed 22.8km/h	3rd survey Wind-speed 21km/h	1st survey Wind-speed 21.6km/h
Mean Pitch	11.05^o	10.53^o	7.25^o	5.41^o	8.42^o	6.7^o
Mean Roll	4.2^o	2.67^o	3.59^o	4.51^o	3.4^o	5.5^o

4.7.3 Effect of Wind Direction on Attitude

In addition to wind speed, wind direction also affected the drone speed and attitude measurement. As previously discussed, this thesis defines downwind as the wind that blows in the direction of the drone's travel, increasing the drone's speed, while upwind is the wind that blows against the direction of the drone and reduces the drone's speed (Soares, 2013).

In this analysis, a comparison was made between the impact of different flight directions on the attitude angles of a drone. Figure 4.14 explains what happens when a flight direction of a drone survey is away from the wind direction and Figure 4.15 explains what happens when a drone flight is in the same direction of the wind. One finding from the test is that when the flight direction of a drone survey is away from the wind, there is less impact on the attitude angles.

The results from Figure 4.15 also demonstrate that flying in the direction of the wind (downwind) has an impact in the attitude angles and is exacerbated when the wind speed is high. The mean Pitch angle was calculated to be 13.5^o when flying downwind and 8.5^o when flying upwind. This meant that the Pitch angle increased with downwind and slightly decreased with upwind. The increase in Pitch angle when flying downwind was due to the fact that the drone's airspeed increases when it is being pushed by the wind. This can potentially lead to a higher angle of attack. In this experiment, the wind speed that was recorded during the survey was high, therefore contributing to the increase of the drone speed, especially in the downwind direction. The drone's speed recorded when flying downwind was 13.5m/s, while upwind was 9.5m/s. This therefore explains the reason for the high Pitch angle of the drone. Also, the slight decrease in Pitch angle when flying upwind was due to the fact that the drone's airspeed decreases when it is flying against the wind. Overall, it can be concluded that the impact of flying in the direction of the wind could be increased when the wind speed is high and it will cause the images captured to be tilted.

Figure 4.14: This image shows a flight path where it is away from the wind direction. In this scenario, the effect of the wind is minimized. The attitude angles in the image are categorised according to near nadir (0-1), low tilt (1-3) and high tilted (> 3) images

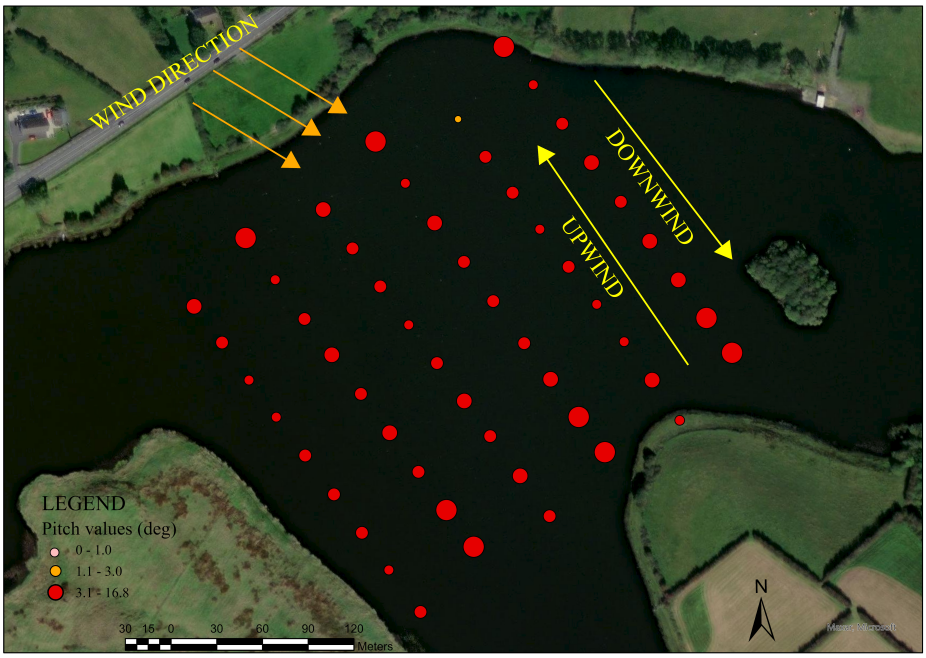

Figure 4.15: This image shows the effect of wind direction on the Pitch angle of the drone. During downwind flights the airspeed of the drone increases and this appears to significantly increase the Pitch angle during surveys

4.7.4 Comparison of Omega/Phi Angles Against Benchmark Data

This section focused on evaluating the Pitch and Roll angles derived from the DG method. In photogrammetry, Pitch and Roll are converted to Omega and Phi, respectively. To evaluate the orientation angles derived from the traditional DG method, residual errors were calculated and plotted in a line graph. The residuals erros were calculated by subtracting the derived attitude angles ((ω) and (ϕ)) of the traditional DG method and BA method without GCPs from BA method with GCPs. The BA with GCPs was used as the benchmark dataset. The results from the analysis are explained in Section 4.7.4.1 and 4.7.4.2.

4.7.4.1 Evaluation of Omega Angle

A comparison of the (ω) angle residual error was done between the BA approach without GCPs and the Traditional DG method as shown in Figure 4.16. The findings revealed that the residual errors for the (ω) angle were 0.09^o and 1.38^o for BA without GCPs and DG, respectively. Further, the maximum and minimum (ω) angle obtained were 0.2^o and 4.38^o respectively. From the results, the residual error measured suggests a slightly high error in the X axis and could be attributed to the high wind speed and the flight direction.

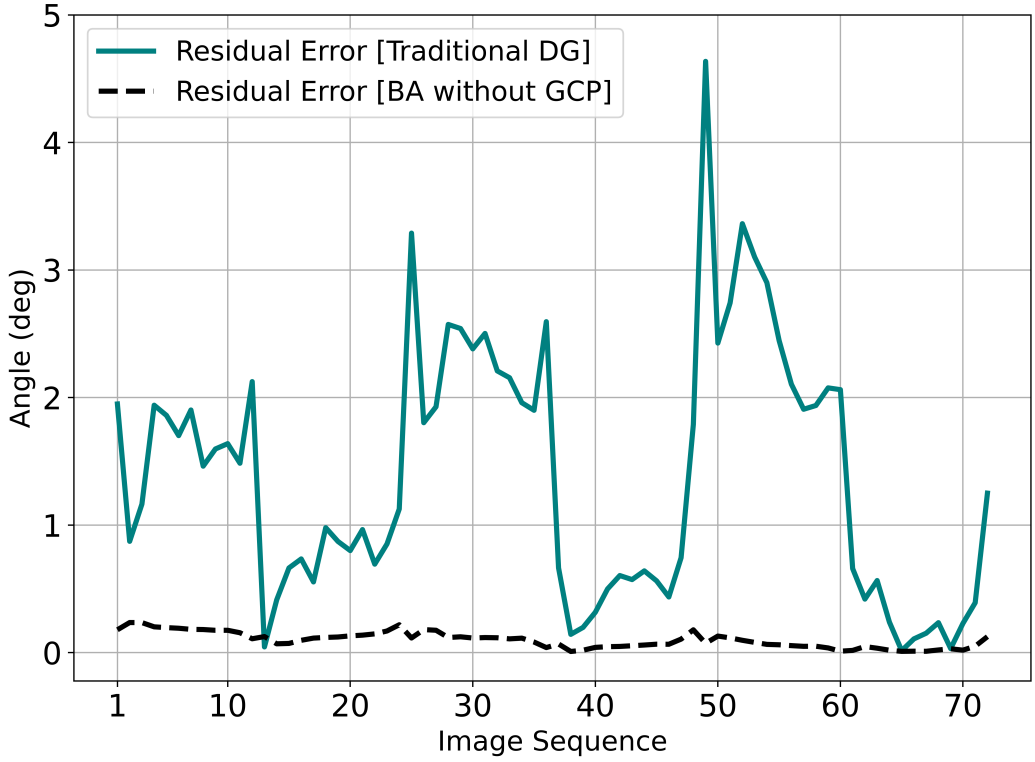

Figure 4.16: A graph showing the (ω) angle residual error for Traditional DG and BA with no GCP. The image sequence on the x-axis refers to the number of individual images used (n=72). The error was calculated at each image using at least four GCPs visible to each.

4.7.4.2 Evaluation of Phi angle

The residual error for the (ϕ) angle was 0.13^o and 0.77^o for BA without GCP and intial DG respectively. Comparing the residual angle in (ϕ) to (ω), the former had a better accuracy. From Figure 4.17, it can be seen that the (ϕ) angle had relatively lower errors and could be attributed to the flight direction. These experiments shows how the (ω)/(ϕ) angles derived from the traditional method using low-cost IMUs compare to the benchmark data. This further reinforces the limitation of traditional DG approach explained in section 4.1; which is its dependence on accurate IMU and GNSS's measurements.

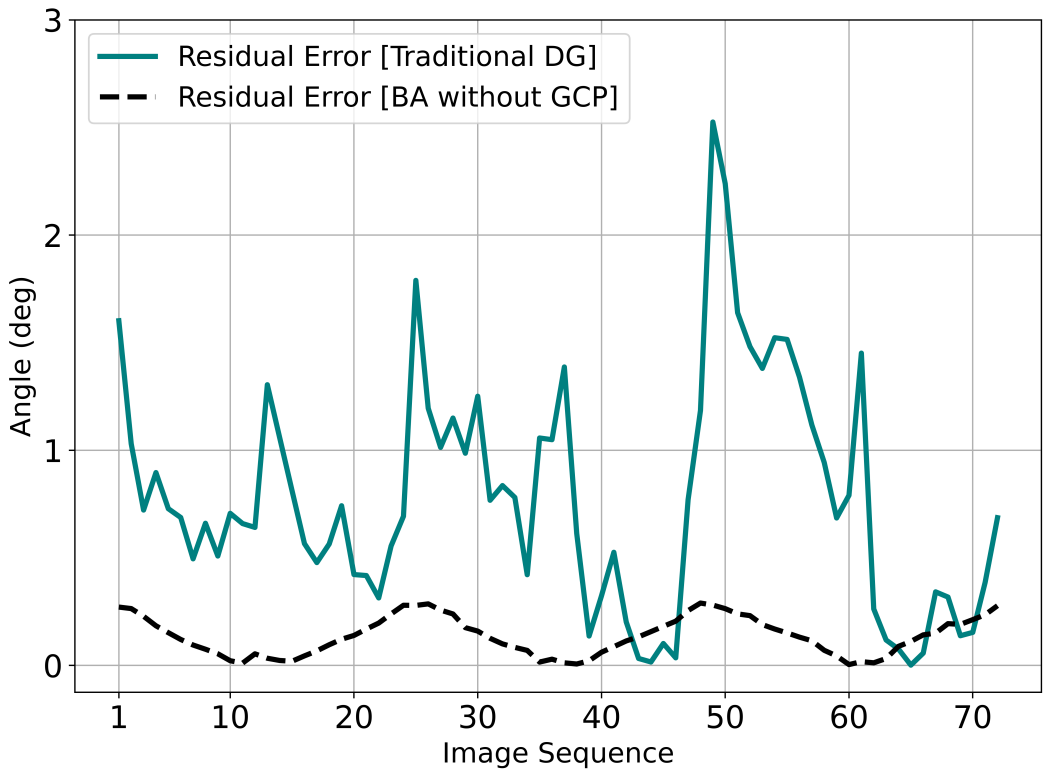

Figure 4.17: A graph showing the (ϕ) angle residual error for DG (Green) and BA with no GCP (Black).The image sequence on the x-axis refers to the number of individual images used (n=72). The error was calculated at each image using four GCPs visible to each.

4.7.5 Evaluation of the Traditional DG method

The results presented thus far obtained from the Traditional DG approach were acquired without applying any of the novel correction methods in ARMFET (as explained in Section 4.6.3). To analyse the effectiveness of the traditional DG approach for mapping water bodies, the accuracy was measured against BA with GCPs and BA without GCPs. The Mean Absolute Errors (MAE) were calculated for each image by using the identified targets and finding the difference between the ground truth data (the GCPs) and the same points in the images reconstructed from the three methods. In an individual image, at least four GCPs were used to calculate the MAE. An overall average was then calculated for all the MAE measured.

The MAE calculated for each test were 0.14m,1.55m and 18.93m for BA with

GCPs, BA with no GCPs and DG respectively. These results indicate that both BA methods achieved acceptable levels of accuracy for topographic mapping. However, as expected the traditional DG approach exhibited a higher MAE compared to the benchmark method. This result can be attributed to the high tilt images, which accounted for over 50% of the dataset, thus introduced tilt effects that affected the DG results. The minimum MAE error recorded was 2.5m, while the maximum MAE measured was 18.9m. Further analysis was conducted by categorizing the MAE values based on three types of images by (Wolf et al., 2014): nadir/near-nadir, low tilt, and high tilt. The MAE calculated for these categories were 2.4m, 8.9m, and 18.9m respectively. Figure 4.18 shows a line graph that compares the three approaches. Furthermore, Figure 1 in Appendix B provides an alternative representation to enhance the understanding of MAE in relation to the trajectory of the drone.

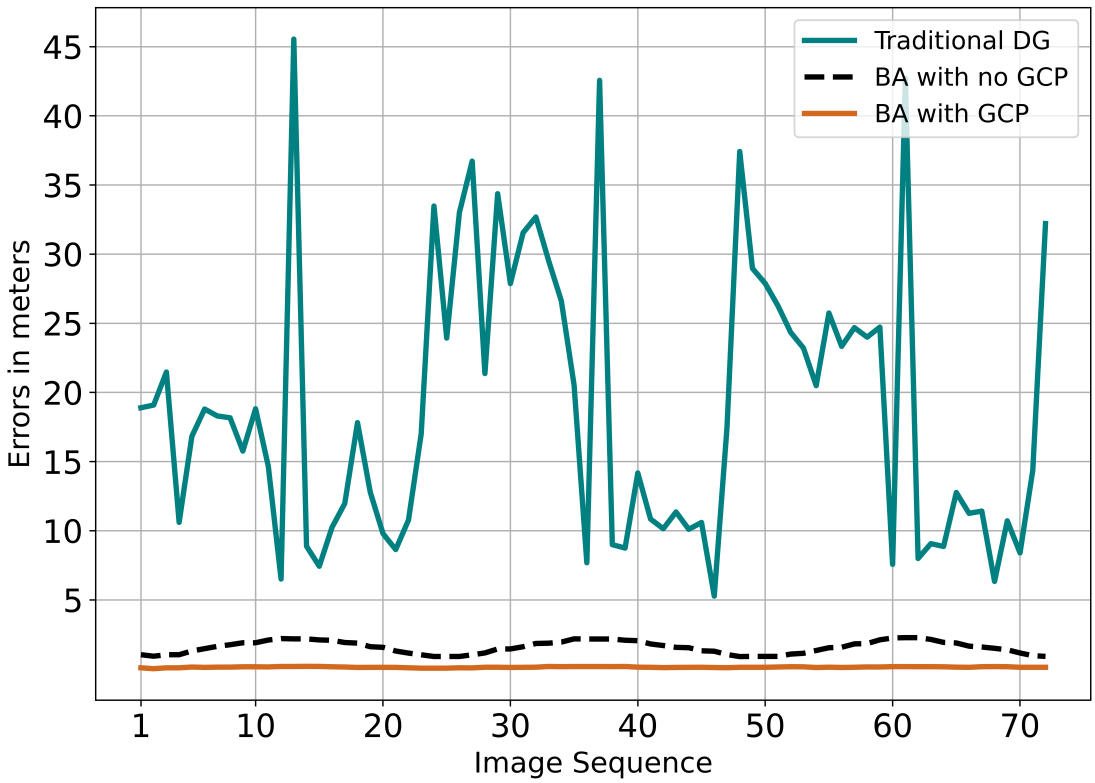

Figure 4.18: Analysis of MAE for positional accuracy using DG before the proposed correction and compares the result to BA with GCPs and BA with no GCPs.

Additionally, to understand the influence of high Pitch and Roll angles on the positional accuracy, a line graph was plotted to juxtapose or overlay the Pitch angle and the MAE. From Figure 4.19, it can be seen that, high MAE directly coincide with periods of high Pitch and Roll angle.

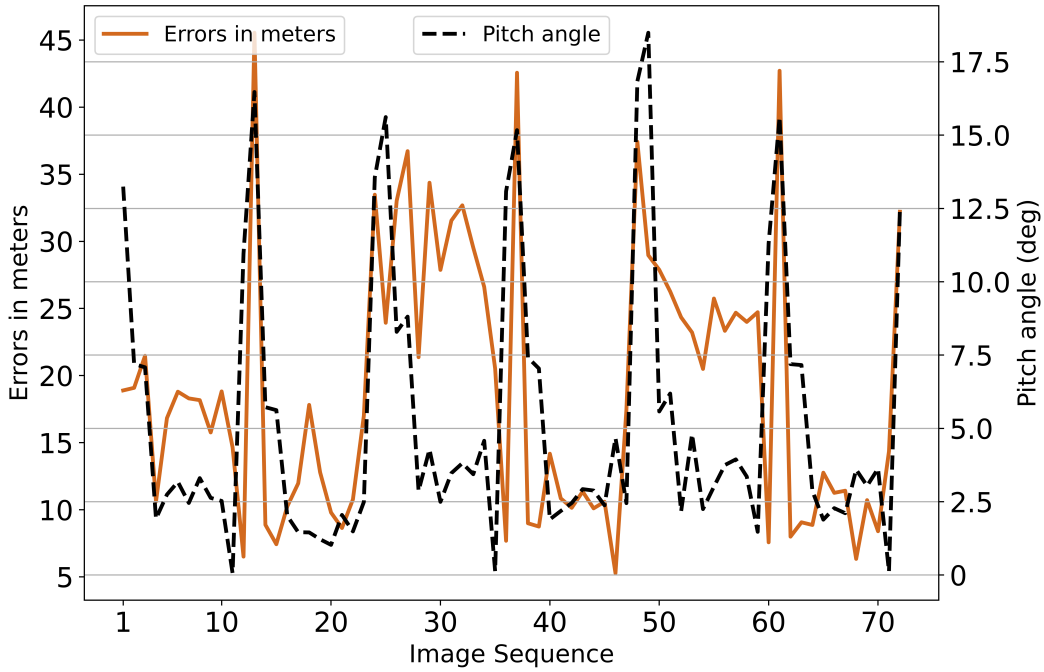

Figure 4.19: Positional accuracy for Direct Georeferencing compared with corresponding Pitch angle. The graph illustrates how high Pitch angles negatively influence positional accuracy.

4.7.6 Accuracy Assessment of the ARMFET Approach

The Traditional DG result was improved by applying the ARMFET method described in Section 4.6.4. From Figure 4.20, it can be seen that the MAE for DG was improved from 18.93m to 9.34m. Furthermore, there was a significant improvement in the standard deviation, decreasing from the traditional DG result of 10.09m to 2.9m. This means that MAE errors are reduced by ARMFET.

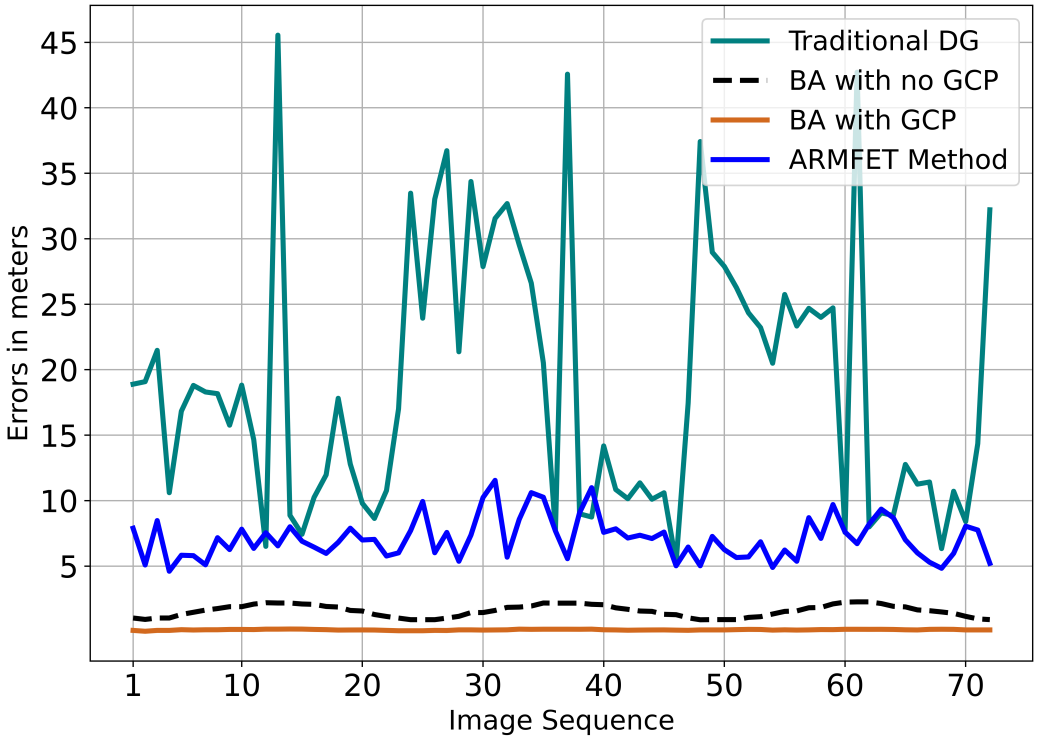

Figure 4.20: Comparison of the positional accuracy for the initial result for DG and after the proposed correction method has been applied. The graph shows the significant improvement between the traditional DG result and the proposed correction method

The ARMFET method proved to be instrumental in reducing the MAE of DG by 53.54%, thus reducing the error by more than half. This approach successfully addressed the tilt and scale effects, resulting in an acceptable MAE. Also, the image rectification helped smooth the peak errors and high tilt angles which were caused by the high Pitch and Roll values during the survey. These findings highlight that images with both low and high tilt angles over featureless terrain can be rectified without the need for GCPs.

4.8 Discussion

The accuracy assessment of the result showed that there was a significant improvement as ARMFET was able to reduce the MAE by 53.54%. This means that by applying the image rectification method, low-cost drones have the potential of producing accurate reconstruction of 2D images over featureless terrain. Over the past few years, the use of low-cost drones for reconstructing 2D images over featureless terrain like water using the DG method has been hindered by inaccurate measurements from their navigational sensors, resulting in low accuracy. This is evident in the traditional DG result, here a positional accuracy of 18.9m was obtained. Similarly, a study by Stam (2010) employing a low-cost drone with the DG method achieved an accuracy of 10-25 meters. This low accuracy hinders the use of reconstructed 2D images for further applications such as water quality monitoring. The benchmarking of the DG method performed in this study has provided valuable insights into the limitations of low-cost drones.

The findings from the result demonstrates the significant impact of the proposed approach on improving positional accuracy. It was observed that removing the errors from tilted images contributed to improving the positional accuracy. Tilted images are known to have errors in image displacement and tilt displacement, which are directly proportional to the angle of tilt (Schofield and Breach, 2007). Therefore, rectifying the images is an important process for removing distortions from images, as explained in Wolf et al. (2014). The results show that ARMFET can potentially make an important contribution to improving positional accuracy. The inclusion of the ARMFET method in the overall image reconstruction process for tilted images can be adopted even for drone surveys over flat featureless terrain such as snow and desert areas and not solely water. ARMFET provides a possible solution to the long-lasting problem of rectifying images over water where it is near impossible to place visible targets as Ground Control Points (GCPs).

Although the ARMFET method is a practical approach for image rectification over water, it does not fully correct the images. For example, the calculations for the tilt displacements are based on the IMU measurements. Therefore, inaccurate estimation of sensor orientation can lead to the calculation of assumed tilt displacements that do not reflect the real ground displacement accurately. Further, one limitation of the the ARMFET method is that it could be laborious if the workflow is not automated through programming language like python, especially if the acquired dataset is large.

4.9 Conclusion

This chapter presented the outcomes of utilizing Direct Georeferencing as an approach for mapping featureless terrain - inland water. An empirical study was conducted to (i) evaluate the accuracy of the DG method using a low-cost IMU/GNSS (ii) analyse the errors associated with DG and (iii) develop a new approach to correcting tilt effects. The findings revealed that errors originating from angular elements had a more pronounced influence compared to those arising from the IMU and GNSS. These results emphasized the significance of addressing angular errors in achieving accurate output. To address this, an improved method was developed to adapt the traditional DG approach. The MAE was reduced from 18.93m to 9.34m, indicating that the proposed methods for rectifying images could achieve acceptable accuracy. These promising results highlight the feasibility of employing low-cost drones for mapping featureless terrains.

In summary, this chapter provided the following contributions:

1. Provided insights into the performance of the DG approach using drones with low-cost GNSS/IMU.

2. Explored the influence of wind speed and direction on attitude angles.

3. Developed an analytical photogrammetry method called ARMFET to im-

prove the traditional DG approach.

This chapter is based on a published peer-review paper: Essel, B.; McDonald, J.; Bolger, M.; Cahalane, C. (2022) INITIAL STUDY ASSESSING THE SUITABILITY OF DRONES WITH LOW-COST GNSS AND IMU FOR MAPPING OVER FEATURELESS TERRAIN USING DIRECT GEOREFERENCING. In: ISPRS eds. International Archives of the Photogrammetry, Remote Sensing and Spatial Information Sciences, Volume XLIII-B2-2022 XXIV ISPRS Congress Nice, France, pp.37-44

Chapter 5

ADGEO - An Assisted Direct Georeferencing Approach

This chapter presents another novel method for improving the accuracy when mapping water bodies known as Assisted Direct Georeferencing (ADGEO). It is an advance on the analytical photogrammetric method in the previous chapter (ARMFET) because it leverages sparsely populated features along the shore to learn and propagate corrections that can refine the images over the water. The method was incrementally developed by creating synthetic data and was validated by using real-world data to analyze ADGEO's performance, analyze the sensitivity of the variables, and identify the limitations. In this chapter, the motivation for this method is explained in the introduction in Section 5.1 and the concept of the ADGEO is explained in Section 5.1.1. The method used for the theoretical analysis is described in Section 5.2.1 and the ADGEO technical development is described in Section 5.3. The results and analysis for this chapter are broadly categorized into theoretical analysis in Section 5.4.1 and 5.4.2 and experimental analysis in Section 5.5. The results are discussed in Section 5.6 and the conclusions in Section 5.7.

5.1 Introduction

In the previous chapter, the ARMFET method demonstrated that when used to correct reconstructed 2D images derived from the traditional DG method, an analytical photogrammtric approach that explores how the image interacts with the ground plane can improve the planimetric accuracy for flat terrain by 50.74%. However, an important limitation of the ARMFET approach is that its accuracy improvement is tied to the accuracy of the attitude angles measured by the IMU. Thus, inaccurate estimation of sensor orientation can lead to the calculation of assumed tilt displacement corrections that do not accurately reflect the real displacement of a point on the ground. Therefore, to further close the gap between low-cost drones and high-end drones, the novel research in this chapter will explore whether it is possible to combine the advantages of both DG and BA in an established photogrammetric technique known as Integrated Sensor Orientation (ISO).

In photogrammetry, ISO is a well-known technique that combines both BA and DG methods to process block of images (Heipke et al., 2002; Ip, 2005; Tanathong and Lee, 2014). The ISO approach has been widely used in photogrammetry to achieve high accuracy and reliable results but importantly, ISO reduces the need for a large number of GCPs (Mitishita et al., 2016). It does this by relying on DG for much of the block, but will have a sparse network of GCPS distributed around the edges of the survey area, generally at the end of the flight lines as demonstrated in Section 2.10. The ISO technique is able to perform better than the traditional DG method, (Ip et al., 2007; Mitishita et al., 2016) because it uses GCPS to carry out the BA to refine the sensor orientation but includes the object position estimates from DG. Because the DG method relies solely on the accuracy of the GNSS/IMU, the ISO technique has been shown to improve the accuracy of reconstructed drone imagery, even those with low-cost GNSS/IMU (Tanathong and Lee, 2014). Thus, the ISO technique can improve the accuracy of low-cost drones because it is not as dependent on the accuracy of the GNSS/IMU as the

DG method. This means that even if the GNSS/IMU measurements are of low accuracy, the ISO technique can still help to improve the results. The problem with the ISO method is that it requires a sparse network of GCPs (Heipke et al., 2002), but, as previously established, fixing visible targets over water is impractical. Therefore, in this chapter, the aim is to combine the strengths of both the DG and the BA methods in an adaptation of the ISO workflow for image reconstruction for mapping water bodies.

The novel concept behind the third objective of this thesis is that this approach utilizes the BA method in feature-rich segments of the survey area, such as the shore, and then uses that as a reference to apply and constrain the DG for featureless areas, such as water. In brief, the BA can both be used to first reconstruct images over the shore and then to propagate corrections, thereby refining the accuracy of the images over the water. ADGEO is primarily intended for case studies where the shore is in view during parts of the survey - which generally can be expected for surveys of water bodies.

A theoretical assessment was first conducted to help develop this method. Theoretical assessments serve as a valuable procedure for quantifying the capabilities of the model (Yuan and Zhang, 2008). It allows definitions of assumptions, helps improve model accuracy and identifies limitations and constraints. This process lends itself to refining the model and enhancing reproducibility, providing a solid foundation for further implementation and validation of the proposed method to practical and real-world scenarios. Therefore, this chapter seeks to test the ADGEO method using real-world data to investigate the viability of this concept. Hence, the objectives of this chapter were to:

1. Develop the ADGEO method by explaining the assumptions and the underlying mathematical model.

2. Theoretically assess the accuracy of the ADGEO method using synthetic data.

3. Evaluate the performance of the ADGEO method under different scenarios using real-world drone data.

4. Identify and provide an analysis of the strengths and limitations of the ADGEO method.

5.1.1 Overview and Assumptions of the ADGEO Method

The aim of the ADGEO method is to improve the accuracy of reconstructed 2D images for mapping water bodies by using features from the shore and combining the benefits from both DG and BA. The DG approach is used to project all the images over the water surface onto the ground plane using the IMU/GNSS, and the BA approach is used to refine EOPs to reconstruct only the images with the shore in view. For the purposes of this thesis, the term "shore" will be used to refer to any land that lies along the edge of a lake, river, or sea. This land in a broader sense could be understood as artificial surfaces, or natural features such as sand, shingles, larger stones and vegetation.

The workflow for this method began with data acquisition as seen in Figure 5.6. The second stage involved automatically sorting the images by grouping them into two categories: images that had a part of the shore in view and images without any shore in view. The third step was to reconstruct all images with the shore in view using any method or software that utilizes BA such as PIX4D, Agisoft Metashape etc. Following this, a separate image reconstruction was performed for all images over the water without shore in view by using the DG method. Step 5 calculated the offset errors at known points for the shore images by calculating the difference between BA and DG. These offset errors were then used to predict the errors for an image over the water using the mathematical model developed in Section 5.3.2. The predicted errors were used to calculate the predicted coordinates for a point over the water without the shore in view. The final step was to perform an image transformation between the predicted coordinate point and the observed coordinate point.

The fundamental assumption that underpins this approach is the presence of a shore in the survey area. Since drone surveys over water are typically carried out close to the shore due to operational and line-of-sight restrictions (Román et al., 2023), the ADGEO requirement for a shore in view is therefore applicable for many water scenarios. For instance, EU aviation regulations mandate that drones operating under open category operate within visual line of sight (European Union Aviation Safety Agency, 2019), which often requires setting up the drone survey at the shore and monitoring the drone's flight from that vantage point. Another important assumption is that the drone must fly out and return to the shoreline during its flight trajectory. This way, the shore remains constantly in view during the data acquisition process, ensuring that each flight line will have at least one image captured with the shoreline in view (start and end of the flightline).

5.2 Data

This section explains all the data used in the initial theoretical design and analysis. Firstly, it explains how the synthetic dataset used for the theoretical analysis was generated in Section 5.2.1. The synthetic data was generated for two scenarios: low variability and high variability. The low variability simulated data defines a scenario where a drone encounters ideal flying conditions and exhibited low variability in IMU measurements during the period and is detailed in Section 5.2.2.1, while those with high variability describe strong wind conditions and are in Section 5.2.2.2. The following section details the dataset used.

5.2.1 Overview of the Method in Generating the Synthetic Data

The synthetic data generated in this chapter were used in place of real-world data to help develop the concept, assess the model's accuracy and identify any constraints and limitations. Synthetic data in this thesis can be considered to

refer to artificially generated data that mimics a real-world image (Jordon et al., 2022). Instead of capturing data directly from the physical environment, this synthetic data is created using computer graphics techniques. These synthetic datasets are designed to closely resemble real-world data, allowing computer vision models to be trained and evaluated on a larger and more diverse set of examples (Lu et al., 2021). Synthetic data allows researchers and practitioners to generate large datasets and introduce diverse variations, which can be helpful in scenarios where real data is scarce or difficult to obtain (Jordon et al., 2022). This is very useful for a study exploring the accuracy of a photogrammetric method for water bodies - due to the inability to place GCPs in the water for assessment and survey these using traditional GNSS RTK.

All synthetic images were created using a Python environment. The process of generating synthetic data using Python typically involves using various image processing and computer vision libraries, such as OpenCV, NumPy, and Python Imaging Library (PIL). These libraries provided tools and functions that were used to generate synthetic images by manipulating existing images and creating new images. For the theoretical evaluation, forty (40) synthetic images were created for each of the two scenarios: low variability and high variability attitude measurement. Out of these, five images were defined as those that would have the shore in view (to be used by the BA method), while the remaining images represented the majority of the drone survey over a featureless water environment with no shore in view where DG would apply. Additionally, each synthetic image was overlaid with grid lines using Python's image processing libraries such as OpenCV, which provide functions to draw lines, shapes, and other elements on images. Grid lines are commonly used in image processing for various purposes, such as image alignment, object detection and measurement. In this case, the grid lines were added as a visual aid in assessing the accuracy and image misalignment.

Figure 5.1 shows the design of a survey with 5 flight lines that were simulated in a standard grid pattern. This design distinguishes between those images that had a shore in view and those that had no shore in view. It is important to note that this method mandates that the drone flies out and returns to the shore during the survey. Table 5.1 describes the sensor parameters used to define the sensor during the synthetic image creation.

Table 5.1: The Parameters Used for Generating the Synthetic Images for the Grid Survey in Figure 5.1.

Parameters	**Value**
Focal length	3.98 mm
Image size	1280×960 pixel
Sensor size	4.8mm×3.6mm
Principal point	2.4mm×1.81mm
Flight height	120m

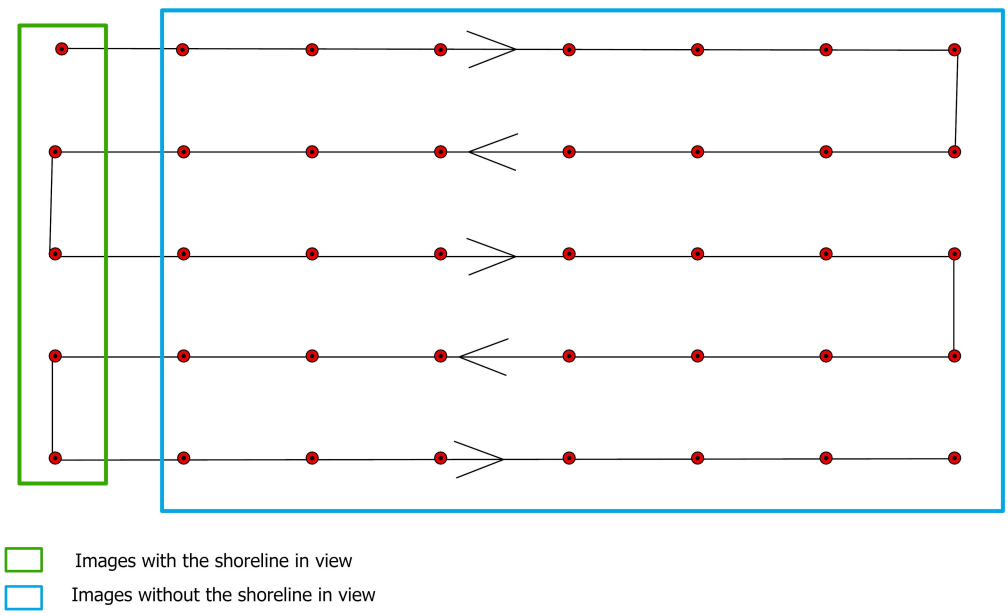

Figure 5.1: The flight plan for the synthetic data. The green boundary line shows simulated images with the shore in view and the blue boundary line shows simulated images captured over the water surface and without shore in view. Note the requirement for alternate flight lines to begin/end at the shore - a necessity for ADGEO

5.2.2 Description of the Simulated Attitude Data

The low variability attitude data was generated for situations where there are relatively stable flight conditions, and the high variability attitude data was for situations such as high wind speed. Table 5.2 gives an overview of the two sets of simulated data for the variables that were identified in Section 3.4.1 as having the greatest influence on DG accuracy, namely - Pitch and Roll. The mean, standard deviation, kurtosis, and skewness were reported for each variable for both datasets.

Table 5.2: Statistical Analysis of the Simulated Attitude Data

Item Description	**1st Simulated Data**		**2nd Simulated Data**	
	Pitch	**Roll**	**Pitch**	**Roll**
Mean	1.80^o	2.07^o	5.21^o	6.02^o
Std Dev.	0.61	0.63	4.61	6.01
Kurtosis	-0.31	-0.62	-1.24	-1.13

5.2.2.1 Attitude Data I - the Low Variability Scenario

In this study, a "low variability attitude measurement" refers to rotational angular measurement in Pitch and Roll that has little/minimal variation. Essentially, it represents instances where the sensor remains stable, resulting in consistent readings without any significant deviations. In practice, this would be a low wind-speed scenario.

In the first scenario, 54% of the images were classed as nadir or near-nadir, while the remaining 46% were categorized as low tilt images as previously defined in Chapter 4 section 4.2.1. The mean values for the Pitch and Roll angles in this low variability dataset were calculated at 1.8^o and 2.07^o respectively. The standard deviation was 0.61^o and 0.63^o in Pitch and Roll respectively. This is shown in Figure 5.2 where an error bar was plotted to show each measured data and how it deviates from the mean. The graph showed that only a few of the data points had high standard deviations depicted in longer error bars, while the majority of the data points had low standard deviations. This suggests that the data are

correlated, indicating little variation in the measured attitude angle.

Further, the kurtosis was measured to understand the tailedness of the data distribution. A higher kurtosis indicates that the data distribution has a more peaked shape, with more outliers. In this simulation, the calculation showed a low kurtosis as shown in Table 5.2 above. The low kurtosis indicated that the attitude values were relatively consistent and not prone to extreme variations, making it suitable for analysis under low variability conditions.

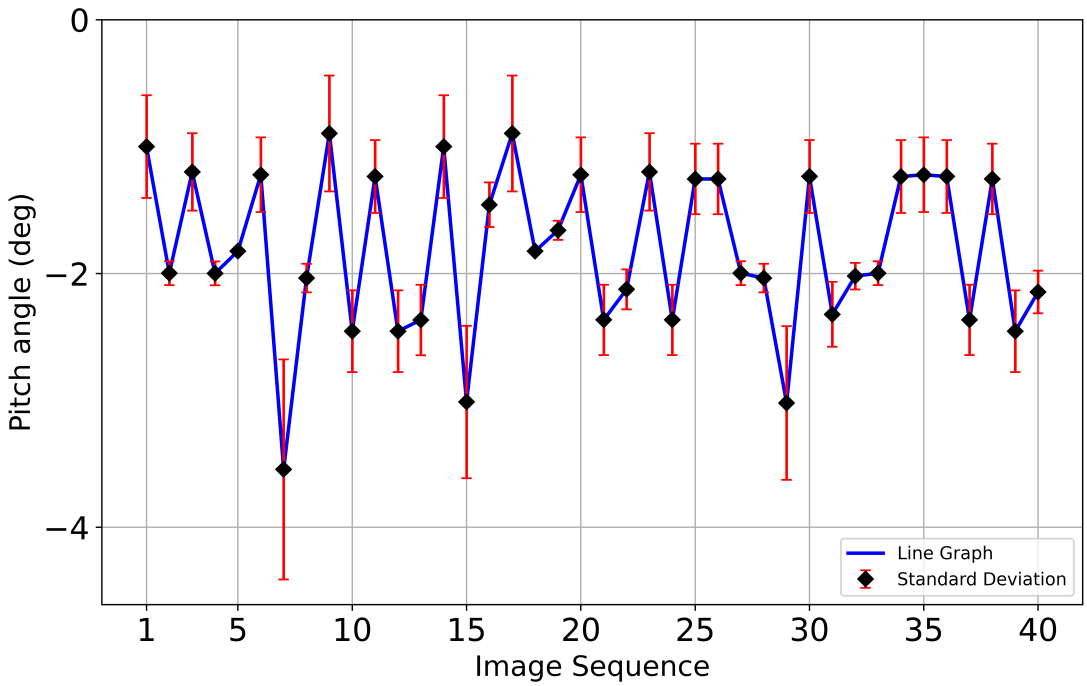

Figure 5.2: A graph showing the Pitch angles and standard deviation represented as error bars for the low variability simulated data. The longer the error bar, the higher the standard deviation.

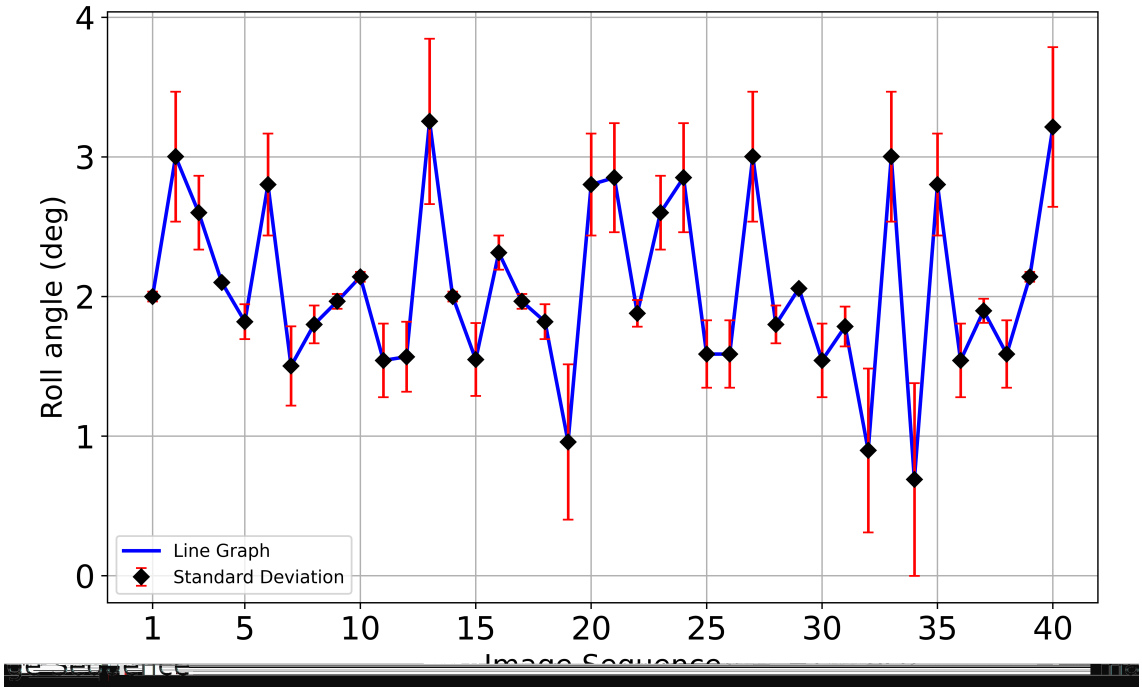

Figure 5.3: A graph showing the Roll angles and standard deviation represented as error bars for the low variability simulated data. The longer the error bar, the higher the standard deviation.

5.2.2.2 Attitude Data II -the High Variability Scenario

Another simulation was done to create a dataset with high attitude variability. A high variability attitude measurements refers to the rotational angular measurement in Pitch and Roll that have significant variation. In real-world scenarios, high variability measurements often result from factors like strong winds and high flight speeds. These conditions lead to unevenly distributed attitude data. For this simulation, 14 % of the images were considered as nadir/near-nadir images, 24% were low tilt and 46 % were high tilt images. The mean Pitch and Roll were measured at 5.21^o and 6.02^o respectively. The standard deviation was measured at 4.61^o and 6.01^o for Pitch and Roll respectively, which indicates a significant range of angular variations experienced and therefore approximates a typical high variability scenario for a drone flight in medium to high wind conditions. This is shown in Figure 5.4 and 5.5, where error bars are plotted to illustrate the degree to which each data deviates from the mean. This shows that the majority of the data points had higher standard deviations while only a few had

low standard deviations. The kurtosis measured was high, indicating extreme values or more outliers in the attitude measurement. This explains situations where the drone is not stable during the flight, resulting in IMU readings that are more prone to deviations from the expected value. Hence, making a suitable representation for analysis under high variability conditions.

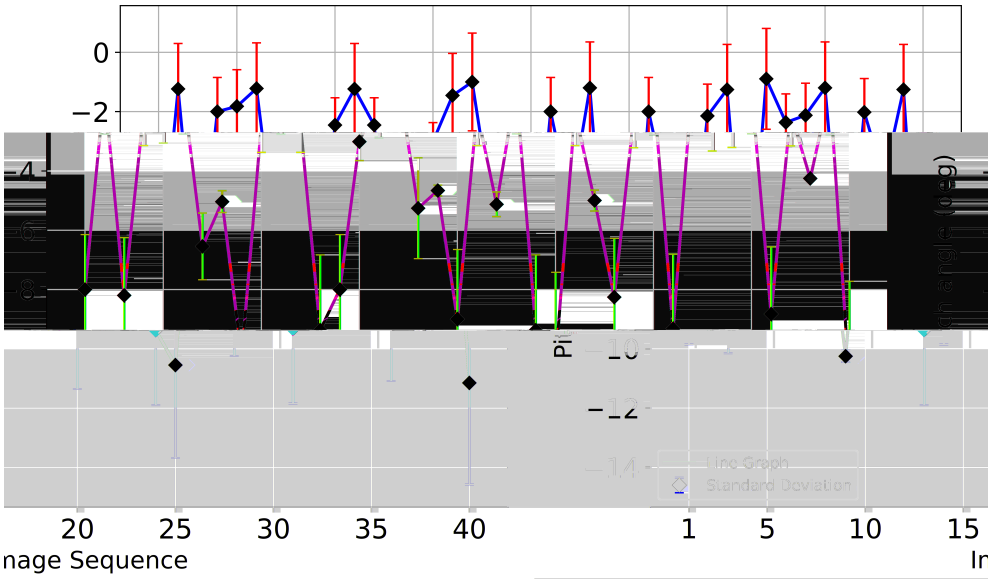

Figure 5.4: A graph showing the Pitch angles and standard deviation represented as error bars for the high variability scenario. The longer the error bar, the higher the standard deviation.

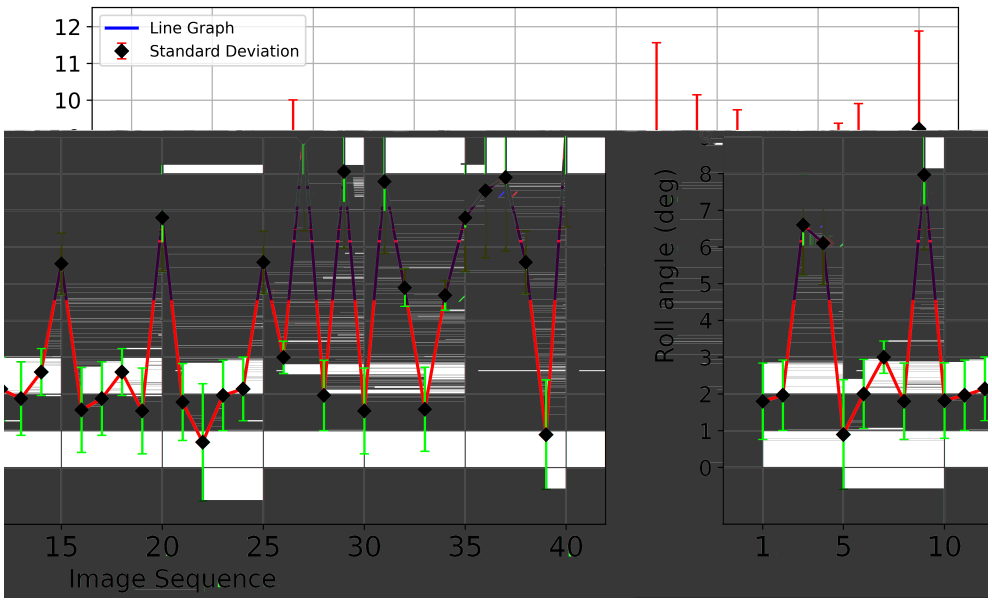

Figure 5.5: A graph showing the Roll angles and standard deviation represented as error bars for the high variability scenario. The longer the error bar, the higher the standard deviation.

5.2.3 Validation Dataset

The importance of incrementally validating a theoretical model during development cannot be over-emphasized. A detailed description of the dataset used to validate the ADGEO method can be found in Chapter 4, Section 4.5.1. This section describes the real-world drone datasets and the GCPs acquired from the Enfiel survey. The validation dataset was used to test ADGEO method under two different scenarios as described in Section 5.5.1.

5.3 Method

This section explains the step-by-step process involved in developing and implementing the ADGEO approach. The workflow is broadly broken down into three main steps. The first step in Section 5.3.1 explains the calculation of the offset errors for images with the shore in view. The second step explains the prediction of offset errors for images over the water in Section 5.3.2. The last step explains the image transformation process that was used to carry out the final correction of the image. The entire workflow is illustrated in Figure 5.6, where the detailed step-by-step process is explained.

Figure 5.6: A flow diagram showing the novel ADGEO process of improving the accuracy by combining BA and DG. It illustrates the three main stages - moving from image acquisition to image transformation. The stages in yellow shows the novel steps developed to improve accuracy

5.3.1 Step 1: The Shore - Calculation of Offset Errors

In ADGEO, the offset errors were first determined from the images with the shore in view by finding the cartesian XY difference between the DG and the BA at a given point on the reconstructed 2D image. The offset errors were then calculated and used to improve the accuracy of all images that do not have the shore in view. The main aim of the ADGEO method is to improve the positional accuracy by using the offset errors calculated from images over the shore to refine the accuracy of images without the shore in view. Figure 5.7 highlights the steps involved, proceeding from image projection through to the calculation of the offset errors. Details and explanations of the DG workflow for image reconstruction from the object to sensor $(\boldsymbol{M}_{ext})$, sensor $(\boldsymbol{M}_{proj})$ and image $(\boldsymbol{M}_{image})$ coordinate system can be found in Equation (5.1),(5.2) and (5.3) respectively.

Figure 5.7: An illustration showing the steps and their mathematical equations used from the image projection process to calculating the offset error between Bundle Adjustment and Direct Georeferencing

In Equation (5.1), $(\boldsymbol{M_{ext}})$ is a transformation matrix that converts a point from the object coordinate system into the camera coordinate system by rotation and translation. The extrinsic rotation matrix is represented as $(\boldsymbol{M_{m11-m33}})$ and the location is represented as $(\boldsymbol{t_x}, \boldsymbol{t_y}\ \boldsymbol{t_z})$. The $(\boldsymbol{M_{proj}})$ is a perspective projection that converts a point from the camera coordinate system to the sensor coordinate system on a 2D plane as shown in Equation (5.2). The focal length is denoted as (f) and principal point is denoted as $(\mathbf{C}_x, \mathbf{C}_y)$. The $(\boldsymbol{M_{image}})$ represent a transformation matrix that converts a point from the sensor coordinate system into the image coordinate system as shown in Equation (5.3). The $(\boldsymbol{M_r})$ represent the residual/offset errors in a matrix as shown in Equation (5.4). In the diagram above, the offset error at a given point is denoted by $(\boldsymbol{\Delta X_r}, \boldsymbol{\Delta Y_r})$ in the image coordinate system and is calculated by finding the difference between BA which is denoated by $(\boldsymbol{X_{BA}}, \boldsymbol{Y_{BA}})$ and the DG which is represented as $(\boldsymbol{X_{DG}}, \boldsymbol{Y_{DG}})$. In a given single image, the offset errors can be calculated for at least four points with an even distribution across the image. The offset errors can only be calculated for images with the shore in view. This is because identifiable ground features are needed to calculate the difference in errors between the DG and the BA. Equation (5.2) below details the formula for calculating the offset errors.

$$M_{\text{ext}} = \begin{pmatrix} m_{11} & m_{12} & m_{13} & t_x \\ m_{21} & m_{22} & m_{23} & t_y \\ m_{31} & m_{32} & m_{33} & t_z \\ 0 & 0 & 0 & 1 \end{pmatrix} \tag{5.1}$$

$$M_{\text{proj}} = \begin{pmatrix} f_x & 0 & C_x & 0 \\ 0 & f_y & C_y & 0 \\ 0 & 0 & 1 & 0 \end{pmatrix} \tag{5.2}$$

$$M_{\text{image}} = \begin{pmatrix} f_x & 0 & C_x & 0 \\ 0 & f_y & C_y & 0 \\ 0 & 0 & 1 & 0 \end{pmatrix} \begin{pmatrix} m_{3\times3} & t_{3\times1} \\ 0_{1\times3} & 1_{1\times1} \end{pmatrix} \begin{pmatrix} X_w \\ Y_w \\ Z_w \\ 1 \end{pmatrix} \tag{5.3}$$

$$M_{\mathrm{r}} = \begin{pmatrix} \Delta X_r \\ \Delta Y_r \end{pmatrix} = \begin{pmatrix} X_{BA} \\ Y_{BA} \end{pmatrix} - \begin{pmatrix} X_{DG} \\ Y_{DG} \end{pmatrix} \tag{5.4}$$

5.3.2 Step 2: The Water - Prediction of Offset Errors

Importantly, the offset errors cannot be calculated over the water using the approach in section 5.3.1 due to the absence of features. Thus, the practical option is to use the shore to measure the offset errors. Building on Equation (5.4), a prediction model was developed to predict the offset errors for those images without identifiable features. ADGEO proposes an innovative approach that uses the offset errors measured from those images that have the shore in view to create a prediction model that can estimate the errors for all subsequent images over water (i.e. without features). The dependent variables required are the (i ii) attitude angles in Roll and Pitch (from the low-cost IMU), (ii) the initial coordinate of a given point (from a low cost GNSS) and (iv) the offset errors derived from earlier images with the shoreline in view.

Figure 5.8 explains the steps involved from image projection to developing the prediction model. From Equations (5.5) and (5.6), A represents an image from the shore with Pitch and Roll values denoted as θ_{SL} and φ_{SL} and (P_w , P_h) denoted as the coordinate of a point measured in the image coordinate system. B represents a transformation matrix with θ_{FT} and φ_{FT} denoted as Pitch and Roll values for an image without a shore in view, and $(\Delta X_r$, $\Delta Y_r)$ representing the residual/offset error at a given known point calculated from images with the shore in view. From Equation (5.7), X represents the unknown offset error from an image without features (no shore in view) and is represented as $(\Delta A_U$, $\Delta B_U)$. In Equation (5.8), an inverse matrix is used to predict the unknown offset errors at a given point in an image without features to derive Equation (5.9). The predicted offset error is added to a measured point at a given location to derive the

predicted coordinate values which is denoted as $\boldsymbol{X}'$ and $\boldsymbol{Y}'$ as shown in Equation (5.10). This then gives a new planimetric position of a given point in which the true position of that point has been predicted. The unknown offset errors can be calculated using a minimum of four points, which are evenly distributed across the image. The next step is to perform an image transformation as represented in Equations (5.11) and (5.12). The image is transformed using the original location of a given point in conjunction with the predicted coordinate point via affine transformation. The transformed coordinate after the affine transformation is denoted as $\boldsymbol{X1}'$ and $\boldsymbol{Y1}'$ and is derived from A, B, C, D, E, and F which are determined by comparing the location of source and predicted point and the x and y which are the coordinates generated from the predicted model. In the final stage, this affine transformation method warps the image to the true position of the image in a predefined coordinate system.

$$A = \begin{pmatrix} \theta_{SL} & \varphi_{SL} & P_w \\ \theta_{SL} & \varphi_{SL} & P_h \\ 1 & 1 & 1 \end{pmatrix} \tag{5.5}$$

$$B = \begin{pmatrix} \theta_{FT} & \varphi_{FT} & P_w \\ \theta_{FT} & \varphi_{FT} & P_h \\ 1 & 1 & 1 \end{pmatrix} \begin{pmatrix} \Delta X_r \\ \Delta Y_r \\ 1 \end{pmatrix} \tag{5.6}$$

$$X = \begin{pmatrix} \Delta A_U \\ \Delta B_U \\ 1 \end{pmatrix} \tag{5.7}$$

$$\begin{pmatrix} \theta_{SL} & \varphi_{SL} & P_w \\ \theta_{SL} & \varphi_{SL} & P_h \\ 1 & 1 & 1 \end{pmatrix} \begin{pmatrix} \Delta A_U \\ \Delta B_U \\ 1 \end{pmatrix} = \begin{pmatrix} \theta_{FT} & \varphi_{FT} & P_w \\ \theta_{FT} & \varphi_{FT} & P_h \\ 1 & 1 & 1 \end{pmatrix} \begin{pmatrix} \Delta X_r \\ \Delta Y_r \\ 1 \end{pmatrix} \tag{5.8}$$

$$\begin{pmatrix} \Delta A_U \\ \Delta B_U \\ 1 \end{pmatrix} = \begin{pmatrix} \theta_{SL} & \varphi_{SL} & P_w \\ \theta_{SL} & \varphi_{SL} & P_h \\ 1 & 1 & 1 \end{pmatrix}^{-1} \begin{pmatrix} \theta_{FT} \cdot \Delta X_r + \varphi_{FT} \cdot \Delta Y_r + P_w \cdot 1 \\ \theta_{FT} \cdot \Delta X_r + \varphi_{FT} \cdot \Delta Y_r + P_h \cdot 1 \\ \Delta X_r + \Delta Y_r + 1 \end{pmatrix} \tag{5.9}$$

$$\begin{pmatrix} X' \\ Y' \\ 1 \end{pmatrix} = \begin{pmatrix} \Delta A_U \\ \Delta B_U \\ 1 \end{pmatrix} + \begin{pmatrix} X \\ Y \\ 1 \end{pmatrix} \tag{5.10}$$

$$X_1' = Ax + By + C \tag{5.11}$$

$$Y_1' = Dx + Ey + F \tag{5.12}$$

Figure 5.8: An image showing the image projection process, the offset error calculated between BA and DA, the prediction of the offset errors and the final affine transformation of the image.

5.4 Results and Analysis

This section presents the results obtained for both the theoretical and the experimental analysis. Section 5.4.1, validates the theoretical analysis by first assessing the accuracy of the simulated low variability dataset. This was followed by assessing the models's accuracy in Section 5.4.1.2 under low variability. In Section 5.4.2, the second theoretical analysis, which included accuracy assessment and model accuracy, was carried out for the high variability dataset. Additional analysis was conducted on sensitivity analysis of the variables in Section 5.4.3. For more robust testing, experimental analysis was conducted in Section 5.5 using the real-world data introduced in Section 4.5.3 that approximates a pure planar surface such as a water body. This analysis included an accuracy assessment of the two scenarios in Section 5.5.1, inter-rater reliability analysis of the two scenarios in Section 5.5.3 and analysis of the influence of overlapping percentage in Section 5.5.4.

5.4.1 Theoretical Analysis 1: Low Variability Attitude Measurement

5.4.1.1 Planimetric Accuracy Assessment

The theoretical assessment was conducted using the synthetic dataset. The analysis began by reconstructing the images using the traditional DG approach as shown in Figure 5.9. The initial outputs of the DG approach revealed misalignments in the grid lines, indicating a relatively low level of accuracy in the reconstructed images. The resulting MAE measured for the traditional DG was 5m. To improve the accuracy, the ADGEO method was subsequently employed to refine the reconstructed 2D images, as shown in Figure 5.10. A cursory evaluation of the outputs between the DG and ADGEO approaches suggests considerable improvements in geometric accuracy for the latter. In Figure 5.10, the grid lines exhibit better alignment, signifying an improvement in the accuracy of the reconstructed images. The resulting MAE obtained was 2.2m, indicating a significant

improvement when compared to the initial DG results. The visual comparison of the two approaches in Figures 5.9 and 5.10 clearly illustrated the effectiveness of the ADGEO approach in improving accuracy.

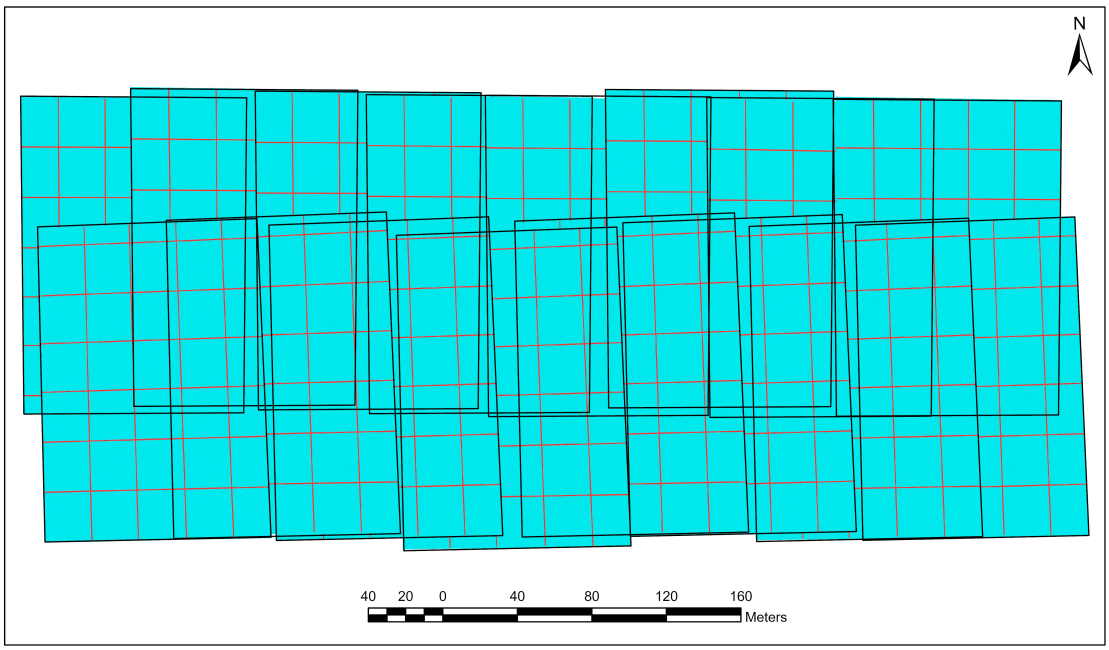

Figure 5.9: Initial results for the low variability scenario of the reconstructed 2D images using the traditional DG approach with grid lines overlaid to aid in visual analysis. The results show significant misalignment in the grid lines.

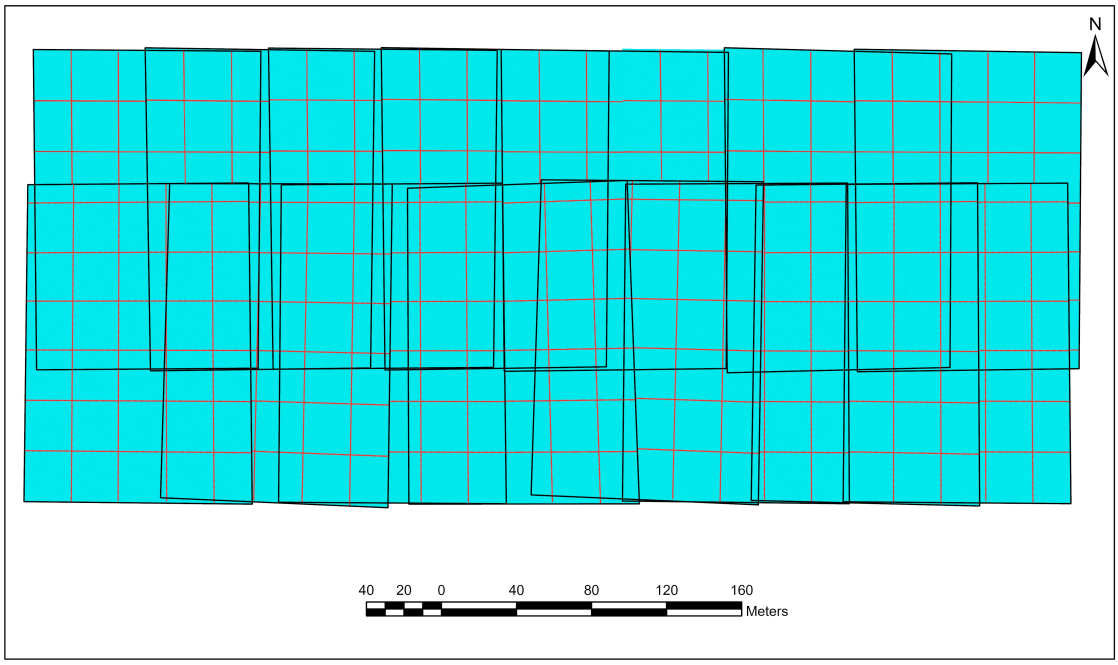

Figure 5.10: ADGEO results for the low variability scenario of the reconstructed 2D images with grid lines overlaid to aid in visual analysis. The result showed significant improvement in the grid lines.

5.4.1.2 Accuracy Assessment of the ADGEO Method - Low variability

Model accuracy assessment is an important step in evaluating the performance and reliability of any proposed model (Teppati Losè et al., 2021). In this study, the widely accepted linear regression method was applied to assess the accuracy of the ADGEO method. The coefficient value provides valuable insights into the degree of correlation between the predicted and observed values. The observed values were derived by reconstructing images that were derived from perfectly vertical position. This was to ensure that there were no tilt distortions in the reconstructed 2D images. This provided the best approximation of an image without corrections.

Analysing ADGEO's performance in the low variability scenario using the R-squared method revealed a high value of 0.93 as shown in Figure 5.11. This result signifies a strong correlation between the predicted and observed values, indicating the model's robustness and reliability if used processing imagery captured during low wind conditions.

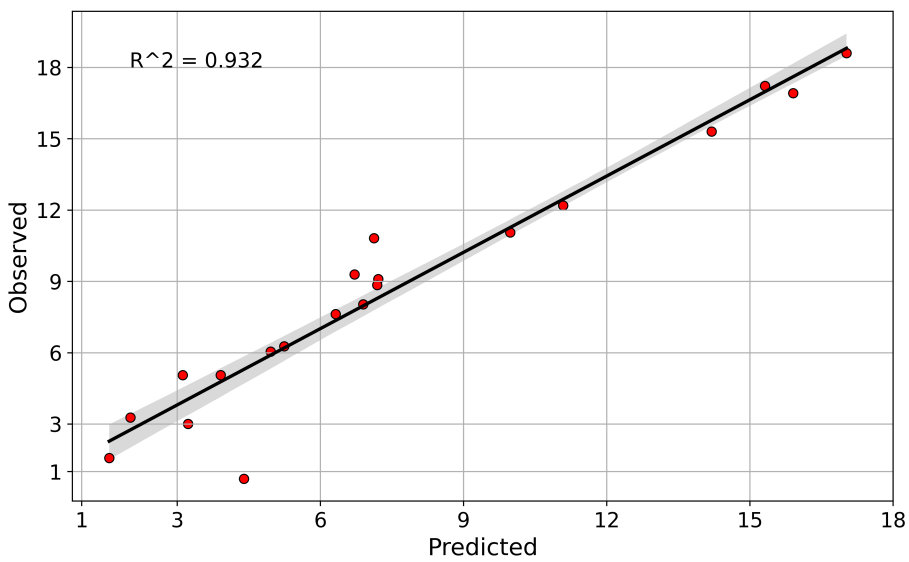

Figure 5.11: Assessment of the model's accuracy under low variability attitude measurement.

5.4.2 Theoretical Analysis 2: High variability Attitude Measurement

5.4.2.1 Planimetric Accuracy

The performance of the ADGEO method was also tested to assess its ability to handle noisy measurements. This was done to simulate real-world scenarios where strong winds or high flight speeds could affect the readings from the IMU. To evaluate the performance of ADGEO method under these challenging conditions, a second simulated dataset was generated as described in Section 5.2.1. This enabled analysis of the method's tolerance for high variability attitude measurements, which is important for understanding the consistency and accuracy of the method's results and applicability for real-world environments.

To assess the accuracy, both the DG approach and the ADGEO method were tested using a simulated dataset following the procedure described in Section 5.2.1. The analysis of the results revealed that the DG approach produced a MAE of 11.1m, while the ADGEO method achieved a MAE of 9.8m. Thus, the ADGEO method was able to improve the accuracy by approximately 12% but suggests that there was no significant improvement in the accuracy as in the low-variability tests. Further, it was evident from visual examination of the reconstructed images in Figure 5.12 and 5.13 that improvement in the alignment of the grid lines was not as apparent as the tests in the preceding section. These results imply that the accuracy derived from the ADGEO method was constrained by the noisy measurement.

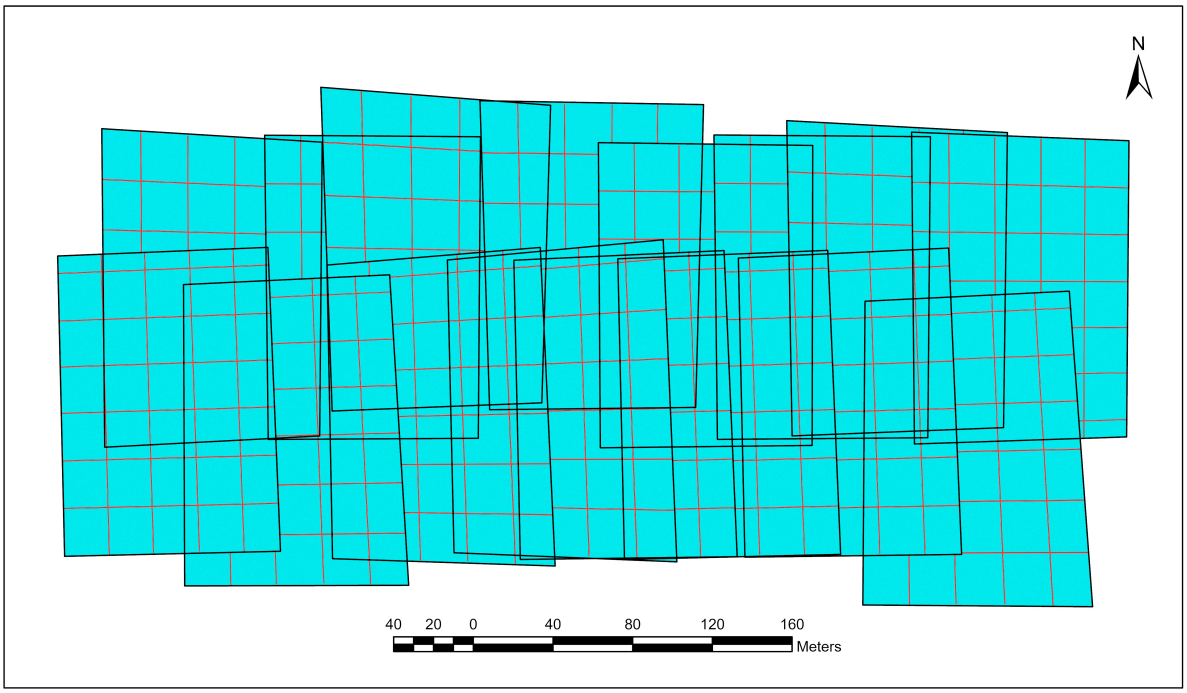

Figure 5.12: An illustration of initial results of the reconstructed images using the traditional DG approach with overlaid grid lines under high variability measurement.

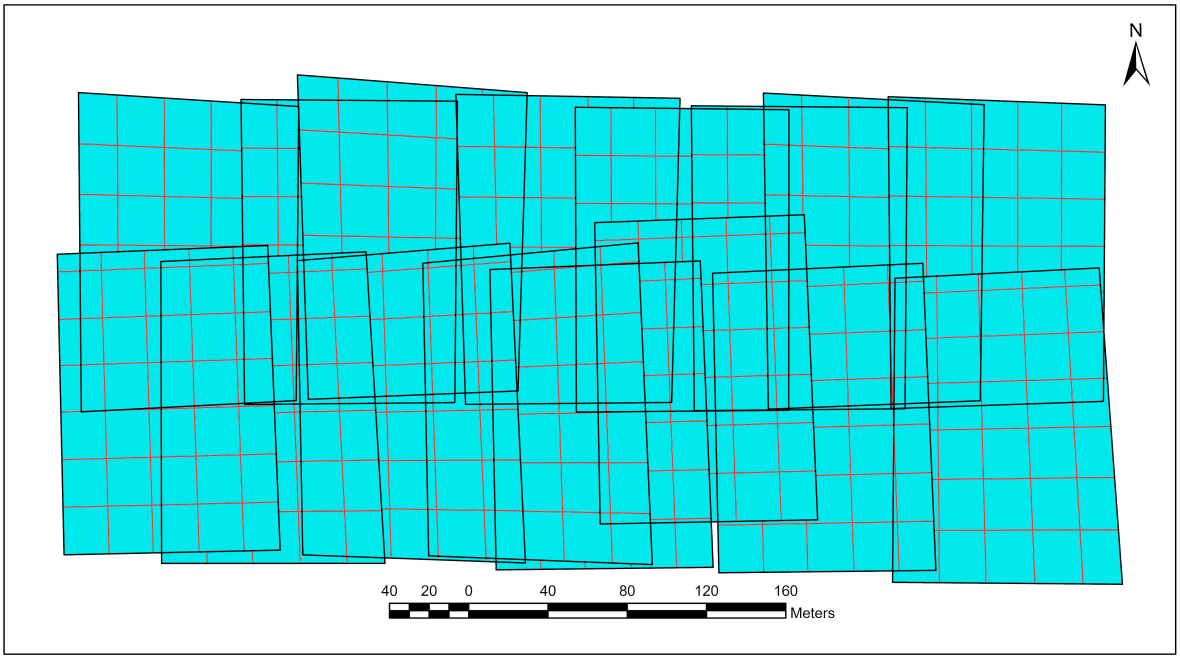

Figure 5.13: An image of the initial results of the reconstructed images using the ADGEO method with overlaid grid lines under high variability measurement.

5.4.2.2 Accuracy Assessment of the ADGEO Method - High Variability

A model accuracy assessment was also carried out to help evaluate the performance and reliability of the proposed model in the high variability scenario. From the analysis of Figure 5.14, an R-squared value of 0.028 was obtained, indicating a weak correlation between the predicted and observed values. This finding suggests that the ADGEO encounters challenges in effectively handling noisy measurement conditions. The low R-squared value signifies that only a minimal portion of the variability in the observed data is explained by the model's predictions.

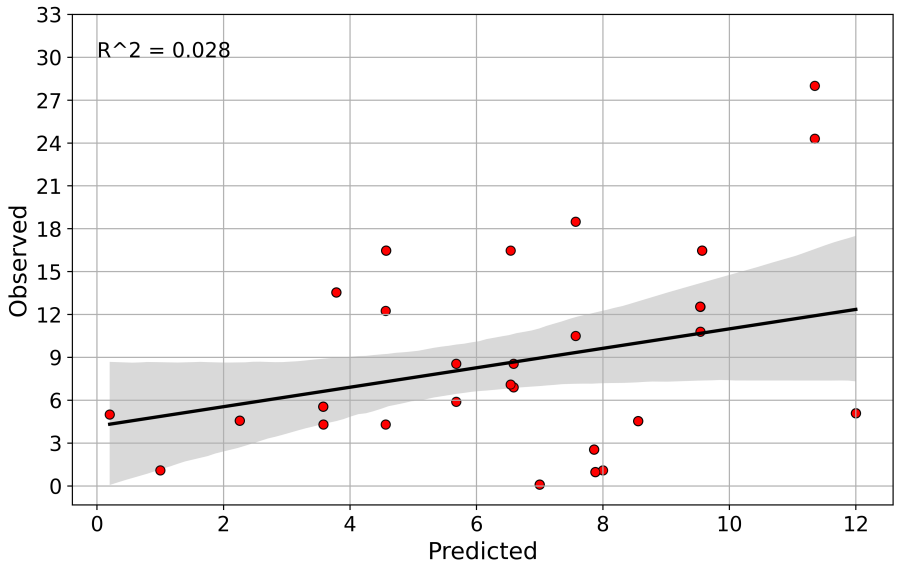

Figure 5.14: Assessment of the model's accuracy under High variability attitude measurement.

5.4.3 Sensitivity Analysis

A sensitivity analysis was also performed - these sensitivity values indicate the magnitude of change in the method's predicted output in response to a unit change in the corresponding input variable. The results in Table 5.3 provide important insight into how the proposed method responds to changes in these input variables. Specifically, the sensitivity value for Pitch and Roll was found to be 0.6, while the sensitivity value for the point location variable was 0.2. A sensitivity

value of 0.6 for Pitch and Roll implies that even a small change in the values of these variables would result in a relatively larger change in the predicted output of the model. This suggested that Pitch and Roll were highly influential factors in determining the accuracy and reliability of the model's predictions. Any variations or errors in the measurements of Pitch and Roll could significantly impact the model's output, highlighting the need for surveys during low variability conditions.

Table 5.3: Sensitivity analysis of the input variables for the ADGEO method

Input variables	Roll	Pitch	Point location
Value	0.6	0.6	0.2

5.5 Experimental Results

The accuracy of the ADGEO method was also tested in a real-world scenario using real-world data. This was done by exploring the various scenarios in which the method could be used. The experimental analysis was conducted using the open field dataset described in Chapter 4, Section 4.5.3, which can be categorized as a low variability measurement. In this section, two scenarios were explored and the findings are explained.

5.5.1 Description of the Two Scenarios

5.5.1.1 Scenario 1: Experiment conducted on Images Having Two Separate Shores in View During the Survey

This experiment was conducted using the open field dataset, though it was adapted to approximate a set-up for a survey over water. The experiment explored a situation where there were two shores in view on opposite sides of the water. In this test, the first and last images of each flight line were assigned as the hypothetical image with the shore in view, and the remaining images were classed as those without the shore in view (featureless terrain). In predicting the offset errors,

GCPs which were visible in the first images of each flight line were used to model the offset errors using the ADGEO method in Equation (5.10). Figure 5.15 illustrates what images were used to model the offset errors and are numbered from 1 to 6. After reconstructing the images using the ADGEO method as described in Figure 5.8, the accuracy was assessed using the 30 GCPs placed on the open field.

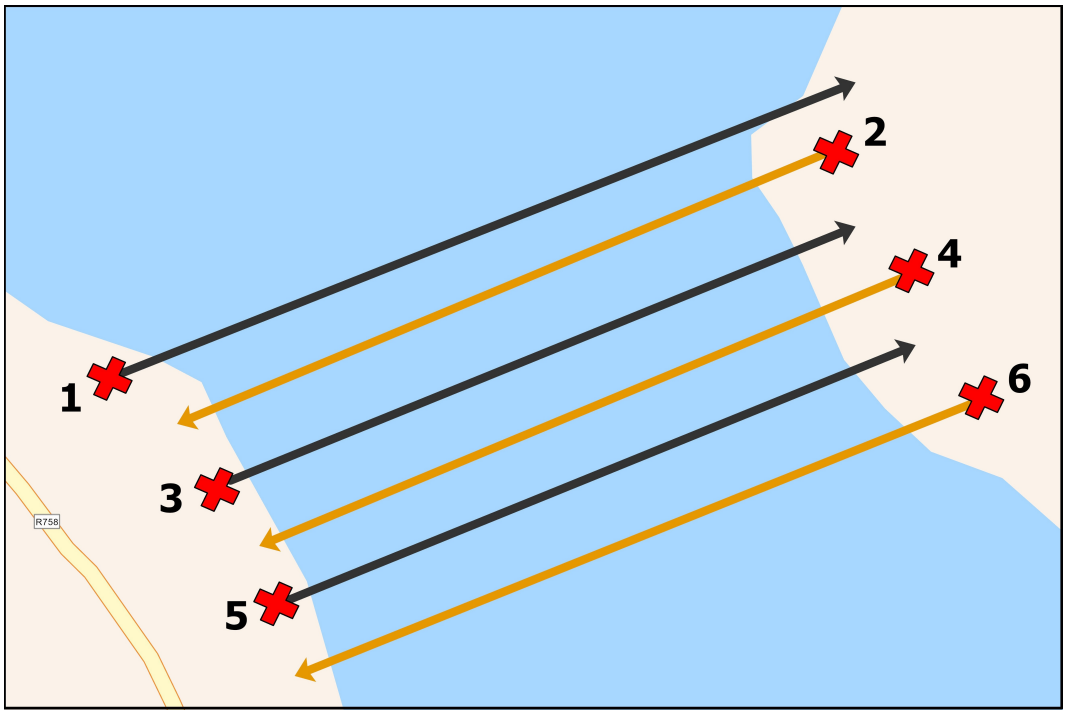

Figure 5.15: An illustration for Scenario 1. This is a scenario where two different shores are in view during the survey. The black and yellow arrows show the flight direction from the shore and back to the shore.

5.5.1.2 Scenario 2 : Experiment Conducted on Images Having Only One Shore in View

The second experiment explored a situation where only one shore was in view during the drone survey. In this test, the first image for the first flightline and the last image of the next flight line were defined as the image with the shore in view and this order continued for the rest of the flightline. As illustrated in Figure 5.16, the numbered images from 1 to 6 were used to predict the offset errors using the ADGEO method.

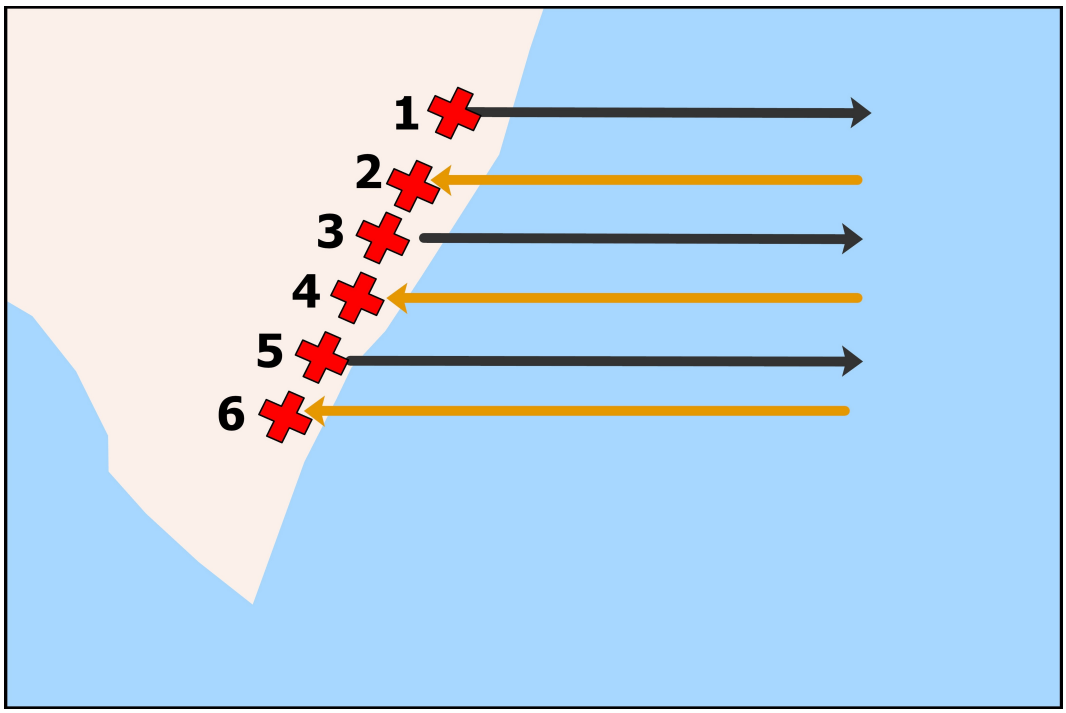

Figure 5.16: An illustration for Scenario 2. This is a scenario where one shore is in view during the survey. The black and yellow arrows show the flight direction from the shore and back to the shore.

5.5.2 Planimetric Accuracy

Figure 5.17 shows the calculated accuracy for each individual image without the shore in view. The ADGEO method achieved a MAE of 3.7m and 3.91m in scenarios 1 and 2, respectively. This represents an improvement of 80% over the traditional DG method, which had a MAE of 18.9m. The accuracy of the approach was also evaluated against the established BA method. While the BA method cannot be applied over water bodies, the standard accuracy achievable in terrestrial environments using BA can be used as a benchmark for comparison. The Mean Absolute Error (MAE) obtained for the BA method was recorded at 1.8 m.

From the results, the ADGEO method helped smooth the peak errors in the DG approach, which were caused by high Pitch and Roll values experienced during the survey. From Table 5.4, it was also found that the standard deviation of the MAE errors was reduced by applying the ADGEO method. Additionally, there was no significant difference in the performance of the ADGEO method between

scenarios 1 and 2, meaning that it can produce equally accurate results for both scenarios. It was observed that the lowest MAEs measured were for images that also exhibited low standard deviation. It was also found that the images captured closest to the shore (but not the 'shore' images) did not display significantly higher accuracy than those images captured further away from the shore. Possible explanations could be related to the calm winds during the survey however, this could change in real surveys over water where as the drone moves away from the shore, the wind speed tends to increase.

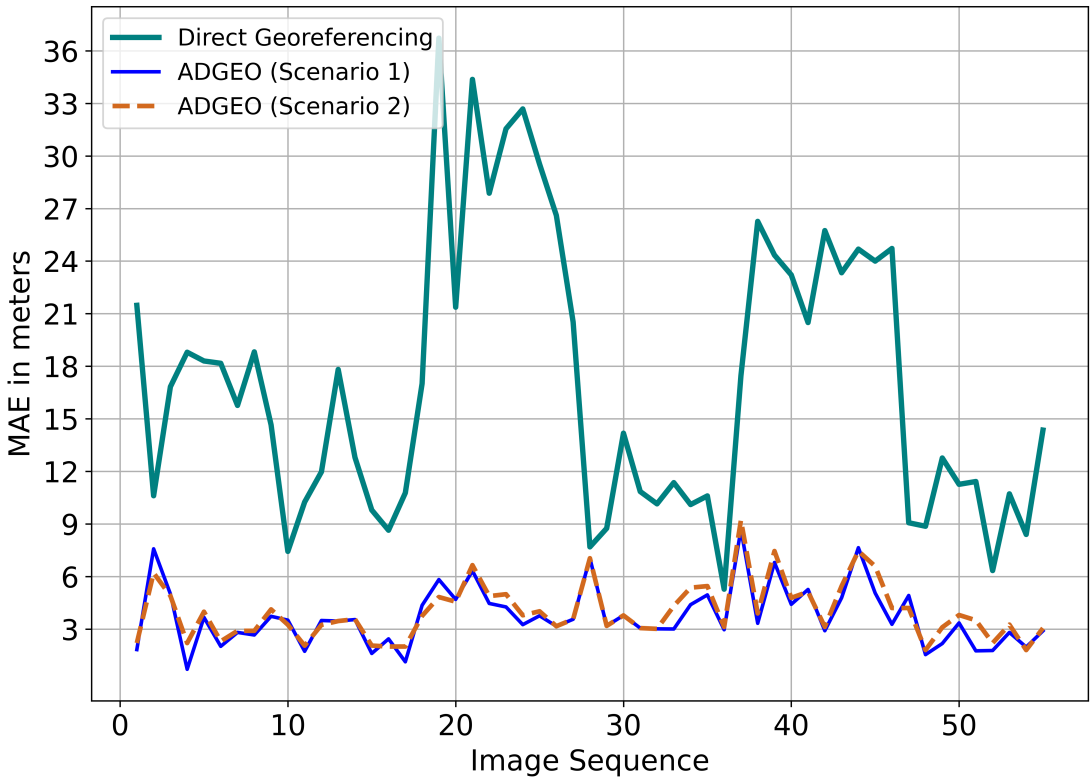

Figure 5.17: A graph showing the accuracy of the ADGEO method for Scenario 1 and 2 and compared with the traditional DG method. Both scenarios produced similar accuracy.

5.5.3 Inter-Rater Reliability of the Two Scenarios

Inter-rater reliability is a measure of the consistency with which two or more raters agree on the same observation (Gisev et al., 2013). Measuring the reliability of a model is important to ensure that the model is reliable. In this study, the inter-rater reliability was assessed between Scenario 1 and 2. This was done by

comparing the MAE measured from Scenario 1 to the MAE measured from Scenario 2. The goal of this comparison was to assess if the model was able to provide a reliable result under different scenarios. To evaluate the inter-rater reliability, the results were evaluated using paired sample t-test and intra-class correlation (ICC) coefficient. The ICC is a statistical measure of the consistency of measurements and provides information on the ability to differentiate variations between measurements (Lim et al., 2022). The ICC value ranges between 0 and 1, where a value of 0 indicates that there is no consistency in the measurements, whereas a value of 1 indicates that the measurements are perfectly consistent. For this analysis, the null hypothesis is that there is no difference in the measurement of offset errors between Scenario 1 and 2.

From the results in Table 5.4, the mean and standard deviation difference revealed that there were no significant differences between Scenario 1 and 2. The ICC coefficient was measured at 0.81. This indicates that there is a high degree of consistency in the prediction of the offset errors between Scenario 1 and 2, suggesting ADGEO produces reliable results under different scenarios. The p-value of 0.460 obtained from the paired sampled t-test also supports this conclusion. A p-value greater than 0.05 indicates that there is not enough evidence to reject the null hypothesis.

Table 5.4: Statistical Analysis Showing Mean Difference, Standard Deviation Difference, and Reliability Analysis Between Scenario 1 and 2

Scenario 1		Scenario 2		Mean and SD differences		ICC Coefficient	p-value
Mean (m)	SD (m)	Mean (m)	SD (m)	Mean (m)	SD (m)		
3.73	1.67	3.95	1.55	0.22	0.12	0.821	0.460

5.5.4 Influence of Overlapping Percentage on the ADGEO Method

The impact of forward and side overlap on the accuracy of the ADGEO method was evaluated using different overlap percentages. The evaluation was performed by calculating the MAE for images reconstructed over the shore using the BA

method, as well as the flight time and the number of tie points obtained. For this analysis, different images with the shore in view were reconstructed using different overlap percentages. The MAE for reconstructed images over the shore, the flight time and number of tie points obtained for each overlap percentage were calculated as shown in Table 5.5. The results showed that the higher the forward and side overlap percentages, the better the accuracy of the reconstructed image over the shore. This is because a sufficient number of tie points could be identified for higher image overlaps for the image reconstruction process. However, higher forward and side overlap percentages also increase the flight time. Based on the results, the optimum overlap percentage that produced a better accuracy and less flight time was 30%/70% overlap. This is because it had lower forward overlap and higher side overlap. Higher side overlap ensures that enough matching points are found between two adjacent images over the shore, while lower forward overlap ensures less images are captured, hence less flight time. It is important to note that for 30%/30% overlap, the image reconstruction over the shore performed poorly because there were not enough tie points found. This analysis is important because the ADGEO prediction model is dependent on the accuracy of the reconstructed image over the shore. Therefore, the higher the accuracy obtained from the shore, the more accurate the prediction of the offset errors for correcting the images without shore in view.

Table 5.5: Analysis on the Influence of Overlapping Percentages on ADGEO

Forward/Side Overlap %	MAE (m)	Flight time	Altitude	No of tie points
70%/70%	2.1m	11mins	120	2007
50%/50%	3.0m	7mins	120	1684
30%/30%	4.8m	6mins	120	202
30%/70%	2.2m	9mins	120	1950
70%/50%	2.8m	7 mins	120	1705

5.5.5 Example Results of Images Reconstructed Through Traditional DG and ADGEO Methods

This section shows sample images of the outputs produced by the traditional DG and the ADGEO methods. To evaluate and demonstrate the applicability of the ADGEO method, a survey over Blessington Lake, an inland waterbody in Co. WIcklow, Ireland, was used for the assessment. Due to the difficulty of placing targets, as previously explained in Chapter 4, the assessment was carried out using static targets on the shore. The survey captured 10 images with the shore in view but for the purpose of illustration, 3 images are presented in Figure 5.18. The images are shown in pairs, with the traditional DG method on the left and the ADGEO method on the right. The ground truth image for the accuracy assessment was obtained from Ordnance Survey Ireland high resolution aerial orthoimagery which was acquired in 2018. This is a georeferenced aerial photo with an accuracy in XY of 10cm. This provided a reliable benchmark dataset to compare the two methods. It can be visually observed that after the application of the ADGEO method, the location of the point measured in the ADGEO image (i.e the red point) is closer to the ground truth point (i.e the green point) measured. Additionally, as a proof of concept, an orthomosaic of the entire survey over the Blessington lake has been produced from the ADGEO method and can be seen in Appendix C.

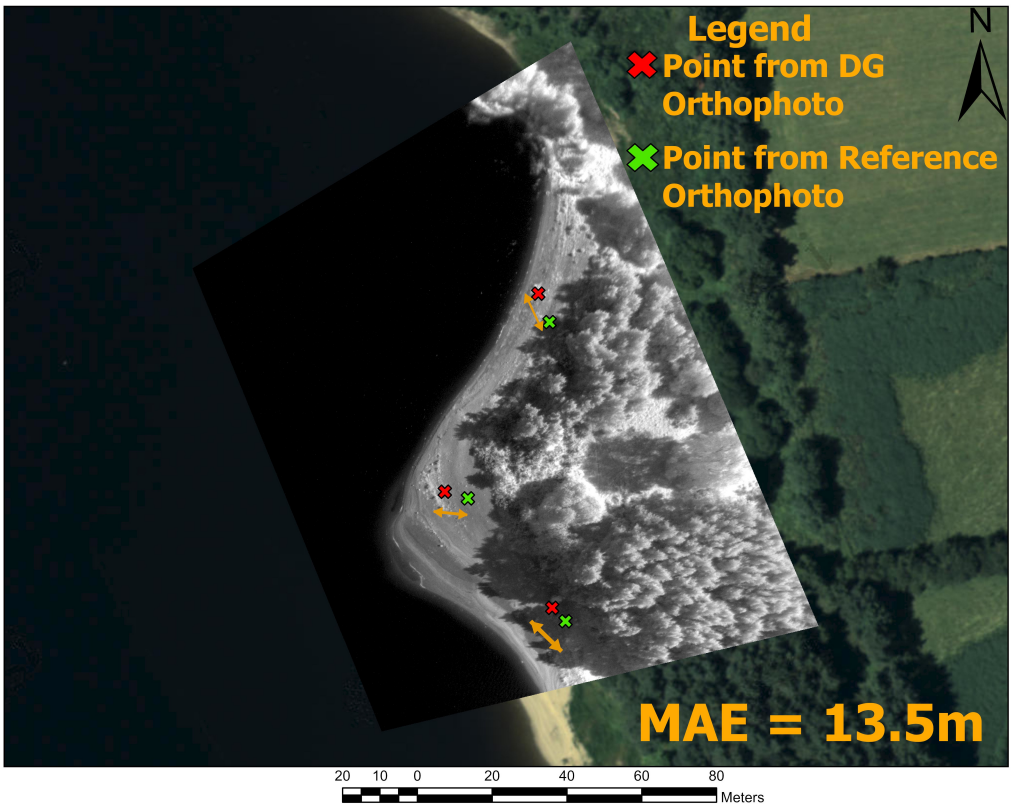

(a) DG Method

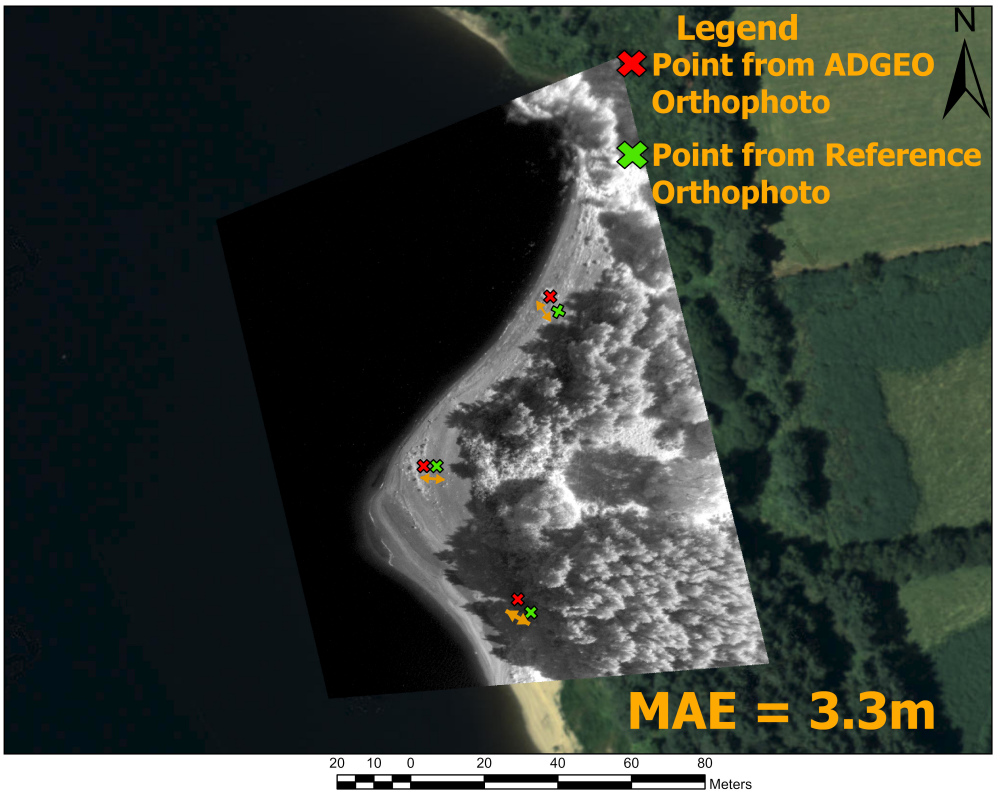

(b) ADGEO Method

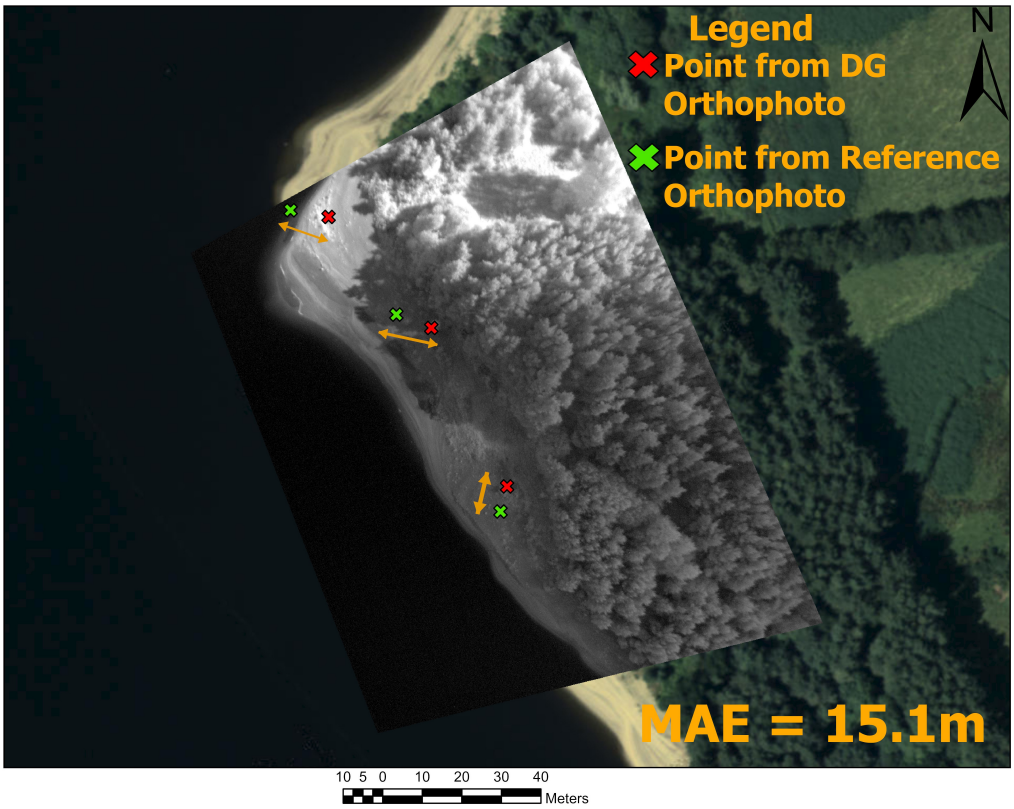

(c) DG Method

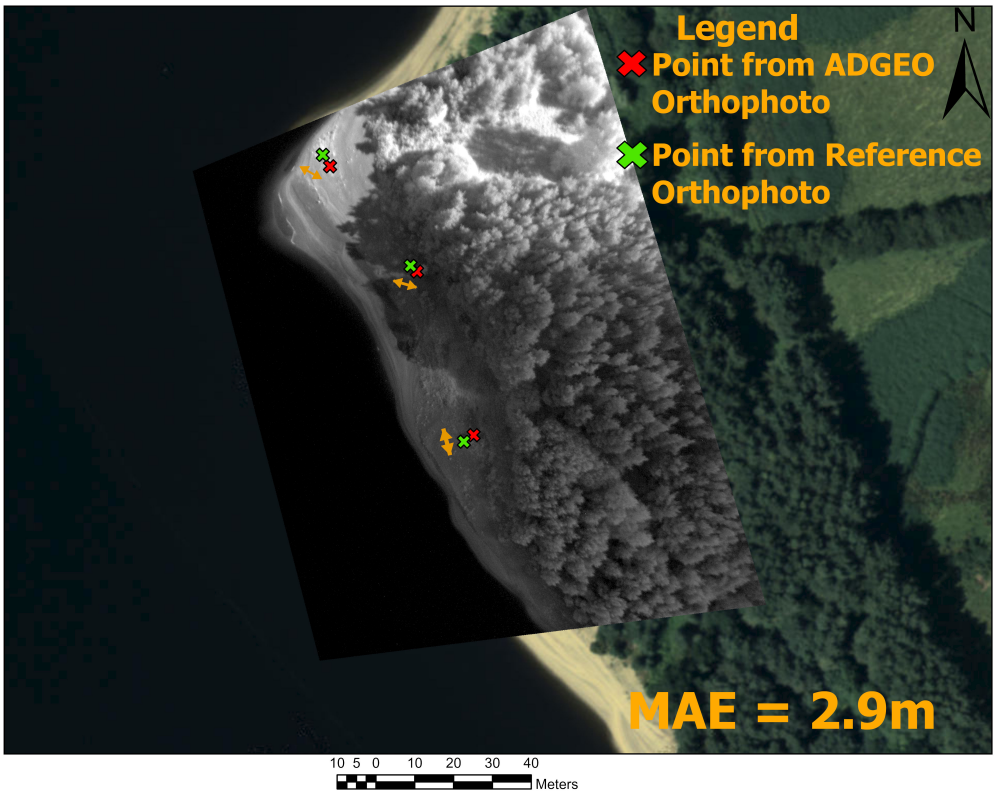

(d) ADGEO Method

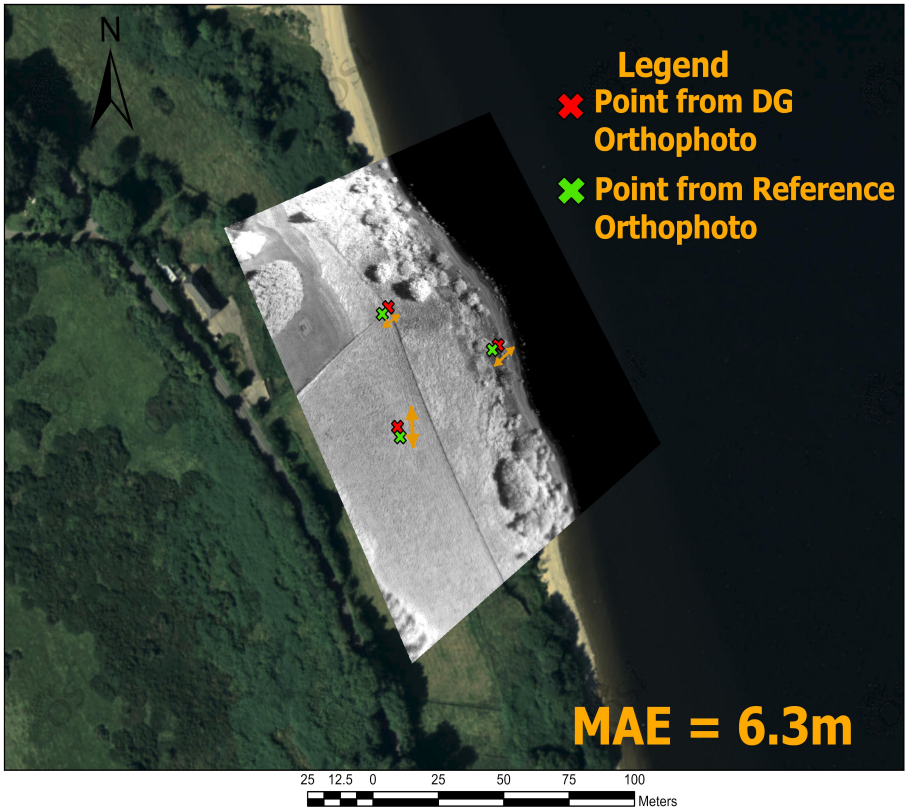

(e) DG Method

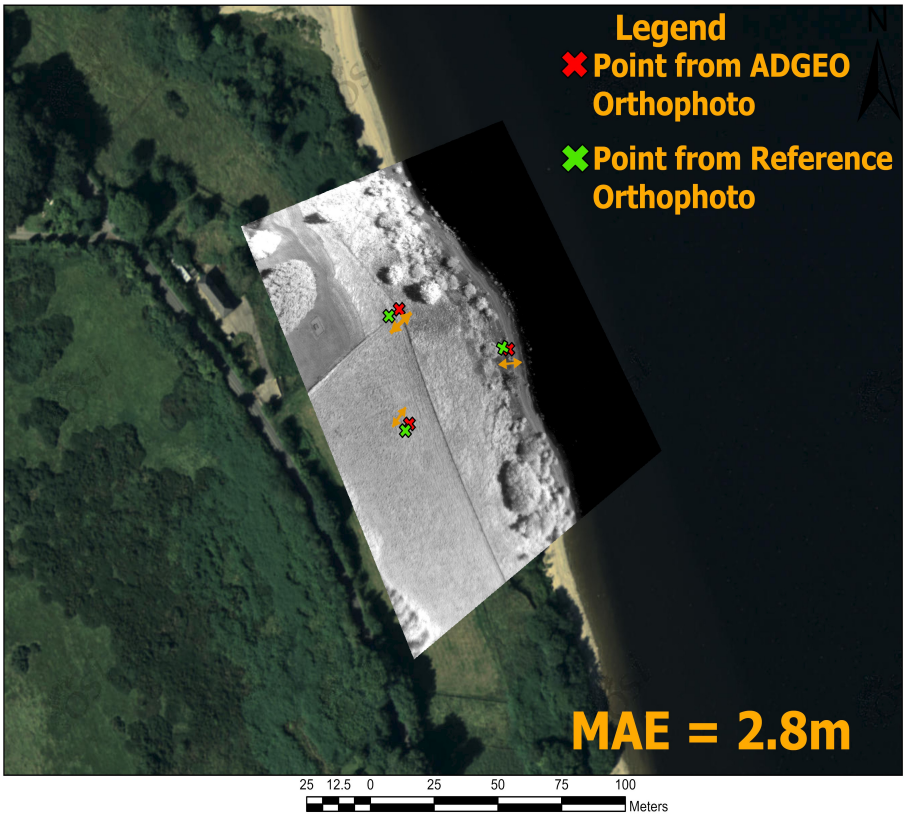

(f) ADGEO Method

Figure 5.18: Example results of selected orthophotos and their MAE via traditional DG and ADGEO method. The images are overlaid on OSI high-resolution aerial orthophoto for accuracy assessment.

5.6 Discussion

5.6.1 Accuracy Assessment of the ADGEO Method

Based on the findings, the ADGEO method was found to be effective in improving the accuracy under both simulations. However, it was more effective under low variability attitude measurement conditions. ADGEO's high accuracy under low variability could be attributed to the low standard deviation of the data, suggesting a high level of similarity in the data (Nagele, 2003). According to Bouthillier et al. (2021) algorithms or models with low standard deviations tend to have accurate predictions.

It therefore follows that high variability in data tends to affect the accuracy of the model. The reason for this limitation is the inability of the ADGEO method to effectively account for any extreme variations. This implies that when confronted with significant variations in the measured attitude data, the ADGEO method will struggle. In a study by Bishop (2006), it was explained that high variation in datasets makes it difficult for algorithms or models to learn the pattern within the data. Also, according to Hastie et al. (2009), if the dataset used to predict the values contains a limited number of input variables, the model may not have enough information to predict. Thus, if the dataset input data contains a limited number of different Roll and Pitch values, the model may not have enough information to generalize well. In the case of this study, because the model uses only images over the shore, it tends not to have enough representation to help the model to predict accurately.

5.6.2 Planimetric Accuracy

From the experimental analysis, the ADGEO method obtained a MAE of 3.7m, thus out-performing the DG approach by 80%. Furthermore, when compared to the BA accuracy of 1.8m in Chapter 4, Section 4.7.5, it is evident that the ADGEO method closely approximates the BA's accuracy. This means that the ADGEO

method has the potential to incrementally close the accuracy gap with the BA method. In the BA approach, changes in orientation of the sensor have limited impact on the final reconstructed 2D image because the effect is mitigated by the overlapping images with sufficient tie points which improve the POSE (Yuan and Zhang, 2008; Rehak and Skaloud, 2016). However, in the traditional DG approach, the accuracy of the reconstructed 2D image is directly linked with the accuracy of the measurement of the IOPs and EOPs, as well as environmental factors such as wind speed and flight speed (Cramer et al., 2000; Jaud et al., 2018; Dreier et al., 2021). ADGEO is able to increase the accuracy and outperform traditional DG because it combines some of the benefits of both BA and DG. This helps to reduce the errors that are introduced by the orientation effect and the environmental factors, and reduces the reliance on accurate EOP measurements.

The accuracies achieved through the ADGEO method provide further evidence to suggest that drones with low-cost IMU/GNSS can play a role in mapping over water if they employ these corrective procedures. This is because no method has previously been developed to improve the planimetric accuracy of drones when mapping over water. Hence, this method offers a practical solution to mapping over water. Studies over water have not focused on improving positional accuracy because it is extremely difficult to improve accuracy by placing visible targets (Román et al., 2023; De Keukelaere et al., 2023). As a result, the accuracy of mapping over water has been left to the accuracy of the IMU/GNSS. Consequently, low-cost drones are often automatically considered unsuitable for mapping over water. The ADGEO method is the first of its kind that can be applied to improve planimetric accuracy, and it opens up the possibility of using low-cost drones for mapping over water.

These results suggest that ADGEO can best be applied in cases where there are : (1) two shores in view and (2) one shore in view. This is achievable, as water surveys will often be carried out close to the shore due to operational/Line of Sight

restrictions. As a a guide, it is very important that images captured over the shore cover 80% - 100% of the area being terrestrial. This requirement is important because the BA approach relies heavily on the ground features for accurate image reconstruction. When stitching images together along the shore, insufficient terrestrial area can lead to poor reconstruction outcomes. Hence, errors in BA image reconstruction have the potential to affect the accuracy of the measured offset errors.

Additionally, it can be posited that the choice of sensor, whether multi-lens or single-lens, will not affect or influence the performance of the ADGEO method or its results. The ADGEO method is a reproducible method that can be used with any frame sensor.

5.6.3 Influence of Flight Parameters

The influence of image overlap was analyzed by considering different forward and side overlap percentages. In this thesis, analysis was made to provide a reasonable overlap percentage as a guide when using the ADGEO method. The results revealed that 30%/70% was the optimum overlap percentages. The lower forward overlap percentage ensures that less images are captured in the X-direction of the drone survey. On the other hand, the higher side overlap percentage ensures that enough tie points are identified when performing BA at the shore. Based on the combination of higher side overlap and lower forward overlap, the flight time and the area covered are improved. Also, since the prediction accuracy of the offset errors for the ADGEO method is dependent on the accuracy of the reconstructed shore image via BA, the higher side overlap ensure there is good image reconstruction. The recommended overlap percentage in this study should only be applied in context where the ADGEO method is to be applied.

5.6.4 Reliability of the ADGEO Method

From the analysis, there was strong inter-rater reliability between the different scenarios. There was also no significant difference in mean and standard deviation. This result means that the ADGEO method can produce the same result under different scenarios. This is important because it means that the method can be used to reliably predict the offset errors. Thus, in situations where the survey was conducted with one side of the shore in view, it can produce similar results to a survey where there are two sides of the shore in view.

Also, the lack of significant difference in mean and standard deviation between the different scenarios means that the method is not biased towards any particular scenario. In general, the most important element in this concept is to have at least one side of the shore in view. However, one advantage that scenario 1 might have over scenario 2 is that both images from the sides of the shore can be used in the reconstruction process. For example, in scenario 1, the first and last image both have the shoreline in view. Therefore, in the instance where the mean attitude difference between the first image over the shore and images over the water is significantly high, the last image over the shore can be used - supposing the mean difference is lower than the first image. On the contrary, when there is only one side of the shore in view, there is no other alternative, especially in cases where you have high mean attitude difference. In reality, when surveying over water, the farther you move away from the shore, the stronger the winds. This means that images captured even further away from the shore might show characteristics of high attitude recording. As a result, the mean difference will be significant. In such instances, scenario 1 might perform better than scenario 2 because the last image over the shore can be used to correct the images that are farther away from the first image with the shore in view.

5.6.5 Sensitivity Analysis

From the result, the input variables that are more sensitive to the output were identified as the Pitch and Roll. This means that those attitude angles have the greatest influence on the output of the model and explains why high variability attitude measurements impact accuracy. The attitude angles are an important element that introduces errors such as tilt distortions in images. This implies that, in real-world applications, it is important to conduct drone surveys within calmer weather conditions. This will ensure that the attitude measurements are correlated.

5.6.6 Sources of Errors and Limitations

As already established in the methodology, one fundamental input variable in the ADGEO process is the offset errors. The offset values between the BA and the DG can be measured from identifiable features on the shore or alternatively placing visible targets. These offset errors are crucial because they are used to predict errors in images where the shore is not visible and use them to refine the images without the shore in view. One main limitation of this method is that the accuracy is dependent on the accuracy of the offset errors that are measured from the shore. Thus, if the offset errors are measured with high accuracy, it means that the observed points are close to the true values on the ground. In such cases, the method can provide accurate predictions. Therefore, errors in the offset measurements will tend to propagate into the predictions. This error could have different causes, such such as low overlap side percentage and human error in measuring the offset error. Further, the ADGEO method is dependent on having favourable shore terrain. Therefore, in instances where the shore terrain is rugged and has high vegetation cover such as trees, it might affect the ADGEO method.

5.7 Conclusion

One of the main contributions of this chapter was the demonstration of the applicability of a novel ADGEO method for improving accuracy when mapping water bodies. This chapter also contributes to the understanding of the potential of ADGEO in overcoming the limitations of traditional DG for mapping water bodies and provides explanations on the mathematical model and context where the model can be used in real-world scenarios. In this chapter, the theoretical accuracy assessment of the ADGEO method was conducted to evaluate its performance and limitations under different attitude measurements. The findings demonstrated a potential for significant improvements in accuracy compared to the traditional DG approach. The results from the theoretical analysis showed that the ADGEO method was able to reduce the MAE from 5m to 2.2m under low variability attitude measurement. Also, it was found that the attitude angles were highly influential factors in determining the accuracy of the model's prediction. However, it was found that under high variability attitude measurement, the ADGEO method cannot significantly improve the accuracy. Furthermore, the result from the experimental analysis with real world data confirmed that the ADGEO method was able to improve the accuracy from the traditional DG method of 18.9m to 3.7m. Also, the result showed that the ADGEO method can be applied under two scenarios: (1) where there are two shores in view, and (2) where there is one shore in view.

From these results, it can be concluded that using low-cost drones with ADGEO provides a viable approach for improving the accuracy of the reconstructed 2D images over water if care is taken to avoid high-wind environments. Importantly, the ADGEO method is reproducible, sensor independent and can be applied to different study areas. This approach is efficient, less expensive and less time-consuming as ground targets are not necessarily needed in improving accuracy. Thus, eliminating the risk of placing ground targets in inaccessible or difficult areas.

Considering the limitations outlined above, particularly with the limitation of the ADGEO method dependent on the shore, the next chapter seeks to develop a method that can be implemented even without the shore in view.

This chapter is based on a published peer-review paper: Essel, B., Bolger, M., McDonald, J., Cahalane, C. (2023) Developing a Theoretical Assessment Method for an Assisted Direct Georeferencing Approach To Improve Accuracy When Mapping Over Water: the Concept, Potential and Limitations. International Archives of the Photogrammetry, Remote Sensing and Spatial Information Sciences - ISPRS Archives. 48(1/W1-2023), 139–144.

Chapter 6

AirMAP – An Automated Image Registration Model for Mapping Water Bodies using Multi-Sensor Drone Data

This chapter presents a new method for improving the accuracy of image registration when mapping water bodies known as Automated Image Registration Model for Mapping over Water (AirMAP). This novel method requires a pre-trained model created from drone datasets captured with diverse attitude angles. This model was trained using ML algorithms and was validated and tested to analyse the model's performance and to perform accuracy assessment for the new datasets. In this chapter, the motivation and the objectives are first explained in section 6.1. The datasets used for the training, validation and testing are described in section 6.2. The step-by-step methods developed for the AirMAP approach are described in section 6.3 to give a clear understanding of the operational framework. The results and analysis for this methodology are presented in section 6.4. Finally, the findings are discussed in section 6.5 and the conclusions in section 6.6.

6.1 Introduction

As demonstrated through theoretical and experimental analysis in the previous chapter, the ADGEO model effectively improves the accuracy of reconstructed 2D images over water. This method was found to significantly improve the accuracy of a reconstructed 2D image over the water by up to 80% when compared against traditional DG. However, as discussed in section 5.6.6, this approach exhibits certain limitations. These limitations primarily include: 1) reliance on the presence of a shore in some of the images, 2) sensitivity to favourable shore geometry, and 3) reduced accuracy in conditions of highly variable attitude measurements. These limitations could potentially hinder the applicability of the ADGEO model in certain scenarios. For instance, in areas with dense vegetative cover, such as trees and shrubs, identifying ground-truth features to determine offset errors proves challenging. To address these limitations, it is important to develop an approach capable of overcoming each of these constraints.

As explained in Section 2.5.1, image registration is a technique that can be used to achieve accurate alignment of an image with no spatial information onto a georeferenced image (Xiong and Zhang, 2010; Zhang et al., 2023). In a broader sense, image registration functions by aligning a target image onto a reference image (Ihmeida and Wei, 2021; Coulter et al., 2019). Over the years, the techniques employed in image registration have evolved significantly, driven by technological advancements, increased computational power, and diverse application requirements. In recent years, advanced ML and Deep Learning (DL) techniques have been integrated into image registration. According to Cao et al. (2019), various ML algorithms can be employed to learn from pre-trained image registration models to register new images. In Chen and Jiang (2021) for example, a novel two-stage deep learning registration method for estimating transformation parameters was developed to perform an image registration of a matching sub-image. Their results demonstrated that their method can significantly improve the geometric accuracy of remotely sensing image. Also, in studies such as Kim

et al. (2012) and Wei et al. (2017), ML algorithms such as SVM and RF have been used to learn from a trained medical imaging dataset to register new images. Additionally, in Reddy et al. (2018), an Artificial Neural Network (ANN) based ML approach was developed to register satellite images and achieved higher positional accuracy compared to conventional Rational Functional Models (RFM) which is used to approximate the physical sensor model for geometric corrections. These studies demonstrate that supervised ML can be employed to train models using image datasets. The trained models can then estimate the transformation of unseen images, which, when applied, enhances the accuracy of new images.

As of the time of this study, no research has been carried out using ML to create a pre-trained model that can be used to perform image registration of drone imagery captured over water. Therefore, this chapter will explore the possibility of using a supervised ML approach for drone image registration. Supervised learning is a type of ML in which algorithms are trained on labelled data to learn the relationship between input and output data (Barbarella et al., 2021). The goal is to accurately define the mapping function so that the output variables for new, previously unseen input data can be predicted (Brownlee, 2023).

In this chapter, a novel method which is called AirMAP is proposed for the purpose of mapping water bodies by using drones. This method utilises a pre-trained model to enable image registration. This approach broadly seeks to accomplish three main objectives: (1) to explore and evaluate different ML algorithms for this purpose, (2) to utilise ML to train datasets over relatively flat terrestrial terrain with varying viewing angles and sensors, and, (3) to apply the trained model to predict the transformation matrix necessary for registering an image acquired over water. This approach is once again based on the fundamental assumption in this thesis that water can be considered a flat surface. It is this assumption that allows the pre-trained model from the flat terrestrial dataset to also be applied to

water. The model uses two type of input images: a reference image and a target image. The reference image is an image that has been accurately georeferenced while the target image is a direct georeferenced image with no corrections applied (thus the ARMFET and ADGEO techniques have not been applied). The model seeks to first map and learn the transformation that maps the target image to the reference image and this links back to the illustration in Section 2.5.1 where a target image is mapped onto a reference image. Subsequently, the model predicts the transformation parameters that can be used to register a new unknown image (water).

6.2 Data

6.2.1 Description of the Training, Validation and Testing Dataset

Having adequate drone data for the training, validation and testing of a ML model is essential. In this chapter, the datasets used were sourced from two primary areas: data obtained through drone surveys conducted by the researcher as part of this thesis (primary data) and data retrieved from online repositories (secondary data). The inclusion of secondary data sources was necessitated by factors such as time, cost and resources of collecting adequate drone data from field surveys over a flat terrestrial terrain with varying flight direction, flight dynamics, viewing angle and sensors. Thus, this study leveraged drone data repositories available on the internet (references to sources are in Table 6.1, supplementing the primary data obtained through field surveys as detailed in Chapter 4, Section 4.5.3.

The two primary constraints encountered in obtaining suitable secondary data that adhere to the assumptions of this thesis from Section 1.7 were: having images captured with a sensor over a relatively flat area, and navigation data captured with a low-cost drone. The datasets for the ML model were obtained from two sensors: a drone without a self-levelling gimbal and a drone with self-levelling

gimbal. The latter was introduced to ensure the replicability of AirMAP for drones with self-levelling gimbals, as well as testing the AirMAP approach on a low variability dataset. In ML, the mapping relationship learned from the training dataset is highly dependent on how representative the data is. This means that the training data for the ML task must adequately capture the underlying distribution of the ML problem being solved. Therefore, this study ensured that adequate data were acquired which were representative of the navigational data that can be derived during different conditions (low wind, moderate wind and high wind) when surveying over water.

A detail breakdown of the datasets used for the training, validation and testing is provided in Table 6.1.

Table 6.1: A detailed Description of the Characteristics and Sources of the Dataset.

Sensor	**No. of images**	**Flight height**	**Pitch Analysis**			**Roll Analysis**			**Type of land-cover**	**Stdv for elevation**	**Source**	**Total**
			Mean	Std	Pitch range	Mean	Std	Roll range				
Sequoia	70	120m	5.0^o	4.3	Max: 16.8 Min: 0.06	5.6^o	1.4	Max: 8.06 Min: 1.3	Open field	0.54m	Field survey	1221
Sequoia	54	120m	5.2^o	4.2	Max: 16.9 Min: 0.4	4.12^o	1.94	Max: 9.6 Min: 0.3	Open field	0.54m	Field survey	
Sequoia	59	120m	5.8^o	5.0	Max: 17.6 Min: 0.21	1.2^o	1.6	Max: 8.9 Min: 0.02	Open field	0.54m	Field survey	
Sequoia	444	120m	3.1^o	2.7	Max: 17.5 Min: 0.007	6.6^o	3.0	Max: 16.0 Min: 0.05	Open Field	0.8m	PIX4D	
Sequoia	594	120m	5.5^o	3.5	Max: 15.8 Min: 0.01	4.0^o	3.4	Max: 17.7 Min: 0.005	Farmland	0.73m	Kallimani et.al., 2020	
DJI FC6310 (Phantom 4 pro)	250	120m	0.2^o	0.02	Max: 1.3 Min: 0.01	0.2^o	0.02	Max: 1.3 Min: 0.02	Open field	0.86m	GeoNadir	350
DJI FC6310R (DJI Phantom 4 RTK)	100	120m	0.12^o	0.01	Max: 1.1 Min: 0.01	0.12^o	0.01	Max: 1.3 Min: 0.01	Open field	1.01m	GeoNadir	
Total	1571											1571

6.2.2 Statistical Overview of the Datasets

This section provides a detailed examination of the datasets used in the training, validation and testing the ML model. This examination focuses on analysing the distribution of attitude angles and assessing the overall characteristics of the data. The description of the datasets are categorized based on the type of sensor used to acquire the images: Sequoia and DJI FC6310 sensor.

6.2.2.1 Sequoia Dataset

The Sequoia datasets comprised 1221 images, with a slightly imbalanced distribution across the different types of images: nadir/near nadir (14.6%), low tilt (25.9%), and high tilt (59.5%), replicating the classes defined in Chapter 4, Section 4.2.1. This imbalance was due to the sensor not having a self-levelling gimbal and is typical of the datasets used in previous chapters. Drones without self-levelling gimbals struggle to maintain the sensor at nadir/near-nadir position or even at low tilt in moderate or high wind conditions. These sensors are most stable at very low wind speeds, up to a maximum of 3 m/s. However, the Sequoia dataset provides a good representation across the different types of images. This representativeness ensures that the model is trained on sufficient data within each image category, enhancing its generalizability. Further, the mean Pitch and Roll angles for the Sequoia dataset were 5.3^o and 3.7^o respectively. Also, the standard deviation was calculated at 4.5^o and 2.4^o in Pitch and Roll respectively. Figure 6.1 and 6.2 shows the distribution of Pitch and Roll angles.

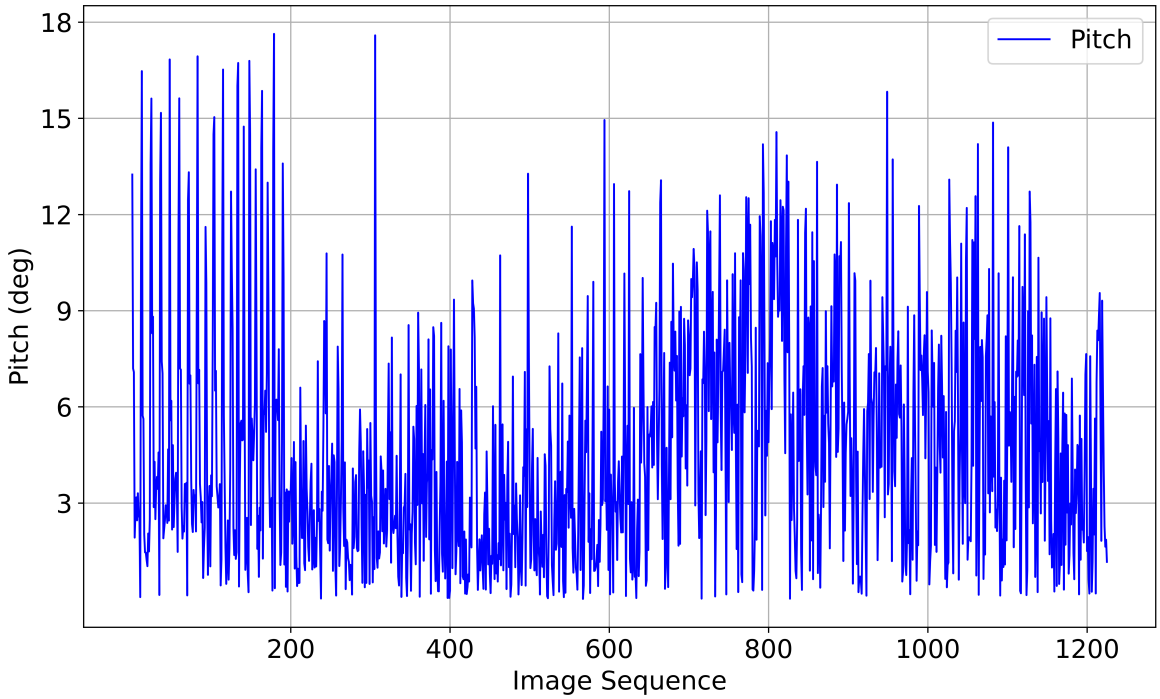

Figure 6.1: An image showing the distribution of Pitch angles for the Sequoia dataset. The image sequence on the x-axis refers to the number of individual images used (n=1221). The distribution of the angles shows a well-balanced dataset which is required for effective training of the model.

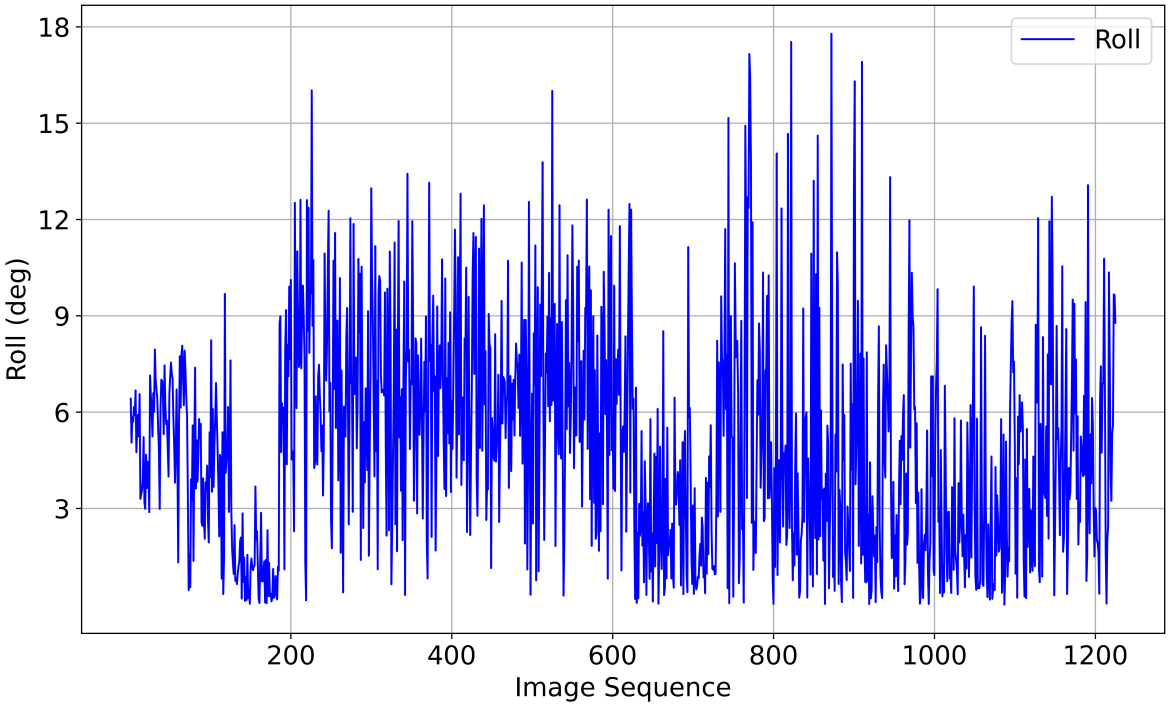

Figure 6.2: An image showing the distribution of roll angles for the Sequoia dataset. The image sequence on the x-axis refers to the number of individual images used (n=1221). The distribution of the angles shows a well-balanced dataset which is required for effective training of the model.

6.2.2.2 DJI FC6310 Sensor Dataset

The DJI FC6310 sensor (from the Phantom 4 pro and RTK drone) dataset comprised of 350 images. Out of these images, 97% were categorized as nadir/near-nadir images and 3% as low tilt images. Almost all of the datasets were within the nadir/near category because the drone contains a gimbal which stabilises the sensor. The mean Pitch and Roll angles were 0.3^o and 0.28^o respectively. Also, the standard deviation were 0.21^o and 0.2^o for Pitch and Roll respectively, indicating a very low variability in the attitude angles. Figure 6.3 and 6.4 shows the distribution of Pitch and Roll angles.

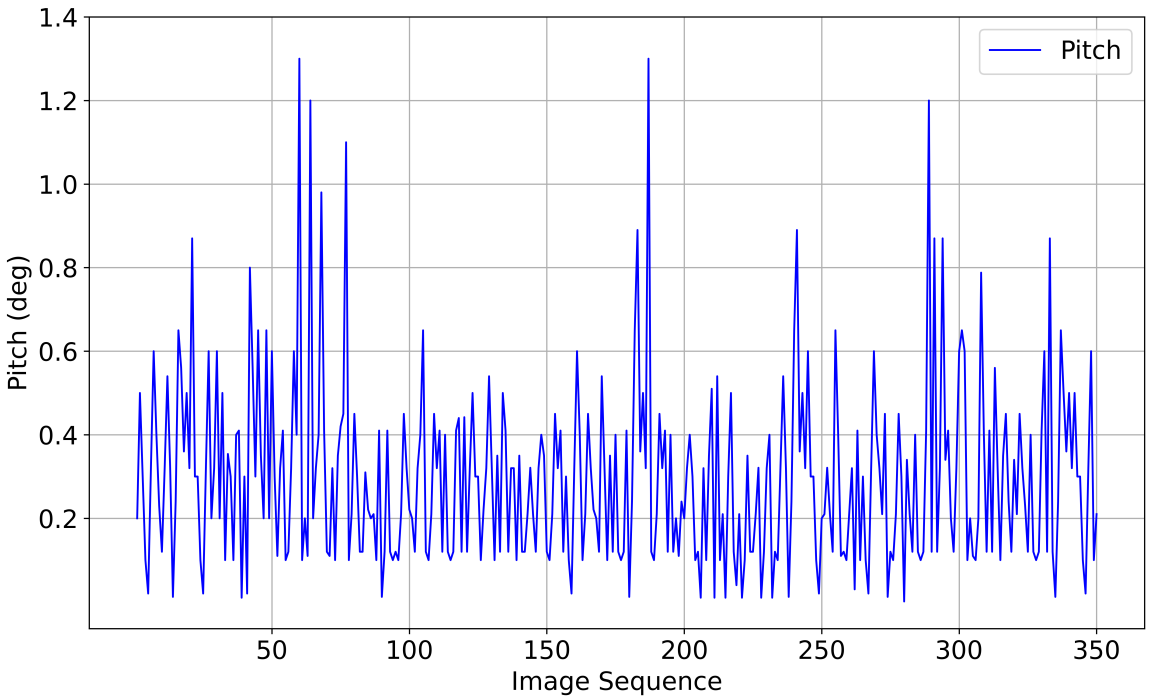

Figure 6.3: An image showing the distribution of Pitch angles for the DJIFC6310 dataset. The image sequence on the x-axis refers to the number of individual images used (n=350). The distribution of the angles shows a very correlated dataset which is typical of a sensor with a gimbal.

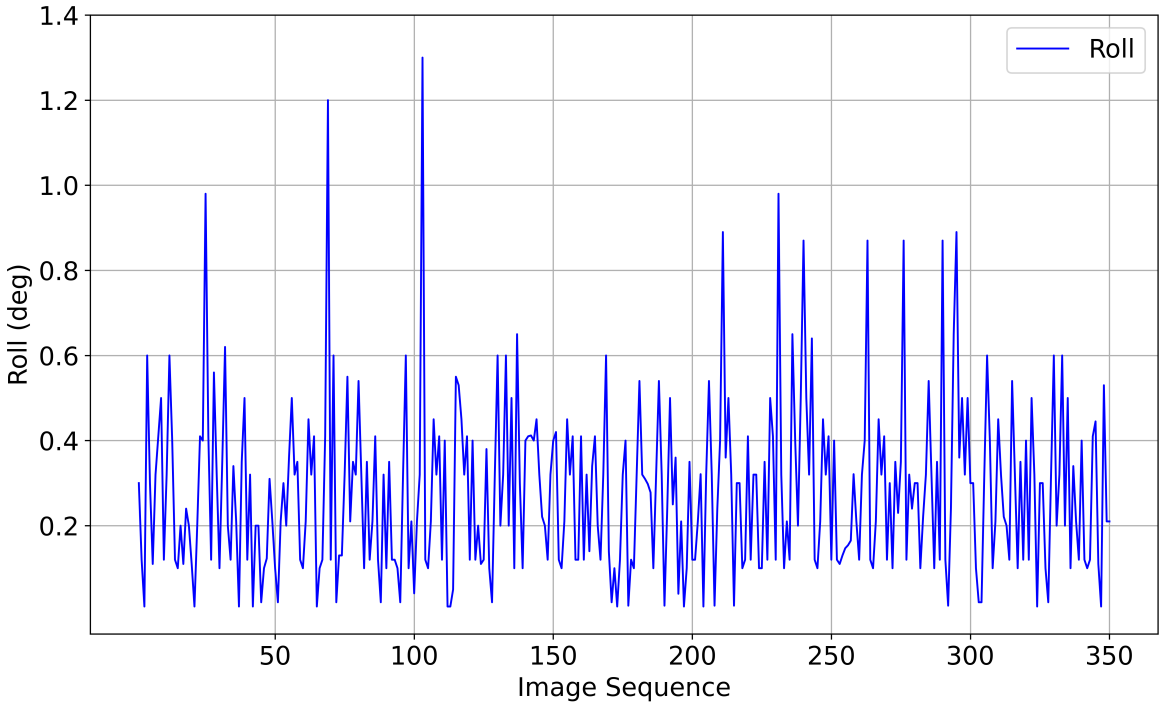

Figure 6.4: A graph showing the distribution of Roll angles for the DJI FC6310 dataset. The image sequence on the x-axis refers to the number of individual images used (n=350). The distribution of the angles shows a very correlated dataset which is typical of a sensor with a gimbal.

6.3 Methods

This section details the development of the AirMAP methodology, which is broadly broken down into two main stages. The first stage describes the data preparation steps, and the second stage describes the process involved in training and assessment of the model. This workflow is illustrated in Figure 6.5, where each process is depicted.

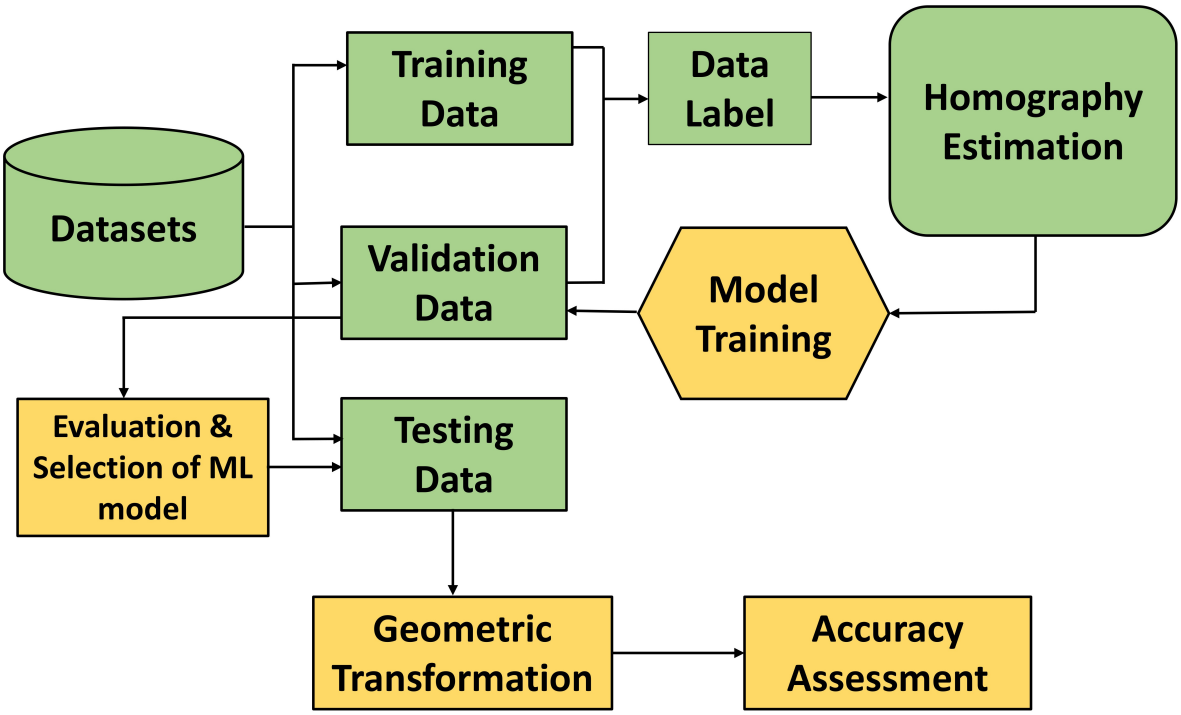

Figure 6.5: Illustration of the novel AirMAP approach: the first stage is highlighted in green and second stage in yellow. It leads from the data acquisition and training to homography estimation and accuracy assessment. This method ensures that an image captured over the water for varied attitude angles can be improved by registering the image using a pre-trained ML model.

6.3.1 Data Preparation for the ML Model

Data preparation can be defined as the transformation of raw data into a form that is more suitable for modelling. Data preparation is an important step in the methodology that ensures that the data is suitable for training and evaluating the model (Brown et al., 2020). Data preparation is one of the most important steps in ML process because each dataset is different and specific to a project, requiring specific preparation. Hence, the data was first prepared by labelling the datasets.

6.3.1.1 Labelling data

Labelling data or data annotation in ML is an important task that involves assigning class labels to data points (Desmond et al., 2021). This process is one of the essential stages in preparing data for supervised ML. For supervised ML to work, labelling the dataset is needed for the model to learn and make accurate

predictions.

In ML, data labelling is the process of identifying raw data and adding one or more meaningful and informative labels to provide context so that a ML model can learn from it. In supervised ML, the accuracy of your trained model will depend on the quality of the data labelling.

As part of the data preparation step, all the training and validation datasets were carefully labelled. The goal was to label the data using parameters that directly influences the image registration process of a given image. The dataset was labelled using input and output variables. The input variables, also known as features or independent variable can be described as the attributes of the data that are used to make predictions while the output variables, also known as target or dependent variables are the variables that the ML model is designed to predict. The input variables used in this chapter include the attitude angles (Pitch, Roll, Yaw), sensor parameters (focal length and sensor size), and flying height. The output variable included the 3*3 homography parameters represented as $h11, h12, h13, h21, h22, h23, h31, h32$ and $h33$ (the matrix representation can be found in Equation (6.1) below).

6.3.1.2 Homography Estimation for Individual Images

The next step was to obtain the output variable that the ML is to predict. The first step in this process was to obtain point correspondences between the target and reference images using a feature detector algorithm. This links back to the explanation of how these correspondences are derived in Section 2.5.2.1. The next step was to derive the true correspondences by filtering or removing the bad matches using the RANSAC algorithm. In this step, multiple thresholds were experimented and the suitable threshold that best filters the points was chosen using a weighted sum score. After a set of true correspondences have been identified, the homography matrix is then computed. According to Zeng et al. (2019), the widely

and common way to parameterize a homography (H) is with a 3x3 matrix as shown Equation (6.1). In this equation, $h11, h12, h13, h21, h22, h23, h31, h32$, and $h33$ are the nine parameters that define the homography transformation. These parameters can be parameterized in various ways, but one common method is to use a set of eight parameters and normalize the matrix such that $h33 = 1$. This normalization ensures that the matrix is not scale-dependent and remains a valid homography. The homography matrix H as detailed in Luo et al. (2023) is defined as follows:

$$H = \begin{pmatrix} h_{11} & h_{12} & h_{13} \\ h_{21} & h_{22} & h_{23} \\ h_{31} & h_{32} & h_{33} \end{pmatrix} \tag{6.1}$$

In computer vision, the homography transformation can be represented by Equation (6.2). In this equation, point p, represent the location of a point in the target image that is mapped onto point p', as shown in Equation (6.3), which is the corresponding point in the reference image.

$$p' = Hp \tag{6.2}$$

$$p = \begin{pmatrix} x \\ y \\ 1 \end{pmatrix} \qquad p' = \begin{pmatrix} u \\ v \\ 1 \end{pmatrix} \tag{6.3}$$

The Equation (6.2) can therefore be expanded to derive Equation (6.4).

$$\begin{pmatrix} u \\ v \\ 1 \end{pmatrix} = \begin{pmatrix} h_{11} & h_{12} & h_{13} \\ h_{21} & h_{22} & h_{23} \\ h_{31} & h_{32} & h_{33} \end{pmatrix} \begin{pmatrix} x \\ y \\ 1 \end{pmatrix} \tag{6.4}$$

To find H, the most common approach is to use the DLT method. In this thesis, the DLT method was chosen because it can be computed directly from the corresponding points without the need for any iterative or optimization algorithms, as well as its robustness.

6.3.1.3 Direct Linear Transformation Method

DLT is a method that estimates the homography between a target image and a reference image from a set of correspondences. DLT is a technique used to compute a matrix equation of the form $Ax = 0$, where A represents a specific matrix, and x denotes the vector of unknown variables we aim to determine.
By observing Equation (6.4) from above, it can be rewritten in a linear form to get Equations (6.5) and (6.6) below:

$$u = \frac{h_{11}x + h_{12}y + h_{13}}{h_{31}x + h_{32}y + h_{33}} \tag{6.5}$$

$$y = \frac{h_{21}x + h_{22}y + h_{23}}{h_{31}x + h_{32}y + h_{33}} \tag{6.6}$$

By rearranging Equation (6.5) and (6.6), Equations (6.7) and (6.8) can then be derived :

$$h_{31}xu + h_{32}yv + h_{33}v - h_{11}x - h_{12}y - h_{13} = 0 \tag{6.7}$$

$$h_{31}xu + h_{32}yv + h_{33}u - h_{21}x - h_{22}y - h_{23} = 0 \tag{6.8}$$

Each correspondence (identical keypoints between the target and reference images) provides two rows of matrix A. For a point correspondence, the Equation (6.7) and (6.8) can be written in matrix form as Ax = 0 as shown in Equation (6.9) where:

$$A = \begin{pmatrix} -x & -y & -1 & 0 & 0 & 0 & ux & uy & u \\ 0 & 0 & 0 & -x & -y & -1 & vx & uy & v \end{pmatrix} \tag{6.9}$$

and h_9 is set to 1 as shown in Equation (6.10) :

$$h = \begin{pmatrix} h_{11} & h_{12} & h_{13} & h_{21} & h_{22} & h_{23} & h_{31} & h_{32} & 1 \end{pmatrix}^T \tag{6.10}$$

The eight degrees of freedom of the homography matrix H can then be determined with at least four true point correspondences. When solving for H, it's important to note that no three points can be collinear, e.g. it should be evenly distributed. This is because a well-distributed points ensures a robust and accurate estimation of the homography transformation across the entire image. Thus, it will preserve the spatial relationship between different parts of the image, leading to a more accurate alignment.

6.3.1.4 Removal of Outliers

Outliers can be described as data points that significantly differ from the rest of the dataset. In ML, outliers can disproportionately influence the learning process and compromise the model's ability to generalize effectively to new data. As such, it is required to identify and correct such mistakes or errors in the data. Accordingly, data cleaning was performed by using the statistical description in section 6.2.2 to identify the outliers. Attitude angles in Pitch and Roll that were above 18° was considered as an outlier because they were unusual or extreme observations.

6.3.1.5 Normalisation of Data

Data normalisation is an important step in the ML process that involves transforming the data into a consistent scale, ensuring that all features have a similar range of values (Magee, 2023). Due to the different scales associated with the features in the training datasets such as the attitude angles and the homography parameters, data normalisation was performed. The Min-Max scaling data normalisation method was used to scale all the features from 0 to 1. The *MinMaxScaler* function from the *scikit-learn* (Pedregosa et al., 2011) library in Python was used for this process.

6.3.1.6 Data Splitting

Data splitting is a process that involves dividing all data into subsets (Magee, 2023). Typically, the data is broken down into a training, validation, and testing dataset (Cruz et al., 2023b). A training dataset is used to actually teach a machine learning model to recognize patterns and relationships between input and target variables, and is typically the largest dataset. Further, a validation dataset is a subset of data that is used to evaluate the performance of the ML model during training. It helps fine-tune the model by adjusting hyperparameters and also helps prevent overfitting of the training data. Lastly, a testing dataset is a subset of data that is used to evaluate the performance of the trained model. Its goal is to assess the accuracy of the model for new, unseen data. The testing dataset is only used after the model has been trained and fine-tuned on the training and validation datasets.

In this study, a stratified random sampling technique was used to split the data into three subsets which replicate best practice for ML drone applications used by (Cruz et al., 2023b; Thiruchittampalam et al., 2023). This technique was employed because of the slightly imbalanced proportion of the image type. The data was split in such a way that the proportion of each image class is the same in both the training and the validation dataset. Overall, 70% of the data was used for training, 15% was used for validation and 15% was used for testing. The datasets obtained from the field survey were used solely for the testing of the ML model. This was because these datasets contained GCPs, which enabled the accuracy assessment of the ML model.

6.3.2 Training and Assessment of the ML model

6.3.2.1 Model Training

After preparing the data, the next step of the ML process is to train the model. During this process, different ML algorithms were employed on the training dataset to identify and learn the patterns in the data. As indicated in section

2.5.4, the model was trained on three supervised algorithms: KNN, RF and SVM. The training process involved exploring the best hyperparameters to be used.

6.3.3 Hyperparameter Selection

In ML, hyperparameters are parameters that control the learning process of an ML model. They are set prior to training and guide the learning process and their choice can significantly impact the performance of an ML model (Bishop, 2006). Optimal hyperparameters can lead to a model that generalizes well to new data, while incorrect or poorly chosen hyperparameters can result in overfitting or underfitting (Jordan, 2017). The choice of hyperparameters for all the ML algorithms that were examined in this chapter were selected using the GridSearchCV module in Sklearn to iterate over a range of hyperparameters. In this process, the hyperparameters with the best results on the validation data were chosen to train the model.

6.3.4 Selection of ML Model

As the ML problem being investigated is a regression problem, the assessment of each ML algorithm used was evaluated using Root Mean Square Error (RMSE). RMSE is a commonly used method to assess the accuracy of a ML model because it shows how far predictions fall from measured true values using Euclidean distance and also provides a measure of error that is in the same unit as the target variable, making it easier to interpret and compare (Chai and Draxler, 2014). This process involved making a prediction of the homography matrix and testing it on the validation dataset. The evaluation was then carried out in order to help select the best performing ML algorithm. In the end, the selected best performing ML algorithm was used to test against the test dataset.

6.3.5 Geometric transformation of the model

The next step was to apply the pre-trained model on a new dataset (testing dataset) to geometrically transform the image. This geometric transformation

can be understood as a mathematical operation that transforms the target image onto a reference image (GIRARD and Girard, 2003). The different transformations comprise scaling, shearing, rotation, and translation of the target image (Cao et al., 2019). The geometric transformation was performed using the perspective transformation method. One of the key characteristics of perspective transformation is that straight lines remain straight even after the transformation. In the process, for a given pixel (x, y) in the original image, the homography transformation would yield a new position (x', y') in the transformed image. The transformation was applied in Python using the *cv.warpPerspective* function in OpenCV (Bradski, 2000).

6.3.6 Evaluation of the Trained Model

After the testing dataset has been transformed, an accuracy assessment was performed on the dataset. This assessment was performed to measure the accuracy of the transformed images by comparing its against a ground truth image (an image rectified using GCPs). The assessment was performed using the MAE method. The MAE was used for easy interpretation of the errors and also, it is less sensitive to outliers (Chai and Draxler, 2014).

6.4 Results

6.4.1 Analysis of Feature Detectors

The performance of the feature detectors were assessed by calculating the precision percentage. The precision percentage is calculated as the percentage of correct matches after filtering through RANSAC over the total matches. The test was conducted on selected images (n=200) comprising of 150 from the Sequoia dataset and 50 from the DJI FC6310 dataset. This sample size was chosen because it gives a good representation of the entire datasets and also to reduce the processing time of testing the feature detectors on the entire datasets. From the result in Table 6.2, the SIFT algorithm had the highest average keypoints detected. Also, the precision percentage analysis shows that SIFT provides the highest precision of 38% while the ORB had the lowest precision of 2%. Furthermore, it was found that all the detectors struggled to detect significant number of keypoints on the Sequoia datasets because of low sensor resolution of the Sequoia sensor (1.2 mega pixel resolution) coupled with the usual difficulty of finding keypoints over farmland due to its repetitive nature.

In contrast, the average number of keypoints detected from the DJI FC6310 sensor datasets was significantly higher, thus 50% higher than the Sequoia dataset. This was due to the very high sensor resolution (20 mega pixel). However, the higher resolution resulted in significantly longer processing times, approximately 60% longer than the Sequoia dataset.

Table 6.2: Analysis of Various Feature Detectors Showing the Precision Percentage and Average Number of Keypoints Detected.

Feature detector	Precision percentage			Average No. of keypoints		
	Sequoia	DJI FC6310 sensor	Total	Sequoia	DJI FC6310 sensor	Total
SIFT	30%	46%	38%	1570	2367	3937
KAZE	26%	40%	33%	1122	2184	3306
AKANZE	2%	9%	5%	646	970	1616
ORB	2%	3%	3%	352	777	1129

6.4.2 Analysis of the RANSAC threshold

This RANSAC threshold analysis was done to assess the best performing threshold to remove the outliers, an important step because the initial points detected contain incorrect matches and this helps to reduce the matching error. The accuracy of the RANSAC algorithm for outlier removal is greatly influenced by the threshold parameter used. For example, if the threshold is too large, then the RANSAC algorithm will generate a line which has higher probability to include outliers. However, if the threshold is too small then the RANSAC algorithm may find very few matches. As a result, selecting an optimal threshold that will give high accuracy while producing good number of matches is important. This optimum threshold was selected by calculating the weighted sum score. The two metrics used for the weighted sum score calculation were (i) accuracy in RMSE and (ii) the average number of keypoints detected for each threshold with both metrics normalised to have the same scale. The first metric was normalised to have the maximum value as 0 and the minimum value as 1. This is because the lower the RMSE, the better. In contrast, the second metric was normalised to have maximum value as 1 and the minimum value as 0 because the higher the number of keypoints detected the better. A higher weighting of 0.6 out of 1 was assigned to the first metric because it has greater influence on the accuracy of the derived homography while a lower score of 0.4 was assigned to the second metric.

From the Table 6.3, different thresholds from 0.8 to 0.2 were explored. From the result, high RMSE values were recorded for thresholds ranging from 0.6 to 0.8. This is because higher thresholds increases the tolerance of the algorithm, which leads to inclusion of bad matches in the filtering. Also, very low RMSE was recorded for thresholds ranging from 0.2 to 0.4. This is because, in such instances, the tolerance of the RANSAC algorithm is reduced, which is less sensitive to bad matches. However, these reduced thresholds produced very few good matches. Hence, this will likely increase the chances of uneven distribution of keypoints, which is essential for accurate estimation of the homography.

For these reasons, the highest weighted score which was the 0.5 threshold was selected as the optimum threshold. This threshold produces a low RMSE and as well a good number of correspondences which will ensure a fair and even distribution of keypoints.

Table 6.3: Accuracy Assessment of the Various Thresholds Explored and their Corresponding Average Number of Good Matches Detected

Threshold	**Accuracy**		**Correspondence detected**		**Score**
	Weighted score = 0.6		Weighted score = 0.4		
	RMSE	Normalisation	Average No. of correspondence	Normalisation	
0.8	20	0	1250	1	0.40
0.6	9	0.55	924	0.39	0.48
0.5	0.5	0.97	750	0.07	0.61
0.4	0.03	0.99	722	0.02	0.60
0.2	0.021	1	710	0	0.60

6.4.3 Evaluation of the ML Models on Validation Dataset

Assessing the performance of the ML algorithms in predicting the homography matrix is important in selecting the best-performing model. After the best feature detector algorithm and the optimal threshold has been identified to remove outliers, the next analysis was to evaluate the performance of the supervised algorithms used to train the model. This analysis assessed the accuracy of the ML models in predicting the output variables (homography parameters) using the input features. From the results in Table 6.4, the Sequoia dataset shows that KNN outperformed the other ML models. Also, the SVM recorded the poorest RMSE. Additionally, the DJI FC6310 sensor datasets on the other hand produced comparable accuracy among all the ML algorithms. As a result, there was no significant difference in their performance. The ML algorithms were able to produce similar results because the attitude angles from the DJI FC6310 sensor dataset were highly correlated as described in section 6.2.2.

Table 6.4: Accuracy Assessment of the ML Algorithms

Dataset	**ML model**	**Accuracy (RMSE)**
Sequoia	KNN	5.2
	RF	8.4
	SVM	12.3
DJI FC6310	KNN	2.8
	RF	3.1
	SVM	3.8

6.4.4 Accuracy Assessment on Test Data

After the evaluation of the ML model, the accuracy assessment was performed using the KNN algorithm on the testing dataset. The first accuracy assessment was conducted on the Sequoia datasets using the drone datasets acquired from the field survey. This dataset was used for the testing because it contained recorded GCPs which provided a reliable ground truth data. The DJI FC6310 sensor dataset was assessed using the Phantom 4 RTK dataset as indicated in the Table 6.1. This dataset was used for testing because it was acquired using an RTK GNSS mode, providing reliable ground truth data.

The result from Figure 6.6 and 4 showed that the Sequoia dataset had a MAE of 2.8m and MAE of 1.8m for the DJI FC6310 dataset. The results suggest that the AirMAP model is able to improve the accuracy by 84% for the Sequoia sensor and 63% for the DJI FC6310 sensor. Typically, due to the high tilt displacement effects in high tilted images, they tend to have significant MAE in XY. However, from the results in Figure 6.6, the AirMAP model was able to reduce the MAE in XY. The results shows that the model was also able to significantly reduce the MAE for high tilt images by 80%. Overall, the AirMAP model performed well across the different types of images, thus showing its robustness.

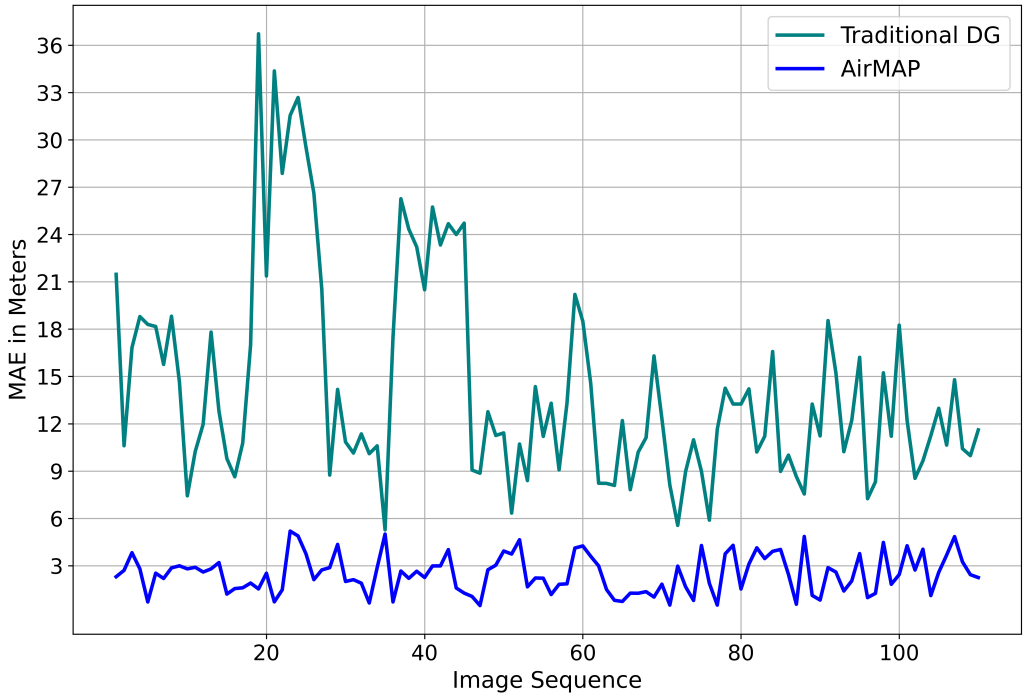

Figure 6.6: A graph showing the accuracy Assessment of the Sequoia dataset. This graph shows that the AirMAP is able to reduce the MAE by approximately 84%.

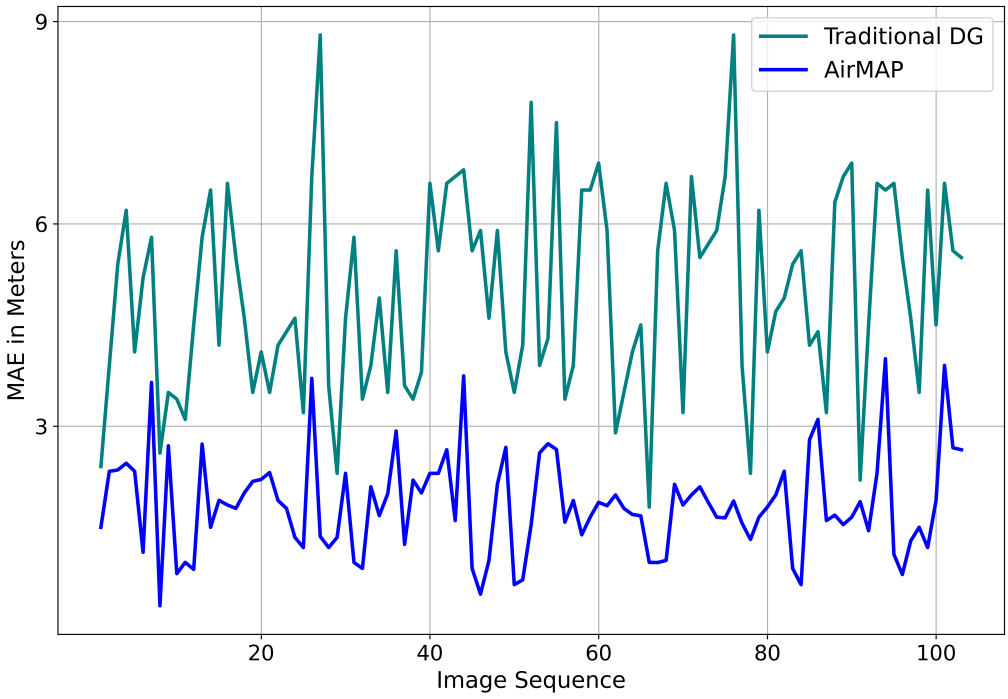

Figure 6.7: A graph showing the accuracy Assessment of the DJI FC6310 dataset. This graph shows that the AirMAP is able to reduce the MAE by approximately 63%.

6.4.4.1 Example of Test Results

This section compares sample images of the results produced by the AirMAP approach and the traditional DG method. To evaluate and demonstrate the applicability of the AirMAP approach, a survey over Blessington Lake, an inland water was used for the assessment. Due to the difficulty of placing targets as previously explained in Section 4.3, the assessment was carried out using static features on the shore. The survey had about 10 images captured with the shore in view. For the purpose of illustration, 3 images are presented in the Figure 6.8. The images are shown in pairs, with the traditional DG method on the left and the AirMAP method on the right. Additionally, an orthomosaic of the entire survey over the water produced from the AirMAP model has been produced and can be seen in Appendix C. The ground truth for the accuracy assessment was obtained from Ordnance Survey Ireland (OSI) high resolution aerial photo. This provided a good benchmark dataset to compare the two methods. From the example results, the AirMAP method improved the accuracy of the reconstructed image, hence providing evidence of its applicability and effectiveness over water.

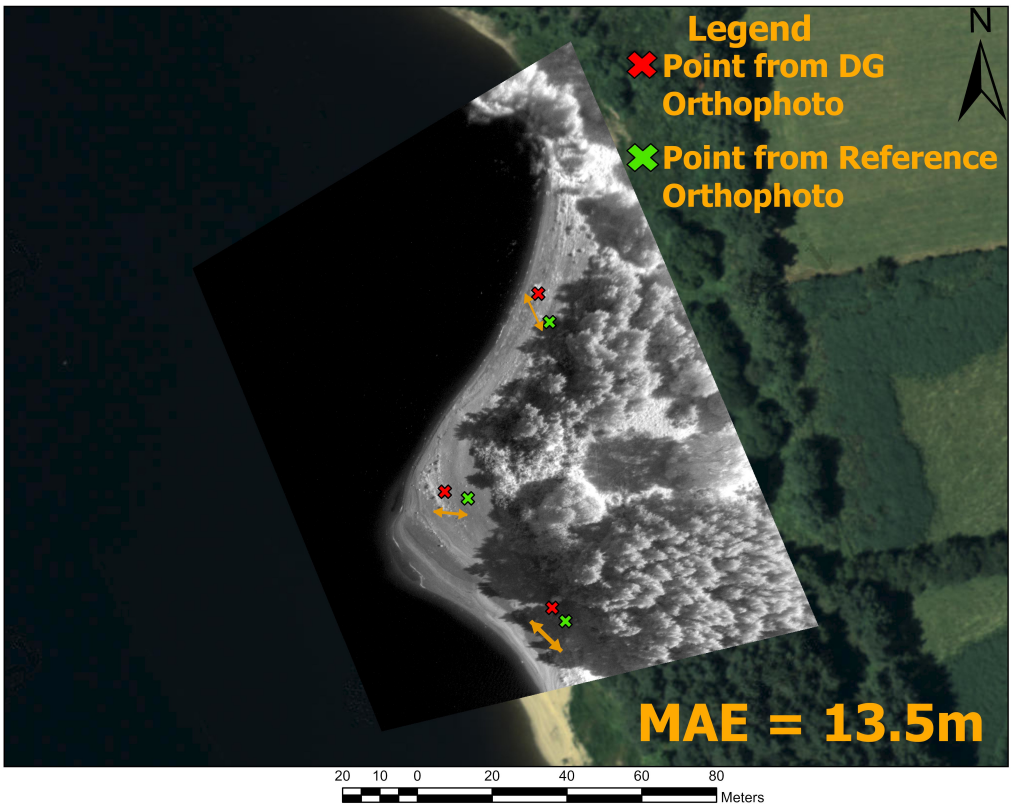

(a) DG Method

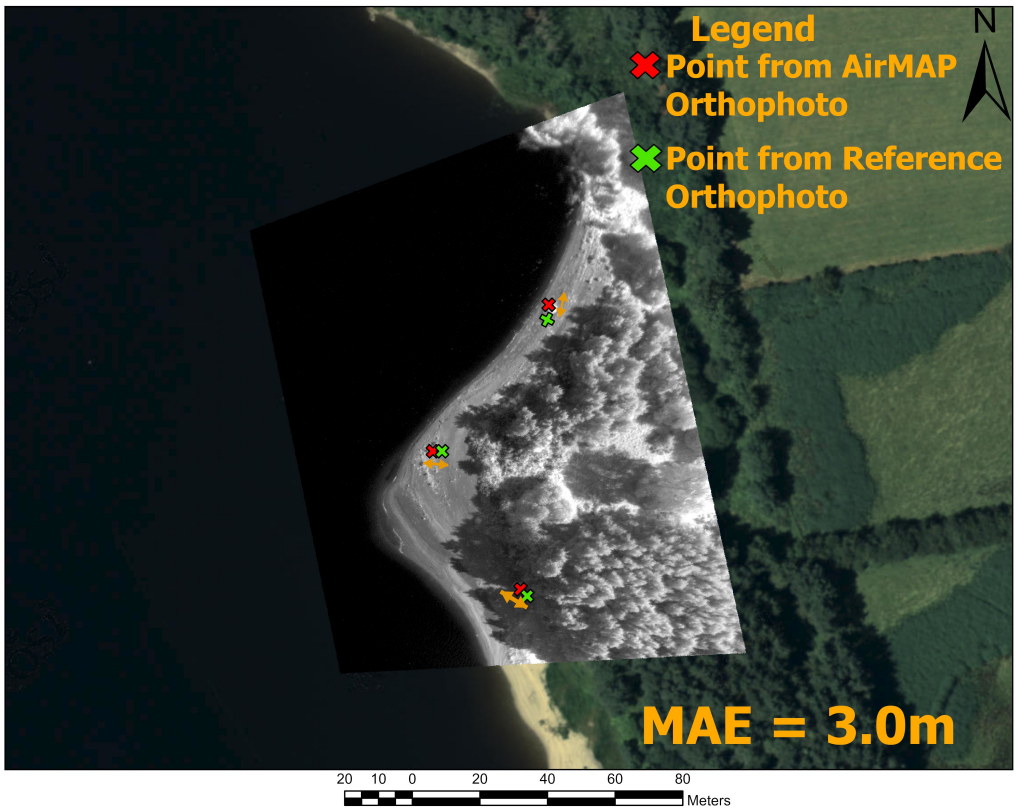

(b) ADGEO Method

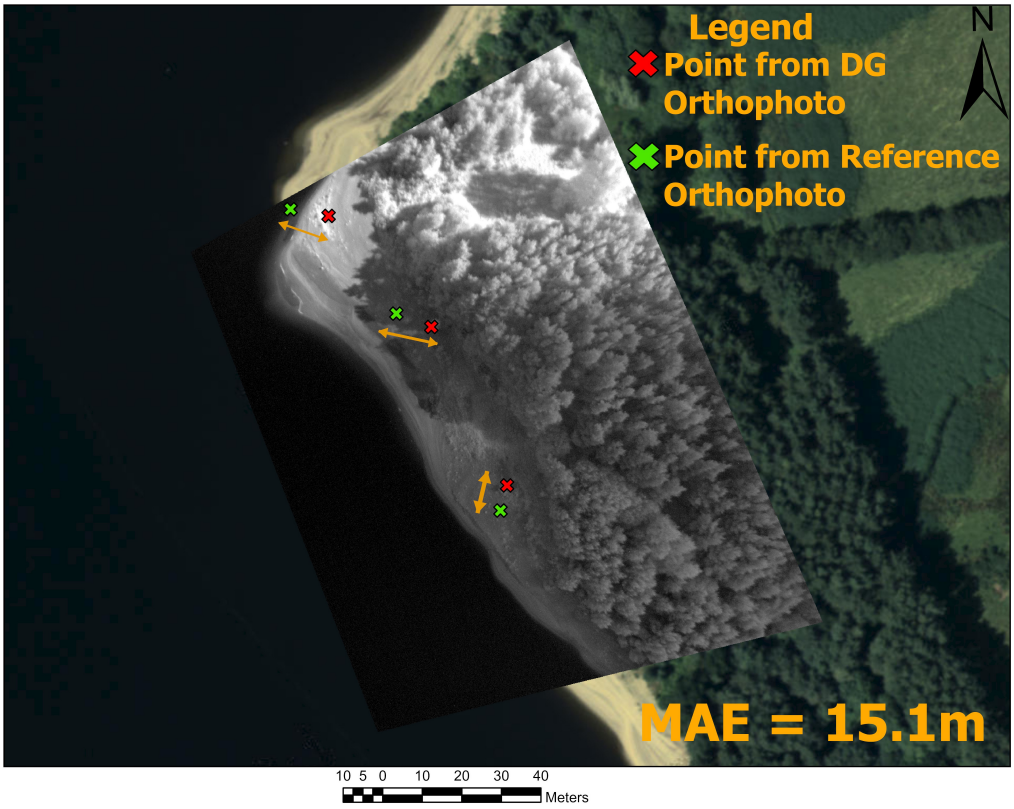

(c) DG Method

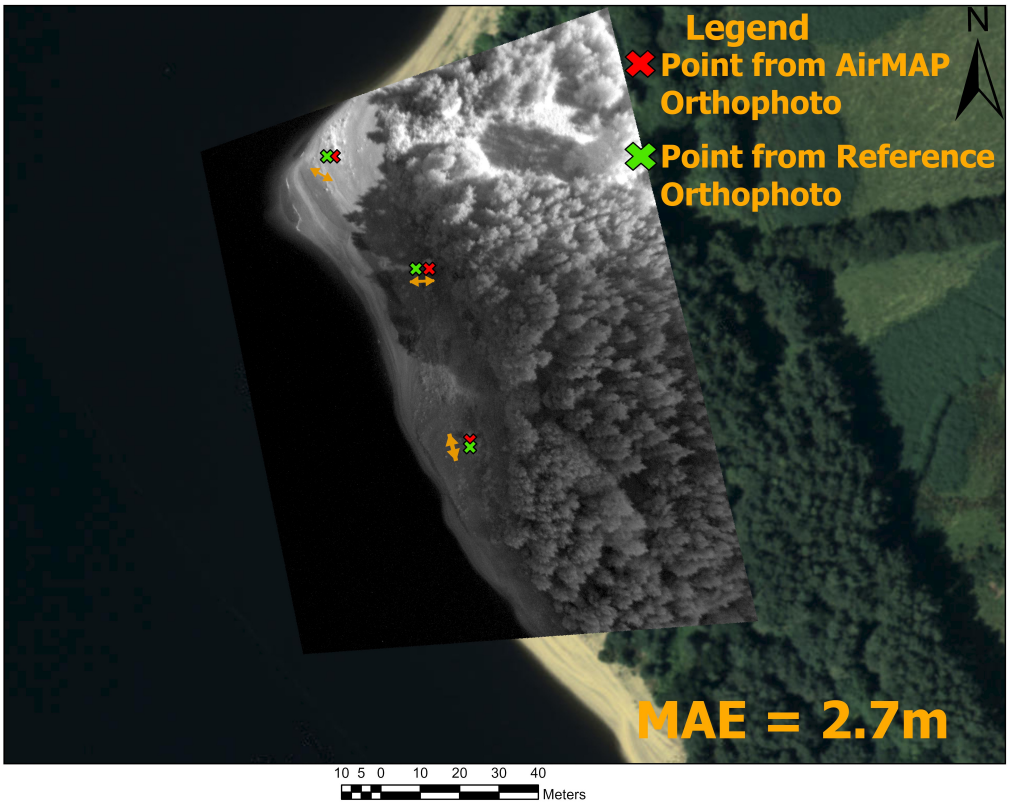

(d) ADGEO Method

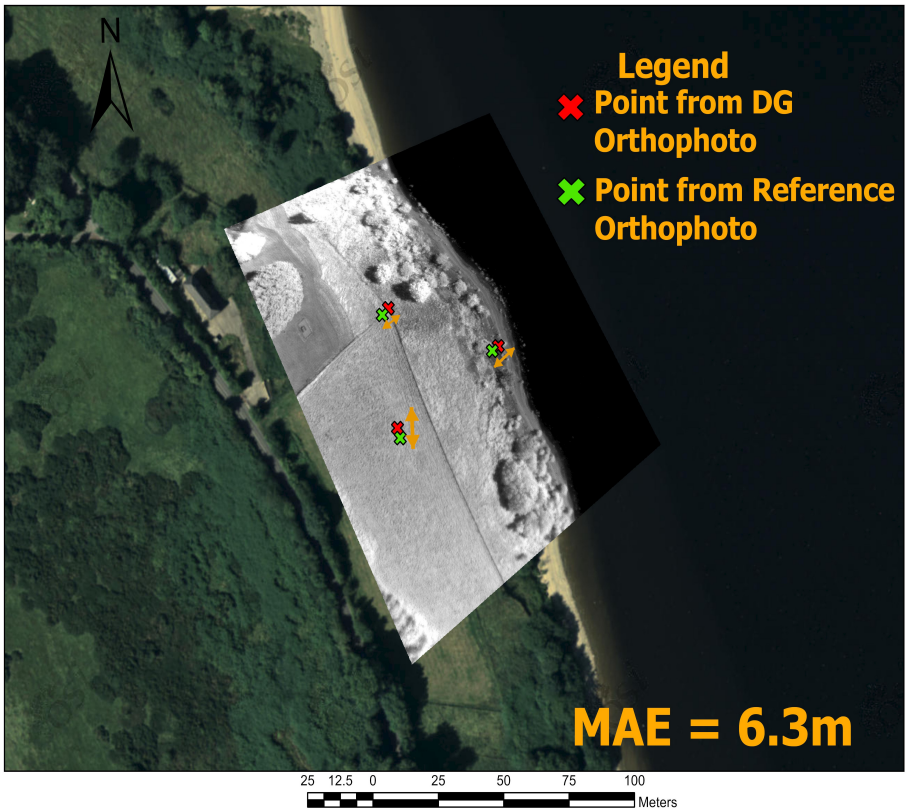

(e) DG Method

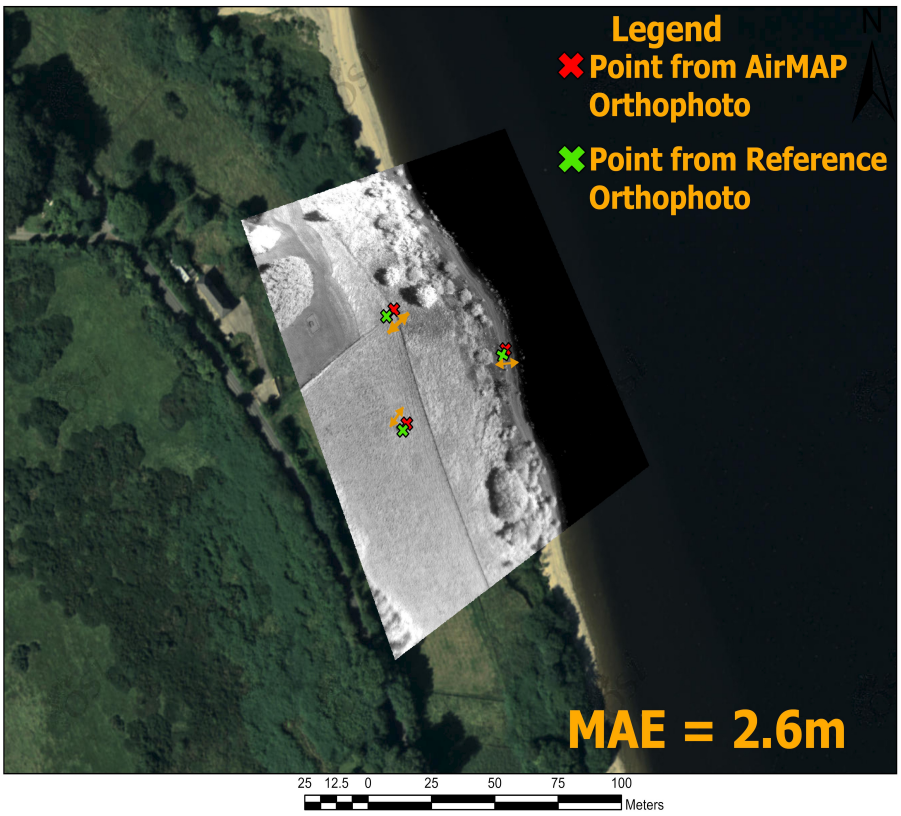

(f) ADGEO Method

Figure 6.8: Example results of selected reconstructed images and their MAE via traditional DG and AirMap. The images are overlaid on OSI high-resolution aerial photo. The red arrow indicated on the map illustrates the magnitude of the misalignment.

6.5 Discussion

6.5.1 Data Quality

As postulated in Priestley et al. (2023); Chen (2022) and Magee (2023), the importance of data quality in ML cannot be overstated, as the performance and reliability of any ML models are heavily dependent on the quality of the data used for training and testing. Due to this, it is essential to explore the quality of data used to train the model.

Firstly, one of the most significant factors ensuring data suitability for a drone methodology intended for water surveys was the acquisition of sufficient data over flat terrain. Secondly, having representative training data is crucial for the model to learn and generalize well. This will mean that acquiring a drone dataset with varying viewing angles in Pitch and Roll is important for the model to learn. As explained in Kotsiantis (2007), one of the goals of ML model is to learn from examples and generalize with some degree of knowledge. From the description of the dataset in section 6.2.2, it can be seen that the dataset acquired provides a good representation for each of the three categories of images. In this case, the trained model will not be biased. Models with high bias often suffer from underfitting, poor generalisation and inability to learn complex relationship (Jordan, 2017). In this study, the results from Figure 6.6 demonstrate that both low and high MAE values from the traditional DG are reduced. This suggests that the AirMAP is not biased in only enhancing images with low MAE, which is typically caused by low wind speeds, but can also improve images with high MAE, which is often due to moderate to high wind conditions.

Further, another data quality issue that has significant impact on the ML performance is data labelling (Magee, 2023). The process of data labelling could be susceptible to various sources of errors that can introduce noise and inaccuracies into the training dataset (Schubert et al., 2023). Given the potential error sources

such as human annotation errors and misclassification that can be incorporated into labelled datasets, it is important to correct for labelling errors. In this proposed AirMAP model, data label errors will directly affect the accuracy of the predicted homography matrix. Inaccurate data labels introduce noise into the data training process. The sensitivity of noisy data means that even a small number of mislabelled features can have a disproportionate impact on the accuracy. This can lead to poor registration of images which will affect the MAE in XY of the registered images.

6.5.2 Evaluation of the ML Model

The performances of ML algorithms depend greatly on the general characteristics of the training dataset (Boateng et al., 2020). Thus, there is no specified ML algorithm that works best on any given problem. Therefore, to determine the best ML algorithm for a given problem or datasets, multiple ML algorithms with different hyperparameters are tested to decide on the best algorithm.

From the results, the KNN algorithm was the best performing ML model for the Sequoia and DJI FC6310 sensor datasets. The high performance of the KNN ML model could be influenced by various factors. Firstly, the characteristic of the dataset had an influence on the performance of the KNN algorithm. This was because the dataset was fairly balanced with sufficient data on the different viewing angles. KNN is a type of machine learning algorithm that makes predictions based on the similarity of data points. Hence, it could perform well if similar data points are found.

As explained in computer vision and remote sensing papers by Boateng et al. (2020) and Srivastava (2020), KNN works on the assumption that similar things exist in close proximity. In this process, the training data is stored and when a prediction is required, the K-most similar records from the training datasets are located and from this, a prediction is made. In the context of this study, the

training data used had a good distribution of different viewing angles. In this case, when a prediction is supposed to be made, the KNN model is able to search through the trained data for similar records to make an accurate prediction. Unlike the other ML models where the prediction is based on learning the patterns from the data. Thus, these methods assume a specific mathematical form for the data for prediction. Also, in scenarios where the features are highly correlated, the decision boundaries of RF and SVM may be affected. Thus, high correlation between features can affect their ability to create accurate decision boundaries. The KNN on the other hand, doesn't draw explicit decision boundaries. Instead, it looks at the distance between data points to make predictions. This makes it less sensitive to the specific mathematical relationships between features.

Further, KNN is a non-parametric algorithm, meaning it makes minimal assumptions about the underlying distribution of the data. Thus, the structure of the model is determined by the data itself and this is quite convenient, because in the "real world", most data do not obey pre-established patterns (Barbarella et al., 2021). Also, it can adapt well to different types of datasets without assuming a specific functional form for the decision boundaries. This flexibility can be advantageous when dealing with complex relationships that may not be easily captured by parametric models like SVM. Overall, the result from the KNN ML algorithm demonstrates and confirms the predictive performance of ML (Kigo et al., 2023).

6.5.3 Accuracy Assessment of the AirMAP Method

Based on the results in section 6.4.4, the accuracy assessment demonstrated that the AirMAP model was able to improve the planimetric accuracy of the orthoimagery by 84% and 63% for the Sequoia and the DJI FC6310 sensor dataset respectively.

Comparing the results to the ARMFET and the ADGEO methods presented in the Chapter 4 and 5 respectively, the AirMAP model significantly outperformed the former while marginally outperforming the latter in improving the planimetric of the orthoimagery. This can be attributed to the AirMAP model's ability to learn from large datasets that contains different viewing angles. This ability enables the model to learn the patterns, fostering a robust learning process that significantly contributes to its accuracy. Thus, it can be concluded that the AirMAP approach closely approximates the BA's accuracy to a greater extent than the two aforementioned methods. Nonetheless, the intention of the proposed AirMAP is not primarily to outperform the BA method. Rather, it strives to achieve a higher operational applicability by enabling its application in situations such as high attitude measurement and not dependent on the shores to improve accuracy while reliably reaching an accuracy below 3m.

Further, one main limitation of the traditional DG method is that the accuracy of the resultant reconstructed image is dependent on the orientation influence. Thus, higher attitude measurement in Pitch and Roll will lead to higher MAE in XY. However, the findings from the Sequoia dataset suggest that the AirMAP model's accuracy is less sensitive to high attitude angular measurements. This means that the AirMAP method can effectively enhance the planimetric accuracy in conditions of low and high attitude measurement. Nevertheless, to achieve a much better or optimum result, the larger proportion of the dataset to be registered should not fall between 15°-18°. This is because the model might struggle to produce an optimum result to improve the accuracy of images that falls within such range. While the operation threshold for the AirMAP model is between 0°-18°, the insufficient training data within this range prevents the model from generalizing effectively. Hence, to optimise the performance of the AirMAP model, it is important to ensure that only a limited proportion of attitude angles in a given dataset falls within that range.

6.5.4 Applicability of the AirMAP Model

The AirMAP method will provide an opportunity to map over water surfaces at different geographic scales. Particularly, it can effectively map large-sized, medium and small size water bodies. Mostly, mapping a large to medium sized water body has limitations such as extensive and prolonged data collection, varying viewing angles, as well as distinct data processing techniques (Lo et al., 2023). Due to these existing limitations, the AirMAP method provides the technique that can seamlessly reconstruct a high quality orthomosaic over a large-sized water body. Hence, the AirMAP method can particularly be useful in mapping water bodies in Ireland.

In Ireland, the EPA's reporting cut-off for lake water quality monitoring is 50 ha or 0.5 km^2 (Dalton, 2018). Thus, a total of 224 lakes are currently included in the EPA's national surface waters monitoring programme (Delaney et al., 2023). Out of these lakes, 111 are greater than 1 km^2 or 100 ha, which can be considered as large sized lakes. This effectively highlights the significance and the potential applicability of the AirMAP method.

Furthermore, this model provides the opportunity to map over water without relying on the shore as a reference to improve accuracy. This model closes the gap of the main limitation of the ADGEO method in situations where the shore might have unfavourable terrain such as high vegetative cover, hilly areas, etc. Additionally, the model can effectively work in situations where there is high attitude measurement as a result of strong winds.

Further, one of the main problems with drone mapping over water is the standardisation of the accuracy of orthoimagery for water pollution time series analysis. Typically, when monitoring the evolution of water pollution, significant differences in positional accuracies of the orthoimageries acquired over different dates will lead to image overlay mismatches, consequently causing mixed

change or inaccurate detections. These constrains are affected by the tradional DG method where accuracies are dependent on the attitude measurement. The development of the AirMAP method provides the opportunity to standardise the accuracy derived from multiple orthoimageries over water. This will ensure timely intervention and mitigation of pollution events.

Another advantage of the model is that it does not require a specific overlap percentage. Thus, the performance of the model is not dependent on the overlap percentage and lower overlap percentages can be leveraged during surveys to increase the efficiency of flight time. On the other hand, the specified flight height recommended for data collection is 120m. This is because the training of the model was based on data collected at this specified flying height. Hence, the model is fine-tuned to perform best at the height of 120m. This specified height was used because that is the maximum height an operator can fly a drone in the open category under the EU drone regulations (European Union Aviation Safety Agency, 2019). This height helps maximize the area coverage and improves the flight time as well.

In summary, the workflow for the AirMAP model can be replicated for different sensors. Also, regarding its usability, the pre-trained model can easily be used for a new datasets in Python. This offers an easy way to automate the process.

6.5.5 Limitations of the AirMAP Model

The main limitation of the model is that it is computationally demanding. Over the years, one key disadvantage of using ML models is that it requires powerful computers to process large datasets. Also, the model is data driven and requires sufficient training data to be collected and labelled. Labelling large datasets can be very tedious and time consuming Cruz et al. (2023a); Magee (2023). Moreso, the model is sensor specific and would require a similar process to be followed

when training for different sensors. This makes the model less transferrable than use of the shore in ADGEO or image corrections through ARMFET.

6.6 Conclusion

This chapter presented a method called AirMAP - a method for improving the accuracy of reconstructed images over water using image registration techniques coupled with ML. This model was built and trained on large datasets containing varying viewing angles. One of the main contributions of this chapter was to develop a novel method that can be applied to map water bodies at different geographic scales while not depending on the shore as reference to improve accuracy. In this chapter, the dataset for the training, validation and testing were acquired from two sensors: Sequoia and DJI FC6310. These datasets were trained on three ML algorithms: KNN, RF and SVM. The findings revealed that the KNN algorithm was the best-performing algorithm for predicting the homography matrix. The results from the accuracy assessment demonstrated that the AirMAP model can achieve a MAE of 2.8m and 1.9m for the Sequoia and the DJI FC6310 sensor respectively. It was found that to optimise the performance of the model, it is imperative to ensure that only a limited proportion of attitude angles in a given dataset fall within 15 deg to 18 deg.

Furthermore, the findings demonstrated that the proposed model closely approximate the BA's accuracy as compared to the traditional Direct Georeferencing (DG) approach. The usability of the model can be achieved by using the pre-trained model in python. Moreover, the workflow for the model can be replicated for different sensors. The novelty of the AirMAP model is particularly seen in its robustness, its operational applicability, and its automated approach.

Chapter 7

Conclusions and Future Works

The main goal of this thesis was to explore and enhance the traditional photogrammetric methods that are employed to map water bodies using low-cost drones. The core contributions of this thesis included: 1) a theoretical assessment to benchmark the accuracy of navigational errors, which was validated using real-world data, 2) development of a novel analytical photogrammetric method to improve the traditional DG approach, 3) development of a novel method that exploits the features from the shore to further enhance the DG approach and 4) development of a scalable method for mapping larger water bodies.

This chapter first summarises the methods from this doctoral thesis in Section 7.1. It follows this with a presentation of the main novel contributions to the area of mapping water bodies with low-cost drones in Section 7.2. Potential improvements to the methods developed in this thesis are detailed in Section 7.3. This chapter concludes with some final remarks on the work in this thesis in Section 7.4.

7.1 Thesis Summary

This thesis investigated the area of mapping water bodies with low-cost drones, and through a detailed literature review, gaps in the current knowledge were identified. Based on these gaps in knowledge, four research objectives were identified.

7.1.1 Objective 1: Benchmark and Test the Accuracy of the DG Method

The literature review identified that to-date, no research had been carried out to benchmark the accuracy of drone images of water bodies generated using the DG method. As a result, benchmarking and testing the accuracy of imagery obtained from low-cost drones required developing a simulator for theoretical analysis. These theoretical tests were carried out to determine the effects of errors from navigational sensors identified in Chapter 3. These errors were divided into three: GNSS errors, IMU errors and sensor rotation angle influence.

7.1.2 Objective 2: To Analyse the associated errors in the images derived using the DG method and propose an analytical photogrammetric method to improve them

This phase of the research was the natural progression on the theoretical test and was essential for validating the traditional DG method using real-world datasets. Identifying and quantifying the errors associated with imagery derived from the DG method was crucial to developing novel photogrammetric methods that can effectively improve the accuracy of the reconstructed 2D images. The lack of attention among photogrammatrist in minimising these errors provided the motivation to develop the novel ARMFET method. This method was explored and discussed in Chapter 4.

7.1.3 Objective 3: To develop a method that integrates BA and DG in a single workflow by using the features from the shore as a reference to enhance the accuracy of drone imagery over water bodies

The methodology designed for the second objective had a limitation: the accuracy improvement was tied to the accuracy of the attitude angles measured by the IMU. To further close the gap between low-cost drones and high-end drones, there was the need to explore whether it was possible to combine both DG and BA in an established photogrammetric technique known as ISO. This novel methodology was theoretically tested using synthetic data and validated using real-world data. The results from the test and the validation were detailed in Chapter 5.

7.1.4 Objective 4: To develop a method that aims to improve accuracy, efficiency, and scalability for generating orthoimagery for larger water bodies

The last objective of this thesis was to develop a generalisable methodology that does not rely on the shore as a reference for improving the accuracy of drone imagery over water. This novel methodology involved training ML algorithms on drone datasets containing diverse attitude angles. This methodology required the estimation of transformation parameters from a pre-trained model to improve the accuracy of drone imagery over water. This method was explored and discussed in Chapter 6.

7.2 Main Contributions to the Field of Mapping Water Bodies with Low-cost Drones

The work carried out in this thesis contributed to four primary areas relating to the field of mapping water bodies with low-cost drones. In the following sections, the methodology designed to complete each objective and the tests carried out are briefly assessed in terms of their contribution to the body of knowledge in this field.

7.2.1 Benchmarking the DG Method

One area in which the DG method has not received attention is its potential for use with low-cost drones for mapping water bodies. During the literature review, it was identified that no research had been carried out **to benchmark** the accuracy of drone images of water bodies generated using the DG method. Although existing studies have employed the DG method for mapping water bodies, neither of these studies benchmarked the accuracy of the DG method.

The thesis addressed these shortcomings by developing a simulator that enabled benchmarking and that was validated with real-world data. The simulator was developed using the standard photogrammetric collinearity equations to quantify and analyse the error sources that limit the accuracy of a reconstructed 2D image in Chapter 3. The error sources that most contributed to this were identified as GNSS and IMU errors and sensor rotation angle influence. The theoretical test results revealed that the accuracy of the sensor orientation had the greatest influence on the accuracy of the reconstructed 2D image compared to the GNSS and IMU errors. A central finding of the application of the DG method was that it yielded significant errors in the resulting reconstructed 2D images. Such errors have a detrimental effect on its potential application in water monitoring applications. The work done in this study has provided a detail understanding of the accuracy of DG method when using low-cost drones for mapping water bodies.

This will help drone operators to be well informed of the error tolerance of their drone. The focus in subsequent chapters of the thesis was to develop methods to improve the accuracy.

7.2.2 Developing an Analytical Photogrammetric Method

One of the core contributions of this thesis was to develop the analytical photogrammetric method, ARMFET, which is presented in Chapter 4. During the literature review, it was also identified that no studies have been carried out **to improve** the accuracy of the resulting imagery derived through the DG method. Additionally, no studies had explored or analysed the errors associated with using the DG method for low-cost drones for mapping water bodies. These errors were identified as ground principal point offsets, tilt displacement and scale variations. The ARMFET method was therefore developed to correct for these errors without using GCPs and was compared to the traditional DG images. The results confirmed that this method was able to improve the accuracy of reconstructed 2D images derived from the DG method. Furthermore, the influence of wind speed and direction on attitude angles was quantified. The work done in this study has shown that analytical photogrammetric method can be used to remove errors associated with images captured over water. This method enhances the filed of photogrammetry as no such method has been explored in correcting for the errors associated with DG without using GCPs.

7.2.3 Developing a Method that Exploits the Shore

Although the novel ARMFET method performed well and had its strengths, Chapter 5 identified limitations that required improvement. The main limitation was that its accuracy relied heavily on measuring accurate attitude angles and this led to inaccuracies in the calculated tilt corrections which did not reflect the true error on the ground. To further close the gap between low-cost drones and high-end drones, there was a need for further exploration on developing a method that could exploit the shore in an adaption of the ISO technique. This led to the de-

velopment of the novel ADGEO method, which combined the benefits of BA and DG to improve the accuracy of drone imagery over water.

To evaluate and test the ADGEO method's accuracy, a two-part assessment was carried out. The first assessment was a theoretical analysis that detailed the performance and limitations under different attitude measurements using synthetic data. The effects of the attitude angles in influencing accuracy were also investigated. The results from the theoretical analysis demonstrated that ADGEO could achieve significantly better accuracy than the traditional DG method and this was validated using real-world data in the second part of the assessment for two scenarios: (1) where there were two shores in view, and (2) where there was one shore in view. It was observed that the ADGEO method significantly improved the accuracy of the reconstructed 2D images. The optimum overlap percentage that produced a better accuracy when using the ADGEO method was identified. The work done in this study has provided a method that drone operators or photogrammetrist can adopt to map water bodies. This method provides a solution to the long-lasting problem that photogrammetrist face in terms of improving the accuracy of images over the water when using low-cost drones. In broader context, this method can be applied both in coastal and inland waters.

7.2.4 Scaling for Mapping Larger Water Bodies

Although ADGEO improves on the traditional DG method through the integration of BA in areas of visual features (i.e. the shore), it has a built-in shortcoming in that it requires such areas to have favourable shore geometry. Also, it has a limitation of reduced accuracy in conditions with highly variable attitude measurements such as strong winds. Consequently, these limitations hinder the applicability of ADGEO in certain situations.

In Chapter 6, these shortcomings were addressed through a novel ML approach called the AirMAP. The advantage of this approach was that it allowed enhance

accuracy without the need for shore features. Additionally, it is a scalable method that can be applied to map larger water bodies. This method presented a novel approach for mapping water bodies using image registration techniques and a ML approach. The results identified the best-performing ML algorithm for predicting the transformation parameters for image registration. The experimental tests identified the best-performing feature detector algorithm and threshold for removing bad keypoint matches. The accuracy assessment demonstrated that the AirMAP method could significantly improve the accuracy of drone imagery when mapping water bodies. The AirMAP method was observed to closely approximate the BA's accuracy compared to the traditional DG approach. This study is important work as we start to refine our understanding of our environment and for Monitoring, Reporting and verification (MRV) that is now required under various Environmental legislation. Also there are several moves to build digital twins that will demand the most accurate data. The techniques devised here could integrate with those goals to deliver highly accurate data and aid with advanced environmental monitoring using low cost drones.

7.3 Future Work

This thesis explored and enhanced photogrammetric methods for mapping water bodies using low-cost drones. In the course of the development of these methods, several areas were identified for future work where further research and analysis could advance and benefit the methods developed as part of this thesis.

7.3.1 Additional Data Source

One significant challenge encountered during the development of the AirMAP method was acquiring training data with diverse flight parameters and sensor models as collecting real-world drone datasets through extensive flight campaigns over large flat open fields proved challenging. Therefore, additional work is required to generate synthetic data to supplement real-world data. As demon-

strated in various ML studies, synthetic data plays a crucial role in building robust models. Platforms like Microsoft AirSim, an open-source and cross-platform simulation environment designed for autonomous systems like drones, cars, and robots, offer the potential to simulate the drone's sensor and flight dynamics in any virtual 3D environment. This would allow incorporating diverse flight parameters into the model, which will lead to the overall robustness and adaptability of the model.

7.3.2 Algorithm Improvements

In the course of this research, avenues where ADGEO and AirMAP methods can be improved have been identified.

7.3.2.1 ADGEO Method

ADGEO currently calculates and predicts offset errors independently for each flight line, based on images captured with the shore in view. One potential improvement could be to combine all flight lines to collectively predict the offset errors. However, this requires modifying the model architecture to handle input data from every flight line. Exploring mathematical techniques such as Singular Value Decomposition (SVD) to decompose the ADGEO matrix equation into singular values and vectors that could allow handling a larger number of input data.

7.3.2.2 AirMAP Method

The AirMAP model was trained using supervised ML algorithms. While these algorithms provided a solid foundation for the model's functionality, an opportunity exists to further enhance its robustness. Deep learning approaches, such as Neural Networks and Multilayer Perceptrons (MLPs), present compelling avenues for achieving this goal. Neural Networks, characterised by their ability to learn complex patterns from large datasets, offer significant potential for improving the performance of the AirMAP model. Similarly, MLPs, a type of feed-

forward neural network architecture, offer another promising approach for enhancing the AirMAP model's capabilities.

7.4 Final Remarks

The initial motivation for this thesis was to monitor water quality using low-cost drones. This motivation led the researcher to focus on the development of photogrammetric techniques that can be used to prepare a dataset to monitor water quality. Despite the challenges identified, this study proposed solutions that successfully enhanced the performance of low-cost drones for mapping water bodies. The contributions from this thesis add to the current knowledge, providing robust and practical techniques that can be utilised by state institutions like the Environmental Protection Agency, local government authorities, researchers, and non-governmental organisations. While the use of low-cost drones for mapping water bodies remains understudied, it is the author's opinion that significant advancements in the field are likely to occur in the coming years.

Bibliography

Aber, J., Marzolff, I., Ries, J., and Aber, S. (2019). *Small-Format Aerial Photography and UAS Imagery: Principles, Techniques and Geoscience Applications*. Elsevier, Oxford, second edition.

Adelson, J. H. (2020). *Remote sensing of suspended sediment in san francisco bay using satellite and drone imagery*. PhD thesis, Stanford University.

Adjovu, G. E., Stephen, H., James, D., and Ahmad, S. (2023). Overview of the Application of Remote Sensing in Effective Monitoring of Water Quality Parameters. *Remote Sensing*, 15(7).

Ahmed, U., Mumtaz, R., Anwar, H., Shah, A. A., and Irfan, R. (2019). E ffi cient Water Quality Prediction Using Supervised. *Water (Switzerland)*, 11:1–14.

Airbus (2018). Airbus Specifications. https://www.intelligence-airbusds.com/en/8693-spot-67 (accesed 20 october 2023).

Alatise, M. B. and Hancke, G. P. (2017). Pose estimation of a mobile robot based on fusion of IMU data and vision data using an extended kalman filter. *Sensors (Switzerland)*, 17(10).

Arango, J. G. and Nairn, R. W. (2019). Prediction of Optical and Non-Optical Water Quality Parameters in Oligotrophic and Eutrophic Systems Using a Small Unmanned Aerial System. *Drones*, 4(1):1–21.

Azim, S., Rasmussen, J., Nielsen, J., Gislum, R., Laursen, M. S., and Christensen, S. (2019). Manual geo-rectification to improve the spatial accuracy of

ortho-mosaics based on images from consumer-grade unmanned aerial vehicles (UAVs). *Precision Agriculture*, 20(6):1199–1210.

Bagherbandi, M., Jouybari, A., Nilfouroushan, F., and gren, J. (2022). Deflection of Vertical Effect on Direct Georeferencing in Aerial Mobile Mapping Systems: A Case Study in Sweden. *Photogrammetric Record*, 37(179):285–305.

Barbarella, M., Di Benedetto, A., and Fiani, M. (2021). Application of supervised machine learning technique on lidar data for monitoring coastal land evolution. *Remote Sensing*, 13(23):8–21.

Bäumker, M., Heimes, F., and Bochum, F. (2002). New Calibration and Computing Method for Direct Georeferencing of Image and Scanner Data Using the Position and Angular Data of an Hybrid Inertial Navigation System. In *OEEPE Workshop on Integrated Sensor Orientation*, pages 1–17.

Behan, A. (2004). *Digital Photogrammetry: Theory and Applications*, volume 19. Dusseldorf.

Bernardes, E. and Viollet, S. (2022). Quaternion to Euler angles conversion: A direct, general and computationally efficient method. *PLoS ONE*, 17(11 November):1–13.

Bikov, T., Mihaylov, G., Iliev, T., and Stoyanov, I. (2022). Drone Surveillance in the Modern Agriculture. In *2022 8th International Conference on Energy Efficiency and Agricultural Engineering, EE and AE 2022 - Proceedings*, number July, pages 1–4, Ruse, Bulgaria. IEEE.

Bishop, C. M. (2006). *Pattern Recognition and Machine Learning*. Springer Science+Business Media, LLC, Singapore.

Blackwell, R. J. and Boland, D. H. (1979). Trophic classification of selected Colorado lakes. *Earth Resources Application Group*, pages 78–100.

Bláha, M., Eisenbeiss, H., Grimm, D., and Limpach, P. (2012). Direct Georefer-

encing of Uavs. *ISPRS - International Archives of the Photogrammetry, Remote Sensing and Spatial Information Sciences*, XXXVIII-1/(September):131–136.

Boateng, E. Y., Otoo, J., and Abaye, D. A. (2020). Basic Tenets of Classification Algorithms K-Nearest-Neighbor, Support Vector Machine, Random Forest and Neural Network: A Review. *Journal of Data Analysis and Information Processing*, 08(04):341–357.

Bossoukpe, M., Faye, E., Ndiaye, O., Diatta, S., Diatta, O., Diouf, A. A., Dendoncker, M., Assouma, H., and Taugourdeau, S. (2021). Low-cost drones help measure tree characteristics in the Sahelian savanna. *Journal of Arid Environments*, 187:1–8.

Bouchiha, R. and Besbes, K. (2015). Comparison of local descriptors for automatic remote sensing image registration. *Signal, Image and Video Processing*, 9(2):463–469.

Bouthillier, X., Delaunay, P., Bronzi, M., Trofimov, A., Nichyporuk, B., Szeto, J., Sepah, N., Raff, E., Madan, K., Voleti, V., Kahou, S. E., Michalski, V., Serdyuk, D., Arbel, T., Pal, C., Varoquaux, G., and Vincent, P. (2021). Accounting for Variance in Machine Learning Benchmarks. In *4th Conference on Machine Learning and Systems*.

Bouziani, M., Amraoui, M., and Kellouch, S. (2021a). Comparison assessment of digital 3d models obtained by drone-based lidar and drone imagery. *International Archives of the Photogrammetry, Remote Sensing and Spatial Information Sciences - ISPRS Archives*, 46(4/W5-2021):113–118.

Bouziani, M., Chaaba, H., and Ettarid, M. (2021b). EVALUATION of 3D BUILDING MODEL USING TERRESTRIAL LASER SCANNING and DRONE PHOTOGRAMMETRY. *International Archives of the Photogrammetry, Remote Sensing and Spatial Information Sciences - ISPRS Archives*, 46(4/W4-2021):39–42.

Bradski, G. (2000). The OpenCV Library. *Dr. Dobb's Journal of Software Tools*, 25:120–123.

Brown, K. M., Foody, G. M., and Atkinson, P. M. (2007). Modelling geometric and misregistration error in airborne sensor data to enhance change detection. *International Journal of Remote Sensing*, 28(12):2857–2879.

Brown, L., Morris, H., Bourg, L., Goryl, P., Dransfeld, S., and Dash, J. (2020). The Sentinel-3 OLCI Terrestrial Chlorophyll Index (OTCI): Algorithm Improvements , Spatiotemporal. (Lcc):1–22.

Brownlee, J. (2023). Supervised and Unsupervised Machine Learning Algorithms.

Cabreira, T. M., Brisolara, L. B., and Ferreira Paulo, R. (2019). Survey on coverage path planning with unmanned aerial vehicles. *Drones*, 3(1):1–38.

Cahalane, C., Walsh, D., Magee, A., Mannion, S., Lewis, P., and McCarthy, T. (2017). Sensor pods: Multi-resolution surveys from a light aircraft. *Inventions*, 2(1):1–16.

Cao, Z., Ma, R., Duan, H., and Xue, K. (2019). Effects of broad bandwidth on the remote sensing of inland waters: Implications for high spatial resolution satellite data applications. *ISPRS Journal of Photogrammetry and Remote Sensing*, 153(2018):110–122.

Carpenter, D. J. and Carpenter, S. M. (1983). Modeling inland water quality using Landsat data. *Remote Sensing of Environment*, 13(4):345–352.

Castro, C. C., Antonio, J., Delgado, J., Alejandro, B., Hinojo, S., Luis, J., Arango, C., Andr, F., Tuya, C., and Ramon, D. (2020). An UAV and Satellite Multispectral Data Approach to Monitor Water Quality in Small Reservoirs. *Remote Sensing*.

Chai, T. and Draxler, R. R. (2014). Root mean square error (RMSE) or mean absolute error (MAE)? -Arguments against avoiding RMSE in the literature. *Geoscientific Model Development*, 7(3):1247–1250.

Chen, H. (2022). *Data Quality for Big Data and Machine Learning" Frontiers in Big Data*. PhD thesis, UNIVERSITY OF NORTH TEXAS.

Chen, Y. and Jiang, J. (2021). A two-stage deep learning registration method for remote sensing images based on sub-image matching. *Remote Sensing*, 13(17).

Cheng, K. H., Chaen, S. N., and Lee, J. H. (2020). Remote sensing of coastal algal blooms using unmanned aerial vehicles (UAVs). *Marine Pollution Bulletin*, 152:1–14.

Chiabrando, F., Giulio Tonolo, F., and Lingua, A. (2019). Uav direct georeferencing approach in an emergency mapping context. the 2016 central Italy earthquake case study. *International Archives of the Photogrammetry, Remote Sensing and Spatial Information Sciences - ISPRS Archives*, 42(2/W13):247–253.

Chrysochou, G. (2016). The evolution of safe navigation: An overview of the technological advance through time. *Marine Sciences and Naval Operations*, (E):49–78.

Colomina, I. (2000). T . O . P . CONCEPTS FOR SENSOR ORIENTATION. *International Archives of Photogrammetry and Remote Sensing*, XXXIII:191–197.

Corbane, C., Politis, P., Kempeneers, P., Simonetti, D., Soille, P., Burger, A., Pesaresi, M., Sabo, F., Syrris, V., and Kemper, T. (2020). A global cloud free pixel-based image composite from Sentinel-2 data. *Data in Brief*, 31:1–8.

Correia, C. A., Andrade, F. A., Sivertsen, A., Guedes, I. P., Pinto, M. F., Manhães, A. G., and Haddad, D. B. (2022). Comprehensive Direct Georeferencing of Aerial Images for Unmanned Aerial Systems Applications. *Sensors*, 22(2):1–25.

Corrigan, O. (2018). *An Investigation Into Machine Learning Solutions Involving Time Series Across Different Problem Domains*. PhD thesis, Dublin City University.

Coulter, L. L., Plummer, M. J., Zamora, N. H., Stow, D. A., and McCreight, R. W. (2019). Assessment of automated multitemporal image co-registration using

repeat station imaging techniques. *GIScience and Remote Sensing*, 56(8):1192–1209.

Cramer, M. (1999). Direct Geocoding - is Aerial Triangulation Obsolete ? *Photogrammetric Week 1999*, pages 59–70.

Cramer, M., Stallmann, D., and Haala, N. (2000). Direct georeferencing using gps/inertial exterior orientations for photogrammetric applications. *International Archives of Photogrammetry and Remote Sensing*, 33(B3):198–205.

Cruz, C., McGuinness, K., Perrin, P. M., O'Connell, J., Martin, J. R., and Connolly, J. (2023a). Improving the mapping of coastal invasive species using UAV imagery and deep learning. *International Journal of Remote Sensing*, 44(18):5713–5735.

Cruz, C., O'Connell, J., McGuinness, K., Martin, J. R., Perrin, P. M., and Connolly, J. (2023b). Assessing the effectiveness of UAV data for accurate coastal dune habitat mapping. *European Journal of Remote Sensing*, 56(1).

DAFM (2015). Food Wise 2025: A 10-year vision for the Irish agri-food industry. Technical report.

Dalton, C. (2018). Natural capital: An inventory of Irish lakes. *Irish Geography*, 51(1):75–92.

De Keukelaere, L., Moelans, R., Knaeps, E., Sterckx, S., Reusen, I., De Munck, D., Simis, S. G., Constantinescu, A. M., Scrieciu, A., Katsouras, G., Mertens, W., Hunter, P. D., Spyrakos, E., and Tyler, A. (2023). Airborne Drones for Water Quality Mapping in Inland, Transitional and Coastal Waters—MapEO Water Data Processing and Validation. *Remote Sensing*, 15(5).

Defrise, M. and Grangeat, P. (2010). Analytical Methods. *Tomography*, pages 21–62.

Delaney, C., Mccarthy, V., French, K., Karki, S., Veerkamp, V., Ahmed, M., Ghaffar, A., Hanafin, J., Mckinstry, A., Jennings, E., and Golden, A. (2023). Remote

Sensing of Irish Surface Waters. Technical Report 443, Environmental Protection Agency, Co. Wexford.

Desmond, M., Duesterwald, E., Brimijoin, K., Brachman, M., and Pan, Q. (2021). Semi-Automated Data Labeling. *Proceedings of Machine Learning Research*, 133:156–169.

DJI (2023). DJI Store. https://store.dji.com/ie/product-search?q=phantom+4 (accessed 20 October 2023).

Dlamini, S., Nhapi, I., Gumindoga, W., Nhiwatiwa, T., and Dube, T. (2016). Assessing the feasibility of integrating remote sensing and in-situ measurements in monitoring water quality status of Lake Chivero, Zimbabwe. *Physics and Chemistry of the Earth*, 93:2–11.

Dreier, A., Janßen, J., Kuhlmann, H., and Klingbeil, L. (2021). Quality analysis of direct georeferencing in aspects of absolute accuracy and precision for a uav-based laser scanning system. *Remote Sensing*, 13(18).

Dwyer, N. (2012). CCRP26 - Status of Ireland's Climate 2012.

Ehmann, K., Kelleher, C., and Condon, L. E. (2019). Monitoring turbidity from above: Deploying small unoccupied aerial vehicles to image in-stream turbidity. *Hydrological Processes*, 33(6):1013–1021.

Ekaso, D., Nex, F., and Kerle, N. (2020). Accuracy assessment of real-time kinematics (RTK) measurements on unmanned aerial vehicles (UAV) for direct georeferencing. *Geo-Spatial Information Science*, 23(2):165–181.

Ellum, C. (2009). *New Strategies for Combining GNSS and Photogrammetric Data*. PhD thesis, UNIVERSITY OF CALGARY.

Engelhardt, F. R. (1999). Remote sensing for oil spill detection and response. *Pure and Applied Chemistry*, 71(1):103–111.

EPA (2023). Water Quality in 2022. Technical report, ENVIRONMENTAL PROTECTION AGENCY, Wexford.

ESA (2023a). SPOT 1,2,3 - https://earth.esa.int/eogateway/missions/spot-2 (accessed 01/02/2024).

ESA (2023b). WorldView - 2. https://earth.esa.int/eogateway/missions/worldview-2 (accessed 20 2023).

European Union Aviation Safety Agency (2019). Easy Access Rules for Unmanned Aircraft Systems (Regulations (EU) 2019/947 and (EU) 2019/945). Technical report.

Faraji, M., Qi, X., and Jensen, A. (2016). Computer vision – based orthorectification and georeferencing of aerial image sets Mohammad Reza Faraji. *Journal of Applied Remote Sensing*, 10(3).

Förstner, W. and Wrobel, B. P. (2016a). *Geometry and Orientation of the Image Triplet*.

Förstner, W. and Wrobel, B. P. (2016b). *Photogrammetric Computer Vision*, volume 64. Springer International Publishing, Bonn.

Franzini, M., Ronchetti, G., Sona, G., and Casella, V. (2019). Geometric and radiometric consistency of parrot sequoia multispectral imagery for precision agriculture applications. *Applied Sciences (Switzerland)*, 9(24).

Fristedt, H. (2017). Homography Estimation using Deep Learning for Registering All-22 Football Video Frames. *Degree Project Computer Science and Engineering*.

Gerum, R. C., Richter, S., Winterl, A., Mark, C., Fabry, B., Le Bohec, C., and Zitterbart, D. P. (2019). CameraTransform: A Python package for perspective corrections and image mapping. *SoftwareX*, 10:100333.

Gevaert, C. M. (2018). *Unmanned aerial vehicle mapping for settlement upgrading*.

Gholizadeh, M. H., Melesse, A. M., and Reddi, L. (2016). A comprehensive review on water quality parameters estimation using remote sensing techniques. *Sensors (Switzerland)*, 16(8).

GIRARD, M.-C. and Girard, C. (2003). *PROCESSING OF REMOTE SENSING DATA*, volume 4. A.A. BALKEMA PUBLISHERS, Dunod, Paris.

Gisev, N., Bell, J. S., and Chen, T. F. (2013). Interrater agreement and interrater reliability: Key concepts, approaches, and applications. *Research in Social and Administrative Pharmacy*, 9(3):330–338.

González-Jaramillo, V., Fries, A., and Bendix, J. (2019). AGB estimation in a tropical mountain forest (TMF) by means of RGB and multispectral images using an unmanned aerial vehicle (UAV). *Remote Sensing*, 11(12):1–22.

Granshaw, S. I. (1980). Bundle Adjustment Methods in Engineering Photogrammetry. *The Photogrammetric Record*, 10(56):181–207.

Granshaw, S. I. (2018). Structure from motion: origins and originality. *Photogrammetric Record*, 33(161):6–10.

Grejner-Brzezinska, D. (2001). Direct Sensor Orientation in Airborne and Land-based Mapping Applications. (461):461.

Grussenmeyer, P. and Al Khalil, O. (2002). Solutions for exterior orientation in photogrammetry: A review. *Photogrammetric Record*, 17(100):615–634.

Gustavsson, K. (2015). *UAV Pose Estimation using Sensor Fusion of Inertial, Sonar and Satellite Signals*. PhD thesis, Uppsala University.

Hajiyev, C., Ersin Soken, H., and Yenal Vural, S. (2015). *State Estimation and Control for Low-cost Unmanned Aerial Vehicles*.

Han, J. Y., Guo, J., and Chou, J. Y. (2011). A direct determination of the orientation parameters in the collinearity equations. *IEEE Geoscience and Remote Sensing Letters*, 8(2):313–316.

Hardy, A., Makame, M., Cross, D., Majambere, S., and Msellem, M. (2017). Using low-cost drones to map malaria vector habitats. *Parasites & Vectors*, 10(29):1–13.

Harris, C. R., Millman, K. J., van der Walt, S. J., Gommers, R., Virtanen, P., Cournapeau, D., Wieser, E., Taylor, J., Berg, S., Smith, N. J., Kern, R., Picus, M., Hoyer, S., van Kerkwijk, M. H., Brett, M., Haldane, A., del Río, J. F., Wiebe, M., Peterson, P., Gérard-Marchant, P., Sheppard, K., Reddy, T., Weckesser, W., Abbasi, H., Gohlke, C., and Oliphant, T. E. (2020). Array programming with NumPy. *Nature*, 585(7825):357–362.

Hastie, T., Tisbshirani, R., and Friedman, J. (2009). *The Elements of Statistical Learning - Data Mining, Interface and Prediction*, volume 2nd. Springer Series in Statistics, second edi edition.

Heipke, C., Jacobsen, K., and Wegmann, H. (2002). Integrated Sensor Orientation Test Report and Workshop Proceedings. Technical Report 43, EUROPEAN ORGANIZATION for EXPERIMENTAL PHOTOGRAMMETRIC RESEARCH, Hannover.

Hunter, J. D. (2007). MATPLOTLIB: A 2D GRAPHICS ENVIRONMENT. *Computing in Science and Engineering*, 9(3):90–95.

Hussnain, Z. (2020). *Position Estimation of Mobile Laser Scanner using Aerial Imagery*. PhD thesis, Universiteit Twente.

Hutton, J. and Mostafa, M. M. (2005). 10 years of Direct Georeferencing for airborne photogrammetry. *Geo-Informations-Systeme*, 2005(11):33–41.

Iglhaut, J., Cabo, C., Puliti, S., Piermattei, L., O'Connor, J., and Rosette, J. (2019). Structure from Motion Photogrammetry in Forestry: a Review. *Current Forestry Reports*, 5(3):155–168.

Ihmeida, M. and Wei, H. (2021). Image Registration Techniques and Applications: Comparative Study on Remote Sensing Imagery. In *Proceedings - International Conference on Developments in eSystems Engineering, DeSE*, pages 142–148. IEEE.

Ip, A., El-Sheimy, N., and Mostafa, M. (2007). Performance analysis of integrated

sensor orientation. *Photogrammetric Engineering and Remote Sensing*, 73(1):89–97.

Ip, A. W. L. (2005). *Analysis of Integrated Sensor Orientation for Aerial Mapping*. PhD thesis, UNIVERSITY OF CALGARY.

Jacobsen, K. (2002). Calibration aspects in direct georeferencing of frame imagery. *International Archives of Photogrammetry Remote Sensing and Spatial Information Sciences*, 34:82–88.

Jacobsen, K. (2005). Direct / Integrated Sensor Orientation - Pros and Cons. *International Archives of the Photogrammetry, Remote Sensing and Spatial Information Sciences - ISPRS Archives*, pages 1–7.

Jaud, M., Le Dantec, N., Ammann, J., Grandjean, P., Constantin, D., Akhtman, Y., Barbieux, K., Allemand, P., Delacourt, C., and Merminod, B. (2018). Direct georeferencing of a pushbroom, lightweight hyperspectral system for mini-UAV applications. *Remote Sensing*, 10(2):1–15.

Jen, Y.-H., Huang, C.-H., Tsai, S., and Chiang, K.-W. (2023). A Multi-IMU Based Self-contained Pedestrian Navigation Algorithm Yi-Han. *International Archives of the Photogrammetry, Remote Sensing and Spatial Information Sciences*, XLVIII(May):1–15.

Jordan, J. (2017). Evaluating a machine learning model.

Jordon, J., Szpruch, L., Houssiau, F., Bottarelli, M., Cherubin, G., Maple, C., Cohen, S. N., and Weller, A. (2022). Synthetic Data – what, why and how? *Cryptography and Security*.

Kabiri, K. (2020). Mapping coastal ecosystems and features using a low-cost standard drone: case study, Nayband Bay, Persian gulf, Iran. *Journal of Coastal Conservation*, 24(5):1–8.

Kellaris, A., Gil, A., Faria, J., Amaral, R., Moreu-Badia, I., Neto, A., and Yesson, C. (2019). Aquatic Conservation - 2019 - Kellaris - Using low-cost drones to mon-

itor heterogeneous submerged seaweed habitats A case.pdf. *Aquatic Conserv: Mar Freshw Ecosyst*, 29:1909–1922.

Keller, S., Maier, P. M., Riese, F. M., Norra, S., Holbach, A., Börsig, N., Wilhelms, A., Moldaenke, C., Zaake, A., and Hinz, S. (2018). Hyperspectral data and machine learning for estimating CDOM, chlorophyll a, diatoms, green algae and turbidity. *International Journal of Environmental Research and Public Health*, 15(9):1–15.

Khaghani, M. and Skaloud, J. (2016). Application of vehicle dynamic modeling in uavs for precise determination of exterior orientation. *International Archives of the Photogrammetry, Remote Sensing and Spatial Information Sciences - ISPRS Archives*, 41(July):827–831.

Khoshelham, K. (2009). Role of tie points in integrated sensor orientation for photogrammetric map compilation. *Photogrammetric Engineering and Remote Sensing*, 75(3):305–311.

Kigo, S. N., Omondi, E. O., and Omolo, B. O. (2023). Assessing predictive performance of supervised machine learning algorithms for a diamond pricing model. *Scientific Reports*, 13(1):1–23.

Kim, M., Wu, G., Yap, P.-T., and Shen, D. (2012). A General Fast Registration Framework by Learning Deformation–Appearance Correlation. *IEEE Trans Image Process*, 21(4):1823–1833.

Knaeps, E., Moelans, R., Strackx, G., Keukelaere, L. D., and Lemey, E. (2019). Mapping Water Quality With Drones Drones : Test Case in Texel. Technical report.

Knaeps, E., Raymaekers, D., Sterckx, S., Bertels, L., and Odermatt, D. (2009). MONITORING INLAND WATERS WITH THE APEX SENSOR , A WAVELET APPROACH VITO – Flemish Institute for Technological Research RSL – Remote Sensing Laboratories , University of Zurich. *Proceedings Whispers conference*, pages 3–6.

Kotsiantis, S. (2007). Supervised Machine Learning: A Review of Classification Techniques. *Informatica*, 237(1):249 –268.

Kraus, K. (2007). *Photogrammetry - Geometry from Images and Laser Scans*, volume 53.

Kubiak, K. A., Kotlarz, J., and Mazur, A. M. (2016). Monitoring cyanobacteria blooms in freshwater lakes using remote sensing methods. *Polish Journal of Environmental Studies*, 25(1):27–35.

Kumar, D. and Simic, M. (2024). What Is Bundle Adjustment ?

Kupssinskü, L. S., Guimarães, T. T., and Souza, E. M. D. (2020). A Method for Chlorophyll-a and Suspended. *Sensors*, 20(2125):1–18.

Ledrew, E. F. and Franklin, S. E. (1983). Small format, hand held helicopter based photography for monitoring industrial water effluent plumes. *Canadian Water Resources Journal*, 8(3):26–38.

Li, H., Li, X., Ding, W., Shi, Y., and Li, Y. (2017). Multi-sensor based high-precision direct georeferencing of medium-altitude unmanned aerial vehicle images. *International Journal of Remote Sensing*, 38(8-10):2577–2602.

Li, J., Ma, L., Fan, Y., Wang, N., Duan, K., Han, Q., Zhang, X., Su, G., Li, C., and Tang, L. (2021). An image stitching method for airborne wide-swath hyperspectral imaging system equipped with multiple imagers. *Remote Sensing*, 13(5):1–24.

Li-Chee-Ming, J., Armenakis, C., and Lee, R. (2012). Mobile Stereo-Mapper: a Portable Kit for Unmanned Aerial Vehicles. *The International Archives of the Photogrammetry, Remote Sensing and Spatial Information Sciences*, XXXVIII-1/(September):241–246.

Lim, Y. C., Abdul Shakor, A. S. a., and Shaharudin, R. (2022). Reliability and Accuracy of 2D Photogrammetry: A Comparison With Direct Measurement. *Frontiers in Public Health*, 9(January):1–9.

Lo, C. F., Tsai, M. L., Chiang, K. W., Chu, C. H., Tsai, G. J., Cheng, C. K., El-Sheimy, N., and Ayman, H. (2015). The Direct Georeferencing application and performance analysis of UAV helicopter in GCP-free area. *International Archives of the Photogrammetry, Remote Sensing and Spatial Information Sciences - ISPRS Archives*, 40(1W4):151–157.

Lo, Y., Fu, L., Lu, T., Huang, H., Kong, L., Xu, Y., and Zhang, C. (2023). Medium-Sized Lake Water Quality Parameters Retrieval Using Multispectral UAV Image and Machine Learning Algorithms : A Case Study of the Yuandang Lake , China. *Drones*.

Losè, L. T., Chiabrando, F., and Tonolo, F. G. (2020). Boosting the timeliness of UAV large scale mapping. Direct georeferencing approaches: Operational strategies and best practices. *ISPRS International Journal of Geo-Information*, 9(10).

Lu, Y., Shen, M., Wang, H., van Rechem, C., and Wei, W. (2021). Machine Learning for Synthetic Data Generation: A Review. *Journal of latex class files*, 14(8):1–18.

Luan, K., Chen, P., Zhang, S., Tong, X., Ma, Y., Wang, W., Shu, R., and Liu, S. (2012). Accuracy analysis of MAMS data using direct georeferencing. *Proceedings of the 2nd International Workshop on Earth Observation and Remote Sensing Applications, EORSA 2012*, (2009):206–209.

Lunetta, R. S., Knight, J. F., Paerl, H. W., Streicher, J. J., Peierls, B. L., Gallo, T., Lyon, J. G., Mace, T. H., and Buzzelli, C. P. (2009). Measurement of water colour using AVIRIS imagery to assess the potential for an operational monitoring capability in the Pamlico Sound Estuary, USA. *International Journal of Remote Sensing*, 30(13):3291–3314.

Luo, Y., Wang, X., Liao, Y., Fu, Q., Shu, C., Wu, Y., and He, Y. (2023). A Review of Homography Estimation: Advances and Challenges. *Electronics (Switzerland)*, 12(24):49–77.

Magee, A. (2023). *A Decision-level Multi-sensor Data Fusion approach to Land Cover Classification*. PhD thesis, Maynooth University.

Maravilla, R. M. G., Quinalayo, J. P., Blanco, A. C., Candido, C. G., Gubatanga, E. V., and Ticman, K. D. V. (2019). Estimation of Chlorophyll-a Concentration in Sampaloc Lake Using Uas Multispectral Remote Sensing and Regression Analysis. *ISPRS - International Archives of the Photogrammetry, Remote Sensing and Spatial Information Sciences*, XLII-4/W19(November):297–303.

Marceau, D. J. and Hay, G. J. (1999). Remote sensing contributions to the scale issue. *Canadian Journal of Remote Sensing*, 25(4):357–366.

Maria, B. and Santana, G. (2021). *Direct Georeferencing of Fire Front Aerial Images using Iterative Ray-Tracing and a Bearings-Range Extended Kalman Filter*. PhD thesis.

Mattivi, P., Pappalardo, S. E., Nikolić, N., Mandolesi, L., Persichetti, A., De Marchi, M., and Masin, R. (2021). Can commercial low-cost drones and open-source gis technologies be suitable for semi-automatic weed mapping for smart farming? A case study in ne italy. *Remote Sensing*, 13(10).

McEliece, R., Hinz, S., Guarini, J. M., and Coston-Guarini, J. (2020). Evaluation of nearshore and offshore water quality assessment using UAV multispectral imagery. *Remote Sensing*, 12(14).

Meersman, R., Tari, Z., and Schmidt, D. C. (2003). *LNCS 2888 - On The Move to Meaningful Internet Systems 2003: CoopIS, DOA, and ODBASE*.

Met Éireann (2023). Sunshine and Solar Radiation - Ireland.

Miller, R. L., Castillo, C. E. D., and Mckee, B. A. (2005). *Remote Sensing of Coastal Aquatic Environments*.

Mitishita, E., Ercolin Filho, L., Graça, N., and Centeno, J. (2016). Approach for Improving the Integrated Sensor Orientation. *ISPRS Annals of Photogrammetry, Remote Sensing and Spatial Information Sciences*, III-1(July):33–39.

Mostafa, M. and Hutton, J. (2001). Direct positioning and orientation systems: How do they work? What is the attainable accuracy. *Proceedings, American Society of Photogrammetry and Remote Sensing Annual Meeting*, page 11.

Mostafa, M. M. R., Hutton, J., and Hill, R. (2010). THEORETICAL GROUND ACCURACY ANALYSIS DERIVED FROM TODAY ' S AIRBORNE DIGITAL FRAME CAMERAS AND DIRECT GEOREFERENCING. In *ASPRS 2010 Annual Conference*, San Diego, California.

Mostafa, Y. and Abdelhafiz, A. (2017). Shadow identification in high resolution satellite images in the presence of water regions. *Photogrammetric Engineering and Remote Sensing*, 83(2):87–94.

Mousavi, V., Varshosaz, M., and Remondino, F. (2021). Evaluating tie points distribution, multiplicity and number on the accuracy of UAV photogrammetry blocks. *International Archives of the Photogrammetry, Remote Sensing and Spatial Information Sciences - ISPRS Archives*, 43(B2-2021):39–46.

Mueksch, M. C. (1995). Airborne hyperspectral monitoring of lake—, river- and estuary pollution in Great Britain and Germany. *Pure and Applied Chemistry*, 2503:122–130.

Murray, C., Larson, A., Goodwill, J., Wang, Y., Cardace, D., and Akanda, A. S. (2022). Water Quality Observations from Space: A Review of Critical Issues and Challenges. *Environments*, 9(125):1–19.

Nagele, P. (2003). Misuse of standard error of the mean (SEM) when reporting variability of a sample. A critical evaluation of four anaesthesia journals. *British Journal of Anaesthesia*, 90(4):514–516.

Narkhede, P., Joseph Raj, A. N., Kumar, V., Karar, V., and Poddar, S. (2019). Least square estimation-based adaptive complimentary filter for attitude estimation. *Transactions of the Institute of Measurement and Control*, 41(1):235–245.

Nex, F., Armenakis, C., Cramer, M., Cucci, D., Gerke, M., Honkavaara, E., Kukko, A., Persello, C., and Skaloud, J. (2022). UAV in the advent of the twenties:

Where we stand and what is next. *ISPRS Journal of Photogrammetry and Remote Sensing*, 184(January):215–242.

Nolze, G. (2006). Representing attitude: Euler angles, unit quaternions, and rotation vectors. *Crystal Research and Technology*, 58:1–35.

Nowakowski, M., Dudek, E., and Rosiński, A. (2023). The Influence of Varying Atmospheric and Space Weather Conditions on the Accuracy of Position Determination. *Sensors*, 23(5).

O'Hara, R. (2019). *The Application of Earth Observation for Mapping Soil Saturation and the Extent and Distribution of Artificial Drainage on Irish Farms*. PhD thesis, Maynooth University.

Otarola, A., de Breuck, C., Travouillon, T., Matsushita, S., Nyman, L., Wootten, A., Radford, S. J., Sarazin, M., Kerber, F., and Pérez-Beaupuits, J. P. (2019). Precipitable water vapor, temperature, and wind statistics at sites suitable for mm and submm wavelength astronomy in Northern Chile. *Astronomical Society of the Pacific*, (February).

Otsuka, H., Sasaki, D., and Nagatani, K. (2018). Reduction of the head-up pitching moment of small quad-rotor unmanned aerial vehicles in uniform flow. *International Journal of Micro Air Vehicles*, 10(1):85–105.

O'Boyle, S., Trodd, W., Bradley, C., D.Tierney, Wilkes, R., Longphuirt, S. N., Smith, J., Stephens, A., Barry, J., Maher, P., McGinn, R., Mockler, E., Deakin, J., Craig, M., and Gurrie, M. (2019). Water Quality in Ireland 2013-2018. Technical report, ENVIRONMENTAL PROTECTION AGENCY, Johnstown Castle, Co. Wexford.

Parrot (2017). Parrot Sequoia - User Guide. Technical report, Parrot.

Pedregosa, F., Varoquaux, G., Gramfort, A., Michael, V., and Thirion, B. (2011). Scikit-learn: Machine Learning in Python Fabian. *Journal ofMachine Learning Research*, 127(9):2825–2830.

Pepe, M., Fregonese, L., and Crocetto, N. (2019). Use of SfM-MVS approach to nadir and oblique images generated throught aerial cameras to build 2.5D map and 3D models in urban areas. *Geocarto International*, 37(1):120–141.

Pfeifer, N., Glira, P., and Briese, C. (2012). Direct Georeferencing With on Board Navigation Components of Light Weight Uav Platforms. *ISPRS - International Archives of the Photogrammetry, Remote Sensing and Spatial Information Sciences*, XXXIX-B7(September):487–492.

PIX4D (2019). Bundle Adjustment.

Pont, T. (2021). Classification Algorithms - Random Forest.

Priestley, M., O'Donnell, F., and Simperl, E. (2023). A Survey of Data Quality Requirements That Matter in ML Development Pipelines. *Journal of Data and Information Quality*, 15(2):11–39.

Prior, E. M., Donnell, F. C. O., Brodbeck, C., Donald, W. N., Runion, G. B., and Shepherd, S. L. (2020a). Measuring High Levels of Total Suspended Solids and Turbidity Using Small Unoccupied Aerial Systems (sUAS) Multispectral Imagery. *Drones*, 4(54):1–15.

Prior, E. M., O'Donnell, F. C., Brodbeck, C., Runion, G. B., and Shepherd, S. L. (2020b). Investigating small unoccupied aerial systems (sUAS) multispectral imagery for total suspended solids and turbidity monitoring in small streams. *International Journal of Remote Sensing*, 00(00):1–26.

Pugnaire, F. I. and Valladares, F. (2007). Functional plant ecology, second edition. *Functional Plant Ecology, Second Edition*, pages 1–727.

Rambat, S. (2011). *A Los-cost Remote Sensing System for Agricultural Applications*. PhD thesis, Aston University.

Reddy, D. S., Reddy, D. R., Usha, R., Chaudhary, A., and Solanki, S. S. (2018). A Machine Learning Approach to Georeferencing. *Proceedings of the 8th International Advance Computing Conference, IACC 2018*, pages 91–95.

Rehak, M. (2017). *Integrated_Sensor_Orientation_Icc.Pdf*. PhD thesis, École Polytechnique Fédérale de Lausanne.

Rehak, M., Mabillard, R., and Skaloud, J. (2013). a Micro-Uav With the Capability of Direct Georeferencing. *ISPRS - International Archives of the Photogrammetry, Remote Sensing and Spatial Information Sciences*, XL-1/W2(September):317–323.

Rehak, M. and Skaloud, J. (2016). Applicability of New Approaches of Sensor Orientation To Micro Aerial Vehicles. *ISPRS Annals of Photogrammetry, Remote Sensing and Spatial Information Sciences*, III-3(July):441–447.

Richards, K. (2009). *Key Concepts in Geography*. SAGE, London, second edi edition.

Robinson, T. R., Rosser, N., and Walters, R. J. (2019). The Spatial and Temporal Influence of Cloud Cover on Satellite-Based Emergency Mapping of Earthquake Disasters. *Scientific Reports*, 9(1):1–9.

Roman, A., Heredia, S., Windle, A. E., Tovar-s, A., and Navarro, G. (2024). Enhancing Georeferencing and Mosaicking Techniques over Water Surfaces with High-Resolution Unmanned Aerial Vehicle. *Remote Sensing*, 16(290):1–18.

Román, A., Tovar-Sánchez, A., Gauci, A., Deidun, A., Caballero, I., Colica, E., D'Amico, S., and Navarro, G. (2023). Water-Quality Monitoring with a UAV-Mounted Multispectral Camera in Coastal Waters. *Remote Sensing*, 15(1).

Roth, K. L., Roberts, D. A., Dennison, P. E., Peterson, S. H., and Alonzo, M. (2015). The impact of spatial resolution on the classification of plant species and functional types within imaging spectrometer data. *Remote Sensing of Environment*, 171:45–57.

Salahat, E. and Qasaimeh, M. (2017). Recent advances in features extraction and description algorithms: A comprehensive survey. *Proceedings of the IEEE International Conference on Industrial Technology*, pages 1059–1063.

Sathishkumar, V. E. and Cho, Y. (2020). A rule-based model for Seoul Bike sharing demand prediction using weather data. *European Journal of Remote Sensing*, 53:166–183.

Scarpace, F. L., Holmquist, K. W., and Fisher, L. T. (1979). Landsat analysis of lake quality. *Photogrammetr. Eng. Remote Sens.*, 45(5):623–633.

Scheffler, D., Hollstein, A., Diedrich, H., Segl, K., and Hostert, P. (2017). AROSICS: An automated and robust open-source image co-registration software for multi-sensor satellite data. *Remote Sensing*, 9(7).

Schofield, W. and Breach, M. (2007). *Engineering Surveying*, volume 2.

Schubert, M., Riedlinger, T., Kahl, K., Kröll, D., Schoenen, S., Šegvić, S., and Rottmann, M. (2023). Identifying Label Errors in Object Detection Datasets by Loss Inspection. *Computer Vision and Pattern Recognition*, pages 1–16.

Sekrecka, A., Wierzbicki, D., and Kedzierski, M. (2020). Influence of the sun position and platform orientation on the quality of imagery obtained from unmanned aerial vehicles. *Remote Sensing*, 12(6).

Shariat, M., Azizi, A., and Saadatseresht, M. (2008). Analysis and the solutions for generating a true digital ortho photo in close range photogrammetry. *The International Archives of Photogrammetry, Remote Sensing, and Spatial Information Sciences*, 37:439–422.

Shylaja, P. and Sanil Shanker, K. P. (2022). A systematic investigation on Geometric Transformation. *Proceedings of the 2022 3rd International Conference on Intelligent Computing, Instrumentation and Control Technologies: Computational Intelligence for Smart Systems, ICICICT 2022*, pages 343–350.

Soares, A. P. (2013). Exploring the Range of Weather Impacts on Uas Operations. *Journal of Chemical Information and Modeling*, 53(9):1689–1699.

Song, H., Yang, C., Zhang, J., Hoffmann, W. C., He, D., and Thomasson, J. A.

(2016). Comparison of mosaicking techniques for airborne images from consumer-grade cameras. *Journal of Applied Remote Sensing*, 10(1):016030.

Srivastava, A. (2020). Advances in Smart Communication and Imaging Systems. In Agrawal, R., Goyal, A., and Singh, C., editors, *Impact of K-Nearest Neighbour on Classification Accuracy in KNN Algorithm Using Machine Learning.*, chapter 25, pages 363–373. Springer Nature Singapore.

Stam, J. (2010). *Accuracy Assesment of Direct Sensor Orientation in UAV Photogrammetry*. PhD thesis, TU Delft.

Stöcker, E. C. (2021). *Unmanned Aerial Vehicle Mapping for Responsible Land Administration*. PhD thesis, University of twente.

Strong, A. E. (1974). Remote sensing of algal blooms by aircraft and satellite in Lake Erie and Utah Lake. *Remote Sensing of Environment*, 3(2):99–107.

Su, T. C. and Chou, H. T. (2015). Application of multispectral sensors carried on unmanned aerial vehicle (UAV) to trophic state mapping of small reservoirs: A case study of Tain-Pu reservoir in Kinmen, Taiwan. *Remote Sensing*, 7(8):10078–10097.

Suo, C., McGovern, E., Gilmer, A., and Cahalane, C. (2020). A comparison of high-end methods for topographic modelling of a coastal dune complex. *Journal of Coastal Conservation*, 24(4).

Syetiawan, A., Gularso, H., Kusnadi, G. I., and Pramudita, G. N. (2020). Precise topographic mapping using direct georeferencing in UAV. *IOP Conference Series: Earth and Environmental Science*, 500(1).

Taha, A., Rabah, M., Mohie, R., Elhadary, A., and Ghanem, E. (2022). Assessment of Using UAV Imagery over Featureless Surfaces for Topographic Applications. *MEJ. Mansoura Engineering Journal*, 47(1):25–34.

Tamás Fráter, Tatjána Juzsakova, János Lauer, László Dióssy, and Ákos Rédey (2015). Unmanned Aerial Vehicles in Environmental Monitoring—An Efficient

Way for Remote Sensing. *Journal of Environmental Science and Engineering A*, 4(2):85–91.

Tanathong, S. and Lee, I. (2014). Integrated sensor orientation simulator: Design and implementation. *European Journal of Remote Sensing*, 47(1):497–512.

Tazartes, D. (2014). An historical perspective on inertial navigation systems. *1st IEEE International Symposium on Inertial Sensors and Systems, ISISS 2014 - Proceedings*, pages 2–6.

Teppati Losè, L., Chiabrando, F., Giulio Tonolo, F., and Lingua, A. (2021). Uav photogrammetry and vhr satellite imagery for emergency mapping. The october 2020 flood in limone piemonte (Italy). *International Archives of the Photogrammetry, Remote Sensing and Spatial Information Sciences - ISPRS Archives*, 43(B3-2021):727–734.

Thiruchittampalam, S., Singh, S. K., Banerjee, B. P., Glenn, N. F., and Raval, S. (2023). Spoil characterisation using UAV-based optical remote sensing in coal mine dumps. *International Journal of Coal Science and Technology*, 10(1).

Toso, M., Pennestrì, E., and Rossi, V. (2015). ESA multibody simulator for spacecrafts' ascent and landing in a microgravity environment. *CEAS Space Journal*, 7(3):335–346.

Triggs, B., McLauchlan, P. F., Hartley, R. I., and Fitzgibbon, A. W. (2000). Bundle adjustment – a modern synthesis. *Vision Algorithms*, 1883:298–372.

Trodd, W., O'Boyle, and Gurrie, M. (2022). Water Quality in Ireland Water Quality in Ireland : A Summary. Technical report, Environmental Protection Agency, Wexford.

Trodd, W. and O'Boyle, S. (2021). Water Quality in 2020.

Tzanidou, G., Climent-Pérez, P., Hummel, G., Schmitt, M., Stütz, P., Monekosso, D. N., and Remagnino, P. (2015). Telemetry assisted frame registration and

background subtraction in low-altitude UAV videos. *AVSS 2015 - 12th IEEE International Conference on Advanced Video and Signal Based Surveillance*.

United Nations (2015). UN General Assembly, Transforming our world: The 2030 agenda for sustainable development. *Resolution adopted by the General Assembly on 25 September 2015*, 16301(October):1–35.

United Nations Water (2017). Integrated Monitoring Guide for SDG 6 Step-by-step monitoring methodology for indicator 6.3.2 on ambient water quality. Technical Report January.

USGS (2017). *Landsat 8 (L8) Full Resolution Browse (Frb) Data Format Control Book (Dfcb)*, volume 8. South Dakota.

Utlu, M. and Özdemir, H. (2020). How much spatial resolution do we need to model a local flood event? Benchmark testing based on UAV data from Biga River (Turkey). *Arabian Journal of Geosciences*, 13(24).

Verykokou, S. and Ioannidis, C. (2018). Oblique aerial images: a review focusing on georeferencing procedures. *International Journal of Remote Sensing*, 39(11):3452–3496.

Vitti, D. M. d. C., Marques Junior, A., Guimarães, T. T., Koste, E. C., Inocencio, L. C., Veronez, M. R., and Mauad, F. F. (2019). Geometry accuracy of DSM in water body margin obtained from an RGB camera with NIR band and a multispectral sensor embedded in UAV. *European Journal of Remote Sensing*, 52(sup1):160–173.

Wang, S., Ding, L., Chen, Z., and Dou, A. (2018). A rapid UAV image georeference algorithm developed for emergency response. *Journal of Sensors*, 2018.

Warner, T. A., Nellis, M. D., and Foody, G. M. (2008). Remote Sensing Scale and Data Selection Issues. *The SAGE Handbook of Remote Sensing*, pages 3–32.

Wegmann, H. (2002). Image Orientation by Combined (A)AT with GPS and IMU. *Proceedings of ISPRS Commission I Mid-term Symposium*, 11(1):278–283.

Wei, L., Cao, X., Wang, Z., Gao, Y., Hu, S., Wu, G., Wang, L., and Sen, D. (2017). Learning-based deformable registration for infant MRI by integrating random forest with auto-context model. *Medical Physics*, 44(12):6289–6303.

Williams, T., Williams, B., Song, B., O'Halloran, T. L., and Forsythe, J. (2022). Mapping Natural Forest Stands With Low-Cost Drones. *Mathematical and Computational Forestry and Natural-Resource Sciences*, 14(1):33–43.

Windle, A. E. and Silsbe, G. M. (2021). Evaluation of Unoccupied Aircraft System (UAS) Remote Sensing Reflectance Retrievals for Water Quality Monitoring in Coastal Waters. *Frontiers in Environmental Science*, 9(May):1–15.

Wolf, P. R., Dewitt, B. A., and Wilkinson, B. E. (2014). *Elements of Photogrammetry with Application in GIS*, volume 110.

Wu, D., Li, R., Liu, J., and Khan, N. (2023). Monitoring Algal Blooms in Small Lakes Using Drones: A Case Study in Southern Illinois. *Journal of Contemporary Water Research & Education*, 177(1):83–93.

Wu, D., Li, R., Zhang, F., and Liu, J. (2019). A review on drone-based harmful algae blooms monitoring. *Environmental Monitoring and Assessment*, 191(4).

Wu, H. and Li, Z. L. (2009). Scale issues in remote sensing: A review on analysis, processing and modeling. *Sensors*, 9(3):1768–1793.

Wu, Y., Fang, S., Xu, Y., Wang, L., Li, X., Pei, Z., and Wu, D. (2021). Analyzing the Probability of Acquiring Cloud-Free Imagery in China with AVHRR Cloud Mask Data. *Atmosphere*, 12(2):214.

Xiao, Y., Guo, Y., Yin, G., Zhang, X., Shi, Y., Hao, F., and Fu, Y. (2022). UAV Multispectral Image-Based Urban River Water Quality Monitoring Using Stacked Ensemble Machine Learning Algorithms—A Case Study of the Zhanghe River, China. *Remote Sensing*, 14(14).

Xiong, Z. and Zhang, Y. (2010). A critical review of image registration methods. *International Journal of Image and Data Fusion*, 1(2):137–158.

Yan, W. (2017). *Development of an Algorithm for a GNSS/MEMS- IMU/Imaging Coupled System for Direct Georeferencing*. PhD thesis.

Yang, Y., Liu, Z., and Zhang, J. (2019). Remote Sensing Image Registration Algorithm Based on Multi-scale Corner and Haar Transformation. *IOP Conference Series: Earth and Environmental Science*, 300(2).

Yastikli, N. and Jacobsen, K. (2005). Influence of system calibration on direct sensor orientation. *Photogrammetric Engineering and Remote Sensing*, 71(5):629–633.

Yastikli, N., Jacobsen, K., and Faculty, C. E. (2002). Investigation of direct sensor orientation for dem generation. *International Archives of Photogrammetry and Remote Sensing*, xxxiv:298–304.

Ye, Z., Kang, J., Yao, J., Song, W., Liu, S., Luo, X., Xu, Y., and Tong, X. (2020). Robust fine registration of multisensor remote sensing images based on enhanced subpixel phase correlation. *Sensors (Switzerland)*, 20(15):1–21.

Ying, H., Xia, K., Huang, X., Feng, H., Yang, Y., Du, X., and Huang, L. (2021). Evaluation of water quality based on UAV images and the IMP-MPP algorithm. *Ecological Informatics*, 61(January):101239.

Yu, X., Lu, D., Jiang, X., Li, G., Chen, Y., Li, D., and Chen, E. (2020). Examining the roles of spectral, spatial, and topographic features in improving land-cover and forest classifications in a subtropical region. *Remote Sensing*, 12(18):1–24.

Yuan, X. and Zhang, X. (2008). Theoretical accuracy of direct georeferencing with position and orientation system in aerial photogrammetry. *International Archives of the Photogrammetry, Remote Sensing and Spatial Information Sciences - ISPRS Archives*, 37:617–622.

Zeng, R., Eng, M., and Thesis, P. (2019). *Homography Estimation: From Geometry to Deep Learning*. PhD thesis.

Zhang, X., Zhou, Y., Qiao, P., Lv, X., Li, J., Du, T., and Cai, Y. (2023). Image Registration Algorithm for Remote Sensing Images Based on Pixel Location Information. *Remote Sensing*, 15(2).

Zhao, X., Li, H., Wang, P., and Jing, L. (2020). An Image Registration Method for Multisource High-Resolution Remote Sensing Images for. *Sensors*, 20(2286):1–22.

Zhao, X., Li, Y., Chen, Y., Qiao, X., and Qian, W. (2022). Water Chlorophyll a Estimation Using UAV-Based Multispectral Data and Machine Learning. *Drones*, 7(1):2.

Zheng, G. and DiGiacomo, P. M. (2017). Remote sensing of chlorophyll-a in coastal waters based on the light absorption coefficient of phytoplankton. *Remote Sensing of Environment*, 201(September):331–341.

Appendices

Appendix A : Detail Calculation of Changes in Pitch and Roll

Table 1: Below gives a detail calculation for changes in Pitch angle and its corresponding error

	Ori Error in X and Y (m)		**Total Error (m)**	**Ori and GNSS Error in X and Y (m)**		**Total Error (m)**	**Ori and IMU Error in X and Y (m)**		**Total Error (m)**	**Ori, GNSS and IMU Error in X and Y (m)**		**Total Error (m)**
Pitch	X	Y	Error (X,Y)	X	Y	Error (X,Y)	X	Y	Error (X,Y)	X	Y	Error (X,Y)
1°	0.02	2.11	2.11	1.09	3.18	3.61	1.02	3.11	3.51	2.09	4.18	5.01
2°	0.04	4.23	4.23	1.11	5.30	5.73	1.04	5.23	5.63	2.11	6.30	7.13
3°	0.06	6.36	6.36	1.13	7.43	7.86	1.06	7.36	7.76	2.13	8.43	9.26
4°	0.08	8.50	8.50	1.15	9.57	10.00	1.08	9.50	9.90	2.15	10.57	11.40
5°	0.11	10.65	10.65	1.18	11.72	12.15	1.11	11.65	12.05	2.18	12.72	13.55
6°	0.14	12.81	12.81	1.21	13.88	14.31	1.14	13.81	14.21	2.21	14.88	15.71
7°	0.18	14.99	14.99	1.25	16.06	16.49	1.18	15.99	16.39	2.25	17.06	17.89
8°	0.22	17.18	17.18	1.29	18.25	18.68	1.22	18.18	18.58	2.29	19.25	20.08

Table 2: Below gives a Detailed Calculation for Changes in Roll Angle and its Corresponding Error

	Ori Error in X and Y (m)		**Total Error (m)**	**Ori and GNSS Error in X and Y (m)**		**Total Error (m)**	**Ori and IMU Error in X and Y (m)**		**Total Error (m)**	**Ori, GNSS and IMU Error in X and Y (m)**		**Total Error (m)**
Roll	X	Y	Error (X,Y)	X	Y	Error (X,Y)	X	Y	Error (X,Y)	X	Y	Error (X,Y)
1°	2.11	0.02	2.11	3.18	1.09	3.61	3.11	1.02	3.51	4.18	2.09	5.01
2°	4.23	0.04	4.23	5.30	1.11	5.73	5.23	1.04	5.63	6.30	2.11	7.13
3°	6.36	0.06	6.36	7.43	1.13	7.86	7.36	1.06	7.76	8.43	2.13	9.26
4°	8.50	0.08	8.50	9.57	1.15	10.00	9.50	1.08	9.90	10.57	2.15	11.40
5°	10.65	0.11	10.65	11.72	1.18	12.15	11.65	1.11	12.05	12.72	2.18	13.55
6°	12.81	0.14	12.81	13.88	1.21	14.31	13.81	1.14	14.21	14.88	2.21	15.71
7°	14.99	0.18	14.99	16.06	1.25	16.49	15.99	1.18	16.39	17.06	2.25	17.89
8°	17.18	0.22	17.18	18.25	1.29	18.68	18.18	1.22	18.58	19.25	2.29	20.08

Appendix B : Drone Trajectory

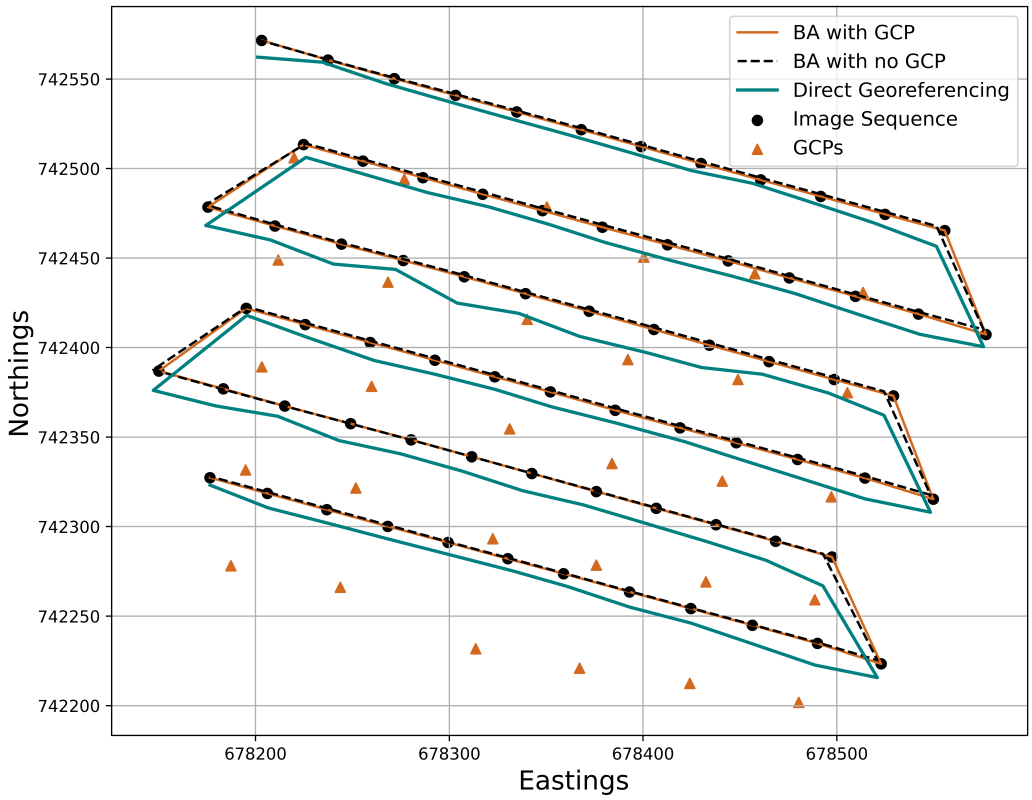

Figure 1: Drone trajectory with photo centers and GCP's showing the positional accuracy for Direct Georeferencing before correction,and compares the result to BA with GCPs and BA with no GCPs.

Appendix C : Example Results of Mosaicked Drone Datasets

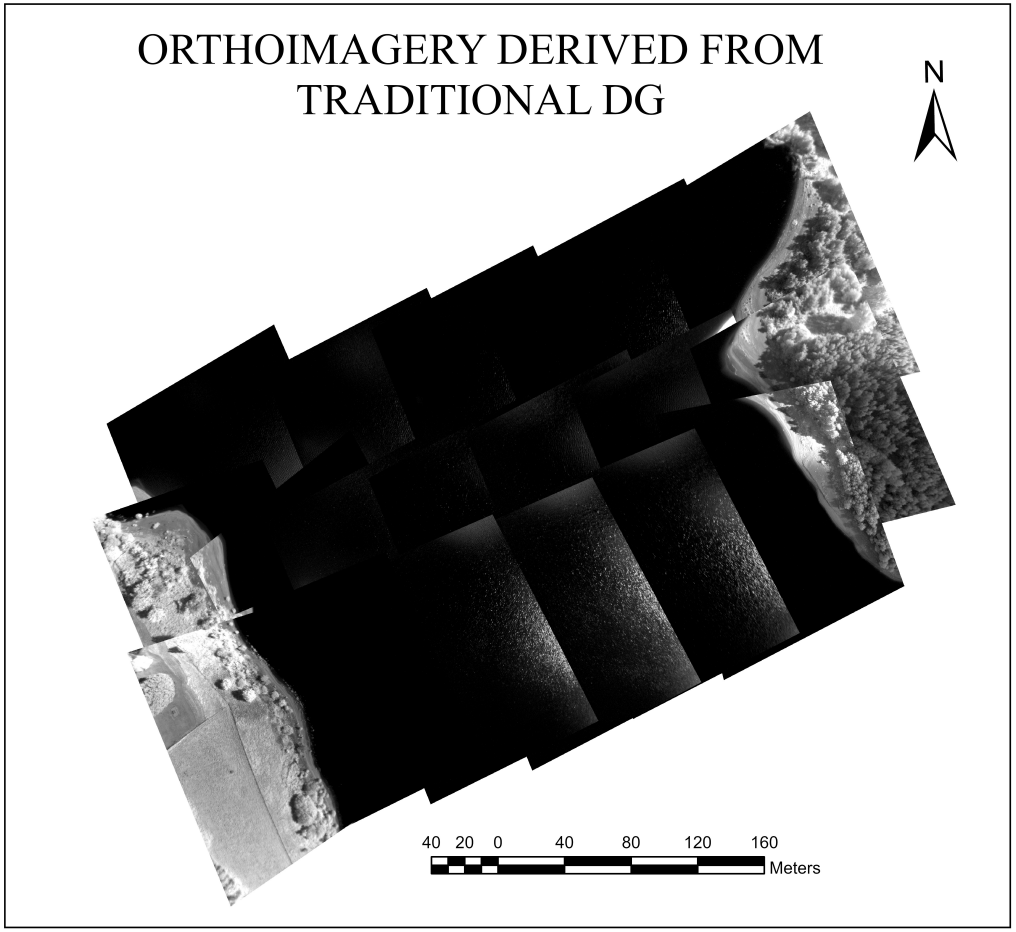

Figure 2: An orthomosaic of a drone dataset over water via the traditional DG.

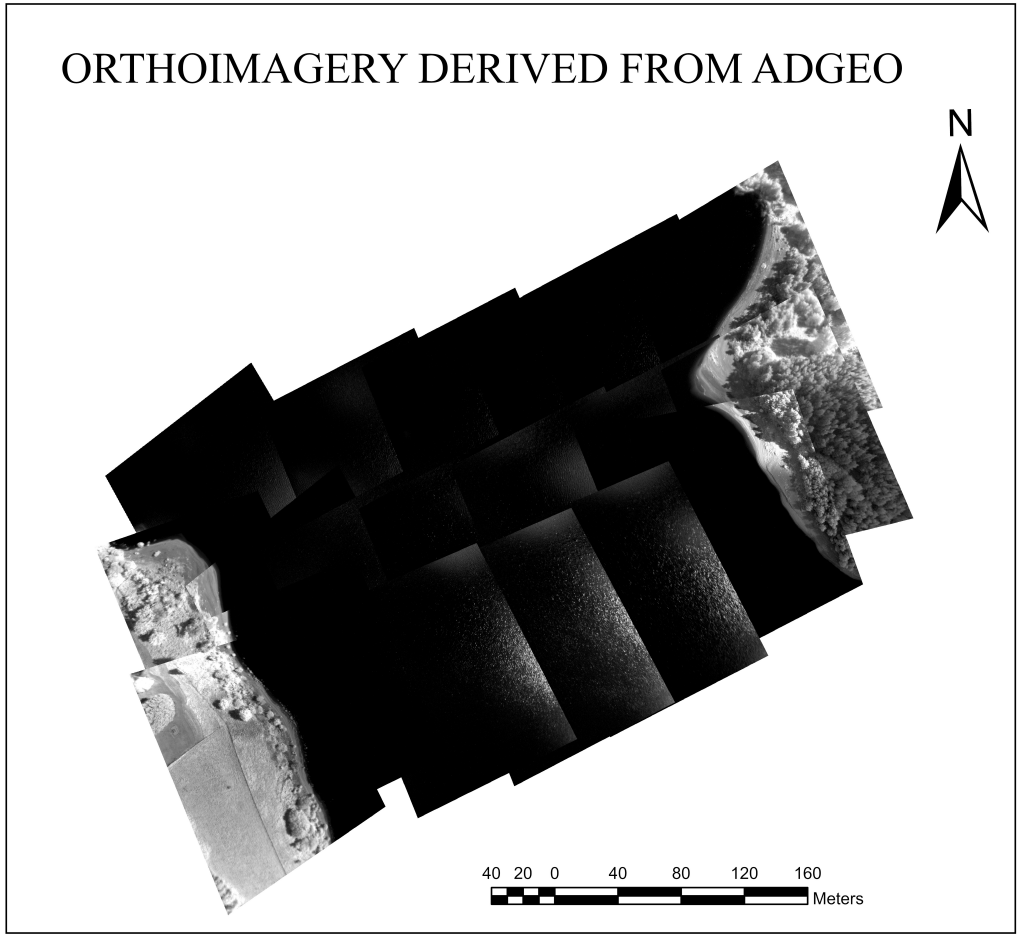

Figure 3: An orthomosaic of a drone dataset over water via the ADGEO method

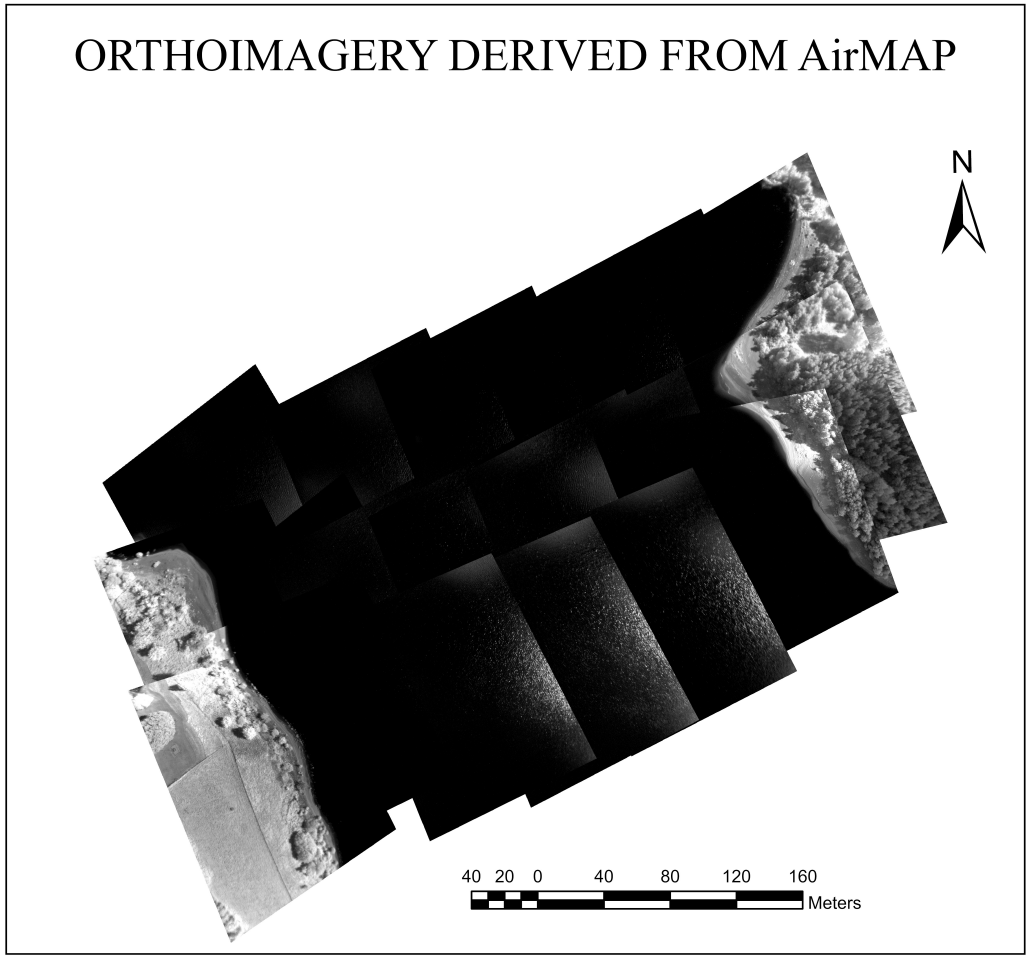

Figure 4: An orthomosaic of a drone dataset over water via the AirMAP method